Anisotropic galaxy clustering measurements in Fourier space and cosmological implications from the BOSS DR12 sample

Jan Niklas Grieb

München 2016

Anisotropic galaxy clustering measurements in Fourier space and cosmological implications from the BOSS DR12 sample

Jan Niklas Grieb

Dissertation

an der Fakultät für Physik
der Ludwig–Maximilians–Universität München
zur Erlangung des Grades
Doktor der Naturwissenschaften (Dr. rer. nat.)

vorgelegt von

Jan Niklas Grieb
aus Gießen

München, den 19.02.2016

Erstgutachter: Prof. Dr. Ralf Bender
Zweitgutachter: Prof. Dr. Eiichiro Komatsu
Tag der mündlichen Prüfung: 05.04.2016

Zusammenfassung

Moderne Rotverschiebungs-Galaxiendurchmusterungen können mittels Mehrfach-Faser-Spektroskopie große Bereiche des Himmels abdecken. Dank der immer größer werdenden Datensätze hat sich die Analyse der großskaligen Galaxienverteilung im Universum zu einer unschätzbaren Wissensquelle für die Kosmologie entwickelt. Zusammen mit den Beobachtungen des kosmischen Mikrowellenhintergrunds (MWH) und Entfernungsbestimmungen anhand von großen Typ-Ia-Supernova-Datensätzen (SN) bilden die Galaxiendurchmusterungen ausschlaggebende Indikatoren für die Korrektheit der Paradigmen des kosmologischen Weltbilds, des ΛCDM-Modells. Die Auswertung der Galaxienverteilung erlaubt mit Hilfe des Standardlineals, das durch die Baryonisch-akustischen Oszillationen gegeben ist, Entfernungsmessungen von ungesehener Präzision. Dies gewährt Einblick in die zugrundeliegende physikalische Natur der Dunklen Energie (DE), welche für die Beschleunigung der Ausdehung unseres Universums verantwortlich gemacht wird, indem die zeitliche Entwicklung der DE-Zustandsgleichung eingeschränkt werden kann. Zudem kann aus dem Signal der Verzerrungen im Rotverschiebungsraum die Wachstumsrate von kosmologischer Struktur bestimmt werden. Dies stellt einen Test der Relativitätstheorie dar, weil mögliche erweiterte Gravitationstheorien abweichende Wachstumsraten vorhersagen können.

Die abgeschlossenen Rotverschiebungsmessungen des ‘Baryon Acoustic Oscillation Survey’-Programms (kurz BOSS) brachten einen Galaxienkatalog hervor, der ein bisher unerreichtes Volumen abdeckt. In dieser Dissertation wird die kosmologische Information, die im räumlichen Leistungsdichtespektrum (LDS) der Rotverschiebungsraum-Galaxienverteilung des BOSS-Katalogs enthalten ist, genutzt, um den Parameterraum des ΛCDM-Modells und der wichtigsten möglichen Erweiterungen einzuschränken. Vorherige Analysen des anisotropen Galaxien-LDS waren auf die Messung der Multipolzerlegung beschränkt. Für die hier präsentierte Analyse wurde das Konzept der sogenannten ‘Clustering Wedges’ auf den Fourierraum übertragen, um einen komplementären Ansatz zur Vermessung des anisotropen LDS zu verfolgen. Dazu wird der varianzoptimierte Schätzer für LDS-Wedges definiert und an die Galaxiengewichtung, die unvermeidbare Beobachtungsfehler im BOSS-Katalog behebt, angepasst. Zudem wird auch

der Formalismus zur Beschreibung der Fensterfunktion auf die Wedges erweitert.

Das verwendete Modell für das anistrope Galaxien-LDS ist auf neuartigen Ansätzen zur Modellierung der nichtlinearen Gravitationsdynamik und der Verzerrungen im Rotverschiebungsraum aufgebaut, welche die Genauigkeit der Modellvorhersagen speziell im Übergang in den nichtlinearen Bereich signifikant verbessern. Daher kann das LDS bis zu kleineren Skalen als in vorherigen Analysen ausgewertet werden, wodurch engere Einschränkungen des kosmologischen Parameterraums erreicht werden. Die Modellierung wurde mit Hilfe von synthetischen Katalogen, die auf großvolumigen Mehrkörpersimulationen basieren, verifiziert. Dazu ist eine theoretische Vorhersage der Kovarianzmatrix der anisotropischen Vermessung der Galaxienverteilung nötig, wofür ein Gaußsches Vorhersagemodell entwickelt wurde. Dieses ist neben den Wedges auch für die komplementäre Multipolzerlegung sowohl des LDS als auch dessen Fouriertransformierten, der Zwei-Punkt-Korrelationsfunktion, anwendbar.

Die LDS-Analyse anhand von Clustering Wedges, wie in dieser Arbeit präsentiert, ist Teil der kombinierten Analyse des finalen Galaxienkatalogs im Rahmen der BOSS-Kollaboration. Unter Verwendung von zwei sich nicht überschneidenden Rotverschiebungsbereichen wird die Winkeldurchmesserentfernung zu $D_\mathrm{M}(z_\mathrm{eff} = 0.38)\,(r_\mathrm{d}^\mathrm{fid}/r_\mathrm{d}) = 1525 \pm 24\ h^{-1}\,\mathrm{Mpc}$ und $D_\mathrm{M}(z_\mathrm{eff} = 0.61)\,(r_\mathrm{d}^\mathrm{fid}/r_\mathrm{d}) = 2281^{+42}_{-43}\ h^{-1}\,\mathrm{Mpc}$ bestimmt. Weiterhin wird der Hubbleparameter zu $H(z_\mathrm{eff} = 0.38)\,(r_\mathrm{d}/r_\mathrm{d}^\mathrm{fid}) = 81.2^{+2.2}_{-2.3}\,\mathrm{km\,s^{-1}\,Mpc^{-1}}$ und $H(z_\mathrm{eff} = 0.61)\,(r_\mathrm{d}/r_\mathrm{d}^\mathrm{fid}) = 94.9 \pm 2.5\,\mathrm{km\,s^{-1}\,Mpc^{-1}}$ vermessen (alle hier angegebenen Bereiche entsprechen einem Konfidenzintervall von 68%). Die Wachstumsrate wird eingeschränkt auf $f\,\sigma_8(z_\mathrm{eff} = 0.38) = 0.498^{+0.044}_{-0.045}$ und $f\,\sigma_8(z_\mathrm{eff} = 0.61) = 0.409 \pm 0.040$. Zusammen mit den Ergebnissen der komplementären Methoden, die innerhalb der BOSS-Kollaboration zur Clustering-Analyse des finalen Galaxienkatalogs eingesetzt werden, werden diese Resultate zu einem abschließenden Konsensergebnis zusammengefasst.

Nur mit den Clustering-Weges-Messungen im Fourierraum, kombiniert mit MWH- und SN-Daten, kann der Materiedichteparameter auf $\Omega_\mathrm{M} = 0.311^{+0.009}_{-0.010}$ und die Hubble-Konstante auf $H_0 = 67.6^{+0.7}_{-0.6}\,\mathrm{km\,s^{-1}\,Mpc^{-1}}$ unter Annahme des ΛCDM-Modells eingeschränken werden. Wird ein Nichtstandard-Modell für DE angenommen, so ergibt sich ein DE-Zustandsgleichungsparameter von $w_\mathrm{DE} = 1.019^{+0.048}_{-0.039}$. Modifikationen der Wachstumsrate, parametrisiert durch $f(z) = [\Omega_\mathrm{M}(z)]^\gamma$, werden auf $\gamma = 0.52 \pm 0.10$ eingeschränkt. Diese beiden Messungen sind in perfekter Übereinstimmung mit den Vorhersagen des ΛCDM-Modells, ebenso wie weitere Ergebnisse, die sich unter der Annahme eines noch großzügigeren DE-Modells (welches eine zeitliche Entwicklung von w_DE erlaubt) ergeben. Daher wird das ΛCDM-Modell durch die hier beschriebene Analyse weiter gefestigt.

Die Summe der Neutrinomassen wird zu $\sum m_\nu < 0.143\,\mathrm{eV}$ bestimmt. Dieses obere Limit befindet sich nicht weit entfernt von der unteren Schranke, die sich aus Teilchenphysik-Experimenten ergibt. Somit ist zu erwarten, dass die kosmologische Signatur, die massebehaftete Neutrinos in der großskaligen Struktur des Universums hinterlassen, in naher Zukunft detektiert werden kann.

Abstract

Galaxy surveys cover a large fraction of the celestial sphere using modern multi-fibre spectrographs. Thanks to ever increasing datasets, the analysis of the large-scale structure (LSS) of the Universe has become a prolific source of cosmological information. Together with the observations of the cosmic microwave background (CMB) and samples of supernova (SN) of type Ia, they helped to establish the standard cosmological paradigm, the ΛCDM model. From the analysis of redshift-space galaxy clustering, the expansion history of the Universe can be inferred using the feature of Baryon Acoustic Oscillations (BAO) as a standard ruler to measure cosmic distances. The growth rate of cosmic structure can also be determined using redshift-space distortions (RSD). These measurements provide insight into competing alternatives of the ΛCDM model. The nature of the Dark Energy (DE), a strange component that is believed to be responsible for the current phase of accelerating expansion of the Universe, can be unravelled from BAO measurements of the late-time expansion. Modified theories of gravity can be constrained from the growth rate extracted from RSD, which can deviate from the prediction of general relativity.

The redshift measurements of the Baryon Acoustic Oscillation Survey (BOSS) program that was completed in 2014 yielded a galaxy sample that covers an unprecedented volume. In this thesis, the standard model and its most important extensions are analysed using the cosmological information in the full-shape of the redshift-space two-point statistics measured from the final BOSS galaxy sample. So far, anisotropic clustering analyses in Fourier space relied on power spectrum multipole measurements. For this work, the concept of clustering wedges was extended to Fourier space to establish a complementary approach to measure clustering anisotropies: we introduce the optimal-variance estimator for clustering wedges, which is designed to account for systematic weights that correct the observational incompleteness of the BOSS sample, and also develop the window function formalism for the wedges.

Our modelling of the anisotropic galaxy clustering is based on novel approaches for the description of non-linear gravitational dynamics and redshift-space distortions. This improved modelling allows us to include smaller scales in our full-shape fits than in previous BAO+RSD

studies, resulting in tighter cosmological constraints. The galaxy clustering model is verified using synthetic catalogues based on large-volume N-body simulations. As this test requires a theoretical description for the anisotropic clustering covariance matrix, a Gaussian formalism was developed for that purpose. As a side project, this formalism is extended to describe clustering wedges and multipoles in Fourier and configuration space.

The Fourier-space clustering measurements presented in this thesis are part of the joint analysis of the final BOSS sample. Using two non-overlapping redshift bins, we measure an angular diameter distance of $D_\mathrm{M}(z_\mathrm{eff} = 0.38)\,(r_\mathrm{d}^\mathrm{fid}/r_\mathrm{d}) = 1525 \pm 24\ h^{-1}\,\mathrm{Mpc}$ and $D_\mathrm{M}(z_\mathrm{eff} = 0.61)\,(r_\mathrm{d}^\mathrm{fid}/r_\mathrm{d}) = 2281^{+42}_{-43}\ h^{-1}\,\mathrm{Mpc}$, as well as a Hubble parameter of $H(z_\mathrm{eff} = 0.38)\,(r_\mathrm{d}/r_\mathrm{d}^\mathrm{fid}) = 81.2^{+2.2}_{-2.3}\,\mathrm{km\,s^{-1}\,Mpc^{-1}}$ and $H(z_\mathrm{eff} = 0.61)\,(r_\mathrm{d}/r_\mathrm{d}^\mathrm{fid}) = 94.9 \pm 2.5\,\mathrm{km\,s^{-1}\,Mpc^{-1}}$ (all limits correspond to the statistical error of a confidence level of 68%). The growth rate is constrained to $f\,\sigma_8(z_\mathrm{eff} = 0.38) = 0.498^{+0.044}_{-0.045}$ and $f\,\sigma_8(z_\mathrm{eff} = 0.61) = 0.409 \pm 0.040$. These measurements will be combined with the complementary results from other galaxy clustering methods in configuration and Fourier space in order to determine the final BOSS consensus measurements.

From our analysis alone, in combination with CMB and SN Ia data, we obtain a matter density parameter of $\Omega_\mathrm{M} = 0.311^{+0.009}_{-0.010}$ and a local Hubble parameter of $H_0 = 67.6^{+0.7}_{-0.6}\,\mathrm{km\,s^{-1}\,Mpc^{-1}}$ assuming a ΛCDM cosmology. Allowing for a non-standard DE model, we find an equation-of-state parameter of $w_\mathrm{DE} = 1.019^{+0.048}_{-0.039}$. Modifications of the growth rate, parametrized as $f(z) = [\Omega_\mathrm{M}(z)]^\gamma$, are constrained to $\gamma = 0.52 \pm 0.10$. These two results, along with those obtained using a more general DE model to identify a time-evolution of w_DE, are in perfect agreement with the ΛCDM predictions. Thus, the standard paradigm is further consolidated by our analysis.

The sum of neutrino masses is found to be $\sum m_\nu < 0.143\,\mathrm{eV}$. As this limit is close to the lower bound from particle physics, a detection of the cosmological signature of massive neutrinos from LSS analyses can be expected in the near future.

Contents

gewidmet meinen Eltern,
Großeltern und Geschwistern

Nomenclature

Throughout the thesis, the summation convention is employed, which requires indices that appear both as super- and subscripts ('dummy labels') to be summed over.

If such indices are used for coordinates, Greek indices run from 0 to 3 (time and spatial coordinates), while Latin indices only run from 1 to 3 (spatial coordinates). For example, $(x^\mu) = (x^0, x^i)$.

The decomposition of 4-vectors in time and spatial coordinates might also be written as $(x^\mu) = (t, \boldsymbol{x})$ if convenient. Spatial coordinates might be further decomposed into an angular and a radial part as $\boldsymbol{x} = (\hat{\boldsymbol{x}}, r)$, where the angular part can, if helpful, be expressed with a polar angle θ and an azimuthal angle φ. On the celestial sphere, these angular coordinates are usually given in form of declination, DEC, and right ascension, RA, respectively.

In general, a bold font face denotes that $\boldsymbol{x}$ is a vector and the inner product of two vectors is written as $\boldsymbol{x} \cdot \boldsymbol{y}$. x might denote the magnitude of a vector $\boldsymbol{x}$ (if the context is clear), $x = |\boldsymbol{x}| = \sqrt{\boldsymbol{x} \cdot \boldsymbol{x}}$ and $\hat{\boldsymbol{x}}$ denotes the (normalized) direction of a vector, $\hat{\boldsymbol{x}} = \boldsymbol{x}/x$. Matrices are denoted with bold capital letters, e.g., $\boldsymbol{\Psi}$, and the outer product of a matrix and a vector is written as $\boldsymbol{\Psi} \cdot \boldsymbol{x}$. The transposed of a vector or matrix is written as $\boldsymbol{x}^{\mathrm{T}}$.

For a complex number c, c^* denotes complex conjugation. And for a function $f(\boldsymbol{x})$, the Fourier transform is written as $\widehat{f}(\boldsymbol{k})$. In this work, only spatial Fourier transformations with coordinate pairs $\boldsymbol{x} \leftrightarrow \boldsymbol{k}$ are used, where $\boldsymbol{x}$ is in configuration space and $\boldsymbol{k}$ in Fourier space.

A spatial 'bin' is denoted as V_r and means the set of points inside it,

$$V_r \equiv \left\{ \boldsymbol{r} \in \mathbb{R}^3 \middle| r - \Delta r/2 \leq |\boldsymbol{r}| \leq r + \Delta r/2 \right\}, \tag{1}$$

when used as a limit in an integration and the volume of the bin when used as a number, $V_r \equiv 4\pi[(r + \Delta r/2)^3 - (r - \Delta r/2)^3]/3$, for a given bin size Δr, so that $\frac{1}{V_r} \int_{V_r} f(\boldsymbol{r}) \mathrm{d}^3 r$ corresponds to the volume-average of $f(\boldsymbol{r})$ over the bin V_r.

Perturbed quantities on a spatially homogeneous background are written $g(t, \boldsymbol{x}) = \bar{g}(t) + \delta g(t, \boldsymbol{x})$. The bar is dropped if the context is clear.

Important definitions, concepts and physical quantities are written in *italics* when introduced first. Names of spacecrafts (*Planck*, *Euclid*, …) are also in italics.

Physical constants

The following table contains the physical constants used in this thesis. In this list, the CODATA-recommended value and error as of January 2016 are given (National Institute of Standards and Technology, 1998).

name	value
speed of light	$c = 299\,792\,458$ m/s (exactly)
Newton's gravitational constant	$G = 6.674\,08(31) \times 10^{-11}$ m^3/kg s^2

The mathematical constant equal to a circle's circumference divided by its diameter is denoted π.

Astronomical units

The following table contains some important derived astronomical and cosmological scales as used and defined by the International Astronomical Union (IAU).

name	value
light year	1 ly = 9 460 730 472 580 800 m (exactly)
astronomical unit	1 a.u. = 149 597 870 700 m (exactly)
parsec	$1\,\mathrm{pc} = 648\,000/\pi$ a.u. (exactly)
	$\simeq 3.261\,564$ ly $\simeq 30.856\,776 \times 10^{15}$ m
astronomical year	1 yr = 365.25 d $\simeq 31.557\,6 \times 10^6$ s
solar mass	$1\,\mathrm{M}_\odot = 1.989\,1 \times 10^{30}$ kg (exactly)

Conventions for frequently used symbols

The following table introduces the conventional meanings and units of symbols frequently used in this thesis (roughly in the order of their first appearance).

symbol	usage	unit
t	time ($t = 0$ at Big Bang)	yr
t_0	present time (age of the universe)	yr
a	scale factor (normalized such that $a(t_0) = 1$)	—

symbol	usage	unit
τ	conformal time ($\mathrm{d}t = a\,\mathrm{d}\tau$)	yr
$\boldsymbol{r}, r$	physical spatial coordinate, absolute distance	Mpc
χ	radial coordinate	Mpc
$\boldsymbol{x}$	spatial comoving position ($\boldsymbol{r} = a\,\boldsymbol{x}$)	Mpc
K	(spatial) curvature constant	Mpc^{-2}
H	Hubble parameter ($H = \dot{a}/a$)	$^{\mathrm{km}}/_{(\mathrm{s\,Mpc})}$
H_0	present Hubble parameter ($H_0 = H(t_0)$)	$^{\mathrm{km}}/_{(\mathrm{s\,Mpc})}$
h	reduced value of the Hubble parameter ($H_0 = 100\,h\ ^{\mathrm{km}}/_{(\mathrm{s\,Mpc})}$)	—
$\mathcal{H}$	conformal Hubble parameter ($\mathcal{H} = a\,H$)	$^{\mathrm{km}}/_{(\mathrm{s\,Mpc})}$
$\boldsymbol{v}$	physical velocity field	$\mathrm{Mpc\,yr}^{-1}$
$\boldsymbol{u}$	comoving velocity field ($\boldsymbol{v} = \mathcal{H}\,\boldsymbol{x} + \boldsymbol{u}$)	$\mathrm{Mpc\,yr}^{-1}$
z	redshift	—
m	mass	$\mathrm{M}_\odot$
T	temperature	K
λ	wavelength	Mpc
k	wavenumber $= 2\pi/\lambda$	Mpc^{-1}
ρ	mass-energy density	$^{\mathrm{M}_\odot}/_{\mathrm{Mpc}^3}$
Λ	cosmological constant	Mpc^{-2}
Ω	density parameter ($\Omega = \rho/\rho_{\mathrm{crit}}$)	—
ϕ	gravitational potential	$\mathrm{Mpc}^2\,\mathrm{yr}^{-2}$
p	hydrostatic pressure	$^{\mathrm{M}_\odot}/_{(\mathrm{Mpc\,yr}^2)}$
w	linear equation-of-state parameter ($p = w\,\rho$)	—
$\mathcal{R}$	comoving curvature perturbation	—
n	number density	Mpc^{-3}
δ	density contrast	—
ξ	(two-point) correlation function	—
P	power spectrum	Mpc^3
B	bispectrum	Mpc^6
Δ^2	dimensionless power spectrum	—
$\xi^{(3)}, \zeta$	(reduced) three-point correlation function	—
φ	cosmological scalar field	—
V	scalar potential	$^{\mathrm{M}_\odot}/_{\mathrm{Mpc\,yr}^2}$
θ	divergence of the comoving velocity field ($\theta = \nabla \cdot \boldsymbol{u}$)	yr^{-1}
σ_{L}	velocity dispersion in Lagrangian PT	Mpc
T	transfer functon	—
n_{s}	scalar spectral index	—

symbol	usage	unit
σ_8	clustering amplitude	—
r_s	sound horizon scale	Mpc
r_d	sound horizon scale at the drag epoch ($r_\mathrm{d} = r_\mathrm{s}(z_\mathrm{d})$)	Mpc
V	volume (e.g., of a survey)	Mpc^3
D_c	comoving distance	Mpc
D_V	angle-averaged BAO distance	Mpc
D_A	angular diameter distance	Mpc
F_AP	Alcock-Paczynski parameter	—
D	growth factor / growth function	—
f	growth rate ($f = \frac{\mathrm{d}D}{\mathrm{d}\ln a}$)	—
$\boldsymbol{q}$	Lagrangian coordinates	Mpc
$\boldsymbol{\Psi}$	(Lagrangian) displacement field	Mpc
G	propagator (in perturbation theory)	—
$b, [b_n]$	local galaxy bias [of order n]	—
β	RSD parameter ($\beta = f/b$)	—
$\gamma_2, \gamma_3, \gamma_3^-$	non-local galaxy bias	—
$F_\cdot$	Fingers-of-God term (for the orbital motion of virialized matter; $\cdot$: FoG, vir, Gauss)	—
a_vir	kurtosis parameter for F_vir	—
σ_FoG	velocity disperion in F_Gauss	Mpc
μ	LoS parameter ($\mu = \hat{\boldsymbol{r}} \cdot \hat{\boldsymbol{k}} = \cos\theta$)	—
$w_\cdot$	weight / weighting function ($\cdot$: star, see, sys, fc, rf, c, tot, FKP)	—
α_ran	(FKP) data-to-randoms ratio	—
Φ	(survey) selection function	—
F	(FKP) weighted density contrast	—
S	(FKP) shot-noise estimate	Mpc^3
I_norm	(FKP) power-spectrum normalization	Mpc^{-3}
f_tp	true-pair fraction (for the shot-noise estimate)	—
N	total number (e.g., of galaxies in a survey)	—
C	(sector) completeness	—
q	(FKP) survey selection function	—
Q	(FKP) window function	—
$\lvert W\rvert^2$	window function estimate	—
$\boldsymbol{M}$	window matrix ($\boldsymbol{M} = (w_{nm}(k_i, k'))$)	—
$\boldsymbol{P}^\mathrm{obs}$	observed power spectrum (PS) measurements ($\boldsymbol{P}^\mathrm{obs} = (P_A(k_i))$)	Mpc^3
$\boldsymbol{P}^\mathrm{theo}$	theoretical predictions for the underlying PS ($\boldsymbol{P}^\mathrm{theo} = \left(\tilde{P}_A(k_i)\right)$)	Mpc^3

symbol	usage	unit
$\boldsymbol{P}^{\text{pred}}$	theoretical predictions for the observed PS ($\boldsymbol{P}^{\text{pred}} = \left(\hat{P}_A(k_i)\right)$)	Mpc^3
$\boldsymbol{C}^P$	covariance matrix for $P(k)$	Mpc^6
$\boldsymbol{C}^\xi$	covariance matrix for $\xi(r)$	—
$\boldsymbol{\psi}^P$	precision matrix for $P(k)$	Mpc^{-6}
$\boldsymbol{\psi}^\xi$	precision matrix for $\xi(r)$	—
$\mathcal{X}$	parameter space of a model	—
$\boldsymbol{\zeta}$	point in the parameter space	—
$\mathcal{P}$	probability distribution	—
$\mathscr{L}$	likelihood	—
χ^2	log likelihood, χ^2 function	—
D, M	precision and parameter rescaling parameters	—
$\mathcal{L}_\ell$	Legendre polynomial of order ℓ	—
j_ℓ	spherical Bessel function of order ℓ	—
$\boldsymbol{R}$	correlation matrix (i.e., normalized covariance matrix)	—
$q_\perp, q_\parallel, q$	(geometrical) distortion parameters ($q^3 = q_\perp^2\, q_\parallel$)	—
$\alpha_\perp, \alpha_\parallel, \alpha$	Alcock-Paczynski parameters ($\alpha^3 = \alpha_\perp^2\, \alpha_\parallel$)	—
A_p	power spectrum amplitude factor	—
N	(free, additional) shot noise parameter	Mpc^3

Important acronyms, initialisms and abbreviations

This thesis uses the acronyms and initialisms in the following table frequently (roughly in the order of their first appearance).

initialism	meaning
GR	general relativity
LSS	large-scale structure
CMB[R]	cosmic microwave background [radiation]
BBN	Big Bang nucleosynthesis
FLRW	Friedman-Lemaître-Robertson-Walker (metric / universe)
DM	Dark Matter
CDM	cold dark matter
DE	Dark Energy
ΛCDM	standard cosmological model (including CDM and Λ)
EoS	equation of state
DoF	degrees of freedom

initialism	meaning
SN(e) [Ia]	supernova(e) [of type Ia]
SNLS	Supernovae Legacy Survey
JLA	(SDSS-II/SNLS-3) Joint Light-curve Analysis
WMAP	Wilkinson Microwave Anisotropy Probe
RSD	redshift-space distortions
BAO	baryon acoustic oscillations
MCMC	Markov chain Monte Carlo
SDSS (II/III)	Sloan Digital Sky Survey (II/III)
DR(1 - 12)	Data Release (1 - 12)
MGS	(SDSS) Main Galaxy Sample
LRG	(SDSS) Luminous Red Galaxy (sample)
BOSS	Bayron Oscillation Spectroscopic Survey
LOWZ	(BOSS) low-redshift sample
CMASS	(BOSS) constant-stellar-mass sample
eBOSS	Extended Bayron Oscillation Spectroscopic Survey
ELG	Emission Line Galaxy (sample)
2dF(GRS)	Two-degree-Field (Galaxy Redshift Survey)
6dFGS	Six-degree-Field Galaxy Survey
AP	Alcock-Paczynski (effect)
Ly-α	Lyman-α (emission line)
LoS	line of sight
(2P)CF	(Two-point) correlation function
PS	power spectrum
FKP	Feldman-Kaiser-Peacock (estimator)
PT	perturbation theory
SPT	Standard (Eulerian) PT
RPT	Renormalized Perturbation Theory
gRPT	Galilean-invariant RPT
LPT	Lagrangian PT
CLPT	Convolution Lagrangian PT
(e)TNS	(extended) Taruya-Nishimichi-Saito (model)
FoG	Fingers of God (non-linear RSD)
FoM	Figure of Merit
CPL	Chevallier-Polarski-Linder (parametrisation)
FT	Fourier transform
FFT	Fast Fourier Transform

initialism	**meaning**
QPM	Quick-Particle-Mesh (simulation)
PATCHY	**P**erturb**A**tion **T**heory **C**atalog generator of **H**alo and galax**Y** distributions
HOD	Halo Occupation Distribution (parametrisation)
NGC	Northern Galactic Cap (of BOSS)
SGC	Southern Galactic Cap (of BOSS)

This thesis uses the abbreviations in the following table in super- or subscripts.

abbreviation	**meaning**
min	minimal (value)
max	maximal (value)
eff	effective (value)
$\parallel, \perp$	parallel and transverse (component)
$3\mathrm{w}, n$	nth clustering wedge (of three)

List of Figures

List of Tables

1 Introduction

> "The physical universe was anthropocentric to primitive man. At a subsequent stage of intellectual progress it was centred in a restricted area on the surface of the earth. Still later, to Ptolemy and his school, the universe was geocentric; but since the time of Copernicus the sun, as the dominating body of the solar system, has been considered to be at or near the centre of the stellar realm. With the origin of each of these successive conceptions, the system of stars has ever appeared larger than was thought before. Thus the significance of man and the earth in the sidereal scheme has dwindled with advancing knowledge of the physical world, and our conception of the dimensions of the discernible stellar universe has progressively changed. Is not further evolution of our ideas probable? In the face of great accumulations of new and relevant information can we firmly maintain our old cosmic conceptions?"
>
> Curtis (1921)

This thesis describes an analysis of the Fourier space galaxy clustering measurements obtained from the final catalogue of the Baryon Oscillation Spectroscopic Survey (BOSS; Dawson *et al.*, 2013), which is part of the Sloan Digital Sky Survey III (SDSS-III; Eisenstein *et al.*, 2011) program. BOSS represents a milestone in the large-scale clustering analysis as it is the largest sample of galaxies obtained in a spectroscopic survey to date. The footprint of the survey covers ca. 10 000 $\deg^2$. As extragalactic light is obscured by dust in the celestial regions around the galactic plane of the Milky Way, the survey consists of two large patches in the Northern and Southern Galactic Caps, as shown in the left-hand panel of Figure 1.1. BOSS is a spectroscopic survey, measuring the redshift of galaxies from their optical spectra. The target galaxies are fainter than in previous programs, which ensures a high number density of objects over the full redshift coverage out to distances of more than 3 000 Mpc. The right-hand panel of Figure 1.1 shows a 2D slice through the survey. Due to its volume, the clustering analysis of the galaxy sample provides access to invaluable cosmological information contained in the large-scale structure of galaxies, the *cosmic web*. The BOSS survey builds upon, first, the rich history of galaxy surveys that preceded it and their fruitful analyses, and secondly, the great effort that was put in the conception and conduction of the SDSS-III programs. This first chapter

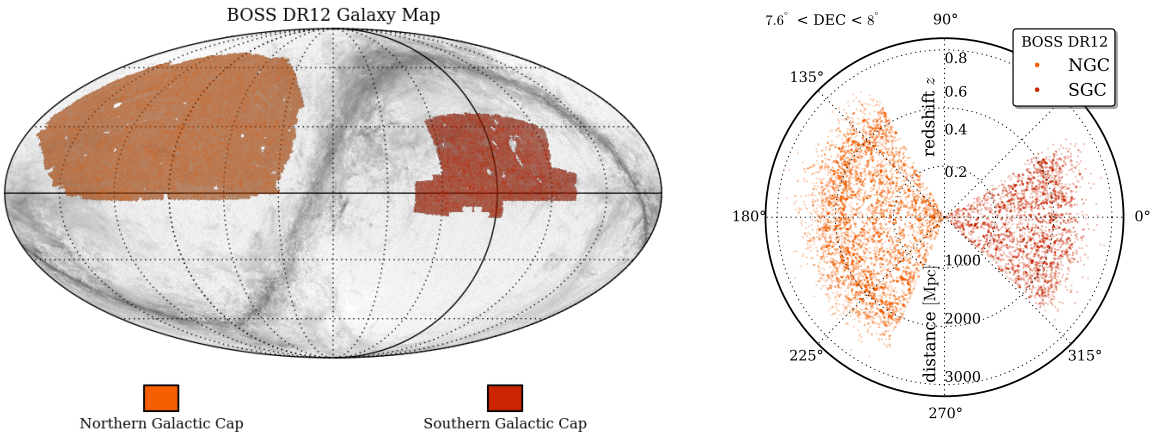

Figure 1.1 – *Left-hand panel:* The BOSS DR12 combined sample footprint* of the galaxies in the subsamples corresponding to the Northern Galactic Cap (NGC, orange) and Southern Galactic Cap (SGC, red). The footprint is plotted over the Galaxy dust map obtained from the *Planck* mission (gray, CMB polarization traces the dust in our Galaxy). The BOSS survey covers ca. 10 000 deg^2, mostly in the Northern Hemisphere of the sky, divided in two large patches in order to avoid the regions around the galactic plane of the Milky way where dust inside our own Galaxy obscures extragalactic light; *Right-hand panel:* A slice $7.6^\circ < \mathrm{DEC} < 8^\circ$ of the full BOSS DR12 combined sample. Redshifts have been converted to distances assuming the fiducial cosmology for the DR12 analysis.

* The galaxy map was made with the help of the LAMBDA FOOTPRINT library, available at http://lambda.gsfc.nasa.gov/toolbox/footprint/.

of the thesis presents a short introduction to large-scale structure (LSS) analysis with galaxy surveys. Besides other cosmological observations, the clustering analysis helped to establish the modern standard cosmological model, which is described in the first section of this chapter. Later sections give a short historical overview over galaxy surveys, describe what cosmological knowledge can be extracted from the cosmic web, and present a summary of the successes in determining the physical nature of the Universe. A special emphasis is placed on the BOSS survey, because this thesis' project was conducted as part of the galaxy clustering working group's efforts to generate the final LSS galaxy catalogue and derive cosmological constraints from its clustering properties. The achievements from the analysis of previous catalogue releases are described in a separate section of this introduction. This chapter is concluded with an outline of this thesis.

Unfortunately, this short overview can only outline the fundamental concepts and techniques applied to the analysis of the cosmic large-scale structure. For detailed studies of the concepts mentioned here, the reader is referred to standard textbooks such as Weinberg (1972) and Liddle (2003) for general relativity and general cosmology, Liddle & Lyth (2000), Mukhanov (2005), and Weinberg (2008) for inflation and cosmological perturbation theory, Dodelson (2003) for growth of structure, and Peacock (1998), Peebles (1993), Martinez & Saar (2001) for galaxy clustering.

1.1 The standard cosmological model

The standard cosmological paradigm is a well established theoretical framework whose predictions match the observations of the cosmic microwave background (CMB) and the large-scale structure of the Universe with high accuracy. This paradigm postulates that the Universe is spatially flat, was formed in a hot *Big Bang* scenario 13.8 billion years ago (*Planck* 2015 results; Ade *et al.*, 2015) and has expanded ever since. The energy budget of the Universe comprises of several components: non-relativistic matter consists of a small fraction of ordinary matter (dubbed *baryonic matter*[1]), but is dominated by a component named cold *Dark Matter* (CDM). Other component are relativistic radiation (light and neutrinos), and also a mysterious form of energy, dubbed *Dark Energy* (DE), whose physical nature is not yet understood. Due to the expansion, the Universe cooled down and the densities of the different components evolved with time, changing their relative ratios such that the Universe successively underwent *epochs* of radiation-, matter-, and dark-energy domination.

Structure originates from quantum fluctuations during an exponentially expanding phase at the onset of the Big Bang known as *cosmic inflation*. Quantum perturbations were stretched to macroscopic scales by the expansion and eventually became classical by decoherence after growing larger than the cosmic horizon. In the decelerating expansion after the Big Bang, these perturbations re-entered the horizon and formed the seeds of the *cosmic web* that we see today, containing structures such as galaxies, galaxy clusters, and filaments of galaxies that connect the clusters. Stars and galaxies are part of the baryonic matter, which clustered in the gravitational potential wells sourced by CDM. This dominance of CDM resulted in a hierarchical growth of structure: self-gravity lead to the formation of small objects first, and larger and more massive objects are formed by merging in a continuous hierarchy.

Caused by DE, the expansion of the late-time universe is accelerating again. The faster rate of expansion slows down the growth of structure. Despite the convincing evidence that DE comprises the largest fraction of the Universe's energy content today and that it is the driver of the late-time expansion, its exact underlying physical nature is unknown. DE can be described by a *cosmological constant* Λ. From this constant and the fact that CDM is the dominant form of matter, the standard cosmological paradigm is referred to as the 'ΛCDM model'.

This cosmological paradigm has passed many tests, most notable from observations of the CMB, galaxy clustering analysis, and type Ia supernovae (SN Ia). The most important CMB observations are measurements of the two- and three-point statistics of the CMB temperature and polarization maps with the space missions *WMAP* (Bennett *et al.*, 2013) and *Planck* (Adam *et al.*, 2015), as well as with Earth-bound radio telescopes such as SPT (George *et al.*, 2015) and ACT (Naess *et al.*, 2014). Cosmological parameters can be inferred from galaxy surveys by means of the spatial two-point statistics of galaxy clustering which are complementary to the CMB measurements on a surface. Recent examples of galaxy clustering analyses make use the 2dF (Sanchez *et al.*, 2006), 6dFGS (Beutler *et al.*, 2011), WiggleZ (Kazin *et al.*, 2014), SDSS (Sanchez *et al.*, 2009; Oka *et al.*, 2014; Ross *et al.*, 2015) and BOSS (Anderson *et al.*, 2014b) sur-

[1] Of the matter that is constituted by known particles, the baryons dominate the total mass. Thus the name baryonic matter was chosen despite the fact that a large fraction of that matter is in atoms and molecules, which are bound structures comprised of nuclei (baryons) and electrons (leptons).

veys. Light curves of SN Ia serve as standardizable candles for distance measurements allowing the detection of the aforementioned late-time acceleration of the Universe (Riess *et al.*, 1998; Perlmutter *et al.*, 1999). They are analysed in samples such as those of the Supernova Cosmology Project (Suzuki *et al.*, 2012), the Supernovae Legacy Survey (Conley *et al.*, 2011), and the joint light-curve analysis sample (JLA; Betoule *et al.*, 2014) that combines the two. Many of these cosmological datasets will be described in more detail in later parts of this introduction.

Due to the fact that most predictions of the ΛCDM model have been well tested with data, the standard paradigm is seen as very robust and clearly favourable over alternative models, even though the answers to some questions are still pending. These open questions concern, for example, the underlying physics of the driver of the expansion and the experimental verification of further cosmological predictions such as the detection of the signal of primordial gravitational waves[2] in the polarization of the CMB. Just as large-scale structure analysis had its part in establishing the standard model, it will certainly also play a major role in shedding light onto the open questions.

1.2 A brief history of large-scale structure analysis

1.2.1 First steps in surveying galaxies

The first essential step for the analysis of galaxy clustering was to realize that galaxies are astronomical objects which emit light to us from outside our own Galaxy, the Milky Way. This discovery was made in the first decades of the 20th century and concluded the 'great debate' between two groups of astronomers which were represented by Harlow Shapley and Heber Curtis. At a time when astronomical observations lacked the benefits of modern technology, the former scientist argued that *spiral nebulae* in question, such as those objects known today as the Pinwheel Galaxy (M101) and the Andromeda Galaxy (M31), were inside the Milky Way. Curtis and his supporters, however, believed these objects to be extragalactic. The resolution of this debate was to a great degree due to the work of Edwin Hubble, who measured the distance to the Andromeda Galaxy using Cepheid variable stars (Hubble, 1925). Doing so, he paved the way to cosmological observations by clarifying that the nebulae are galaxies that must be large and far away from us, populating our Universe in immense numbers.

The theoretical foundations of cosmology were also laid in the second decade of the last century when Einstein postulated the theory of *general relativity* (GR; Einstein, 1915, 1916), the fundamental theory of space, time, and gravitation. Realizing that of all physical interactions, only gravitation acts on astronomical scales, and from the assumption of the *cosmological principle* that postulates that the Universe is spatially homogeneous and isotropic on large scales, the first theories on the Universe as a whole were formulated. Notable are, for example, one of Einstein's formulations which introduced the cosmological constant (Einstein, 1917) and Friedmann's first cosmological descriptions of spherically symmetric (closed) space (Friedmann, 1922) and hyperbolic (open) space (Friedmann, 1924). Extending work from Einstein,

[2]The detection of primordial gravitational waves is even more anticipated since gravitational waves sourced by astrophysical objects were first detected just one week prior to the submission of this thesis (Abbott *et al.*, 2016).

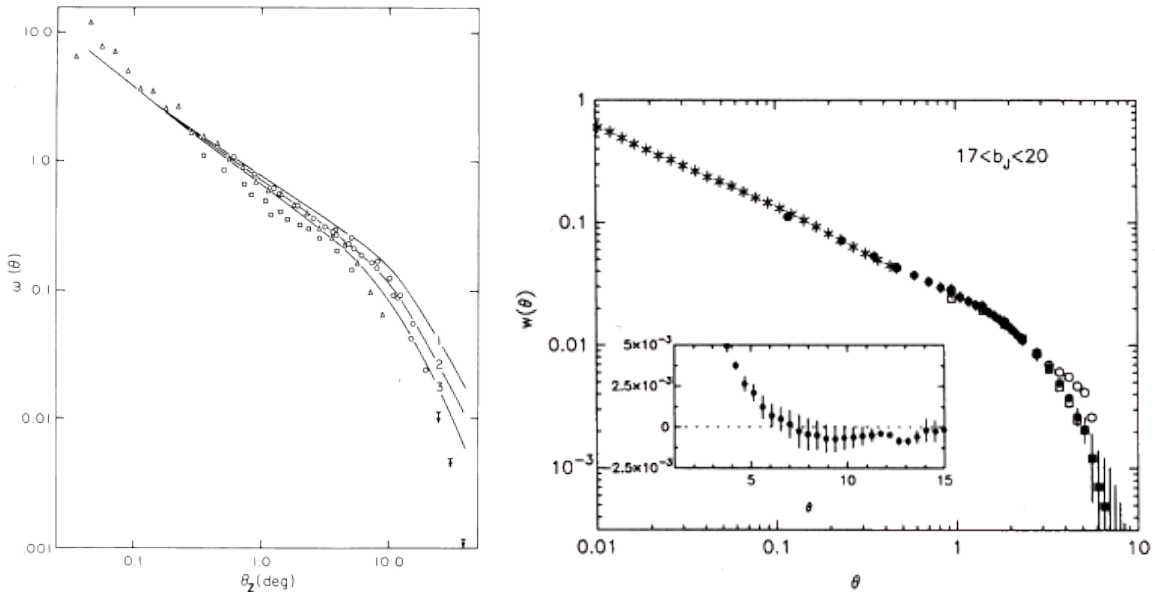

Figure 1.2 – First observations of the angular clustering of galaxies: the left-hand panel shows the angular correlation function from the Shane-Wirtanen and Zwicky galaxy catalogues (taken from Davis *et al.*, 1977); the right-hand panel shows the angular correlation function measured by Maddox *et al.* (1990) from the APM galaxy survey using UK Schmidt plates (inset shows the clustering for larger scales).

de Sitter, Lemaítre, Robertson, and Walker (Einstein & de Sitter, 1932; Lemaître, 1927, 1931; Robertson, 1935a,b, 1936; Walker, 1937), the standard cosmological theory using a spacetime metric with a maximally symmetric spatial part and a time-dependent cosmological *scale factor* — known as the *Friedmann-Lemaítre-Robertson-Walker* (FLRW)-metric — was formulated.

At that time, it was also realized that the extra-galactic *nebulae* we now simply call galaxies are actually moving away from us. A seminal work published by Hubble (1929) measured a close relationship between the distance to spiral nebulae and their velocities, now referred to as 'Hubble's law'. This observation relied on distance measurements using the period-luminosity relationship of Cepheid stars (found by Henrietta Swan Leavitt) and the measurement of radial velocities (rendered possible by the discovery of redshifts by Vesto Slipher). Thereby, the paradigm of the expanding universe formed during a hot 'Big Bang' was created. The questions raised by theoretical cosmologists at that time, like 'Is the Universe limited to what we see? It is finite or infinite? What is its curvature? Is the expansion slowing down or accelerating? Or is the Universe in a steady state after all?', had to remain unanswered for a long time in which cosmological observations were in their infancy, if not to say almost impossible due to technological restrictions.

Between the first postulation of 'Dark Matter' that is undetectable by direct observations by Zwicky (1933, 1937) in order to explain the observed virial masses of galaxy clusters and the discovery of sufficient evidence of the hierarchical growth of cosmological structure dominated by non-relativistic (i.e., *cold*) dark matter, decades passed by. Whether there is just enough matter to make the Universe critically dense (i.e., *flat*) was another important question raised. Addressing these aspects asked for immense dedication from the field. Astronomers could only

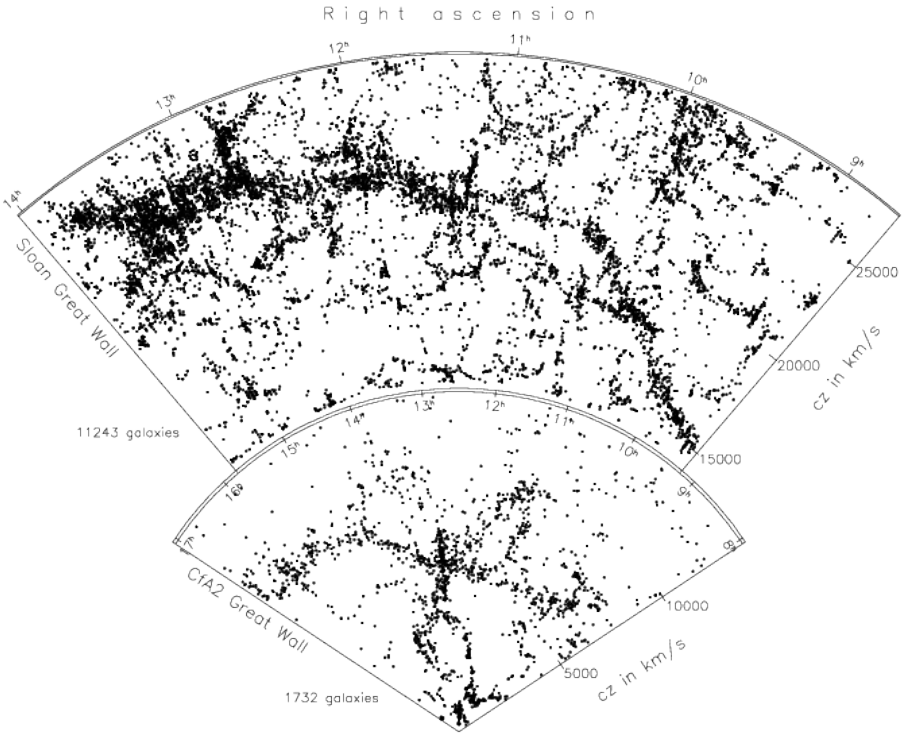

Figure 1.3 – (Image credit: Gott *et al.*, 2005) First wide galaxy-redshift surveys such as the CfA survey (Huchra *et al.*, 1983) and the first Sloan program (York *et al.*, 2000) revealed the clustering properties of galaxies for the first time to such detail that individual large-scale structures of the *cosmic web* like the so-called 'great walls' have been identified (Geller & Huchra, 1989; Deng *et al.*, 2007).

start to analyse the expansion of the Universe by creating catalogues of galaxies from visual inspection of photographic plates in the 1960s (e.g., Zwicky *et al.*, 1961; Zwicky & Kowal, 1968; Shane & Wirtanen, 1967). Zwicky's 'Catalogue of Galaxies and of Clusters of Galaxies' (CGCG, 1961—68) contained ca. 30,000 galaxies and 9,000 galaxy clusters, while the 'Uppsala General Catalogue of Galaxies' (UGC, 1973) contained ca. 13,000 galaxies in the Northern Hemisphere. Both were created from inspections of the photographic plates of the Palomar Observatory Sky Survey (POSS).

With the ground-breaking idea of treating galaxies as — biased — tracers of matter clustering (see series of publications starting with Peebles, 1973; Tonry & Davis, 1979), first studies of the angular clustering (due to lack of accurate measures of the distances via redshifts, see e.g., Davis & Peebles, 1983) were undertaken to probe the cosmological framework of that time, a matter-dominated flat FLRW universe. In a series of first systematic studies of galaxy clustering using machine scans from the UK Schmidt telescope (e.g., Maddox *et al.*, 1990), the power-law behaviour of the angular two-point correlation function[3] was confirmed. Such measurements are illustrated in Figure 1.2, where early measurements of the angular correlation function from the Shane-Wirtanen (Shane & Wirtanen, 1967) and Zwicky catalogues are shown in the left-

[3]For the discussion of two-point statistics, see Section 2.2.1.

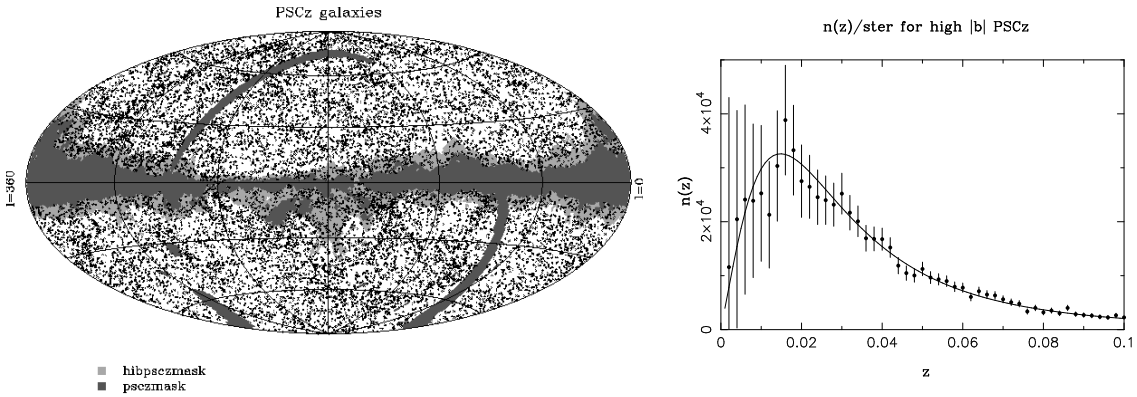

Figure 1.4 – (Image credit: Saunders *et al.*, 2000) Positions of the ca. 15,500 galaxies of the PSCz catalogues on the sky and the number density of the catalogue versus redshift.

hand panel. The scatter of the measurements and the deviation from simulated predictions (lines) show the early stage of the galaxy clustering observations at that time. In the right-hand panel, the more precise measurements of the angular clustering of Maddox *et al.* (1990) taken from automatic scans of photographic plates are showing that the angular correlation function breaks away from a power law at larger distances. Despite the growing evidence for the CDM paradigm in the 1980s, LSS analysis in the early 1990s (Maddox *et al.*, 1990; Efstathiou *et al.*, 1990) indicated that a plain CDM cosmology cannot fully account for the clustering observed in the local universe.

1.2.2 Automatic wide-field surveys

Technological progress such as machine plate scanning and CCDs enabled the construction of automatic wide-field surveys beginning in the 1980s. This revolutionised large-scale structure analysis and galaxies were now detected in large numbers using automated photometric surveys. Galaxies detected in photometry were followed up with a spectroscopic analysis to infer the radial velocities of the galaxies, as pioneered by the CfA survey (Huchra *et al.*, 1983). Such studies allowed the measurements of the 3D clustering properties of galaxies for the first time, giving insight into the morphological structure of the cosmic web. The lower slice in Figure 1.3 shows an example of such a large structure, the so-called 'great wall' found in the first CfA catalogue. Evidence increased that the CDM paradigm is not able to explain the galaxy clustering of CfA galaxies (Vogeley *et al.*, 1992) as well as those identified from the first infrared telescope in space, *IRAS* (Efstathiou *et al.*, 1990; Saunders *et al.*, 1991).

From the IRAS galaxies, the PSCz catalogue (Saunders *et al.*, 2000), containing 15,411 galaxy redshifts across 84% of the sky, was constructed by collections from all redshift databases that were available to the authors. The angular and radial distribution is shown in Figure 1.4. In a milestone analysis, Tadros *et al.* (1999) used the galaxy power spectrum of this sample to detect for the first time distortions of the redshift-space clustering of the galaxies caused by the line-of-sight components of their peculiar velocities, an effect known as redshift-space distortion

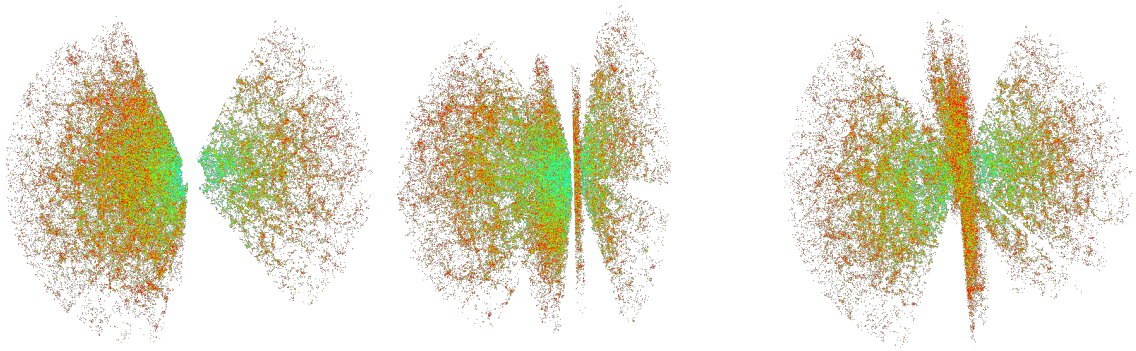

Figure 1.5 – (Image credit: Blanton (2008) and SDSS collaboration) Projections of the SDSS-II main galaxy sample ($0.02 \leq z \leq 0.22$, color coded by g-r color) from different perspectives.

(RSD, see Section 2.4.2).

The spectroscopic follow-up analysis became a rapid redshift-producing machinery with the invention of multi-fibre and multi-split spectrographs. One of the pioneering surveys using the multi-fibre technology was the Las Campanas Redshift Survey (LCRS; Shectman *et al.*, 1996) observing at the Las Campanas telescope (in Chile) where around 100 spectra could be taken at once. Around the turn of the millenium, samples containing up to a hundred thousand spectroscopically or even a million photometrically identified galaxies were produced in the Two-degree-Field Galaxy Redshift Survey (2dFGRS; Colless *et al.*, 2001) and the first iteration of the Sloan Digital Sky Survey (SDSS; York *et al.*, 2000).

The early power spectrum analysis of 2dFGRS helped to establish the paradigm of a ΛCDM universe (Percival *et al.*, 2001; Efstathiou *et al.*, 2002) by providing independent evidence for a non-zero cosmological constant. The detection of the acceleration of the late-time expansion caused by Dark Energy was due to the light-curve analysis of SN Ia (Riess *et al.*, 1998; Perlmutter *et al.*, 1999). The analysis of the first two data releases of SDSS (Abazajian *et al.*, 2003, 2004) contained a 'main galaxy sample' (MGS) catalogue with more than a million photometrically identified galaxies (of which 260,490 were spectroscopically followed up) whose clustering properties were analysed in angular projections (Tegmark *et al.*, 2002; Szalay *et al.*, 2003) and from the full 3D power spectrum (Dodelson *et al.*, 2001; Tegmark *et al.*, 2004b) — projected 3D slices of the catalogue are shown in Figure 1.5. The redshift-space analysis from the early SDSS catalogues further consolidated the picture of a flat ΛCDM universe with a scale-invariant primordial power spectrum (Tegmark *et al.*, 2004a), in consistency with complementary 2dFGRS results and the early CMB observations of *WMAP* (Spergel *et al.*, 2003).

Baryon acoustic oscillations (BAO), density-pressure waves that propagated in the primordial baryon-photon plasma, leave an imprint in the galaxy clustering signal, which can only be resolved with large galaxy samples. The two first detections of the BAO signal were published in 2005. Eisenstein *et al.* (2005) detected it in the two-point correlation function (see the left-hand panel of Figure 1.6) of a sample of ca. 47,000 luminous, red galaxies (LRG; Eisenstein *et al.*, 2001). The LRG selection was optimized for large-scale structure analysis and extends the main sample to fainter and more far away galaxies than the main (flux-limited) portion of the SDSS

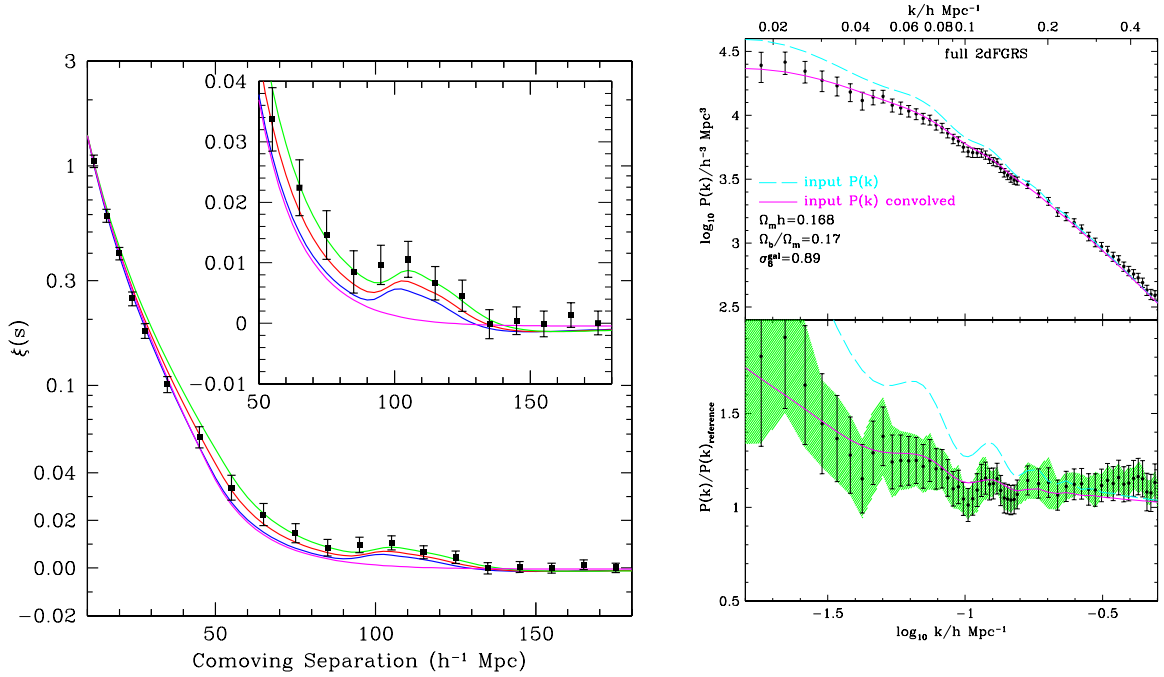

Figure 1.6 – (Image credit: SDSS and 2dFGRS collaborations) The detection of the BAO signal in the two-point correlation function of SDSS LRGs (Eisenstein *et al.*, 2005, left) and the power spectrum of the 2dFGRS sample (Cole *et al.*, 2005, right). In configuration space, the BAO signal can be seen as a single bump in the correlation function around $r \simeq 100\,h^{-1}$ Mpc and the SDSS detection paper finds evidence for this feature with respect to a featureless correlation function at a confidence level of 3.4σ. In Fourier space, the BAO signal appears as a series of wiggles (peaks and troughs). The 2dFGRS paper inferred the cosmological density parameters and baryon fraction from the power spectrum in the wavenumber regime $0.05\,h\,\mathrm{Mpc}^{-1} \lesssim k \lesssim 0.2\,h\,\mathrm{Mpc}^{-1}$.

galaxy spectroscopic sample. The power spectrum analysis of the final 2dFGRS catalogues (Colless *et al.*, 2003) with ca. 220,000 galaxy redshifts proved the existence of BAOs independently (Cole *et al.*, 2005, see the right-hand panel of Figure 1.6). The final 2dFGRS analysis (Cole *et al.*, 2005; Sanchez *et al.*, 2006) also revealed, in agreement with the later analysis of the *WMAP* 3-yr data (Spergel *et al.*, 2007), that the primordial power spectrum is slightly titled as predicted by standard models for inflation.

Measurements of the apparent BAO distance can break degeneracies in the cosmological constraints from CMB observations and thus help to get a more precise knowledge of the parameters of the standard model. Using the final SDSS-II DR7 (Abazajian *et al.*, 2009) LRG sample, the angle-averaged BAO distance, $D_\mathrm{V}(z_\mathrm{eff} = 0.35)$, could be constrained at the level of a few per cent (Reid *et al.*, 2010). Further analysis combined the BAO distance measurements of DR7 LRG and main samples with the 2dFGRS sample to obtain a BAO distance ladder (Percival *et al.*, 2007b, 2010).

At lower redshifts, the BAO signal becomes degraded due to the bulk motion of matter and non-linear structure formation (Meiksin *et al.*, 1999; White, 2005; Eisenstein *et al.*, 2007a;

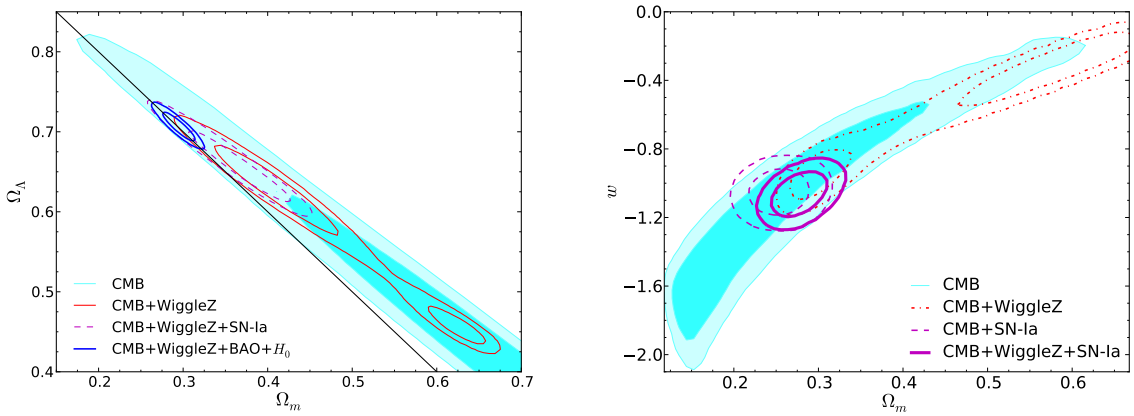

Figure 1.7 – (Image credit: WiggleZ collaboration) Cosmological implication of the full-shape power spectrum analysis of the LSS galaxy sample obtained from the WiggleZ survey (Parkinson *et al.*, 2012). Only the combination of the power spectrum measurements with supernovae data (in addition to the CMB observations) can effectively constrain the density and equation-of-state parameter of Dark Energy.

Crocce & Scoccimarro, 2008). Eisenstein *et al.* (2007b) proposed a simple method to partially remove the effect of the bulk flow by moving the galaxies back on their approximate trajectories given by the linear velocity field in Lagrangian space. The success of this method was proven theoretically (Padmanabhan *et al.*, 2009; Noh *et al.*, 2009) and in N-body simulations (Seo *et al.*, 2010; Mehta *et al.*, 2011). The original method (Eisenstein *et al.*, 2007b; Padmanabhan *et al.*, 2012) has been proven to provide almost optimal access to cosmological information in the BAO (see e.g., Burden *et al.*, 2015; Schmittfull *et al.*, 2015).

The SDSS LRG sample was subject to the first application of density-field reconstruction achieving a reduction of the BAO distance error from 3.5% to 1.9% in the LRG DR7 sample (Padmanabhan *et al.*, 2012). Further, the application of reconstruction to the SDSS DR7 MGS galaxies (Ross *et al.*, 2015) improved the determination of the local Hubble parameter through its 4% distance measurement.

1.2.3 Present-day galaxy surveys

The success of BAO distance measurements led to the emergence of several LSS surveys with a special focus on the BAO probe. For example, the WiggleZ survey (Drinkwater *et al.*, 2010) measured ca. 240,000 redshifts of blue emission line galaxies (ELG) in the range $0.2 \leq z \leq 1.0$, allowing the determination of an independent BAO distance ladder (Blake *et al.*, 2011b; Parkinson *et al.*, 2012). As shown in Figure 1.7, the full-shape WiggleZ power spectrum measurements needed to be combined with supernovae data in order to effectively constrain the density and equation-of-state parameter of Dark Energy due to the smaller volume of WiggleZ compared to other modern surveys. Applying reconstruction to the WiggleZ data corresponds to an effective increase of the survey volume by a factor of 2.5 (Kazin *et al.*, 2014).

One of the present-day surveying programs clearly stands out: the BOSS program. It is the most ambitious of the galaxy-redshift projects that have been completed at the time of writing

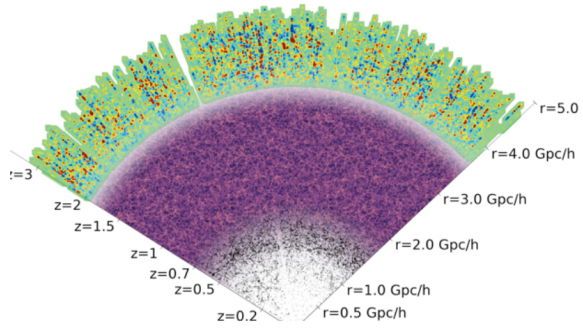

Figure 1.8 – (Image credit: DESI collaboration) Projection of a slice of targets aimed at with the DESI survey: luminous red galaxies, emission line galaxies, and quasars (DESI Collaboration, 2015). This multi-target approach allows for the mapping of the cosmic web out to a redshift of 3.5.

this thesis. It was designed with the aim to provide the most-robust and voluminous galaxy sample for BAO measurements so far. This survey is presented in more detail in Section 1.4.

The 6dF Galaxy Survey (6dFGS; Jones *et al.*, 2004) measured 125,000 near-infrared selected galaxy redshifts in the southern sky. The low effective redshift of this sample provides a good handle on the local BAO distance, Hubble parameter, growth rate, and clustering amplitude (Beutler *et al.*, 2011, 2012). However, as the effective volume is small, 6dFGS can only contribute marginally to the constraining power of the other present-day redshift surveys.

1.2.4 Future galaxy-redshift surveys

Early BAO measurements provide tight constraints on the six parameters of the ΛCDM model, but relaxing the assumptions of the standard model opens up new degeneracies in the parameter space. One example is the open question of whether Dark Energy (DE) can be described by a cosmological constant or is evolving with time. The quest for the true nature of DE is the main driver for the construction of several on-going and future cosmological experiments. The Dark Energy Task Force (Albrecht *et al.*, 2006) has identified BAO distance measurements with large galaxy-redshift surveys as one of the main techniques to address this issue. The constraining power of galaxy surveys can be improved by increasing the probed volume, refining the clustering models in the mild non-linear regime, or by reconstruction of the linear density field. Further, probing BAO distances for multiple redshifts helps to constrain non-standard DE models by probing the late-time evolution of the Universe.

In order to categorize the past, recent and proposed science programs exploring DE, they are classified in stages by the figure-of-merit (FoM), which is an indicator of the intrinsic constraining power of a given cosmological probe or individual experiment on a DE model. Here, only the on-going and future LSS galaxy survey programs will be discussed. Among the on-going (Stage-III) experiments are the continuation programs of the BAO projects in SDSS, BOSS and its extension eBOSS, which are described later in Section 1.4. Other Stage-III galaxy surveys are the photometric Dark Energy Survey (DES; Abbott *et al.*, 2005), which is about to release the analysis of the first-year data in 2016, and the Hobby Eberly Telescope Dark Energy Experiment (HETDEX; Hill *et al.*, 2008), which will start the commissioning of its spectroscopic observations of Ly-α emitters as tracers of the large-scale structure in the fall of 2016. In the future, next-generation (Stage-IV) experiments such as the Dark Energy Spectroscopic Instrument (DESI;

Levi *et al.*, 2013), 4MOST (de Jong *et al.*, 2014), the Subaru Prime Focus Spectrograph (PFS; Ellis *et al.*, 2014) and the space-based *Euclid* mission (Laureijs *et al.*, 2011) will allow for an even more accurate exploration of galaxy clustering over a wide range of redshifts. To illustrate the redshift coverage of future spectroscopic surveys, a projection of a mock slice through the cosmic web as it will be observed with DESI targets (luminous red galaxies, emission line galaxies, and quasars) is shown in Figure 1.8.

1.3 Information content of the cosmic web

The early galaxy surveys revealed the approximate shape of the clustering correlation function and allowed a qualitative description of the cosmic web. This section briefly outlines the main quantitative measurements that have been used successfully in the last decades to infer tight constraints on cosmological parameters from galaxy samples.

1.3.1 Growth of structure and redshift-space distortions

The clustering signal is distorted anisotropically in redshift-space due to the peculiar velocities of the galaxies, which boost the clustering in the direction of the line of sight (LoS). Hence, an LoS-dependent clustering measurement can probe the relation between the velocity and density fields. The RSD will be discussed in more detail in Section 2.4.2

To linear order, this relation is predicted by the Zeldovich equation (Zel'dovich, 1970) whose coefficient is given by the redshift space distortion parameter, β, defined as the ratio of the growth rate and the linear galaxy bias. The linear velocity field describes the 'Kaiser infall' of structure into DM potential wells (Kaiser, 1987). The RSD parameter β has been measured first from PSCz data by Tadros *et al.* (1999) and Hamilton *et al.* (2000). Later, the analysis was repeated for the 2dFGRS sample (Verde *et al.*, 2002; Hawkins *et al.*, 2003; Ross *et al.*, 2007).

Deviations from the ΛCDM predictions for the growth rate could indicate that modifications of the fundamental relations of general relativity (*modified gravity*, or short MG) are required. Alternatives or extensions to GR have been the focus of theoretical analyses since it was realized that Einstein gravity cannot be quantized with the usual recipes applied to the other fundamental forces in physics.

A ground-breaking analysis was performed by Guzzo *et al.* (2008) on the data of the VIMOS-VLT Deep Survey, where a growth rate consistent with ΛCDM predictions was found. Since then, RSD have been of great interest to cosmologists as they are a powerful and complementary cosmological probe to BAO distance measurements. So far, no measurement has shown significant tension with ΛCDM predictions despite improved sensitivity due to ever increasing survey volumes.

1.3.2 The BAO as a standard ruler for distance measurements

A second feature in the galaxy clustering besides RSD are baroynic acoustic oscillations (BAO). The periodic BAO fluctuations were produced when photons were still strongly coupled to

baryons in the early universe, in which the baryonic matter was ionized as the typical thermal energy of photons was larger than the ionization energy of the hydrogen atom. Photons were tied with the free electrons due to a strong interaction between them (Thomson scattering) and all charged particles exchanged energy in frequent collisions between them. Thus, all baryons, leptons and photons formed an ionized plasma, the primordial baryon-photon fluid. In this plasma, counteracting gravitational forces and high photon-baryon pressure resulted in oscillations similar to sound waves propagating away from overdense regions (see a more detailed description in Section 2.3.2). At decoupling, when the Universe became transparent due to re-combination of atoms, the photons were released and formed the CMB due to further redshifting since that time (which was when the Universe was ca. 3000 K hot at a redshift of $z \simeq 1089$). The BAO propagated a distance given by the sound horizon scale between Big Bang and decoupling, when they were frozen in. Due to gravitational interaction with the CDM, the BAO imprint in the matter clustering, which corresponds to an enhanced correlation between density peaks separated by the sound horizon scale, was formed.

Since the detection of the BAO feature imprinted into the matter clustering, using the BAO as a standard ruler for cosmological distance measurements (such as the angular diameter distance discussed later in Section 2.1.2) has become a main science driver for galaxy surveys. The signal becomes anisotropically distorted if redshifts are converted to distances assuming a cosmology which differs from the true one. This geometrical distortion is called the *Alcock-Paczynski* (AP) effect. Measurements of the distorted acoustic peaks in the LSS clustering of large-volume surveys are a robust geometrical probe in the quasi-linear regime (Eisenstein & White, 2004; Seo & Eisenstein, 2005) offering the possibility to constrain the Hubble parameter and the angular diameter distance the level of a few percent (Eisenstein *et al.*, 1998; Seo & Eisenstein, 2003; Blake & Glazebrook, 2003) in the redshift range up to $z \leq 1$. Details of the AP probe on the acoustic scale are discussed later in Section 2.4.7.

1.3.3 Full-shape measurements of galaxy clustering

The BAO distance is probed from a shift in the apparent sound horizon scale, while simple RSD measurements make use of the anisotropic distortions of the clustering signal by taking ratios between different angular projections of the two-point statistics. These two measurements usually marginalize over the large-scale shape of the clustering two-point statistics. But cosmological constraints can be improved by taking the broad-band features of the clustering into account as well. Early examples are the 2dFGRS power spectrum analysis (Percival *et al.*, 2001; Sanchez *et al.*, 2006) and the SDSS MGS analysis (Tegmark *et al.*, 2004b). After the BAO distance ladder (Percival *et al.*, 2007b) had been established, most analyses focussed on BAO-only measurements, especially after these measurements became significantly more precise by applying the reconstruction technique.

To be competitive, the full-shape method needs to rely on accurate modelling of the galaxy clustering signal, which can be achieved, for example, using renormalized perturbation theory (RPT; Crocce & Scoccimarro, 2006a, 2008). Before BOSS, Sanchez *et al.* (2009) used the broad-band shape of the SDSS LRG correlation function and the BAO signal to constrain the ΛCDM parameters as well as non-standard DE models and spatial curvature (Montesano *et al.*, 2012,

the complementary analysis in Fourier space was performed in). Fitting the broad-band features is seen as a necessary complementary probe to the BAO fits using the AP effect; recent applications of this technique are Parkinson *et al.* (2012); Contreras *et al.* (2013, WiggleZ), de la Torre *et al.* (2013, VIPERS), and the BOSS analysis (Sánchez *et al.*, 2014, e.g.).

1.4 Introduction to BOSS

> "Many reports and articles have identified dark energy as the most pressing problem in fundamental physics. However, going beyond the detection of dark energy to informative constraints on its properties requires measurements of the cosmic expansion history with percent-level precision and correspondingly exquisite control of systematic uncertainties. At present, the baryon acoustic oscillation method is believed to have the smallest systematic biases of any dark energy probe. Sound waves that propagate in the opaque early universe imprint a characteristic scale in the clustering of dark matter, providing a 'standard ruler' whose length, 150 megaparsecs, can be computed using straightforward physics and input parameters that are tightly constrained by cosmic microwave background observations."
>
> AS2 Proposal Team (2007)

The Baryon Oscillation Spectroscopic Survey (BOSS; Dawson *et al.*, 2013) was proposed as one of the four main surveys of the third iteration of the Sloan Digital Sky Survey program (SDSS-III; Eisenstein *et al.*, 2011). It is a 5-year program of spectroscopic galaxy observations with the aim to measure the cosmic distance scale and expansion rate to percent-level precision in the redshift ranges $0.2 \leq z \leq 0.75$ (LSS galaxy samples) and $z \simeq 2.5$ (Ly-α forest) making use of the BAO standard ruler (Schlegel *et al.*, 2009). For the selection of the galaxies, the program uses multi-colour SDSS imaging (Fukugita *et al.*, 1996; Smith *et al.*, 2002; Doi *et al.*, 2010) obtained with the drift-scanning mosaic CCD camera (Gunn *et al.*, 1998) installed on the 2.5-meter wide-field telescope (Gunn *et al.*, 2006) at the Apache Point Observatory dedicated to the SDSS programs. The redshifts of selected targets have been measured with the SDSS multi-fibre spectrograph (Smee *et al.*, 2013). The spectral classification and redshift fitting pipeline was specially written for the BOSS program (Aihara *et al.*, 2011; Bolton *et al.*, 2012).

1.4.1 Galaxy clustering analysis with the previous data releases

DR9 (Ahn *et al.*, 2012) was the first release of BOSS galaxy spectra and the two galaxy samples for the LSS analysis. The 'LOWZ' sample ($0.14 \leq z \leq 0.4$) extends the SDSS-II LRG sample to lower luminosities in order to achieve a higher spatial number density. The mean mass of DM haloes hosting LOWZ galaxies is $5.2 \times 10^{13}\ h^{-1}\,\mathrm{M}_{\odot}$ and a fraction of 12% are satellite galaxies (Parejko *et al.*, 2013). Secondly, the 'CMASS' sample ($0.4 \leq z \leq 0.8$) is a nearly complete sample of the most-massive galaxies above the magnitude limit of the survey (Maraston *et al.*, 2013) aiming at a high-redshift sample with an almost constant stellar mass. The CMASS galaxies are mostly red with a prominent 4000 Å break, but there is a small fraction of bluer galaxies. The selection criteria for both samples were chosen to achieve a homogeneous comoving number

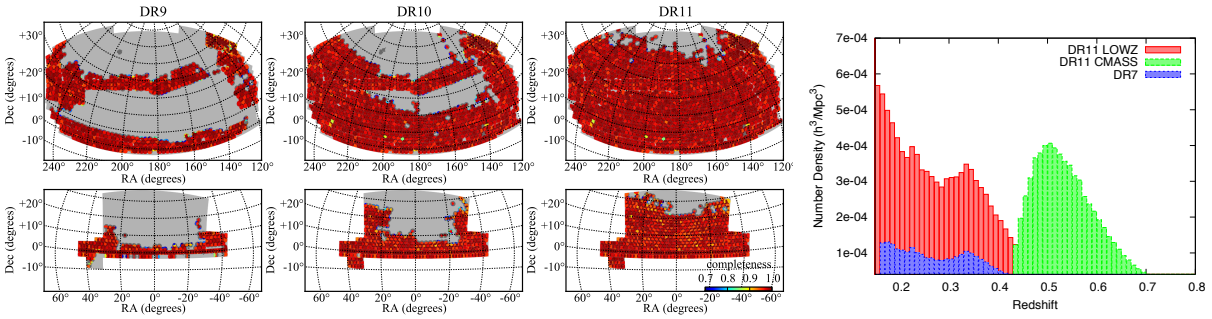

Figure 1.9 – (Image credit: BOSS collaboration) The spectroscopic footprint of the ninth (DR9; Ahn *et al.*, 2012), tenth (DR10; Ahn *et al.*, 2014), and eleventh (internal) data release of BOSS. The top panels show the coverage of the Northern galactic cap (NGC) and the lower panels show the Southern galactic cap (SGC). The spectroscopic completeness of the unique partitioning of the survey into sectors is indicated by colour according to the key in the most left-hand lower panel. The sky coverage increased from ca. 3 300 deg^2 (DR9) over ca. 6 200 deg^2 (DR10) to ca. 8 400 deg^2 in DR11. Legacy redshift observations of the previous SDSS-II program are combined with new BOSS observations to form the two galaxy-redshift catalogues, LOWZ and CMASS (see text).

density of $\bar{n} \approx 3 \times 10^{-4}\, h^3\,\mathrm{Mpc}^{-3}$ (Dawson *et al.*, 2013, the actual number density depends on the radial distance as shown in the right-hand panel of Figure 1.9). The CMASS galaxies live in DM haloes with a mean halo mass of $2.6 \times 10^{13}\ h^{-1}\,\mathrm{M}_\odot$ and the satellite fraction is 10% (White *et al.*, 2011). The galaxies of both samples are a highly biased tracer of the matter clustering with a linear galaxy bias of ~ 2.0 (Nuza *et al.*, 2013), which is ideal for clustering analysis as the power spectrum can be measured with a high signal-to-noise ratio.

With the DR9 version of these samples (containing in total ca. 264,000 galaxies), Anderson *et al.* (2013) measured the BAO distance from the CMASS and DR7 LRG samples and derived the cosmological implication of this measurement in combination with other cosmological probes. Reid *et al.* (2012) presented AP and RSD measurements, whose interpretation with respect to Dark Energy and modified gravity was presented in Samushia *et al.* (2013). A full-shape clustering measurement was performed in Sanchez *et al.* (2012). Tojeiro *et al.* (2012) used a model for passively evolving galaxies to constrain the growth of structure from a low-redshift mix of SDSS-II and -III galaxies to a similar precision to using the standard analysis technique on the CMASS sample.

An anisotropic BAO measurement provides access to more information and thus increases the constraining power on cosmological parameters compared to angle-averaged measurements (Gaztanaga *et al.*, 2009; Chuang & Wang, 2012). As the signal is degraded by RSD (Section 2.4.2), the distortion of the acoustic peak has different properties in the directions parallel and transverse to the LoS. A 2D BAO analysis was performed on the reconstructed sample of SDSS-II LRGs (Xu *et al.*, 2013) using the first two multipole moments of the two-point correlation function (monopole and quadrupole). Alternatively, the full 3D clustering signal can be projected onto clustering wedges (Kazin *et al.*, 2012) of the correlation function. The pure BAO analysis of the two-point correlation function monopole and quadrupole (Anderson *et al.*, 2014a) and wedges (Kazin *et al.*, 2013) measured the angular diameter distance and Hubble parameter to ca. 3% and 8% precision, respectively, from the DR9 CMASS sample by applying

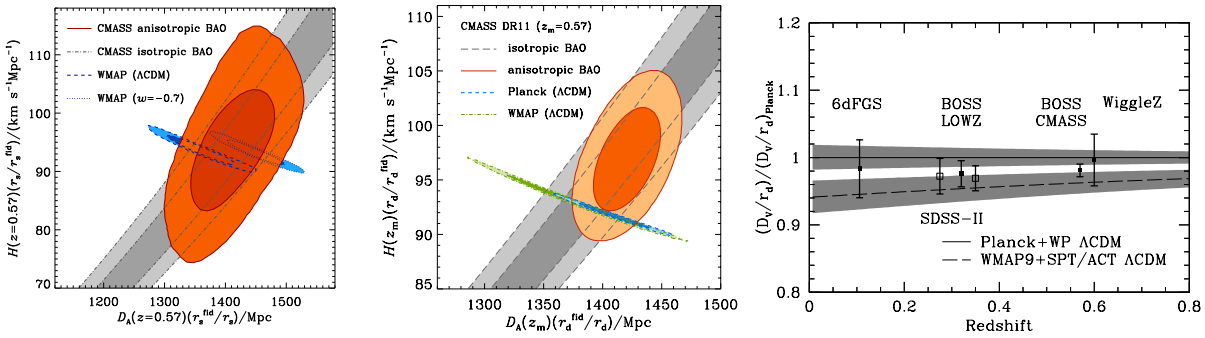

Figure 1.10 – (Image credit: BOSS collaboration) Anderson *et al.* (2014a) measured the anisotropic BAO information in DR9 CMASS. The resulting constraints in the $D_A(z_{\rm eff}^{\rm CMASS})$–$H(z_{\rm eff}^{\rm CMASS})$ plane are shown in the left-hand panel together with the isotropic constraints (Anderson *et al.*, 2013) and WMAP9 predictions (Hinshaw *et al.*, 2013). In Anderson *et al.* (2014b), this analysis was repeated with the extended sky coverage of the DR10 and DR11 samples. The centre panel compares the inferred D_A and H constraints to the WMAP9 and *Planck* 2013 (Ade *et al.*, 2014a) predictions. The derived angle-averaged distance is compared to other BAO measurements and the CMB predictions in the right-hand panel. All measurements use linear-density reconstruction to improve the BAO distance constraints.

reconstruction and marginalizing over the broad-band shape of the clustering statistics. As the broad-band shape can be modelled in the quasi-linear regime, its information content can improve constraints on the BAO distance and growth of structure from RSD. Such an analysis was performed on the DR9 CMASS sample using the Legendre moments (Chuang *et al.*, 2013a) and clustering wedges (Sánchez *et al.*, 2013).

The footprints of the CMASS samples corresponding to the three partial data releases of BOSS are plotted in the three left-hand panels of Figure 1.9. As the spectroscopic sky coverage increased from 3 275 deg^2 in DR9 to 6 161 deg^2 in DR10, and then to 8 377 deg^2 in DR11, the sensitivity of the sample with respect to the BAO distance increased as well. The BAO feature was detected to 7σ in the galaxy correlation function and power spectrum of DR11 CMASS (Anderson *et al.*, 2014b). From the reconstructed LOWZ sample, the isotropic BAO distance was measured in configuration and Fourier space, resulting in a consensus 2.0% distance measurement at $z_{\rm eff} = 0.32$ (Tojeiro *et al.*, 2014). The improved isotropic and anisotropic BAO constraints are shown in Figure 1.10 and individual BAO measurements based on BOSS are listed Table 1.1 (compared to some recent SDSS LRG constraints and WiggleZ measurements).

Besides BAO measurements from reconstructed density fields, the CMASS sample provides tight constraints on the growth of structure at its effective redshift $z_{\rm eff} = 0.57$. The results have been published in a series of papers: Beutler *et al.* (2014a) fitted the power spectrum monopole and quadrupole and measured the growth of structure using a sophisticated model for RSD (see Section 2.4.6 for more details on non-linear RSD modelling). The correlation function

Table 1.1 – Summary of the precision of isotropic and anistropic BAO distance measurements from the reconstructed SDSS and BOSS galaxy samples. 'CF' indicates configuration space analysis of the correlation function, 'PS' represents power spectrum measurements in Fourier space. 'Consensus' results combine $P(k)$ and $\xi(s)$ measurements and the quoted error represents an estimate of the combined statistical and systematic errors.

Publication	Galaxy sample & analysis	D_V	D_A	H
Ross *et al.* (2015)	DR7 MGS consensus	3.8%	-	-
Padmanabhan *et al.* (2012)	DR7 LRG CF	1.9%	-	-
Xu *et al.* (2013)	DR7 LRG CF multipoles	2.4%	3.6%	8.3%
Anderson *et al.* (2013)	DR9 CF	1.7%	-	-
Sanchez *et al.* (2012)	DR9 CF	1.5%	-	-
Anderson *et al.* (2014a)	DR9 CF consensus	1.6%	3.2%	8.4%
Kazin *et al.* (2013)	DR9 CF wedges	1.5%	1.9%	5.0%
Tojeiro *et al.* (2014)	DR10 LOWZ consensus	2.8%	-	-
Tojeiro *et al.* (2014)	DR11 LOWZ consensus	2.0%	-	-
Anderson *et al.* (2014b)	DR10 consensus	1.5%	1.9%	5.0%
Chuang *et al.* (2013b)	DR11 CMASS CF multipoles	1.3%	1.9%	3.1%
Sánchez *et al.* (2014)	DR11 CMASS CF wedges	1.3%	1.9%	3.1%
Anderson *et al.* (2014b)	DR11 consensus	1.0%	1.5%	3.3%
Gil-Marín *et al.* (2015c)	DR12 LOWZ consensus[†]	-	2.2%	6.0%
Cuesta *et al.* (2015)	DR12 CMASS consensus[†]	-	1.4%	2.9%
For comparison:				
Kazin *et al.* (2014)	WiggleZ CF	up to 3.4%	-	-
Beutler *et al.* (2015)	DR11 CMASS & WiggleZ CF	up to 2.4%	-	-

[†] Consensus values of the PS multipole analysis in (Gil-Marín *et al.*, 2015c) and the CF multipole analysis in (Cuesta *et al.*, 2015).

monopole and quadrupole was fitted with an RSD streaming model in Samushia *et al.* (2014). Chuang *et al.* (2013b) used only quasi-linear scales to fit a damped linear-theory model. A model inspired by renormalized perturbation theory (RPT) is used in Sánchez *et al.* (2014) to perform full-shape fits with the LOWZ and CMASS correlation function wedges. After the main series of papers of the BOSS DR11 analysis, the DR11 CMASS sample was fitted using a clustering model based on Convolution Lagrangian Perturbation Theory (CLPT) with Gaussian streaming model (GSRSD) for RSD, improving the growth constraints from the CF multipoles by 10% (Alam *et al.*, 2015b). Further, with the help of HOD fitting methods for the small-scale clustering signal in configuration space, the error on $f\,\sigma_8$ was reduced to 2.5% (Reid *et al.*, 2014), the tightest constraint at the time of writing this thesis. This result is more model-dependent than the other DR11 analyses and relied on a modified correction for galaxies that could not be observed due to collisions of the spectroscopic fibres on the observational plate. The RSD constraints from BOSS measurements are compared to each other and those derived from other datasets in Table 1.2.

In general, RSD measurements using galaxy two-point statistics alone show a correlation of the growth rate f and the clustering amplitude σ_8 as only the product $f\,\sigma_8$ is tightly constrained. As a different alignment of the line of degeneracy is found in fits of the bispectrum Gil-Marín *et al.* (2015a), the combination of the two- and three-point correlation measurements break

Table 1.2 – Summary of growth measurements from RSD observations of the SDSS and BOSS galaxy samples. 'CF' indicates configuration space analysis of the correlation function, 'PS' represents power spectrum measurements in Fourier space. 'Consensus' results combine $P(k)$ and $\xi(s)$ measurements and the quoted error represents an estimate of the combined statistical and systematic errors. The quoted errors on $f\,\sigma_8$ are obtained by varying the background cosmology; many authors also derived constraints by fixing the background cosmology to the most recent CMB observation.

Publication	Galaxy sample & analysis	$z_{\rm eff}$	$D_{\rm A}$	H	$f\,\sigma_8$
Chuang & Wang (2013)	DR7 LRG 2D CF	0.35	7.0%	9.7%	21%
Oka *et al.* (2014)	DR7 LRG PS multipoles	0.3	4.3%	6.1%	17%
Reid *et al.* (2012)	DR9 CMASS CF multipoles	0.57	2.8%	4.9%	16%
Sánchez *et al.* (2013)	DR9 CMASS CF wedges	0.57	2.8%	4.5%	13%
Chuang *et al.* (2013a)	DR9 CMASS CF multipoles	0.57	3.0%	6.9%	15%
Sánchez *et al.* (2014)	DR10 LOWZ CF wedges	0.32	4.1%	4.0%	23%
Sánchez *et al.* (2014)	DR11 LOWZ CF wedges	0.32	4.4%	5.4%	21%
Sánchez *et al.* (2014)	DR10 CMASS CF wedges	0.57	2.2%	3.9%	13%
Sánchez *et al.* (2014)	DR11 CMASS CF wedges	0.57	1.9%	3.2%	11%
Chuang *et al.* (2013b)	DR11 LOWZ CF multipoles	0.32	6.4%	9.1%	25%
Chuang *et al.* (2013b)	DR11 CMASS CF multipoles	0.57	6.2%	6.9%	17%
Beutler *et al.* (2014a)	DR11 CMASS PS multipoles	0.57	1.5%	3.6%	11%
Samushia *et al.* (2014)	DR11 CMASS CF multipoles	0.57	1.7%	3.2%	10%
Alam *et al.* (2015b)	DR11 CMASS CF multipoles	0.57	1.6%	4.0%	8.9%
Reid *et al.* (2014)	DR11 CMASS CF multipoles[‡]	0.57	-	-	2.5%
Gil-Marín *et al.* (2015d)	DR12 LOWZ PS multipoles	0.32	3.0%	6.9%	16%
Gil-Marín *et al.* (2015d)	DR12 CMASS PS multipoles	0.57	1.6%	3.2%	8.6%
For comparison:					
Blake *et al.* (2012)	WiggleZ 2D PS	0.6	6.9%	6.9%	16%
Beutler *et al.* (2012)	6dFGS 2D CF	0.07	-	-	13%

[‡] Reid *et al.* (2014) chose to analyse adopted CF multipoles to better correct for fibre collisions on smale scales.

the degeneracy on f and σ_8 (Gil-Marín *et al.*, 2015b), significantly tightening the marginalized constraints of each parameter individually.

1.4.2 State-of-the-art galaxy clustering analysis with the LOWZ, the CMASS, and the combined sample of the final BOSS release

DR12 (Alam *et al.*, 2015a) is the final release within the SDSS-III series (Eisenstein *et al.*, 2011). The spectroscopic observations for BOSS ended in July 2014 and the final survey footprint covers ca. 10,400 square degrees on the sky with a mean sector completeness of 0.98. The selection colour cuts, sample specifications, and structural properties of the galaxies in the final DR12 samples are described in Reid *et al.* (2016). These samples contain in total ca. 1.5 million massive galaxies corresponding to an increase in effective area of 10% over DR11. A first set of 2D BAO and RSD measurements on the DR12 LOWZ and CMASS samples using fitting and modelling recipes very similar to the ones from previous analyses were published in several

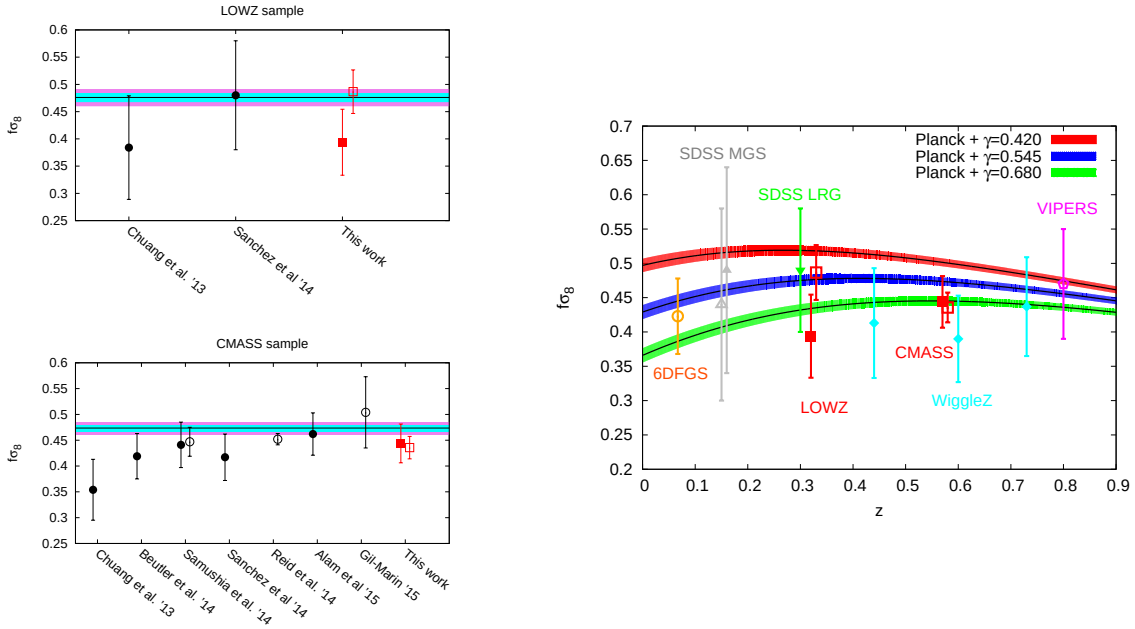

Figure 1.11 – (Image credit: BOSS collaboration) The two panels on the left-hand side show the RSD constraints from the BOSS DR11 LOWZ and CMASS samples using a damped linear-theory model fitted to the CF multipoles (Chuang *et al.*, 2013b), eTNS fits to the PS multipoles (Beutler *et al.*, 2014a), the original streaming model fitted to CF multipoles (Samushia *et al.*, 2014), RPT model constraints from CF wedges (Sánchez *et al.*, 2014), HOD fitting of the small-scale, fibre-collision-corrected CF clustering signal (Reid *et al.*, 2014), Convolution Lagrangian Perturbation Theory (CLPT) with Gaussian streaming model (GSRSD) fits to the CF multipoles (Alam *et al.*, 2015b), RPT+TNS fits to the power spectrum and bispectrum (Gil-Marín *et al.*, 2015a), and fits of the same model to the PS multipoles of the BOSS DR12 LOWZ and CMASS samples (Gil-Marín *et al.*, 2015d). The right-hand panel compares $f\,\sigma_8$ constraints of various LSS probes. In all panels, the *Planck* TT+lowP+lensing (*Planck* 2015; Adam *et al.*, 2015) predictions assuming a ΛCDM cosmology are shown as well.

papers: 2D BAO information from CF multipoles (Cuesta *et al.*, 2015) and PS multipoles (Gil-Marín *et al.*, 2015d) are merged into consensus measurements of $D_A(z)$ and $H(z)$, which show a modest improvement in error compared to the DR11 results. Gil-Marín *et al.* (2015d) performs an RSD growth analysis with recently improved models for the redshift-space clustering fitted to the PS multipoles. As shown in Figure 1.11, the constraints on $f\,\sigma_8$ improve slightly and are completely consistent with previous measurements. They are also compatible with the newest best-fit ΛCDM predictions from *Planck* 2015 observations (Adam *et al.*, 2015).

As the effective volume of the LOWZ sample is less than half of that of CMASS, a unified 'combined sample' was created for the final data release by the combination of the two samples; this is justified by the similarity of the clustering properties of LOWZ and CMASS. A series of companion papers led by (Anderson *et al.*, 2016, *in prep.*) focusses on the analysis of three redshift bins (of which 2 are non-overlapping) of the combined sample. The analysis recipes are modified to optimally extract cosmological information. The research presented in this thesis has been part of these efforts, focussing especially on the BAO+RSD measurements in Fourier space. The results of this analysis are discussed in the main chapters of this thesis and will be

published in Grieb *et al.* (2016b, *in prep.*). Other RSD measurements are presented in Beutler *et al.* (2016b, *in prep.*) and Sánchez *et al.* (2016, *in prep.*), the former employing a very similar modelling for the analysis of the power spectrum multipoles and the latter is using the same recipes for the RSD modelling as this work in configuration space. The analysis of the combined sample CF multipoles with the CLPT-GSRSD model already used in Alam *et al.* (2015b) will be presented in Satpathy *et al.* (2016, *in prep.*). Ross *et al.* (2016, *in prep.*, CF multipoles) and Beutler *et al.* (2016a, *in prep.*, PS multipoles) discuss BAO measurements pre- and post-reconstruction. A consensus BAO+RSD measurement is determined by the covariance-weighted average of the individual measurements and presented in Anderson *et al.* (2016, *in prep.*). The influence of systematics on the reconstructed BAO measurements is analysed in Vargas-Magaña *et al.* (2016, *in prep.*).

The systematic biases and the constraining power of the different RSD approaches are compared in an RSD challenge whose results are presented in Tinker *et al.* (2016, *in prep.*). A different, complementary technique is applied in Salazar-Albornoz *et al.* (2016, *in prep.*) where the angular clustering is analysed in thin redshift shells. This tomographic approach does not rely on the assumption of a fiducial cosmology.

1.4.3 Additional cosmological observations

The Lyman-α (Ly-α) forest, the absorption features from the continuously redshifting Ly-α-line in the spectra of distant galaxies and quasars (QSO) due to neutral hydrogen in the high-redshift universe (Lynds, 1971; McDonald *et al.*, 2000; McDonald, 2003), is the second major cosmological probe of BOSS. The Ly-α signal also has an imprint of the BAO as it depends on the density and ionization fraction of baryonic matter. Thus, the BAO distance can be measured at redshifts before the onset of Dark Energy domination. The BAO was detected with a 3σ confidence level using the DR9 quasar sample in Slosar *et al.* (2013), measuring the BAO distance scale to 2%. Using DR11, an anisotropic BAO measurement with the quasar-Ly-α forest was possible (Font-Ribera *et al.*, 2014; Delubac *et al.*, 2015). The joint BOSS LSS and Ly-α analysis (Aubourg *et al.*, 2015) is able to build an 'inverse distance ladder' using SN 1a data and BAO measurements to measure the local Hubble parameter to 1.7%.

1.4.4 The successor program: eBOSS

The extended Baryon Oscillation Spectroscopic Survey (eBOSS; Dawson *et al.*, 2016) will focus on clustering measurements in the redshift range between current BOSS samples and the quasars and extend the quasar sample (Myers *et al.*, 2015) to improve high-redshift BAO constraints from quasar clustering ($0.6 \leq z \leq 2.2$) and the Ly-α forest ($2 \leq z \leq 2.5$). The LSS samples will comprise of an extended LRG sample in addition with emission line galaxies (ELG; Jouvel *et al.*, 2015) in the redshift range $1 \leq z \leq 1.2$. It is expected that the eBOSS survey can improve the dark energy Figure-of-Merit (FoM) by a factor of up to three for the Chevallier-Polarski-Linder (CPL) parametrisation of Dark Energy (Zhao *et al.*, 2016) compared to current BOSS constraints.

1.5 Outline of the thesis

This PhD thesis is structured as follows: in Chapter 2, the fundamental theoretical concepts of physical cosmology are presented, with an emphasis on those aspects that are most important for the LSS analysis described in this thesis. This includes a discussion of the background cosmology and how structure is modelled as anisotropic perturbations on this background. This chapter pays a special focus to the late-time evolution of density perturbations in our Universe and how they are traced by galaxies in real- and redshift space. The Fourier space measurements of the anisotropic galaxy clustering on the BOSS DR12 combined sample are presented in Chapter 3. The definition of the optimal-variance estimator for clustering wedges in Fourier space, one of the main results of this thesis, is given there. This chapter also explains observational systematics such as the window function effect and presents the Fourier-space wedges measured from the data and synthetic catalogues whose clustering properties are matched to the data.

Chapter 4 discusses covariance matrices for the anisotropic clustering analysis and derives the theoretical Gaussian covariance matrices for redshift-space galaxy clustering (in configuration and Fourier space). These are validated on a set of galaxy catalogues generated from the Minerva simulations. The estimation of the data covariance matrix, however, is obtained from the sets of BOSS mocks. The modelling of the redshift-space galaxy clustering statistics is addressed in Chapter 5, summarizing the model parameter space and the details of the parameter estimation. Further, this chapter presents the verification of the redshift-space clustering model by means of performance test on synthetic catalogues obtained from Minerva simulations, as well as those specifically designed for the BOSS RSD challenge, as well as the Patchy mocks mimicking the full characteristics of the final BOSS sample.

Chapter 6 is the analysis of the measurements in a cosmological context and contains the main results of this thesis. These include the full-shape measurements of the BAO distance and growth rate for each redshift bin of the sample and the derivation of cosmological implications for the standard model and usual extensions using full-shape clustering measurements in combination with CMB and supernovae data. The outcome of this thesis is concluded and discussed in Chapter 7.

Appendix A contains a brief introduction to Bayesian techniques with a special focus on using the Markov chain Monte Carlo method to estimate parameter constraints. In Appendix B, the constraints for all parameters of the full-shape measurements and the basic cosmological and model parameters of the combined fits of CMB data, Fourier space wedges, and optionally SN Ia data are listed in tables.

2 Theory

> "General relativity is the most beautiful physical theory ever invented. It describes one of the most pervasive features of the world we experience — gravitation — in terms of an elegant mathematical structure — the differential geometry of curved spacetime — leading to unambiguous predictions that have received spectacular experimental confirmation. Consequences of general relativity, from the big bang to black holes, often get young people first interested in physics, and it is an unalloyed joy to finally reach the point in one's studies where these phenomena may be understood at a rigorous quantitative level."
>
> Carroll (2004)

In this second chapter of the thesis, I present the theoretical groundwork for the clustering analysis of galaxy-redshift surveys. The structure in our Universe is physically described as perturbations on a homogeneous background whose dynamics are derived in Section 2.1, discussing, for example, the FLRW universe, cosmic distances, and Dark Energy models. Starting the introduction to the inhomogeneous universe, the clustering two-point statistics are introduced in Section 2.2. In Section 2.3, the physics of the inhomogeneities of the early universe are described to a level of detail that is sufficient to discuss the main features of the matter power spectrum and the baryonic acoustic oscillations imprinted on it. Finally, Section 2.4 lays the framework for the analysis of the galaxy clustering measurements. The discussion of the late-time evolution of the density anisotropies includes an introduction to perturbation theory, redshift-space distortions, and the Alcock-Paczynski effect. A special focus lies on the modelling of two-point statistics of the evolved density perturbations, as traced by galaxies in real- and redshift space, in the non-linear regime. Hence, the modelling of the matter clustering in the non-linear regime (Section 2.4.4), galaxy bias (Section 2.4.5), and redshift-space distortions (Section 2.4.6) used in this work are presented in more detail.

This chapter only presents the most relevant aspects of theoretical cosmology. For more in-depth descriptions, the reader is referred to standard cosmology textbooks such as Dodelson (2003).

2.1 The smooth background universe

2.1.1 The background evolution

The only relevant physical interaction at cosmological scales is gravity, which is described by *general relativity* (GR; Einstein, 1915, 1916). This and the *cosmological principle* stating that the Universe is isotropic and homogeneous on large scales are the fundamental hypotheses of cosmology. The space-time metric of the Universe is the spatially maximally symmetric *Friedmann-Lemaítre-Robertson-Walker* (FLRW) metric,[1]

$$\mathrm{d}s^2 = g_{\mu\nu}\,\mathrm{d}x^\mu\,\mathrm{d}x^\nu = -\mathrm{d}t^2 + a^2(t)\left[\frac{\mathrm{d}r^2}{1-K\,r^2} + r^2\left(\mathrm{d}\theta^2 + \sin^2\theta\,\mathrm{d}\varphi^2\right)\right], \tag{2.1}$$

where $a(t)$ is the (dimensionless) *scale factor*, t is the time coordinate, r, θ, and φ are spatial coordinates (in a spherical coordinate system), and K is the *curvature* constant. The last constant defines the spatial geometry of the universe where $K = 0$ corresponds to flat (Euclidean), $K < 0$ to open (hyperbolic), and $K > 0$ to closed (elliptical) spatial hypersurfaces of the Universe.

Equation (2.1) is based on *comoving* coordinates that are chosen to be stationary with respect to changes in $a(t)$. The physical spatial separations $\boldsymbol{r}$, which expand with the scale factor $a(t)$, are related to the comoving distances $\boldsymbol{x}$ by

$$\boldsymbol{r} = a(t)\,\boldsymbol{x}, \quad \text{and} \quad \boldsymbol{v} \equiv \dot{\boldsymbol{r}} = \dot{a}(t)\,\boldsymbol{x} + \boldsymbol{u}, \tag{2.2}$$

where $\boldsymbol{v}$ is the physical velocity field, which is decomposed into a 'cosmic flow' component ($\dot{a}\,\boldsymbol{x}$) and a residual peculiar velocity field in comoving coordinates, $\boldsymbol{u}$. The normalization of the scale factor is chosen such that $a(t_0) = 1$ where t_0 is the time of today. The spatial curvature is given by the scalar of curvature,

$${}^{(3)}R = \frac{6K}{a^2(t)}. \tag{2.3}$$

It is convenient to define the *conformal time* τ by

$$\mathrm{d}t = a(\tau)\,\mathrm{d}\tau, \tag{2.4}$$

so that the FLRW metric can be factorized in a static metric and a time-dependent pre-factor, $\mathrm{d}s^2 = a^2(\tau)\left[-\mathrm{d}\tau^2 + \mathrm{d}\Sigma^2\right]$.

By defining the radial coordinate χ as

$$\mathrm{d}\chi = \frac{\mathrm{d}r}{\sqrt{1-Kr^2}}, \tag{2.5}$$

the spatial part $\mathrm{d}\Sigma^2$ of the FLRW metric of equation (2.1) can be written in an alternative form,

$$\mathrm{d}\Sigma^2 = \mathrm{d}\chi^2 + S_K^2(\chi)\left[\mathrm{d}\theta^2 + \sin^2\theta\,\mathrm{d}\varphi^2\right], \tag{2.6}$$

[1] Note that a unit system where $c = 1$ was adopted.

Table 2.1 – The different components of the energy budget of the Universe and its equation-of-state parameter w_i as defined by equation (2.14).

Component	Abbreviation i	EoS parameter w_i
Radiation	r	1/3
Cold dark matter	c	0
Baryons	b	$\neq 0$, but suppressed
Cosmological constant	Λ	-1
(Dark Energy)	DE	w_{DE}
(Curvature)	K	$-1/3$

where $S_K(\chi)$ is a function of the radial coordinate given by

$$S_K(\chi) = \begin{cases} \frac{1}{\sqrt{k}} \sin(\sqrt{k}\,\chi) & \text{if } K > 0, \\ \chi & \text{if } K = 0, \\ \frac{1}{\sqrt{|k|}} \sinh(\sqrt{|k|}\,\chi) & \text{if } K < 0. \end{cases} \tag{2.7}$$

The dynamics of the metric are governed by the *Einstein equation*,

$$G_{\mu\nu} = R_{\mu\nu} - \frac{1}{2}\, g_{\mu\nu}\, R = 8\pi G\, T_{\mu\nu}, \tag{2.8}$$

where G is Newton's constant, $T_{\mu\nu}$ the *energy-momentum tensor*, $R_{\mu\nu}$ the Ricci tensor and $R = g^{\mu\nu} R_{\mu\nu}$ the Ricci scalar. $G_{\mu\nu}$ and $R_{\mu\nu}$ are tensors describing the curvature and as such fundamental quantities in the *differential geometry of curved spacetime* (GR is an example of such a theory). They are given by non-linear functions of the metric $g_{\mu\nu}$ and its inverse metric $g^{\mu\nu}$. Other important concepts of differential geometry are the Christoffel symbols, the Levi-Cevita connection, contra- and covariant indices and the covariant derivative ∇^μ, which will not be discussed in this brief introduction. The reader is referred to lectures and textbooks on general relativity such as Weinberg (1972) and Carroll (2004).

The most general form of the energy-momentum tensor that is compatible with the hypothesis of homogeneity and isotropy is a *perfect fluid*,

$$T_{\mu\nu} = (p + \rho)\, U_\mu\, U_\nu + p\, g_{\mu\nu}, \tag{2.9}$$

where ρ, p, and U^μ are the energy density, pressure, and four-velocity of the fluid.

With the assumptions of a FLRW metric and a perfect fluid, the Einstein equations in (2.8) reduce to two independent *Friedmann equations*,

$$\left(\frac{\dot{a}}{a}\right)^2 = \frac{8\pi G}{3}\rho - \frac{K}{a^2} \tag{2.10}$$

$$\frac{\ddot{a}}{a} = -\frac{4\pi G}{3}\,(\rho + 3\,p)\,. \tag{2.11}$$

These equations implicitly contain the *continuity equation*,

$$\dot{\rho} + 3\,\frac{\dot{a}}{a}\,(\rho + p) = 0, \tag{2.12}$$

as a result of the energy-momentum conservation equation, $\nabla^\nu T_{\mu\nu} = 0$.

For non-interacting species of particles, the energy-momentum tensor can be written as the sum over contributions of each type. Here, we use the (relativistic) *radiation*, the (non-relativistic and pressureless) *cold dark matter*, the non-relativistic *baryonic*, and the *vacuum energy*[2] components,

$$T_{\mu\nu} = T^r_{\mu\nu} + T^c_{\mu\nu} + T^b_{\mu\nu} + T^\Lambda_{\mu\nu}, \tag{2.13}$$

each modelled as a *barotropic fluid*. This assumes that each component is described as a perfect fluid whose pressure p_i and density ρ_i are related by a linear equation of state (EoS),

$$p = w\,\rho, \quad w = \text{const.} \tag{2.14}$$

The particle species are characterised by their equation-of-state parameters w, which are listed in Table 2.1. These components define the cosmological standard model (ΛCDM).

The energy density of a non-interacting barotropic fluid evolves as

$$\rho \propto a^{-3(1+w)} \tag{2.15}$$

with the scale factor. Due to the varying time dependence of each component, the total energy density of the Universe, $\rho = \sum_i \rho_i$, was dominated by different species at different times. The transition times depend on the exact ratios of today's energy densities: the Universe was radiation-dominated after the Big Bang, then became matter-dominated, and finally the cosmological constant dominates the dynamics. The energy density of the cosmological constant is time-independent, $\rho_\Lambda = (8\pi G)^{-1}\Lambda$, and for any expanding universe in which $\Lambda \neq 0$, this 'vacuum energy' will eventually prevail. In principle, a curvature-dominated era is also possible, but this case is excluded by cosmological observations.

For convenience, the *Hubble parameter* is defined as

$$H \equiv \frac{\dot{a}}{a}, \tag{2.16}$$

whose value today is usually written as

$$H_0 \equiv H(t_0) = 100\ h\,\mathrm{km\,s^{-1}\,Mpc^{-1}}. \tag{2.17}$$

[2] Many textbooks and articles write the Einstein equation as

$$G_{\mu\nu} = R_{\mu\nu} - \frac{1}{2}\,g_{\mu\nu}\,R + \Lambda\,g_{\mu\nu} = 8\,\pi\,G\,T_{\mu\nu},$$

expressing the vacuum energy as the analogous *cosmological constant* Λ. We have adopted the convention to write the vacuum energy, $T^\Lambda_{\mu\nu} = -\frac{\Lambda}{8\pi G}\,g_{\mu\nu}$, as a contribution to $T_{\mu\nu}$.

Equation (2.10) implies that the Universe is flat ($K = 0$) for a critical density given by

$$\rho_{\rm crit} \equiv \frac{3H_0^2}{8\pi G} = 2.773 \times 10^{11}\ M_\odot\, h^{-1} \left(h^{-1}\,{\rm Mpc}\right)^{-3}. \tag{2.18}$$

Normalizing each density by the critical one, we define the *density parameters* for each species in equation (2.13),

$$\Omega_i \equiv \frac{\rho_i(t_0)}{\rho_{\rm crit}} = \frac{8\pi G}{3H_0^2}\,\rho_i(t_0). \tag{2.19}$$

Besides the natural components ($\Omega_{\rm r}$, $\Omega_{\rm c}$, $\Omega_{\rm b}$, and Ω_Λ for a ΛCDM universe), we define the *curvature* component as

$$\Omega_K \equiv -\frac{K}{H_0^2}, \tag{2.20}$$

so that the first Friedmann equation reads $\sum_i \Omega_i + \Omega_K = 1$.

2.1.2 Cosmological distances

Cosmological distances, such as the radial or angular diameter distance, are derived as the natural extension of the analogous distances in a Euclidean universe. In a FLRW universe, the scale factor plays a prominent role as it gives the scaling relation between comoving coordinates and physical distances. The *proper distance*, $D_{\rm p}(t)$, between the origin and an object of coordinates (r, θ, φ) is given by

$$D_{\rm p}(t) \equiv a(t)\, D_{\rm c} = a(t) \int_0^r \frac{{\rm d}r'}{\sqrt{1 - K(r')^2}} = a(t)\chi, \tag{2.21}$$

where χ is the radial coordinate defined by equation (2.5), which coincides with the comoving distance to the object, $D_{\rm c}$. The comoving distance also corresponds to the present-day proper distance $D_{\rm p}(t_0)$ as we chose $a(t_0) = 1$.

The *cosmological redshift* z is given by the ratio of the wavelength shift due to the expansion of the Universe, $\Delta\lambda_{\rm obs}$, and the emitted wavelength $\lambda_{\rm emit}$,

$$1 + z \equiv 1 + \frac{\Delta\lambda_{\rm obs}}{\lambda_{\rm em}} = \frac{\lambda_{\rm obs}}{\lambda_{\rm em}} = \frac{1}{a}. \tag{2.22}$$

Thus, light that is received with a redshift z left the emitting galaxy, when the scale factor was $a = (1 + z)^{-1}$.

In cosmological observations, the redshift is the measured radial coordinate instead of time or the scale length, $a(t)$. Hence, it is useful to relate the proper distance to redshift,

$$D_{\rm p}(z) = \int_0^z \frac{{\rm d}z'}{H(z')}. \tag{2.23}$$

Here, the Hubble parameter at redshift z is given by

$$H^2(z) = H_0^2 \sum_i \Omega_i (1 + z)^{3(1+w_i)}, \tag{2.24}$$

where the EoS parameters w_i can be found in Table 2.1.

For low redshifts, the linear approximation of equation (2.23) is the *Hubble law*,

$$D_\mathrm{p}(z) \approx \frac{c\,z}{H_0}, \tag{2.25}$$

where the speed of light c was written explicitly despite the convention $c = 1$ elsewhere.

Thus, local measurements of the distance-redshift relation allow us to constrain the present-day Hubble parameter H_0, while observations of the redshift-distance relation over a wide range of redshifts allows to infer the decomposition of the Universe into energy components and their EoS parameter via $H(z)$.

As the proper distance is not an observable, alternative concepts of distance are used in cosmology to probe the distance-redshift relation. Here, we discuss the most important one for this work, the *angular diameter distance*, $D_\mathrm{A}(z)$.

Galaxies are extended objects on the sky. Let us assume that such an object at a comoving distance $\chi(z)$ is perceived with an angular diameter $\delta\varphi$. According to the spatial FLRW metric in spherical coordinates, given by equation (2.6), the physical size is

$$\delta l = a(z)\, S_K(\chi(z))\, \delta\varphi. \tag{2.26}$$

As the corresponding relation in a static Euclidean universe is

$$\delta l = D\, \delta\varphi, \tag{2.27}$$

where D is the distance to the object, the angular diameter distance is defined by the comparison of these two equations,

$$D_\mathrm{A}(z) \equiv a(z)\, S_K(\chi(z)). \tag{2.28}$$

For a flat universe, this reduces to $D_\mathrm{A}(z) = D_\mathrm{c}(z)/(1+z)$. Thus, the angular diameter distance follows a different redshift evolution than the comoving distance $D_\mathrm{c}(z)$ for large z. In fact, $D_\mathrm{A}(z)$ has a turning point and galaxies of constant physical size very far away have a larger angular diameter than those closer by (as their comoving size is also larger). Objects with a predictable physical size are known as *standard rulers* and are further discussed in Section 2.4.7.

2.1.3 Dark Energy

Weakening the assumptions of the standard model, Dark Energy (DE) is not represented by a cosmological constant as in the ΛCDM paradigm. A general Dark Energy model does not fix the evolution of the EoS parameter w_DE. In that case, the Hubble parameter $H(z)$ in equation (2.24) has to be modified to

$$H(z)^2 = H_0^2 \left\{ \sum_{i \neq \Lambda} \Omega_i (1+z)^{3(1+w_i)} + \Omega_\mathrm{DE}\, \exp\left[-3 \int_0^z (1 + w_\mathrm{DE}(z'))\, \frac{\mathrm{d}z'}{z'} \right] \right\}. \tag{2.29}$$

Common restrictions of the equation of state of DE are a constant EoS parameter, $w_\mathrm{DE} = \text{const}$, and the Chevallier-Polarski-Linder (CPL) parametrization (Chevallier & Polarski, 2001; Linder, 2003),

$$w_\mathrm{DE}(z) = w_0 + w_\mathrm{a}\,(1-a) = w_0 + w_\mathrm{a} \frac{z}{1+z}. \tag{2.30}$$

Here, the equation of state is allowed to have a linear modification with the scale length of the Universe, $a(z) = (1+z)^{-1}$.

The CPL parametrization is however entirely phenomenological, as the underlying physics of a crossing of the *phantom divide* barrier, $w_{\rm DE} = -1$, is unknown (Vikman, 2005). For instance, a crossing of this barrier cannot be modelled with a scalar field φ, which otherwise can model a perfect fluid with an arbitrary equation of state,

$$w_\varphi = \frac{\frac{1}{2}\dot{\varphi}^2 - V(\varphi)}{\frac{1}{2}\dot{\varphi}^2 + V(\varphi)}, \tag{2.31}$$

where $\frac{1}{2}\dot{\varphi}^2$ and $V(\varphi)$ are the kinetic and potential energy of the scalar field, respectively. This scalar-field description for DE is used, for instance, in the *Quintessence* models (Ratra & Peebles, 1988)

2.2 Two- and N-point statistics

Before the physics of the anisotropic universe is discussed, this section introduces the concepts of N-point statistics, which are used to quantify the cosmological inhomogeneities.

2.2.1 Two-point clustering measurements

All N-point clustering measurements are based on a density contrast or density fluctuation field, $\delta(\boldsymbol{x})$. Here, we assume Euclidean space in three dimensions with Cartesian coordinates $\boldsymbol{x}$. In large-scale structure measurements, galaxies are observed as (biased) tracers of the matter clustering. The density contrast is defined by the spatial density of galaxies, $n(\boldsymbol{x})$, with respect to the mean (background) density $\bar{n}$,

$$\delta(\boldsymbol{x}) \equiv \frac{n(\boldsymbol{x}) - \bar{n}}{\bar{n}}. \tag{2.32}$$

Here and in the following chapters, the Fourier transform is defined as

$$\widehat{\delta}(\boldsymbol{k}) \equiv \int \delta(\boldsymbol{x})\, \mathrm{e}^{-\mathrm{i}\boldsymbol{k}\cdot\boldsymbol{x}}\, \mathrm{d}^3x\,. \tag{2.33}$$

Thus, the inverse Fourier transform is

$$\delta(\boldsymbol{x}) = \frac{1}{(2\pi)^3} \int \widehat{\delta}(\boldsymbol{k})\, \mathrm{e}^{\mathrm{i}\boldsymbol{x}\cdot\boldsymbol{k}}\, \mathrm{d}^3k\,. \tag{2.34}$$

As there is only one Universe to observe, two-point statistics are taken as spatial averages, denoted by $\langle\cdots\rangle$, over products of the density contrast. Clustering analyses measure two-point statistics from a density 'snapshot' of the universe at a certain look-back time. Initially, the density perturbations were small, $|\delta| \ll 1$, so that their evolution from the setting of the initial conditions to the snapshot time can be described by linear approximations of the gravitational

field equations (linear perturbation theory). For large scales, the evolved density fluctuations do not exceed $|\delta| \simeq 1$ and still belong to the regime of linear evolution equations. Thus, uncorrelated Fourier modes evolve independently, so that the two-point function is more naturally described in Fourier space. The *power spectrum* is defined as the covariance of the Fourier density fluctuations,

$$\langle \widehat{\delta}(\boldsymbol{k})\, \widehat{\delta}(\boldsymbol{k}')^* \rangle = (2\pi)^3 \delta_{\mathrm{D}}(\boldsymbol{k} - \boldsymbol{k}')\, P(\boldsymbol{k}), \tag{2.35}$$

where $\delta_{\mathrm{D}}(\boldsymbol{k})$ is the 3D Dirac delta function and $\widehat{\delta}(\boldsymbol{k})^*$ denotes the complex conjugate of the Fourier density field.

The (two-point) *correlation function*, defined as

$$\xi(\boldsymbol{r}) \equiv \langle \delta(\boldsymbol{x}) \delta(\boldsymbol{x} + \boldsymbol{r}) \rangle, \tag{2.36}$$

represents the Fourier transform of the power spectrum,

$$\xi(\boldsymbol{r}) = \frac{1}{(2\pi)^3} \int P(\boldsymbol{k})\, \mathrm{e}^{\mathrm{i}\boldsymbol{k}\cdot\boldsymbol{r}}\, \mathrm{d}^3 k\,. \tag{2.37}$$

According to the cosmological principle, the density field is assumed to be statistically isotropic and homogeneous at large scales, so that the power spectrum depends only on the absolute wavenumber $k \equiv |k|$ and the correlation function only on the distance $r = |\boldsymbol{r}|$. In this isotropic case, the Fourier relation between power spectrum and correlation function reduces to

$$\xi(r) = \frac{1}{2\pi^2} \int P(k)\, j_0(kr)\, k^2\, \mathrm{d}k. \tag{2.38}$$

As the definition of the power spectrum in equation (2.35) has units of volume, it is useful to define a dimensionless power spectrum as

$$\Delta^2(k) = \frac{k^3}{2\pi^2} P(k). \tag{2.39}$$

Another observable derived from the power spectrum is the *spectral index*, n_{s}, which represents the power-law approximation of the power spectrum,

$$n_{\mathrm{s}} \equiv \frac{\mathrm{d} \ln P(k)}{\mathrm{d} \ln k}. \tag{2.40}$$

A power spectrum that satisfies $n_{\mathrm{s}} = 1$ is called *scale-invariant*.

2.2.2 Higher order correlations and Gaussianity

The N-point correlation function, $\xi^{(n)}(\boldsymbol{x}_1, \ldots, \boldsymbol{x}_n)$, is defined by the relation (Peacock, 1998, chapter 16.2):

$$1 + \xi^{(n)}(\boldsymbol{x}_1, \ldots, \boldsymbol{x}_n) = \langle \prod_{i=1}^{n} [1 + \delta(\boldsymbol{x}_i)] \rangle. \tag{2.41}$$

Each n-point function has contributions from lower orders and a reduced term that corresponds to $\xi^{(n)}_{\rm red}(\boldsymbol{x}_1,\ldots,\boldsymbol{x}_n) = \langle\prod_{i=1}^{n}\delta(\boldsymbol{x}_i)\rangle$. Here, we give the relation for the three-point function as an example,

$$\xi^{(3)}(\boldsymbol{x}_1,\boldsymbol{x}_2,\boldsymbol{x}_3) = \xi(\boldsymbol{x}_1-\boldsymbol{x}_2)+\xi(\boldsymbol{x}_1-\boldsymbol{x}_3)+\xi(\boldsymbol{x}_2-\boldsymbol{x}_3)+\zeta(\boldsymbol{x}_1,\boldsymbol{x}_2,\boldsymbol{x}_3), \tag{2.42}$$

where $\zeta(\boldsymbol{x}_1,\boldsymbol{x}_2,\boldsymbol{x}_3) \equiv \xi^{(3)}_{\rm red}(\boldsymbol{x}_1,\boldsymbol{x}_2,\boldsymbol{x}_3) = \langle\delta(\boldsymbol{x}_1)\,\delta(\boldsymbol{x}_2)\,\delta(\boldsymbol{x}_3)\rangle$ is the reduced three-point correlation function.

The Fourier-space higher order correlations are defined likewise. For example, the *bispectrum*, $B(\boldsymbol{k}_1,\boldsymbol{k}_2,\boldsymbol{k}_3)$, is defined as

$$\langle\widehat{\delta}(\boldsymbol{k}_1)\,\widehat{\delta}(\boldsymbol{k}_2)\,\widehat{\delta}(\boldsymbol{k}_3)\rangle = (2\pi)^3\,\delta_{\rm D}(\boldsymbol{k}_1+\boldsymbol{k}_2+\boldsymbol{k}_3)\,B(\boldsymbol{k}_1,\boldsymbol{k}_2,\boldsymbol{k}_3), \tag{2.43}$$

which is the Fourier-space counterpart of the reduced three-point function $\zeta(\boldsymbol{x}_1,\boldsymbol{x}_2,\boldsymbol{x}_3)$.

For a Gaussian density field, the connected correlators of odd order vanish and the reduced n-point functions with even n can be written in terms of the two-point statistics by the *Isserlis theorem* (also known as *Wick theorem*). For the evolved cosmic density field, gravitational mode-coupling produced deviations from Gaussianity, so that the higher-order correlators differ from the predictions by the Isserlis theorem. Thus, a fraction of the cosmological information is only accessible by means of the higher-order correlators as not all information is contained in the two-point statistics.

An alternative to measurements of the higher-order statistics is the *Gaussianisation* of the density field. Such techniques can restore the information in the two-point statistics that was 'lost' to higher-order correlators due to the non-linear evolution.

2.3 The early anisotropic universe

This section gives a summary of the physics of the early anisotropies in the Universe that are relevant for the matter power spectrum at later times, especially for its broad-band shape and the BAO feature imprinted onto it.

2.3.1 The linear-theory matter power spectrum

The primordial power spectrum

In addition to general relativity and the cosmological principle, the standard cosmological paradigm includes an early phase of *inflation*, in which the expansion of the scale factor was very close to an exponential dependence on time (and thus the expansion accelerated). This inflationary epoch took place before the generation of known matter in the baryogenesis and the Big Bang Nucleosynthesis and it is consistent with a number of observations, even though no direct evidence of this scenario has been found yet. Most importantly, inflation provides a mechanism for the origin of the initial seeds of the large-scale structure that we see today. Many inflationary scenarios have been developed, but the most simple ones assume a single

scalar field whose background evolution was in *slow roll*. This means that the potential energy dominated over the kinematic energy and this state lasted for a period in which the scale factor increased at least by a factor of $\exp(60)$ solving the horizon and flatness problem (for more details on inflation, see standard textbooks such as Liddle & Lyth, 2000). Due to the accelerated expansion, the comoving Hubble scale $(aH)^{-1}$ decreased. Outside the horizon, the fluctuations of the scalar field are 'frozen-in' because they loose causal contact. On the spatial hypersheet in which inflation ends (due to the violation of the slow-roll conditions), the fluctuations are converted to time perturbations. Thus, the initial density perturbations have been formed from variations of the potential energy.

This simple scenario leads to a few generic predictions for the density perturbations, which can be tested in cosmological observations:

1. The initial perturbations were *Gaussian* as they correspond to quantum fluctuations of a scalar field residing in its ground state due to the fast dilution. Thus, the density field is fully described by the *primordial power spectrum*.

2. As the structure of all other matter in the Universe can be explained by perturbations of a single degree of freedom, these perturbations are *adiabatic* and can be described with a single power spectrum, the density power spectrum P_δ.

3. Due to the slow-roll condition, this power spectrum is almost scale-invariant and can be described by a power law. In terms of the *comoving curvature perturbation*, $\mathcal{R}$, this power law reads

$$\Delta^2_\delta(\mathcal{R}) = A\left(\frac{k}{k_0}\right)^{n_\mathrm{s}-1}, \tag{2.44}$$

   where $\Delta^2_\mathcal{R}$ is the dimensionless power spectrum, defined in equation (2.39), of $\mathcal{R}$, k_0 is an arbitrary reference scale, the amplitude A is a free parameter, and the *spectral index* is n_s (also known as *tilt*). Due to the slow-roll condition, *ns* is close to unity. In order not to depend explicitly on the power-law assumption, the tilt can also be defined in a scale-dependent manner as

$$n_\mathrm{s}(k) - 1 \equiv \frac{\mathrm{d}\ln\Delta^2_\mathcal{R}(k)}{\mathrm{d}\ln k}. \tag{2.45}$$

4. Apart from scalar inhomogeneities, inflation naturally produces tensors perturbations, which propagate through the Universe as gravitational waves. These waves leave an imprint in the CMB polarization, whose detection would be a strong indication of the correctness of the inflation paradigm.

The first three predictions have been verified in observations to great precision, especially by measurements of the CMB temperature and polarization (e.g., see the *Planck* 2015 results, Ade *et al.*, 2015).

A note on cosmological perturbation theory. Cosmological perturbation theory must take the *gauge freedom* into account. The free choice of the coordinate system that is used to describe the perturbations means that besides physical degrees of freedom (DoF), the evolution equations of a perturbed cosmological model also include DoF that correspond to redefinitions of the coordinates. Restricting the coordinate system to a specific choice removes these unphysical solutions. Alternatively, results can be expressed in terms of *gauge-independent variables* that do not depend on the choice of the coordinate system. One example is the comoving curvature perturbation $\mathcal{R}$ that is used to describe the metric and density perturbations sourced by the inflaton field.

The transfer function and the power spectrum in linear theory

The primordial curvature perturbations are conserved outside the horizon. During the radiation- and matter-dominated epochs after the Big Bang, the Hubble scale increases and becomes successively larger than the scale-length of the primordial fluctuations, which thus re-enter into the horizon. The evolution of the perturbation modes after re-entry has to be described by fully relativistic perturbation theory using the linearised Einstein equations for a perturbed FLRW universe. This treatment is very complex (among other aspects due to gauge freedom) and a full treatment is beyond the scope of the theory chapter of this thesis. The reader is referred to the seminal review of Bardeen (1980) and textbooks such as Dodelson (2003) and Weinberg (2008).

The most important effect on the evolution of density perturbations is the transition from radiation to matter domination. The transition (or turn-over) scale is given by the horizon size at the time of matter-radiation equality ($1 + z_{\mathrm{eq}} \simeq 23900\,\Omega_{\mathrm{M}}\,h^2$),

$$k_{\mathrm{eq}} \simeq 0.073\,\Omega_{\mathrm{M}}\,h^2\,\mathrm{Mpc}^{-1}. \tag{2.46}$$

This scale naturally distinguishes two regimes of the *transfer function*, $T(k;z)$, which is defined by its effect on the comoving curvature perturbation $\mathcal{R}$ via

$$\Delta^2_{\mathcal{R}}(k;z) = T^2(k;z)\,\Delta^2_{\mathcal{R}}(k). \tag{2.47}$$

Thus, the transfer function expresses the time evolution of the power spectrum of scalar perturbations.

For a redshift z well after the transition, it can be shown that the asymptotic behaviour of the transfer function is given by

$$T(k;z) \propto \begin{cases} 1 & \text{if } k \ll k_{\mathrm{eq}}, \\ k^{-2}\,\ln k & \text{if } k \gg k_{\mathrm{eq}}. \end{cases} \tag{2.48}$$

As these asymptotes do not describe the power spectrum around the turn-over scale which is the part probed by cosmological observations, more complex treatments need to be used in practice. Analytical approximations of the transfer of power are the BBKS function (Bardeen

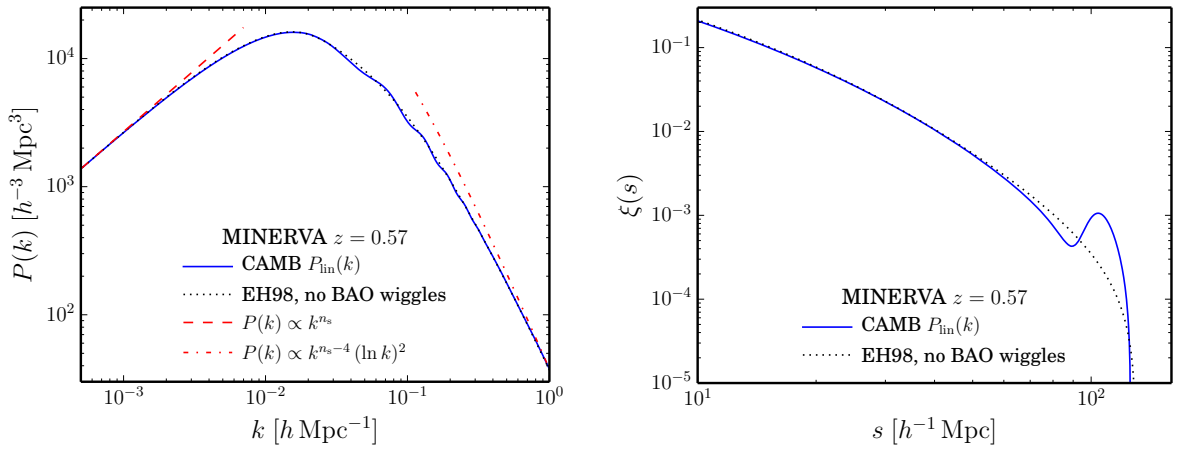

Figure 2.1 – The matter power spectrum (left-hand panel) and two-point correlation function (right-hand panel) as given by linear theory at redshift $z = 0.57$ for the MINERVA cosmology given in Table 3.2. The blue solid line shows the results obtained with CAMB and the black dotted line correspond to the 'smooth' EH98 predictions for which the BAO feature is turned off. The asymptotic trends given by the limits of the transfer function in equation (2.48) are shown as red dashed and dot-dashed lines. The series of wiggles in the power spectrum and the single peak in the correlation function are the signal imprinted by the BAO (cf., Section 2.3.2).

et al., 1986) and the improved fitting formula given in Eisenstein & Hu (1998, EH98). The latter approximation incorporates the effect of baryons on the matter power spectrum (cf., Section 2.3.2), but this can be partly switched off to produce a 'smooth' matter power spectrum without BAO wiggles.

For more accurate results matching the requirements of modern cosmological experiments, astronomers need to rely on numerical solvers of the perturbed Einstein equations for metric and density perturbations and the hierarchy of Boltzmann equations for photon collisions. As the photons are a system of a large number of interacting particles, the set of equations that describe their dynamics can only be solved with an approximate hierarchical approach to the Boltzmann equations, the Boltzmann hierarchy. Standard codes have been developed by the community to solve the perturbed Einstein equations and the Boltzmann hierarchy, like CAMB[3] (Lewis *et al.*, 2000) and CLASS[4] (Lesgourgues, 2011).

An example of the CAMB and 'smooth' EH98 results for the linear-theory matter power spectrum and the corresponding two-point correlation function are shown in Figure 2.1 (for the cosmology that is used for the MINERVA simulations described later in Section 4.3). In the left-hand panel, the asymptotic limits for the matter power spectrum as given by the limits of the transfer function in equation (2.48) are shown as well.

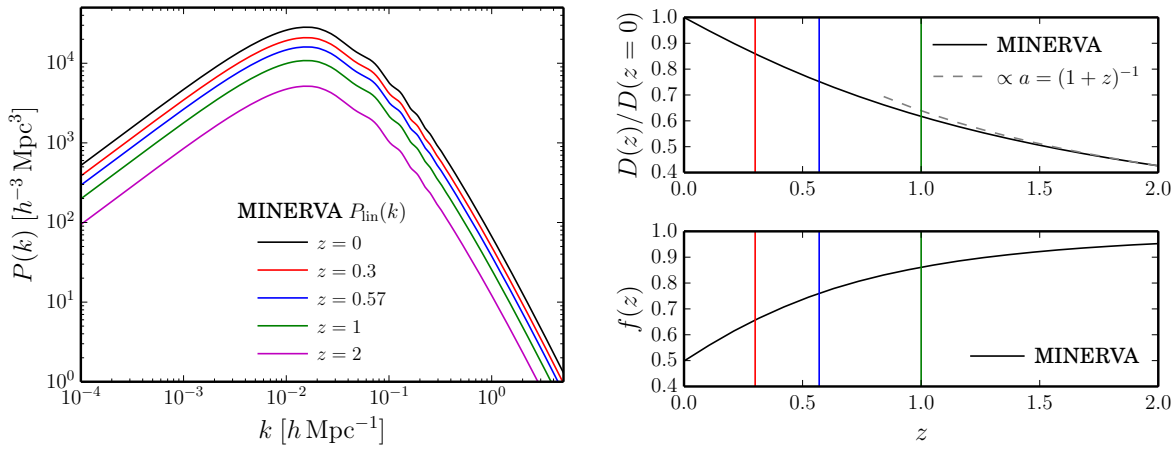

Figure 2.2 – *Left-hand panel:* The matter power spectrum as given by CAMB using the MINERVA cosmological parameters given in Table 3.2 for redshifts $z \in \{0, 0.3, 0.57, 1.0, 2.0\}$. The difference in $P_{\rm lin}(k)$ is only given by the growth $\propto D^2(z)$. *Right-hand panels:* The growth function $D(z)$ defined by equation (2.49) (upper panel) and linear growth rate $f(z)$ defined by equation (2.64) (lower panel) for the MINERVA cosmology. In the matter-dominated era, before the onset of late-time acceleration, these functions are given by $D(z) = (1+z)^{-1}$ and $f = 1$.

The growth factor

For times well in the matter-dominated epoch, the matter power spectrum only evolves by growth with $a^2(t)$. Thus, it can easily be extrapolated in time. In the late-time evolution where the Universe is dominated by Dark Energy (or curvature in the absence of Dark Energy), the power spectrum evolution differs from this behaviour. To account for this, the evolution of the density field is described by factoring out a growth function $D(a)$ defined by

$$P(k,a) = A\frac{D^2(a)}{D^2(a=1)}\left(\frac{k}{k_0}\right)^{n_{\rm s}} T^2(k), \tag{2.49}$$

separating the growth of structure from the transfer function. The growth function is normalized to $D(a) = a$ during matter domination. For the general ΛCDM case, one can easily derive from the Euler and Poisson equations for matter perturbations that the growth factor is given by (Dodelson, 2003)

$$D(a) = \frac{5\Omega_{\rm M}}{2}\frac{H(a)}{H_0}\int_0^a \frac{H_0^3\,\mathrm{d}a'}{(a')^3 H^3(a)}. \tag{2.50}$$

In the left-hand panel of Figure 2.2, the effect of the growth function on the matter power spectrum is illustrated for the MINERVA cosmology. The corresponding growth function is plotted as a black solid line in the upper panel on the right-hand side as a function of redshift, normalized as $D(z)/D(z=0)$. For comparison, the extrapolation of the result for the matter-dominated era, $D(z) \propto (1+z)^{-1}$ is shown as gray dashed line. The lower panel on the right-hand side will be addressed later in Section 2.4.2.

[3] http://www.camb.info
[4] http://www.class-code.net

2.3.2 The baryon-photon plasma and baryonic acoustic oscillations

The explanation of the baryon acoustic oscillations needs a small detour back to the early universe. Due to the high temperatures, baryonic matter primordially existed in form of electrically neutral neutrons and charged protons and electrons. During the Big Bang nucleosynthesis, the neutrons and protons formed charged atomic cores, mostly hydrogen and helium ions. But atoms could not be formed due to absorbed or scattered thermal photons whose mean energy was above the ionization level. Prior to recombination, the baryonic matter (the frequently colliding charged electrons and ions) were strongly coupled with the photons by Thomson scattering, the low-energy limit of Compton scattering, between photons and the free electrons. In this so-called *baryon-photon plasma*, density-perturbations are damped relatively to the CDM perturbations as the baryon-photon pressure prevents the growth due to gravitational instability and gives rise to acoustic waves. These waves, dubbed *baryonic acoustic oscillations* (BAO), propagated away from density peaks in the plasma.

Recombination marks an epoch at which the free particles formed atoms, as the Universe became cold enough that these particle composites could not be ionized again by a typical thermal photon. After recombination, the Universe became neutral and transparent. The photons decouple from the baryon when their mean free path was larger than the Hubble horizon so that light was allowed to cross the observable universe basically without scattering. From the time of decoupling – which was when the Universe was ca. 3000 K hot at a redshift of $z \simeq 1089$ – until today, the CMB photons redshifted in to the microwave regime, forming the cosmic microwave background (CMB).

The acoustic waves propagate further until the baryons are released from the photons at the *drag epoch* at redshift z_d (shortly after the decoupling of the photons). By then, the BAO have travelled a distance

$$r_\mathrm{s}(z_\mathrm{d}) = \int_0^{\tau(z_\mathrm{d})} \frac{\mathrm{d}\tau}{\sqrt{3(1+R)}}, \tag{2.51}$$

where $R = [3\rho_\mathrm{b}(t_0)]/[4\rho_\gamma(t_0)]$ is the baryon-to-photon ratio.

Since the photon decoupling, the baryons are subject to the same growth of structure as CDM so that they fall into the CDM potential wells as the density of CDM dominates over the one of baryons. But the baryon density is non-negligible, so that the dark matter also feels a pull towards the baryon density peaks that correspond to the frozen acoustic waves. This way, the BAO signal is imprinted onto the matter power spectrum as an enhanced correlation of density peaks that are roughly separated by the sound horizon scale $r_\mathrm{s}(z_\mathrm{d})$.

2.4 The late anisotropic universe

2.4.1 Lagrangian perturbation theory

In order to illustrate some aspects of the non-linear evolution of the matter density induced by the gravitational dynamics, we briefly discuss Lagrangian perturbation theory (LPT) here. In Lagrangian coordinates, an infinitesimal fluid element is followed through space and time by

means of the *Lagrangian displacement field* $\Psi(\boldsymbol{q},t)$ that maps the (comoving) initial position $\boldsymbol{q}$ of the fluid element to its (comoving) Eulerian position $\boldsymbol{x}(\boldsymbol{q},t)$ at some late time t,

$$\boldsymbol{x}(\boldsymbol{q},t) = \boldsymbol{q} + \boldsymbol{\Psi}(\boldsymbol{q},t). \tag{2.52}$$

The connection between the Eulerian overdensity, $\delta(\boldsymbol{x},t) = \rho(\boldsymbol{x},t)/\bar{\rho}(t) - 1$, and (comoving) peculiar velocity field, $\boldsymbol{u}(\boldsymbol{x},t)$, is given by the fact that the displacement is the integral of the velocity over the trajectory,

$$\boldsymbol{\Psi}(\boldsymbol{q},t) = \int_0^t \boldsymbol{u}(\boldsymbol{x}(\boldsymbol{q},t'),t')\,\mathrm{d}t', \tag{2.53}$$

and by the continuity equation and the assumption of a uniform initial density,

$$\delta(\boldsymbol{x},t) = \int \delta_{\mathrm{D}}\left[\boldsymbol{x} - \boldsymbol{q} - \boldsymbol{\Psi}(\boldsymbol{q},t)\right]\,\mathrm{d}^3q\, - 1. \tag{2.54}$$

This relation allows to express the power spectrum of equation (2.35) in terms of differences in the displacement field,

$$P(\boldsymbol{k},t) = \int \mathrm{e}^{\mathrm{i}\boldsymbol{k}\cdot\boldsymbol{q}}\,\left(\langle \mathrm{e}^{\mathrm{i}\boldsymbol{k}\cdot\Delta\boldsymbol{\Psi}}\rangle - 1\right)\,\mathrm{d}^3q\,, \tag{2.55}$$

where $\Delta\boldsymbol{\Psi}(\boldsymbol{q},t) = \boldsymbol{\Psi}(\boldsymbol{q},t) - \boldsymbol{\Psi}(\boldsymbol{0},t)$.

Gravitational dynamics govern the evolution of the displacement field,

$$\frac{\mathrm{d}^2\boldsymbol{\Psi}(\boldsymbol{q},t)}{\mathrm{d}t^2} + 2\,H(t)\,\frac{\mathrm{d}\boldsymbol{\Psi}(\boldsymbol{q},t)}{\mathrm{d}t} = -\nabla_{\boldsymbol{x}}\phi\,\left[\boldsymbol{q} + \boldsymbol{\Psi}(\boldsymbol{q},t)\right] \tag{2.56}$$

where $H(t)$ is the Hubble parameter as given by equation (2.24) and $\phi(\boldsymbol{x})$ is the gravitational potential sourced by the density field. The LPT approach (e.g. Bouchet *et al.*, 1995; Taylor & Hamilton, 1996) uses a perturbative expansion of Ψ,

$$\boldsymbol{\Psi}(\boldsymbol{q},t) = \sum_{n=1}^{\infty} \boldsymbol{\Psi}_n(\boldsymbol{q},t), \tag{2.57}$$

in order to solve the evolution equation in (2.56).

The first order solution (1LPT; Zel'dovich, 1970) is given by

$$\boldsymbol{\Psi}_1(\boldsymbol{q},t) = \int \frac{\mathrm{d}^3k}{(2\pi)^3}\,\frac{\mathrm{i}\boldsymbol{k}}{k^2}\,\widehat{\delta}_1(\boldsymbol{k},t)\,\mathrm{e}^{\mathrm{i}\boldsymbol{k}\cdot\boldsymbol{q}}. \tag{2.58}$$

where $\widehat{\delta}_1(\boldsymbol{k},t) = D(t)\,\widehat{\delta}_0(\boldsymbol{k})$ for initial conditions $\delta_0(\boldsymbol{k})$ and $D(t)$ is the linear growth function as given by equation (2.50). Assuming an isotropic initial power spectrum, $\langle\widehat{\delta}_0(\boldsymbol{k})\widehat{\delta}_0(\boldsymbol{k}')^*\rangle = (2\pi)^3\,\delta_{\mathrm{D}}(\boldsymbol{k}-\boldsymbol{k}')\,P_0(k)$, the 1LPT prediction for the power spectrum is

$$P_{\mathrm{1LPT}}(k,t) = D^2(t)\,P_0(k)\,\exp\left(-\frac{\sigma_{\mathrm{L}}^2(t)\,k^2}{2}\right). \tag{2.59}$$

Here, the variance of the Zel'dovich displacement $\sigma_{\mathrm{L}}^2(t)$ is given by

$$\sigma_{\mathrm{L}}^2(t) \equiv \frac{D^2(t)}{3\pi^2} \int_0^\infty P_0(k), \tag{2.60}$$

which suppresses the power on small scales by the exponential damping factor in $P_{\mathrm{1LPT}}(k,t)$.

The second-order solution, dubbed 2LPT, is usually used to generate initial conditions for simulations at a very high starting redshift, where LPT is an accurate approximation of the full gravitational evolution. At later times, even higher-order LPT fails to describe the two-point statistics of the evolved density field already in the mildly non-linear regime.

2.4.2 Linear redshift-space distortions and the growth of structure

In LSS analyses, the distances to astronomical objects are inferred from their observed redshifts, z_{obs}. Besides the cosmological redshift z of equation (2.22), there is an additional component due to the peculiar velocities of the galaxies along the line of sight (LoS), $\boldsymbol{u} \cdot \hat{\boldsymbol{n}}$, where $\boldsymbol{u}$ is the (comoving) peculiar velocity and $\hat{\boldsymbol{n}}$ the LoS direction (also in comoving coordinates). This modifies the observed redshift to

$$1 + z_{\mathrm{obs}} = (1 + z)(1 + z_{\mathrm{pec}}), \quad \text{where} \quad z_{\mathrm{pec}} = \frac{\boldsymbol{u} \cdot \hat{\boldsymbol{n}}}{c}, \tag{2.61}$$

introducing LoS-dependent anisotropies in the galaxy clustering statistics.

The peculiar velocity has two major components. First, the large-scale infall into potential wells whose linear-order prediction was first described in Kaiser (1987). Second, small-scale distortions due to orbital motion in virialized structures (Jackson, 1972).

The first effect can be modelled in linear theory. Given initial Gaussian density contrast perturbations $\delta(\boldsymbol{k})$, the continuity and Euler equations imply that the density contrast grows like

$$\delta(\boldsymbol{k}, a) = D(a)\, \delta(\boldsymbol{k}), \tag{2.62}$$

where $D(a)$ is the growth function defined in equation (2.50). Further, the divergence of the velocity field is given by (Zel'dovich, 1970, 1LPT)

$$\boldsymbol{\nabla} \cdot \boldsymbol{u}(\boldsymbol{k}, a) = -a\, H(a)\, f(a)\, D(a)\, \delta(\boldsymbol{k}), \tag{2.63}$$

where f is the *linear growth rate*, the logarithmic derivative of the growth function w.r.t. the scale factor,

$$f \equiv \frac{\mathrm{d} \ln D(a)}{\mathrm{d} \ln a}. \tag{2.64}$$

The linear growth rate for the Minerva cosmological parameters given in Table 3.2 is plotted in the lower panel on the right-hand side of Figure 2.2. At redshifts lower than $\simeq 2$, the Minerva universe is not purely matter-dominated due to the non-zero cosmological constant and this deviation corresponds to $f \neq 1$.

At linear order, the redshift-space ($\xi_{\rm zs}$) and real-space ($\xi_{\rm rs}$) correlation function of a galaxy sample are related by the Kaiser factor, given by (Kaiser, 1987)

$$S \equiv \frac{\xi_{\rm zs}}{\xi_{\rm rs}} = 1 + \frac{2}{3}\beta + \frac{1}{5}\beta^2, \tag{2.65}$$

which depends on the redshift-space parameter $\beta \equiv f/b$, which is the ratio of the growth rate f and the linear bias b of the galaxy sample.

A probe of the RSD anisotropies offers the possibility to test modifications of the growth of structure from the predictions from ΛCDM, especially from modifications to the theory of general relativity, by a measurement of f. In GR, the growth rate depends on the gravitational potential and is approximately given by a power-law dependence on the matter density parameter $\Omega_{\rm M}(z)$ (Linder & Cahn, 2007; Gong, 2008),

$$f(z) = [\Omega_{\rm M}(z)]^{\gamma}\,, \quad \text{where} \quad \gamma \simeq \frac{3(1-w_{\rm DE})}{5-6\,w_{\rm DE}}, \tag{2.66}$$

with an exponent depending on the EoS parameter $w_{\rm DE}$ of Dark Energy as DE dominates the late-time evolution (cf., Section 2.1.3). For the ΛCDM model, $w_{\rm DE} = -1$, the dependence on $\Omega_{\rm M}(z)$ reduces to

$$f \simeq [\Omega_{\rm M}(z)]^{0.55}\,. \tag{2.67}$$

The peculiar velocity on smaller scales has been modelled with simple phenomenological models, where the velocity dispersion of virialized structure has a Gaussian or Lorentzian distribution. For a precise RSD analysis, more sophisticated approaches such as the streaming model (Scoccimarro, 2004) are needed. Examples of non-linear RSD model are described later in Section 2.4.6.

2.4.3 Non-linear gravitational dynamics and N-body simulations

Galaxy clustering analysis is easiest to perform on scales in the linear regime, i.e., scales at which the density contrast satisfies $\delta \ll 1$ (smaller scales can be excluded by applying an appropriate filter to smooth the density field). At these scales, the matter power spectrum can be obtained from linear theory as described in Section 2.3.1. However, the inclusion of a wider range of scales into the clustering analysis is beneficial with respect to cosmological constraints due to an increased sensitivity of the broad-band power spectrum of the evolved density field. Also, the coupling of modes induced by the non-linear gravitational dynamics change the shape of the BAO feature (described later in Section 2.3.2) resulting in a biased standard ruler.

The simplest way to go beyond linear theory is the brute-force simulation of gravitational structure formation using Newtonian dynamics of a system of particles (usually of equal mass $m_{\rm p}$). Such N-body simulations (for further details, see Hockney & Eastwood, 1988; Bertschinger, 1998) solve the initial-value/boundary-value problem by dissecting the CDM density field into particles, each corresponding to millions or even billions of solar masses, $m_{\rm p} \approx 10^{10}\,M_{\odot}$. The numerical code is usually heavily parallelized and uses adaptive time discretization to solve the

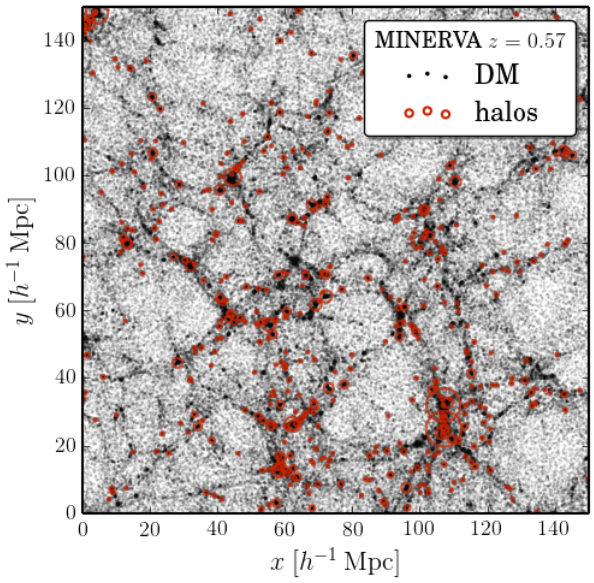

Figure 2.3 – The spatial DM and halo distribution in an N-body snapshot of the set of MINERVA simulations described in Section 4.3 at $z = 0.57$. The shown section has a side length of 150 h^{-1} Mpc and a width perpendicular to the plane of the plot of 30 h^{-1} Mpc. The DM particles are shown as blended black dots, while the halo catalogue that was obtained with SUBFIND is overplotted as orange circles whose sizes correspond to the halo mass.

dynamical equations either using tree methods, a particle-mesh scheme, or a combination of both.

The expansion of the FLRW universe is taken into account by rescaling the comoving coordinates used in N-body simulations to physical distances with the scale factor a, which is also used to redshift the kinetic and potential energy. No further GR corrections are needed as only negligible curvature perturbations are sourced by the gravitational potential and no relativistic particle interaction is simulated.

Besides CDM, modern N-body implementations can also simulate baryonic matter using appropriate approximations of the hydrodynamical equations. One time-efficient method is called *Adaptive Mesh Refinement* (AMR) and uses a mesh whose cell sizes are dynamically adapted to the local density. An alternative approach is to simulate the fluid with a representative number of point masses (*Smoothed Particle Hydrodynamics*, SPH) as implemented in the GADGET suite (Springel, 2005).

The initial conditions for N-body simulations are randomly drawn according to the linear-theory power spectrum (e.g., as obtained with CAMB) for a moderately high redshift. Usually this starting point is chosen to be around $z \approx 50$, because if the perturbations are too small, the N-body technique is inefficient, but for too late times, the analytical approximation, usually 2LPT (cf., Section 2.4.1), becomes invalid. Snapshots of the evolved density field in the observable range $0 \leq z \leq 3$ are stored to disk and usually post-processed to extract information about bound structures, the DM haloes. These haloes are gravitationally bound systems of DM particles, where the relation between kinetic and potential energy was driven to an equilibrium state by gravitational virialization. These structures are identified with halo finding algorithms, for example, by employing a Friends-of-Friends (FoF) algorithm with a fixed linking length. More sophisticated approaches, such as the one adopted in SUBFIND (Springel *et al.*, 2001), calculates the gravitational energy of FoF-identified proto-haloes to remove kinematically unbound

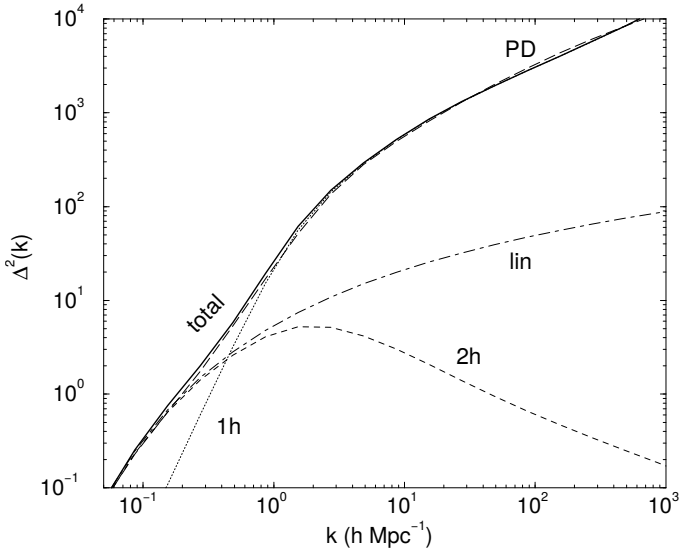

Figure 2.4 – (Image credit: Cooray & Sheth, 2002) The matter power spectrum at present time as predicted by the halo model. The curve labelled 'PD' shows the Peacock & Dodds (1996)-fitting formula, while the dot-dashed curve labelled 'lin' shows the linear-theory $P(k)$. The dotted and dashed curves show the two terms which are summed to give the total power (solid line) in the halo model.

particles, which are only spatially correlated with a halo.

In Figure 2.3, we show a small section of a single snapshot of the set of MINERVA simulations described in Section 4.3 at $z = 0.57$. The DM density field is shown as blended black dots (each corresponding to one DM simulation particle) and the halo catalogue extracted with SUBFIND is overplotted as orange circles. The halo mass is indicated by the size of each circle.

2.4.4 Modeling of the non-linear matter clustering

If the simulation of the non-linear evolution with the N-body technique is computationally too expensive, careful modelling of the (real- and redshift-space) galaxy two-point statistics beyond the linear regime with analytical approaches is required. In the last decade, cosmologists have paid much effort to derive optimal non-linear recipes for the clustering analysis with BAO (Angulo *et al.*, 2008; Sánchez *et al.*, 2008; Smith *et al.*, 2008). The development of novel techniques in the recent past has increased the accuracy of the predictions, enabling the extension of the full-shape analysis in the mildly non-linear regime.

Common approaches: the halo model and cosmological perturbation theory

In this section we discuss the two most common approaches to model the non-linear gravitational dynamics. The first one is motivated by the paradigm that all matter resides in haloes, i.e., overdense, virialized DM structures. The number density of haloes of a given virial mass is given by the halo mass function, for which accurate theoretical recipes have been developed (Press & Schechter, 1974; Jenkins *et al.*, 2001; Tinker *et al.*, 2008). The clustering of halos can be predicted from the mass function using peak theory (Press & Schechter, 1974; Sheth & Tormen, 1999).

The 'halo model' (e.g. Peacock & Smith, 2000; Seljak, 2000; Cooray & Sheth, 2002) is an analytical approach to describe the non-linear clustering by combining the halo mass function

with a halo density profile such as the one given in Navarro *et al.* (1996, NFW). This recipe leads to two different contributions to the two-point statistics. The two-halo (2h) term, dominating the large-scale power, is sourced by DM structures that reside in different haloes. The one-halo (1h) contribution from substructures located in the same halo, dominates the small-scale correlation. These two contributions and their sum are shown in Figure 2.4 compared to the linear real-space matter power spectrum and a simple fitting formula.

This technique has been refined by Smith *et al.* (2003) by introducing fitting terms into the 2h and 1h contributions to the non-linear power spectrum,

$$P_{\mathrm{halofit}}(k) = P_{\mathrm{2h}}(k) + P_{\mathrm{1h}}(k), \tag{2.68}$$

where the fitting parameters in $P_{\mathrm{2h}}(k)$ and $P_{\mathrm{1h}}(k)$ are obtained by comparison with simulations and are found to depend slightly on the cosmology. This method, dubbed 'halofit', has been recalibrated by Takahashi *et al.* (2012) using high-resolution N-body simulations (even accounting for $w_{\mathrm{DE}} \neq -1$), and can be obtained with CAMB, the code that primarily calculates the linear-theory power spectrum (see also Section 2.3.1).

Alternatively, the cosmological perturbation theory approach (see Bernardeau *et al.*, 2002, for a review) derives the non-linear power spectrum using an expansion series in the density contrast $\delta(\boldsymbol{x},\tau) = \rho(\boldsymbol{x},\tau)/\bar{\rho}(\tau) - 1$ and (comoving) peculiar velocity field $\boldsymbol{u}(\boldsymbol{x},\tau)$ to solve the system of Poisson, continuity, and Euler equations. Typically, the single-stream approximation is invoked, which assumes that the velocity field is single valued at each point (i.e., requiring that streams of matter never cross). Gravitational collapse eventually leads to shell crossing, but at that point the perturbation theory approach anyway breaks down. Using comoving coordinates and the conformal Newtonian gauge[5], these equations read

$$\nabla^2\phi(\boldsymbol{x},\tau) - \frac{3}{2}\Omega_{\mathrm{M}}(\tau)\mathcal{H}^2(\tau)\,\delta(\boldsymbol{x},\tau) = 0, \tag{2.69}$$

$$\frac{\partial\delta(\boldsymbol{x},\tau)}{\partial\tau} + \nabla\cdot\{(1+\delta(\boldsymbol{x},\tau)]\,\boldsymbol{u}(\boldsymbol{x},\tau)\} = 0, \tag{2.70}$$

$$\frac{\partial\boldsymbol{u}(\boldsymbol{x},\tau)}{\partial\tau} + \mathcal{H}(\tau)\boldsymbol{u}(\boldsymbol{x},\tau) + \boldsymbol{u}(\boldsymbol{x},\tau)\cdot\nabla\boldsymbol{u}(\boldsymbol{x},\tau) = -\nabla\phi(\boldsymbol{x},\tau) - \frac{1}{\rho}\nabla_j\left(\rho\sigma_{ij}\right), \tag{2.71}$$

where τ is the conformal time, $\mathcal{H} = a\,H$ the conformal expansion rate, $\phi(\boldsymbol{x},\tau)$ the gravitational potential sourced by the density field $\rho(\boldsymbol{x},\tau)$, and σ_{ij} is the stress tensor.

In cosmological perturbation theory, these relations are converted to Fourier space so that derivatives are transformed to multiplications, simplifying the analytical structure of the system of equations. In a general cosmology, the equations do not fully decouple in $\boldsymbol{k}$ and τ (which is the case, e.g., for a Einstein-de Sitter universe, $\Omega_{\mathrm{M}} = 1, \Omega_\Lambda = 0$). None the less, approximative

[5]For a discussion of gauges in cosmological perturbation theory, see Bardeen (1980).

solutions can be derived with an expansion series ansatz of the form

$$\widehat{\delta}(\boldsymbol{k},\tau) = \sum_{n=1}^{\infty} D_n(\tau)\,\widehat{\delta}_n(\boldsymbol{k}), \tag{2.72}$$

$$\widehat{\theta}(\boldsymbol{k},\tau) = -\mathcal{H}(\tau)\,f \sum_{n=1}^{\infty} E_n(\tau)\,\widehat{\theta}_n(\boldsymbol{k}), \tag{2.73}$$

where $\theta(\boldsymbol{x},\tau) \equiv \nabla\cdot\boldsymbol{u}(\boldsymbol{x},\tau)$ is the divergence of the velocity field and f the linear growth rate defined in equation (2.64). It turns out that the time-dependent coefficients are given by the growth function $D(a)$ given in equation (2.50), $D_n(a) \approx D^n(a)$, $E_n(a) \approx D^n(a)$, with a mild dependency on the cosmological density parameters.

At first order, the linear-theory relations for δ_1 and θ_1 discussed in Section 2.4.2 are recovered. The solutions at higher orders of the expansion are taken from the exact Einstein-de Sitter solutions to the system of equations (2.69) to (2.71) for a pressureless perfect fluid (i.e., assuming that the velocity field does not have vorticity, $\sigma_{ij} = 0$),

$$\delta_n(\boldsymbol{k}) = \int \frac{\mathrm{d}^3q_1\cdots\mathrm{d}^3q_n}{(2\pi)^{2n-3}}\delta_{\mathrm{D}}\left(\boldsymbol{k}-\sum_{i=1}^{n}\boldsymbol{q}_i\right) F_n(\boldsymbol{q}_1,\ldots,\boldsymbol{q}_n)\,\delta_1(\boldsymbol{q}_1)\cdots\delta_1(\boldsymbol{q}_n), \tag{2.74}$$

$$\theta_n(\boldsymbol{k}) = \int \frac{\mathrm{d}^3q_1\cdots\mathrm{d}^3q_n}{(2\pi)^{2n-3}}\delta_{\mathrm{D}}\left(\boldsymbol{k}-\sum_{i=1}^{n}\boldsymbol{q}_i\right) G_n(\boldsymbol{q}_1,\ldots,\boldsymbol{q}_n)\,\delta_1(\boldsymbol{q}_1)\cdots\delta_1(\boldsymbol{q}_n), \tag{2.75}$$

where F_n and G_n are the *perturbation theory kernels* (see equations (43) and (44) in Bernardeau *et al.*, 2002).

The expansion in the density field results in a similar one for the power spectrum,

$$P(k,a) = \sum_n P_n(k,a), \quad \text{where} \quad P_n(k,a) = \left(\frac{D(a)}{D(a=1)}\right)^{2n} P_n(k,a=1). \tag{2.76}$$

Here, we have assumed isotropy of the power spectrum and that $D_n(a) = E_n(a) = D(a)$. This series is dubbed standard perturbation theory (SPT) in the following discussion.

The higher order contributions can be derived from the linear-theory matter power spectrum, $P_1(k,a) = [D^2(a)/D^2(a=1)]\,P_{\mathrm{lin}}(k)$, and from the N-point function hierarchy of p-moments of the density field δ^p. For Gaussian initial conditions (as those generated by inflation), odd-order moments vanish and only even powers of the density field survive. Thus, the higher-order 'loop' corrections to the 'tree-level', i.e.linear-order, power spectrum are given by the different combinations that can add up to the next even power of the density field. For example, the first two loop corrections are

$$P_2(k,a) = P_{22}(k,a) + P_{13}(k,a) \quad \text{and} \tag{2.77}$$

$$P_3(k,a) = P_{15}(k,a) + P_{24}(k,a) + P_{33}(k,a). \tag{2.78}$$

Here, the one-loop contributions are

$$P_{22}(k,a) = \frac{1}{4\pi^3} \int |F_2(\boldsymbol{k}-\boldsymbol{q},\boldsymbol{q})|^2 \, P_1(|\boldsymbol{k}-\boldsymbol{q}|,a) \, P_1(q,a) \, \mathrm{d}^3 q \quad \text{and} \tag{2.79}$$

$$P_{13}(k,a) = \frac{3}{4\pi^3} \, P_1(k,a) \int F_3(\boldsymbol{k},\boldsymbol{q},-\boldsymbol{q}) \, P_1(q,a) \, \mathrm{d}^3 q \, . \tag{2.80}$$

The two-loop contributions in $P_3(k,a)$ are given, e.g., in Carlson *et al.* (2009, appendix A); higher-order contributions are rarely used.

SPT is useful to describe the non-linear matter power spectrum in the high-redshift universe if contributions up to the third order in δ are considered (Jeong & Komatsu, 2006, 2009), but the applicability of SPT is limited at lower redshifts. For redshifts $z \approx 0$, taking contributions up to the one-loop level gives good results only for scales $k \lesssim 0.1 \, h\,\mathrm{Mpc}^{-1}$ (Scoccimarro, 2004; Carlson *et al.*, 2009).

Phenomenologically, the non-linear evolution can be described in two effects. First, the propagator that measures the decoherence of the final density field $\widehat{\delta}(\boldsymbol{k},a)$ with respect to the initial conditions given by $\widehat{\delta}_0(\boldsymbol{k})$,

$$G(k,a) \equiv \frac{\langle \widehat{\delta}(\boldsymbol{k},a) \, \widehat{\delta}_0(\boldsymbol{k}) \rangle}{\langle \widehat{\delta}_0(\boldsymbol{k}) \, \widehat{\delta}_0(\boldsymbol{k}) \rangle} \tag{2.81}$$

Secondly, large-scale modes affect the small-scale evolution generating additional power described by mode-coupling terms.

Lagrangian perturbation theory (LPT; Matsubara, 2008a,b), discussed briefly in Section 2.4.1, is a complementary approach to SPT (which is sometimes also called *Eulerian perturbation theory* to point out the analogy). In LPT, particle trajectories are the subjects of the perturbative expansion instead of the density and velocity fields. The transformation between Eulerian positions $\boldsymbol{x}$ and Lagrangian coordinates $\boldsymbol{q}$ mixes the orders in SPT, and thus can be seen as a resummation of the Eulerian PT terms. In that sense, LPT is similar to the renormalization scheme discussed next. The propagator G derived from the 1LPT expression for the power spectrum in equation (2.59),

$$G_{\mathrm{1LPT}}(k,a) = D(a) \, \exp\left(-\frac{\sigma_{\mathrm{L}}(a) \, k}{\sqrt{2}}\right), \tag{2.82}$$

approximates the full non-linear decoherence at a very good level. However, higher-order power spectrum terms for the mode coupling are suppressed at a similar level, so that the LPT expansion does not converge even for small $\delta \ll 1$.

Renormalized perturbation theory and multi-point propagators

In order to improve the accuracy of the PT expansion at low orders, *renormalized perturbation theory* (RPT; Crocce & Scoccimarro, 2006a,b) employs the Dyson-Wyld resummation scheme —

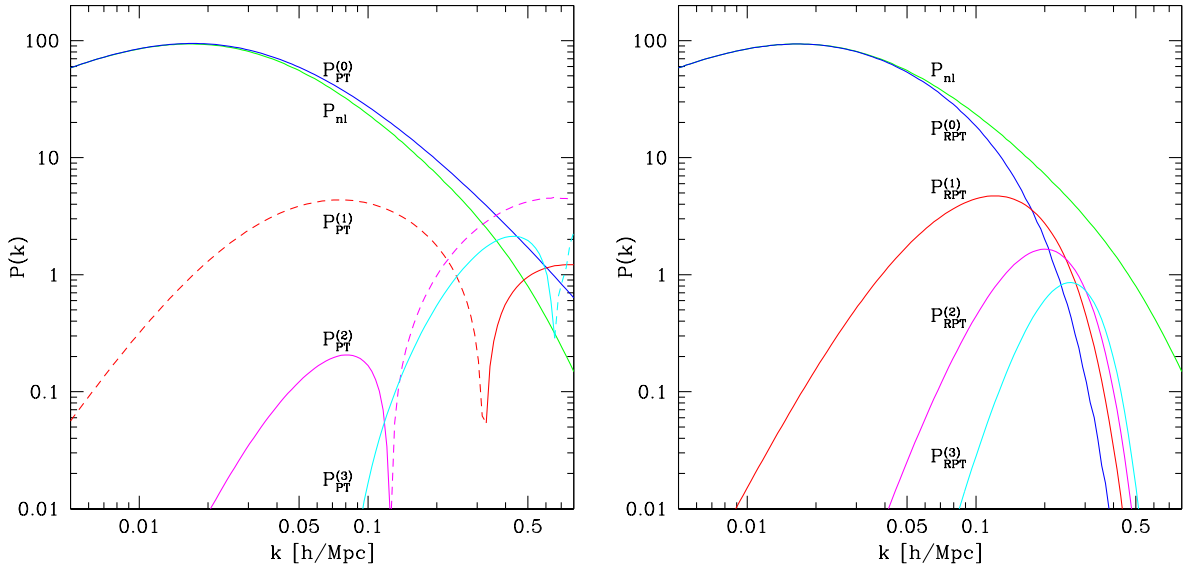

Figure 2.5 – (Image credit: Crocce & Scoccimarro, 2006a) Dissection of the individual loop contributions to the expansion series of the non-linear matter power spectrum (in the Zel'dovich approximation) in SPT (left-hand panel) and RPT (right-hand panel). $P_{\rm nl}$ denotes the exact result for the non-linear power spectrum, whereas $P_{\rm PT}^{(n)}$ ($P_{\rm RPT}^{(n)}$) denotes the n-loop correction in SPT (RPT). Negative values are indicated by a dashed line. The resummation of the propagator involved in RPT leads to a well-defined perturbative expansion, unlike SPT, for which it is not possible to determine where the truncate the expansion in the non-linear regime due to possibly cancelling positive and negative higher-order terms.

known from other contexts such as hydrodynamics (L'vov & Procaccia, 1995) — by a reorganization of the perturbation series such that the propagator is taken out of the perturbative expansion, and the remaining PT expansion collects terms of the same number of mode-couplings allowed to improve convergence. In such an expansion, $G_{\rm 1LPT}(k,a)$ of equation (2.82) becomes the *renormalized propagator*, summing up all orders of the PT expansion that are proportional to $P_{\rm lin}(k)$, such as the $P_{13}(k)$ term of SPT. In order to improve the description, the fixed velocity dispersion $\sigma_{\rm L}(a)$ in the LPT propagator is replaced by a scale-dependent effective damping scale $\sigma^*(k)$ in the renormalized propagator $G_{\rm RPT}(k,a)$. Thus, the series is written as

$$P_{\rm RPT}(k,a) = G_{\rm RPT}^2(k,a)\, P_{\rm lin}(k) + \sum_{n=1}^{\infty} P_{{\rm mc},n}(k), \tag{2.83}$$

where the $P_{{\rm mc},n}(k)$ are the mode-coupling terms ordered by the number of interaction vertices. This recipe can partially resolve the problem that the SPT expansion becomes impossible to truncate at a fixed convergence level in the mildly non-linear regime, $\delta < 1$ (but not $\delta \ll 1$), due to negative and positive contributions from terms of successively higher orders, which have to (at least partially) cancel each other. This issues is illustrated by the dissection of the non-linear power spectrum prediction into the different loop contributions shown in the left-hand panel of Figure 2.5. This failure of convergence of SPT prevents the use of a truncated series of equation (2.76) as a good approximation to the non-linear power spectrum.

The loop expansion in RPT (shown in the right-hand panel of the same figure) is much better behaved in the sense that, i), the loop-terms are strictly positive, ii), each order has a smaller amplitude than the previous one and, iii), each order peaks at a higher k than the previous one, resulting in a series where each loop-order is dominant over a certain range of wavenumbers. This makes it easy to truncate the series at a certain accuracy, as the RPT expansion takes into account the non-linear contributions from all scales larger than a given scale, and the neglected impact of smaller scales as described by the high-order terms is highly suppressed. With this method, an accuracy of 1% for the non-linear matter power spectrum up to scales $k \lesssim 0.17\ h\,\mathrm{Mpc}^{-1}$ at redshift zero can be achieved if contributions up to the second loop order are included (Crocce & Scoccimarro, 2008).

For model fits, the RPT approach has been used to generate a simpler phenomenological model, where the effective mode-coupling term $\tilde{P}_{\mathrm{mc}}(k)$ is taken as an approximation to the full mode-coupling expansion in RPT (Crocce & Scoccimarro, 2008),

$$\tilde{P}_{\mathrm{RPT}}(k,a) = G^2(k,a)\,P_{\mathrm{lin}}(k) + \tilde{P}_{\mathrm{mc}}(k). \tag{2.84}$$

Here, only the coupling of two modes is considered, $\tilde{P}_{\mathrm{mc}}(k) \propto P_{22}(k)$. By introducing the constant velocity dispersion σ^2 in the propagator $G^2(k,a)$ and the relative amplitude of the mode-coupling term P_{22} to the data as fitting parameters and by modelling halo/galaxy bias with a constant linear bias b, this power spectrum model is accurate to scales $k \lesssim 0.15\ h\,\mathrm{Mpc}^{-1}$ for usual redshifts of a galaxy survey (Montesano *et al.*, 2010). It was applied in cosmological full-shape fits of the two-point correlation function of the LRG DR5 sample (Sanchez *et al.*, 2009) and the BOSS CMASS samples of DR9 to DR11 (Sánchez *et al.*, 2013, 2014). The complementary model for the power spectrum was fit to the DR7 power spectrum in Montesano *et al.* (2012).

Performing cosmological parameter estimation beyond this phenomenological scheme of RPT, the computation of the mode-coupling terms is a critical aspect. It was found that the integrals performing the resummations can be sped up using the multi-point propagator expansion (Bernardeau *et al.*, 2008; Crocce *et al.*, 2012, MPT). As a result of the work by Crocce *et al.* (2012), MPTbreeze[6] was published. This is a code that can calculate the non-linear power spectrum up to the two-loop RPT expansion, by using the MPT expansion, in a similar computing time than needed for the linear-theory power spectrum prediction using Camb (cf., Section 2.3.1); the full RPT resummations are computationally much more expensive.

gRPT: improving RPT with Galilean invariance

In this section, we shortly discuss the 'gRPT' model which uses an improved approach for the RPT-like resummation of terms in the perturbative expansion. The propagator is derived using the same recipe as in RPT, while the resummation of the mode-coupling contribution makes use of the Galilean invariances of the equations of motion (gRPT; Blas *et al.*, 2016, *in prep.*) in order to achieve a better convergence of the mode-coupling expansion. This approach allows the prediction of the matter power spectrum to an accuracy required by galaxy clustering analysis up to significantly larger wavenumbers ($k \lesssim 0.25\ h\,\mathrm{Mpc}^{-1}$) than previous approaches. This

[6] http://maia.ice.cat/crocce/mptbreeze/

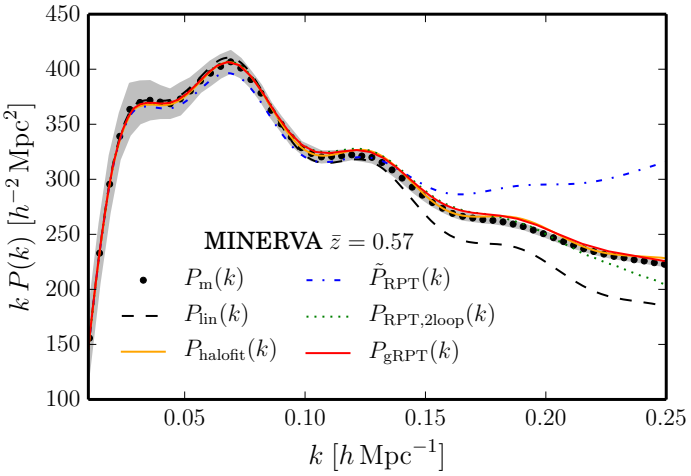

Figure 2.6 – The mean matter power spectrum $P_{\rm m}(k)$ measured from the MINERVA simulations compared with perturbation theory predictions: $P_{\rm lin}(k)$ is the linear-theory prediction from CAMB (Lewis *et al.*, 2000), $P_{\rm halofit}(k)$ is the 'halofit' model (Smith *et al.*, 2003; Takahashi *et al.*, 2012) included in CAMB, $\tilde{P}_{\rm RPT}(k)$ is the phenomenological model of equation (2.84) (Montesano *et al.*, 2010, 2012), $P_{\rm RPT,2loop}(k)$ is the MPTBREEZE result using two-loop multi-point expansion (Crocce *et al.*, 2012), and '$P_{\rm gRPT}(k)$ is the 'gRPT' model used in this thesis (Blas *et al.*, 2016, *in prep.*). Only the 'halofit' and 'gRPT' model are able to describe the matter power spectrum in the mildly non-linear regime ($k \lesssim 0.25\ h\,{\rm Mpc}^{-1}$).

improvement is illustrated in Figure 2.6 where the 'gRPT' results for the MINERVA matter power spectrum is compared with the mean power spectrum of 100 MINERVA simulations described in Section 4.3.1, as well as the predictions of the other modelling approaches discussed in this section.

One of the advantages of the 'gRPT' model is that no free parameter is needed in this solution of the dynamical equations. Thus, the non-linear matter power spectrum can be computed directly from the linear-theory input power spectrum, modifications of the power spectrum amplitude from the clustering strength σ_8 or the growth function $D(a)$ can be approximated using pre-computed look-up tables. The computation time for the model calculations are of a similar order than for CAMB and MPTBREEZE.

The full modelling of the anisotropic clustering measurements requires a description of the velocity field. In particular, the clustering wedges model described in Section 5.1 requires the density-density power spectrum $P_{\delta\delta}$, the cross-spectrum $P_{\delta\theta}$ between density and the velocity divergence, $\theta = \boldsymbol{\nabla u}(\boldsymbol{x})$, and the θ auto-spectrum, $P_{\theta\theta}$. As 'gRPT' provides the one-loop expansion of each of these terms, the redshift-space power spectrum can be obtained readily.

For a more detailed description of the theoretical framework of the model, the reader is referred to Blas *et al.* (2016, *in prep.*). The configuration-space analysis of the BOSS DR12 combined sample that will be presented in Sánchez *et al.* (2016, *in prep.*) contains a more detailed description of the implementation of this model into our analysis pipeline.

2.4.5 Galaxy bias

Galaxies are biased tracers of the matter density. The current understanding of galaxy formation is that galaxies form within DM haloes, which themselves are bound structures located at peaks of the DM density. Galaxies do not necessarily only form in the centre of a halo, but are dispersed in the central region of a halo and follow the substructure of a halo. As the halos themselves are located in density peaks, they alone are already a biased tracer of the density

field. A simple approach to derive the clustering of haloes and galaxies assumes a linear bias and a technique known as the peak-background split (Mo *et al.*, 1997; Sheth & Tormen, 1999). The way in which galaxies populate halos of different masses can be modelled by the halo occupation distribution (HOD) recipe (e.g. Peacock & Smith, 2000).

Regardless of the details of the bias modelling, a usual approach is to expand the galaxy density fluctuations $\delta_\mathrm{g}(\boldsymbol{x})$ as a Taylor series of the local matter density $\delta_\mathrm{m}(\boldsymbol{x})$,

$$\delta_\mathrm{g}(\boldsymbol{x}) = \sum_{n=1}^{\infty} \frac{b_n}{n!}\, \delta_\mathrm{m}^n(\boldsymbol{x}), \tag{2.85}$$

where the expansion coefficients b_n are called *bias parameters*.

In linear theory, the bias is given by b_1, but for the non-linear regime, more bias parameters must be considered. As the convergence of the series in equation (2.85) cannot be guaranteed to be well-behaved, a re-parametrization of the bias coefficients might be beneficial (McDonald, 2006; Schmidt *et al.*, 2013). In this work, we restrict the bias model to the linear bias b_1 and an effective second-order bias b_2 as the scale dependency is neglected in order to increase the computational efficiency. For the modelling of the power spectrum, this was found not to introduce a systematic error into parameter constraints, but for the bispectrum the dependence of b_2 with scale needs to be considered.

The description of equation (2.85) assumes that galaxy bias is purely a function of the local matter density. A non-local bias prescription was proposed by McDonald & Roy (2009), including a functional dependence of δ_g on the velocity divergence and gravitational potential, which both non-locally depend on δ_m. These non-local dependencies are introduced by the gravitational dynamics even if the initial conditions of the galaxy and density perturbations satisfy the local condition of equation (2.85). Here, we follow (Chan *et al.*, 2012) and write the galaxy fluctuations as

$$\delta_\mathrm{g}(\boldsymbol{x}) = \delta_\mathrm{g}^{(\mathrm{loc})}(\boldsymbol{x}) + \delta_\mathrm{g}^{(\mathrm{nonloc})}(\boldsymbol{x}), \tag{2.86}$$

where the local contribution $\delta_\mathrm{g}^{(\mathrm{loc})}(\boldsymbol{x})$ is given by equation (2.85) and the non-local contribution can expressed as

$$\delta_\mathrm{g}^{(\mathrm{nonloc})}(\boldsymbol{x}) = \gamma_2\, \mathcal{G}_2[\phi_u]\,(1 + \beta\, \delta_\mathrm{m}) + \gamma_3\, \mathcal{G}_3[\phi_u] + \gamma_3^-\, \Delta_3\mathcal{G} + \ldots \tag{2.87}$$

Here, only contributions up to the third order are considered and the velocity field is assumed to be bias-free ($\theta_\mathrm{g} = \theta_\mathrm{m} = \nabla \boldsymbol{u}$). The second and third 'Galileon' operator $\mathcal{G}_2$ and $\mathcal{G}_3$ of the velocity potential ϕ_u are given by

$$\mathcal{G}_2[\phi_u] = \left(\nabla_{ij}\phi_u\right)^2 - \left(\nabla^2\phi_u\right)^2, \tag{2.88}$$

$$\mathcal{G}_3[\phi_u] = \left(\nabla^2\phi_u\right)^3 + 2\left(\nabla_{ij}\phi_u\right)\left(\nabla_{jk}\phi_u\right)\left(\nabla_{ki}\phi_u\right) - 3\left(\nabla_{ij}\phi_u\right)^2\nabla^2\phi_u, \quad \text{and} \tag{2.89}$$

$$\Delta_3\mathcal{G} = \mathcal{G}_2[\phi] - \mathcal{G}_2[\phi_u]. \tag{2.90}$$

The coefficients in equation (2.87) are the *non-local bias parameters* $\gamma_i \propto b_1 - 1$ and the 'mixing' parameter $\beta \propto b_2$. These parameters can be related to local Lagrangian bias theory (e.g. Catelan

et al., 2000) that assumes a local dependence $\delta_g[\delta_m]$ in Lagrangian coordinates. Following Chan *et al.* (2012), this comparison yields[7]

$$\gamma_2 = -\frac{2}{7}(b_1 - 1), \qquad \beta = \frac{b_2}{b_1 - 1}, \tag{2.91}$$
$$\gamma_3 = \frac{11}{63}(b_1 - 1), \qquad \gamma_3^- = \frac{3}{2}\gamma_3.$$

For now, we keep the non-local contributions up to those terms corresponding to second-order Lagrangian bias. Later in Section 5.1, we perform tests of the modelling with simulations in order to decide for which non-local bias parameters the local Lagrangian relation can be assumed as a valid approximation.

2.4.6 Non-linear redshift-space distortions

In redshift-space, the clustering signal measured from a galaxy survey is distorted as the observed redshift, given in equation (2.61), is affected by the projected peculiar motion of the galaxies (cf., Section 2.4.2). This introduced an anisotropy w.r.t. the LoS direction to the power spectrum which therefore depends on the LoS parameter μ, defined[8] as the cosine of the angle between the LoS direction and the wavenumber vector, as well.

The non-linear Kaiser formula in Fourier space

The velocity field is assumed to be irrotational and thus it can entirely be described by the divergence, $\theta(\boldsymbol{x}) = \nabla \boldsymbol{u}(\boldsymbol{x})$. Another assumption is that the galaxy velocity field is not biased w.r.t. to the matter velocity field, $\theta_g(\boldsymbol{x}) = \theta_m(\boldsymbol{x}) \equiv \theta(\boldsymbol{x})$.

It has become conventional to use the following ansatz for the redshift-space power spectrum $P_{zs}(k,\mu)$ (Scoccimarro, 2004; Percival & White, 2009),

$$P_{zs}(k,\mu) = P_{nonvir}(k,\mu)\, F_{FoG}(k,\mu), \tag{2.92}$$
$$P_{nonvir}(k,\mu) = P_{gg}(k) + 2f\mu^2 P_{g\theta}(k) + f^2\mu^4 P_{\theta\theta}(k), \tag{2.93}$$

where $P_{nonvir}(k,\mu)$ is a non-linear version of the Kaiser formula in Fourier space, which depends on $P_{gg} = \langle \widehat{\delta}_g(\boldsymbol{k})\, \widehat{\delta}_g(\boldsymbol{k})\rangle$, $P_{g\theta} = \langle \widehat{\delta}_g(\boldsymbol{k})\, \widehat{\theta}(\boldsymbol{k})\rangle$, and $P_{\theta\theta} = \langle \widehat{\theta}(\boldsymbol{k})\, \widehat{\theta}(\boldsymbol{k})\rangle$. Further, $F_{FoG}(k,\mu)$ is a non-linear extension modelling the 'Fingers-of-God' (FoG) effect caused by the non-linear velocity component due to virialization.

In the simplest case, we can use the linear Zel'dovich approximation of equation (2.63) for the velocity field. Then, we find $P_{gg}(k)/b^2 = P_{g\theta}(k)/b = P_{\theta\theta}(k) = P_{lin}(k)$, assuming a linear bias $b = \delta_g/\delta_m = \text{const}$. The non-linear Kaiser formula in $P_{nonvir}(k,\mu)$ reduces to the well known Kaiser factor given in equation (2.65) for the large-scale (angle-averaged) power spectrum,

$$S \equiv \frac{\int_{-1}^{1} P_{zs}(k,\mu)\, \mathrm{d}\mu}{P_{\delta\delta}(k)} = 1 + \frac{2}{3}\beta + \frac{1}{5}\beta^2, \tag{2.94}$$

[7] Sometimes, the prefactor of $\delta\mathcal{G}_2[\phi_u]$ is denoted as $\gamma_3^\times = \beta\gamma_2$. Its local Lagrangian relation is $\gamma_3^\times = -\frac{2}{7}b_2$.
[8] The definition of the LoS parameter μ is discussed in more detail in Section 3.1.

where $\beta = f/b$. In Fourier-space, this is a crude approach even at very large scales (Scoccimarro, 2004; Angulo *et al.*, 2008) and imperfections of the linear approach are usually captured in a Gaussian or Lorentzian description of the isotropic FoG term $F_{\rm FoG}(k,\mu) = F_{\rm FoG}(k)$.

Non-linear extension to the streaming model

We already identified RSD earlier as a crucial aspect of the modelling as the velocity field requires a non-linear treatment even at scales where the density perturbations are in the linear regime. It has been noticed by Taruya *et al.* (2010) that the redshift-space power spectrum in N-body simulations has a modulated acoustic peak and trough structure compared to PT predictions that are based entirely on the non-linear Kaiser formula of equation (2.93). These features cannot be captured in a broad-band term $F_{\rm FoG}(k,\mu)$ for the virial motion. Thus, we rely on advanced approaches (developed in Scoccimarro, 2004; Taruya *et al.*, 2010), where the streaming model is extended to one-loop contributions,

$$P_{\rm nonvir}(k,\mu) = P_{\rm gg}(k) + 2f\mu^2 P_{\rm g\theta}(k) + f^2\mu^4 P_{\theta\theta}(k) + (k\mu f)\,A(k,\mu) + (k\mu f)^2\,B(k,\mu), \tag{2.95}$$

by adding corrective terms $A(k,\mu)$ and $B(k,\mu)$ to the expression in equation (2.93). These terms are given by a three-level PT bispectrum contribution and a quadratic linear-theory power spectrum expression,

$$A(k,\mu) = \int \frac{{\rm d}^3p}{(2\pi)^3}\frac{p_z}{p^2}\left[B_\sigma(\boldsymbol{p},\boldsymbol{k}-\boldsymbol{p},-\boldsymbol{k}) - B_\sigma(\boldsymbol{p},\boldsymbol{k},-\boldsymbol{k}-\boldsymbol{p})\right] \tag{2.96}$$

$$B(k,\mu) = \int \frac{{\rm d}^3p}{(2\pi)^3}F(\boldsymbol{p})\,F(\boldsymbol{k}-\boldsymbol{p}), \tag{2.97}$$

where $B_\sigma(\boldsymbol{k}_1,\boldsymbol{k}_2,\boldsymbol{k}_3)$ is given by the following mixed bispectrum,

$$\langle\theta(\boldsymbol{k}_1)\,\sigma(\boldsymbol{k}_2)\,\sigma(\boldsymbol{k}_3)\rangle = (2\pi)^3\delta_{\rm D}(\boldsymbol{k}_1+\boldsymbol{k}_2+\boldsymbol{k}_3)\,B_\sigma(\boldsymbol{k}_1,\boldsymbol{k}_2,\boldsymbol{k}_3), \tag{2.98}$$

using $\sigma(\boldsymbol{k}) = \delta_{\rm g}(\boldsymbol{k}) + f\,\frac{k_z}{k^2}\,\theta(\boldsymbol{k})$ and $F(\boldsymbol{p}) = \frac{p_z}{p^2}\left[P_{\delta\theta}(p) + f\,\frac{p_z^2}{p^2}\,P_{\theta\theta}\right]$. The corrective terms can be evaluated with tree-level SPT (Taruya *et al.*, 2010, Appendix A). Subsequent analysis found that the improved treatment reproduced the redshift-space power spectrum measurements on N-body simulations with an accuracy better then 1% for scales up to $k \lesssim 0.2\ h\,{\rm Mpc}^{-1}$ at the redshifts relevant for galaxy surveys ($z \simeq 0.5$). Neglecting these contributions is found to be accurate only up to $k \lesssim 0.1\ h\,{\rm Mpc}^{-1}$ (Taruya *et al.*, 2010, Fig. 5).

As a scale-independent FoG model does not describe the virial motions accurately, a non-linear correction is introduced to the Gaussian FoG term,

$$F_{\rm FoG}(k,\mu) = F_{\rm vir}(k,\mu) \equiv \frac{1}{\sqrt{1+f^2\,\mu^2\,k^2\,a_{\rm vir}^2}}\exp\left(\frac{-f^2\,\mu^2\,k^2}{1+f^2\,\mu^2\,k^2\,a_{\rm vir}^2}\right), \tag{2.99}$$

where $a_{\rm vir}$ is a free fitting parameter that describes the kurtosis of the small-scale velocity distribution. Again, we refer to Sánchez *et al.* (2016, *in prep.*) where the implementation of this model is explained in greater detail.

eTNS

Non-Gaussian corrections to the RSD streaming model are postulated in a similar way in the so-called 'eTNS' model (Taruya *et al.*, 2010; Nishimichi & Taruya, 2011), where the same corrective terms $A(k,\mu)$ and $B(k,\mu)$ account for a large-scale enhancement in halo clustering, which is sensitive to the galaxy bias.

In its usual form, the galaxy density perturbations are modelled in 'eTNS' using the renormalised linear- and second-order local bias and second- and third-order non-local bias (McDonald & Roy, 2009) and a constant stochasticity term for the galaxy bias. The non-local bias parameters are assumed to be given by the local Lagrangian relations of equation (2.91). The non-linear density and velocity power spectra — $P_{\delta\delta}$, $P_{\delta\theta}$, and $P_{\theta\theta}$ — are calculated up to second-order loop contributions using the RegPT code (Taruya *et al.*, 2012). The treatment of the non-linear RSD effect differs in 'eTNS' from 'gRPT+RSD' as the second-order bias contributions to the corrective term $A(k,\mu)$ are dropped. In our approach, these terms are kept to be consistent with the general consideration of the second-order bias.

The FoG term is assumed to be a scale-independent Gaussian,

$$F_{\rm FoG}(k,\mu) = F_{\rm Gauss}(k,\mu) \equiv \exp\left(-(k\,\mu\,f\,\sigma_{\rm FoG})^2\right), \tag{2.100}$$

where $\sigma_{\rm FoG}$ is a free fitting parameter to capture the velocity dispersion of the orbital motion in bound structures.

Such a galaxy clustering model was used in previous analyses of the BOSS LSS samples, DR7 LRGs (Oka *et al.*, 2014), DR11 CMASS (Beutler *et al.*, 2014a; Gil-Marín *et al.*, 2015a), and DR12 LOWZ and CMASS (Gil-Marín *et al.*, 2015d). These studies differ in the recipes used to obtain the matter power spectrum and details of the implementation for the fitting process. Some analyses use two-loop resummed perturbation theory (Gil-Marin *et al.*, 2012) for the non-linear matter power spectra instead of RegPT.

2.4.7 The Alcock-Paczynski test on the BAO scale

The Alcock-Paczynski test (Alcock & Paczynski, 1979) is an LSS clustering probe of the parameters of the cosmological model. It assumes an spherical object of fixed (but unknown) diameter δl at a known redshift z. Its angular size on the sky is given by the angular diameter distance relation in equation (2.28),

$$\delta\varphi = \frac{\delta l}{D_{\rm A}(z)}. \tag{2.101}$$

From the differential proper distance of equation (2.23), the redshift difference δz between the two endpoints of the object in radial direction can be calculated,

$$c\,\delta z = (1+z)\,H(z)\,\delta l. \tag{2.102}$$

Again here, we include c explicitly to facilitate calculations.

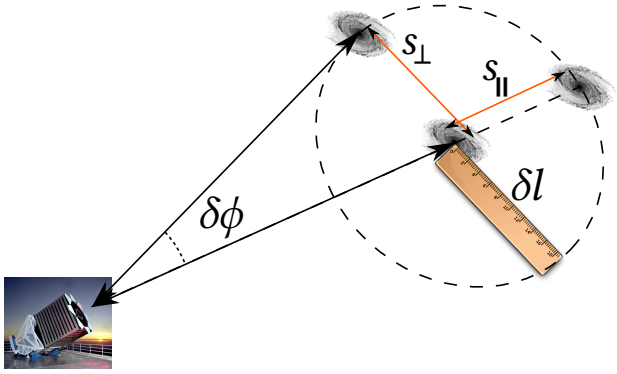

Figure 2.7 – Illustration of the distance measurement using the Alcock-Paczynski effect and a standard ruler such as the BAO scale. Here, galaxies which are physically separated by the BAO scale δl are observed with an angular separation $s_\perp = \delta\varphi\, D_\mathrm{A}(z)$ and a radial separation $s_\parallel = \frac{c\,\delta z}{1+z\,H(z)}$. If the physical size of the standard ruler, δl, is known, $D_\mathrm{A}(z)$ and $H(z)$ can be measured from equating $s_\perp = s_\parallel = \delta l$.

By substituting the unknown δl in these equations, we are able to measure the *Alcock-Paczynski parameter*, $F_\mathrm{AP}(z)$, given by

$$F_\mathrm{AP}(z) \equiv \frac{1+z}{c}\, D_\mathrm{A}(z)\, H(z) = \frac{\delta z}{\delta\varphi} \tag{2.103}$$

entirely from observations (provided that the redshift difference and angular separation can be measured precisely).

A *standard ruler* is an object whose physical size is known or can be predicted from other cosmological observations. With this information, the degeneracy of the factors $D_\mathrm{M}(z) = (1+z)\, D_\mathrm{A}(z)$ and $H(z)$ in equation (2.103) can be broken. The acoustic scale of BAO (cf. Section 2.3.2) is such a measurable physical scale and the BAO peak in $\xi(s)$, or alternative the BAO wiggles in $P(k)$, can be used as a standard ruler for geometric (distance) measurements as proposed in Blake & Glazebrook (2003), by equating $\delta l = r_\mathrm{s}(z_\mathrm{d})$, given by equation (2.51). Using an anisotropic clustering measurement, the combination of a standard ruler and the Alcock-Paczynski test (Hu & Haiman, 2003) provides a precise handle on the Hubble parameter and angular diameter distance,

$$D_\mathrm{A}(z) = \frac{\delta l}{\delta\varphi}, \tag{2.104}$$

$$H(z) = \frac{c\delta z}{1+z}\,\frac{1}{\delta l}. \tag{2.105}$$

This case is illustrated in Figure 2.7.

If anisotropies in the clustering signal are neglected, only an angle-averaged distance measurement can be performed. In that case, the parameter combination

$$D_\mathrm{V}(z) = \left[(1+z)^2\, D_\mathrm{A}(z)^2\, \frac{c\,z}{H(z)}\right]^{1/3} \tag{2.106}$$

is measured with respect to the sound horizon scale, so that results are usually expressed as the combination $D_\mathrm{V}(z)/r_\mathrm{s}(z_\mathrm{d})$. Thus, equivalently to the quantities in equations (2.104) and (2.105), the pair $D_\mathrm{V}(z)/r_\mathrm{s}(z_\mathrm{d})$ and $F_\mathrm{AP}(z)$ are given for anisotropic BAO distance measurements.

As pointed out in several theoretical and numerical studies, BAO distance measurements are a robust cosmological probe, as they relate the measured distance to a physical size which can well measured from CMB observations (and thus is independent from unknown physics prior to recombination, Eisenstein & White, 2004). Further, the BAO scales are in the linear regime of late-time evolution and are thus only moderately degraded by the non-linear evolution of the density field. The observed BAO signal is further degraded by redshift-space distortions. Seo & Eisenstein (2005) show that non-linear redshift-space distortions are the dominant contamination of BAO distance observations, preventing measurements of the Hubble parameter $H(z)$ to be as precise as expected from linear theory Fischer forecasts. This can be ameliorated by improvements of the modelling of the RSD. The latter two effects will be accounted for in full-shape fits of the BAO distance by the modelling recipes described earlier in this section.

In addition, the observed BAO size δl is not exactly the sound horizon scale at the drag redshift, as it is affected by damping due to photon diffusion, known as *Silk damping*. The photons encounter Thomson scattering off electrons prior to recombination, washing out anisotropies at scales smaller than the diffusion length. The true position of the BAO peak in the correlation function and the horizon scale are shown to deviate by as much as 2% (depending on the baryon fraction) in Sánchez *et al.* (2008).

3

Anisotropic clustering measurements of the BOSS galaxy catalogues in Fourier space

> "Telescopes are in some ways like time machines. They reveal galaxies so far away that their light has taken billions of years to reach us. We in astronomy have an advantage in studying the universe, in that we can actually see the past. We owe our existence to stars, because they make the atoms of which we are formed. So if you are romantic you can say we are literally starstuff. If you're less romantic you can say we're the nuclear waste from the fuel that makes stars shine. We've made so many advances in our understanding. A few centuries ago, the pioneer navigators learnt the size and shape of our Earth, and the layout of the continents. We are now just learning the dimensions and ingredients of our entire cosmos, and can at last make some sense of our cosmic habitat."
>
> Lord Martin Rees

This chapter introduces anisotropic two-point statistics for galaxy clustering in Section 3.1 and derives the optimal-variance estimator for clustering wedges in Fourier space, one of the main parts of this thesis, in Section 3.2. The observational systematics of the BOSS galaxy samples, and how the estimator is corrected for these, are described in Section 3.3. Section 3.4 discusses the window function effect due to the survey selection function and introduces our implementation for the modelling of this power spectrum modulation with a window matrix. The two sets of synthetic catalogues mimicking the combined sample clustering properties that are used for the estimate of the data covariance are presented in Section 3.5 explaining the methods used for the generation of large sets of mock catalogues and verifying the estimator. Section 3.6 contains the Fourier space analysis of the combined sample clustering, compares the observed Fourier space wedges of the data with the measurements on the mocks, and also discusses the consistency of the hemispherical subsamples to each other.

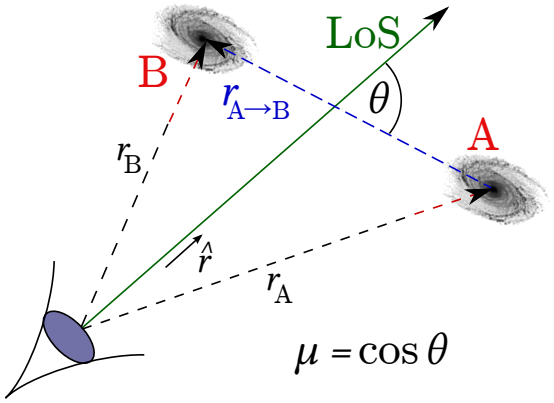

Figure 3.1 – Illustration of the definition of the LoS parameter μ for a pair of galaxies (labelled with A and B) at positions $\boldsymbol{x}_A$ and $\boldsymbol{x}_B$. μ is defined as the cosine of the angle θ between the pair separation vector $\boldsymbol{x}_{A\to B}$ and the LoS direction $\hat{\boldsymbol{r}}$.

3.1 Anisotropic galaxy two-point clustering

Galaxy density fluctuations estimated from a large-scale structure survey are characterized by an anisotropic power spectrum $P(\boldsymbol{k})$. Otherwise, the angle-averaging of equation (2.38) removes valuable information by marginalizing over the angular degrees of freedom. The most important sources of anisotropy are RSD (cf., Section 2.4.2) and the AP effect (cf., Section 2.4.7), which depend on the LoS direction. As there is a remaining invariance w.r.t. rotations around the LoS axis, the two-point statistics are two-dimensional. The second parameter for the power spectrum (correlation function) besides the wavenumber k (distance r) is the LoS parameter μ, defined as the cosine of the angle θ between the LoS direction $\hat{\boldsymbol{r}}$ and the wavevector $\boldsymbol{k}$ of the Fourier modes,

$$\mu \equiv \cos\theta = |\boldsymbol{k}\cdot\hat{\boldsymbol{r}}|\,|k|^{-1}. \tag{3.1}$$

Thus, μ has values in the range -1 to 1 and $\theta \in [0,\pi)$. The definition for the case of configuration space is illustrated in Figure 3.1.

A direct measurement of the 2D power spectrum, $P(\boldsymbol{k}) = P(k,\mu)$, and 2D correlation function, $\xi(\boldsymbol{r}) = \xi(r,\mu)$, is desired to allow for full access to the cosmological information in the galaxy clustering two-point statistics. But as the signal-to-noise ratio (SNR) of the measurement is limited by the size of the sample, it's possible to find a good compromise between resolution and precision by averaging $P(k,\mu)$ in multiple angular bin.

The power spectrum multipoles $P_\ell(k)$ are projections onto multipole moments using Legendre polynomials (Padmanabhan & White, 2008),

$$P(k,\mu) = \sum_\ell P_\ell(k)\,\mathcal{L}_\ell(\mu), \tag{3.2}$$

where $\mathcal{L}_\ell(\mu)$ denotes the Legendre polynomial of order ℓ. Only $P_\ell(k)$ with even ℓ are non-zero due to the symmetry of $\mu \leftrightarrow -\mu$ around the observer. The multipoles can be estimated from the full power spectrum by

$$P_\ell(k) \equiv \frac{2\ell+1}{2}\int_{-1}^{1}\mathcal{L}_\ell(\mu)\,P(k,\mu)\,\mathrm{d}\mu. \tag{3.3}$$

The redshift-space galaxy power spectrum is dominated by the lower-order multipoles as the amplitudes decreases with ℓ (just as the SNR).

Alternatively, clustering wedges (introduced first for configuration-space analysis by Kazin *et al.*, 2012) are projections with a similar SNR, using a fixed number of wide non-intersecting bins of the LoS parameter,

$$P_{\mu_1}^{\mu_2}(k) \equiv \frac{1}{\mu_2 - \mu_1} \int_{\mu_1}^{\mu_2} P(k,\mu)\, \mathrm{d}\mu. \tag{3.4}$$

Here, μ_1 and μ_2 define the lower and upper limits such that $\mu_2 - \mu_1 = \Delta\mu$, where $\Delta\mu$ is defined by the total number of wedges. We use the usual convention for the case of two wedges and label them as $P_\perp$ and $P_\parallel$ for the μ-ranges $[0, 0.5]$ and $[0.5, 1]$, respectively. For the case of three or more (N) wedges, we use the convention to label the measurement bin with $(i-1)/N \leq |\mu| \leq i/N$ (so that $\Delta\mu = \frac{1}{N}$) as $P_{N\mathrm{w},i}$ for i in 1 to N.

The configuration-space counterpart of the power spectrum multipoles is the decomposition of the correlation function in terms of the Legendre multipoles (Hamilton, 1997),

$$\xi_\ell(r) \equiv \frac{2\ell+1}{2} \int_{-1}^{1} \mathcal{L}_\ell(\mu)\, \xi(r,\mu)\, \mathrm{d}\mu, \tag{3.5}$$

Adopting the distant-observer approximation,[1] this decomposition can be derived from the power spectrum multipoles using

$$\xi_\ell(s) = \frac{\mathrm{i}^\ell}{2\pi^2} \int_0^\infty P_\ell(k)\, j_\ell(ks)\, k^2\, \mathrm{d}k, \tag{3.6}$$

where $j_\ell(x)$ is the spherical Bessel function of order ℓ. Clustering wedges in configuration space are defined in a complete analogous way to their Fourier space counterparts,

$$\xi_{\mu_1}^{\mu_2}(s) \equiv \frac{1}{\mu_2 - \mu_1} \int_{\mu_1}^{\mu_2} \xi(s,\mu)\, \mathrm{d}\mu. \tag{3.7}$$

By convention, we use the labels $\xi_\perp$ and $\xi_\parallel$ for the case of two wedges and $\xi_{N\mathrm{w},1}$ to $\xi_{N\mathrm{w},N}$ for the general case of $N \geq 3$ wedges.

The relation between clustering wedges and multipoles are

$$P_{\mu_1}^{\mu_2}(k) = \sum_\ell P_\ell(k)\, \bar{\mathcal{L}}_{\ell,\mu_1,\mu_2}, \qquad \xi_{\mu_1}^{\mu_2}(r) = \sum_\ell \xi_\ell(r)\, \bar{\mathcal{L}}_{\ell,\mu_1,\mu_2}, \tag{3.8}$$

where $\bar{\mathcal{L}}_{\ell,\mu_1,\mu_2}$ is the average of the Legendre polynomial $\mathcal{L}_\ell(\mu)$ over the μ-range of the wedge,

$$\bar{\mathcal{L}}_{\ell,\mu_1,\mu_2} \equiv \frac{1}{\mu_2 - \mu_1} \int_{\mu_1}^{\mu_2} \mathcal{L}_\ell(\mu)\, \mathrm{d}\mu, \tag{3.9}$$

[1] Formally, the natural LoS parameter in configuration space, the cosine of the angle between the separation vector of a galaxy pair and the LoS, is not the same as the Fourier space μ adopted here. However, Yoo & Seljak (2015) showed that the distant-observer approximation which assumes the same LoS parameter in both spaces is a safe choice for surveys such as BOSS, where the galaxies are far away from the observer.

which corresponds to

$$\bar{\mathcal{L}}_{\ell,\mu_1,\mu_2} = \frac{1}{\mu_2 - \mu_1} \left[\mathcal{L}_{\ell+1}(\mu_2) - \mathcal{L}_{\ell-1}(\mu_2) - \mathcal{L}_{\ell+1}(\mu_1) + \mathcal{L}_{\ell-1}(\mu_1) \right] . \tag{3.10}$$

3.2 Estimating the anisotropic clustering of a galaxy sample in Fourier space

We now define the estimators for anisotropic clustering measurements in Fourier space with a special focus on clustering wedges. First, we take into account that the expected number density is not constant for any realistic galaxy survey so that the definition of the density contrast in equation (2.32) needs to be modified. The basic assumption of the two-point clustering analysis with the Landy-Szalay estimator (Landy & Szalay, 1993) for the correlation function and the Feldman-Kaiser-Peacock estimator (FKP, Feldman *et al.*, 1994) for the power spectrum is that the expected number density, n_{exp}, for a constant underlying number density, $\bar{n}$, is given by the *survey selection function* $\Phi(\boldsymbol{x})$,

$$n_{\mathrm{exp}}(\boldsymbol{x}) = \Phi(\boldsymbol{x})\, \bar{n}. \tag{3.11}$$

Analogously, $\Phi(\boldsymbol{x})$ also gives the relation between the observed number density, $n_{\mathrm{obs}}(\hat{\boldsymbol{x}}, z)$, and the true number density of the underlying galaxy sample, $n_{\mathrm{true}}(\hat{\boldsymbol{x}}, z)$.

Usually, the selection function of the survey can be written as the product of an angular selection function Φ_{ang} and a radial part Φ_{rad}, so that

$$n_{\mathrm{exp}}(\hat{\boldsymbol{x}}, z) = \Phi_{\mathrm{ang}}(\hat{\boldsymbol{x}})\, \Phi_{\mathrm{rad}}(z)\, \bar{n}, \tag{3.12}$$

where the spatial coordinate $\boldsymbol{x}$ has been decomposed into an angular part $\hat{\boldsymbol{x}}$ and a radial part z. In the following we will refer to the radial selection function as $n(z) = \Phi_{\mathrm{rad}}(z)\, \bar{n}$.

The expected number density $n_{\mathrm{exp}}(\hat{\boldsymbol{x}}, z)$ is usually represented by a set of random points whose size N_{ran} should be much larger than the number of galaxies to ensure that the survey geometry is well sampled. Statistically the number density of these 'randoms', $n_{\mathrm{ran}}(\boldsymbol{x})$, is required to follow

$$\langle n_{\mathrm{ran}}(\hat{\boldsymbol{x}}, z) \rangle = \alpha_{\mathrm{ran}}^{-1}\, n_{\mathrm{exp}}(\hat{\boldsymbol{x}}, z), \quad \text{where} \quad \alpha_{\mathrm{ran}} \ll 1. \tag{3.13}$$

We denote the randoms-to-galaxies ratio as α_{ran} to prevent a naming conflict with the AP parameter $\alpha = (\alpha_\perp^2\, \alpha_\parallel)^{1/3}$ defined later in Section 5.1.1.

In order to have a distribution of randoms that follows the selection function of the survey, its footprint is fragmented into small angular regions for which the spectroscopic completeness is assumed to be uniform. This is described in more detail in Section 3.3.2. Angular positions are drawn according to the completeness assigned to each sector. The redshifts are randomly drawn from the measured galaxy redshifts .

3.2.1 The FKP power spectrum estimator

As it will be useful as a reference when the estimators for the power spectrum multipoles and wedges are discussed, the FKP estimator for the isotropic power spectrum is described first. This estimator is based on a weighted density contrast defined in terms of $n_{\mathrm{obs}}(\boldsymbol{x})$ and $n_{\mathrm{ran}}(\boldsymbol{x})$,

$$F(\boldsymbol{x}) \equiv \frac{w_{\mathrm{FKP}}(\boldsymbol{x})}{\sqrt{I_{\mathrm{norm}}}} \left[n_{\mathrm{obs}}(\boldsymbol{x}) - \alpha_{\mathrm{ran}}\, n_{\mathrm{ran}}(\boldsymbol{x}) \right] . \tag{3.14}$$

The normalization constant I_{norm} is discussed later and $w_{\mathrm{FKP}}(\boldsymbol{x})$ is an extra weight depending on the expected number density that is designed to minimize the variance of the clustering estimate (Feldman *et al.*, 1994),

$$w_{\mathrm{FKP}}(\boldsymbol{x}) = \frac{1}{1 + n_{\mathrm{exp}}(\boldsymbol{x})\, P_{\mathrm{FKP}}} . \tag{3.15}$$

The expected amplitude of the power spectrum, P_{FKP}, is assumed to be constant and set to $P_{\mathrm{FKP}} = 10{,}000\,\mathrm{Mpc}^3/h^3$, roughly corresponding the amplitude of the CMASS power spectrum at scales where the BAO wiggles are imprinted onto $P(k)$. Later in Section 3.3, this weight is modified to account for the observational incompleteness of BOSS.

The power spectrum is obtained from the weighted density contrast by

$$P^{\mathrm{obs}}(\boldsymbol{k}) = \widehat{F}(\boldsymbol{k})\, \widehat{F}(\boldsymbol{k})^* - S = \widehat{F}(\boldsymbol{k})\, \widehat{F}(-\boldsymbol{k}) - S, \tag{3.16}$$

where $\widehat{F}(\boldsymbol{k})$ is the Fourier transform of $F(\boldsymbol{x})$ and S is a constant *shot-noise* contribution that is subtracted. The shot noise is due to the fact that n_{obs} and n_{ran} correspond to Poisson point processes of the observed and expected number density, respectively.[2] The shot-noise contribution is given by the following integral over the survey volume V_{s} (Feldman *et al.*, 1994),

$$S = \frac{1}{I_{\mathrm{norm}}} \int_{V_{\mathrm{s}}} n_{\mathrm{exp}}(\boldsymbol{x})\, (1 + \alpha_{\mathrm{ran}})\, {w_{\mathrm{FKP}}}^2(\boldsymbol{x})\, \mathrm{d}^3x \, . \tag{3.17}$$

The normalization constant here and in the weighted density field in equation (3.14) is set to

$$I_{\mathrm{norm}} = \int_{V_{\mathrm{s}}} n_{\mathrm{exp}}^2(\boldsymbol{x})\, {w_{\mathrm{FKP}}}^2(\boldsymbol{x})\, \mathrm{d}^3x \, , \tag{3.18}$$

so that the estimated power spectrum corresponds to the usual power spectrum defined by equation (2.35) in the special case where $n_{\mathrm{exp}}(\boldsymbol{x}) = \text{const}$ and consequently $w_{\mathrm{FKP}} = \text{const}$ (i.e., no effect from the survey geometry).

[2] The probability $\mathrm{d}P_{\mathrm{gal}}$ to find a galaxy in the infinitesimal volume element $\mathrm{d}V$ is $\mathrm{d}P_{\mathrm{gal}} = n_{\mathrm{exp}}(\boldsymbol{x})\, [1 + \delta(\boldsymbol{x})]\, \mathrm{d}V$, where $\delta(\boldsymbol{x}) = \left[n_{\mathrm{obs}}(\boldsymbol{x}) - n_{\mathrm{exp}}(\boldsymbol{x}) \right] / n_{\mathrm{exp}}(\boldsymbol{x})$ (Peebles, 1980). The observed field is the point process with $\langle n_{\mathrm{obs}}(\boldsymbol{x}) \rangle = n_{\mathrm{exp}}(\boldsymbol{x})$. Due to the clustering, the expectation value of the squared observed field is $\langle n_{\mathrm{obs}}(\boldsymbol{x})\, n_{\mathrm{obs}}(\boldsymbol{x}') \rangle = n_{\mathrm{exp}}(\boldsymbol{x})\, n_{\mathrm{exp}}(\boldsymbol{x}')\, [1 + \xi(\boldsymbol{x} - \boldsymbol{x}')] + n_{\mathrm{exp}}(\boldsymbol{x})\, \delta_{\mathrm{D}}(\boldsymbol{x} - \boldsymbol{x}')$ (Feldman *et al.*, 1994). The random points are not clustered, $\mathrm{d}P_{\mathrm{rnd}} = \alpha_{\mathrm{ran}}^{-1}\, n_{\mathrm{exp}}(\boldsymbol{x})\, \mathrm{d}V$. Thus, $\langle n_{\mathrm{ran}}(\boldsymbol{x})\, n_{\mathrm{ran}}(\boldsymbol{x}') \rangle = \alpha_{\mathrm{ran}}^{-2}\, n_{\mathrm{exp}}(\boldsymbol{x})\, n_{\mathrm{exp}}(\boldsymbol{x}) + \alpha_{\mathrm{ran}}^{-1} n_{\mathrm{exp}}(\boldsymbol{x})\, \delta_{\mathrm{D}}(\boldsymbol{x} - \boldsymbol{x}')$.

The measurements of the isotropic power spectrum are given by the bin-average of equation (3.16),

$$P^{\rm obs}(k) = \int_{\rm bin} \widehat{F}(\boldsymbol{k})\,\widehat{F}(\boldsymbol{k})^*\,\mathrm{d}\hat{\boldsymbol{k}} - S \equiv \frac{1}{V_k}\int_{V_k} \widehat{F}(\boldsymbol{k})\,\widehat{F}(\boldsymbol{k})^*\,\mathrm{d}^3k\ - S, \tag{3.19}$$

where V_k is the volume of the bin around k. The survey geometry affects the measured power spectrum $P^{\rm obs}(\boldsymbol{k})$, which corresponds to a convolution of the underlying power spectrum $P^{\rm true}(\boldsymbol{k})$ with the *survey window function*, $Q(\boldsymbol{k})$, so that

$$P^{\rm obs}(\boldsymbol{k}) = \int P^{\rm true}(\boldsymbol{k}')\,Q(\boldsymbol{k}-\boldsymbol{k}')\,\mathrm{d}^3k'\ - \frac{Q(\boldsymbol{k})}{Q(\boldsymbol{0})}\int P^{\rm true}(\boldsymbol{k}')\,Q(\boldsymbol{k}')\,\mathrm{d}^3k'\,, \tag{3.20}$$

where the second term is the so-called *integral constraint* that ensures that the convolution does not introduce an artificial zero mode (Peacock & Nicholson, 1991). The window function depends on the expected number density $n_{\rm exp}(\boldsymbol{x})$ and its estimator is given by

$$Q(\boldsymbol{k}) = \widehat{q}(\boldsymbol{k})\,\widehat{q}(\boldsymbol{k})^* - Q_{\rm shot}, \tag{3.21}$$

where $\widehat{q}(\boldsymbol{k})$ is the Fourier transform of

$$q(\boldsymbol{x}) = \frac{\alpha_{\rm ran}}{\sqrt{I_{\rm norm}}} w_{\rm FKP}(\boldsymbol{x})\,n_{\rm ran}(\boldsymbol{x}). \tag{3.22}$$

The shot noise $Q_{\rm shot}$ is due to the stochasticity of the random field $n_{\rm ran}(\boldsymbol{x})$ and can be estimated using

$$Q_{\rm shot} = \frac{\alpha_{\rm ran}}{I_{\rm norm}}\int_{V_{\rm s}} n_{\rm exp}(\boldsymbol{x})\,{w_{\rm FKP}}^2(\boldsymbol{x})\,\mathrm{d}^3x\,. \tag{3.23}$$

This estimate of the window function is used to convolve model predictions as described later in Section 3.4.

3.2.2 The Yamamoto estimator for power spectrum multipoles

In order to take the anisotropies of the power spectrum into account, an optimal-variance estimator for power spectrum multipoles was developed in Yamamoto *et al.* (2006). This estimator uses the 'pairwise-LoS' method to define the LoS direction as the direction to the midpoint of the line that connects a pair of galaxies, as illustrated in Figure 3.2 by solid vectors. Equivalently, another pairwise definition uses the direction that bisects the opening angle of the galaxy pair (Yoo & Seljak, 2015). As the pairwise method needs to compute the LoS parameter μ for each pair of galaxies, the power spectrum multipoles are estimated from a two-fold spatial integration over the survey volume,

$$P_\ell(k) = \frac{2\ell+1}{2}\int_{\rm bin}\mathrm{d}\hat{\boldsymbol{k}}\int_{V_{\rm s}}\mathrm{d}^3x\int_{V_{\rm s}}\mathrm{d}^3x'\,F(\boldsymbol{x})\,F(\boldsymbol{x}')\,\mathrm{e}^{-\mathrm{i}\boldsymbol{k}\cdot\boldsymbol{x}}\,\mathrm{e}^{\mathrm{i}\boldsymbol{k}\cdot\boldsymbol{x}'}\,\mathcal{L}_\ell(\hat{\boldsymbol{k}}\cdot\hat{\boldsymbol{x}}_{\rm mid}) - S_\ell, \tag{3.24}$$

where $x_{\rm mid} = (\boldsymbol{x}+\boldsymbol{x}')/2$ and S_ℓ is the shot-noise contribution discussed later.

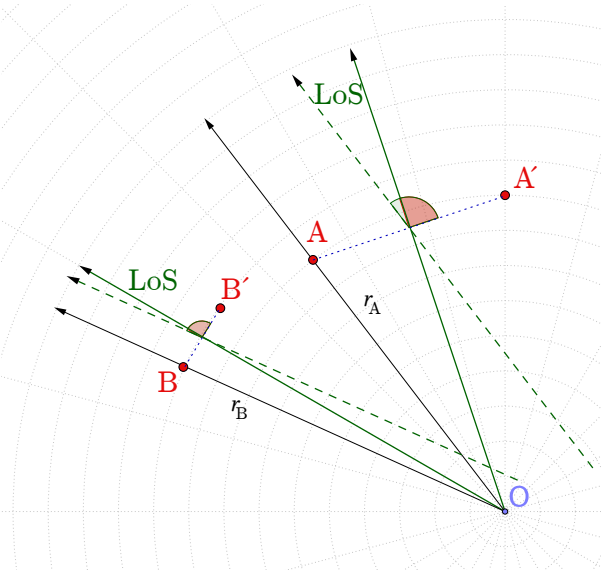

Figure 3.2 – (Modified from Samushia *et al.*, 2015, Fig. 1) The 'pairwise-LoS' method defines the LoS as the direction to the midpoint of the pair separation vector, $\boldsymbol{r}_{\rm mid} = (\boldsymbol{r} + \boldsymbol{r}')/2$. Here, the LoS direction to two galaxy pairs (A, A') and (B, B') is shown by the green solid arrow. The 'moving-LoS' approximation simplifies this assumption by using the distance vector to one of the galaxies, $\boldsymbol{r}$, to define the LoS direction (as indicated by the green dashed arrow). As discussed in the text, this reduces the computational costs of the estimator at the expense of introducing an error to the LoS parameter sourced by the mismatch of the LoS directions used.

The evaluation of the two spatial integrals can only be implemented as a double sum over the galaxies and randoms of the survey leading to immense computational costs for modern galaxy surveys.

The Yamamoto-Blake estimator (Blake *et al.*, 2011a) overcomes this hurdle by use of the distant-observer approximation. In this case, the direction of the distance vector to one of the galaxies in the pair can be used as the LoS direction. This is called the 'moving-LoS' method (illustrated in Figure 3.2 by dashed vectors) and preserves most of the LoS information (as shown by Samushia *et al.*, 2015), in contrast to the plane-parallel approximation for the LoS ('fixed-LoS' method). For wide-angle surveys such as BOSS, assuming the latter approach would significantly bias the anisotropic clustering measurement.

Hence, we follow the 'moving-LoS' approach, which simplifies the integration kernel to

$$P_\ell(k) = \frac{2\ell+1}{2} \int_{\rm bin} \mathrm{d}\hat{\boldsymbol{k}} \int_{V_{\rm s}} \mathrm{d}^3x \int_{V_{\rm s}} \mathrm{d}^3x'\, F(\boldsymbol{x})\, F(\boldsymbol{x}')\, \mathrm{e}^{-\mathrm{i}\boldsymbol{k}\cdot\boldsymbol{x}}\, \mathrm{e}^{\mathrm{i}\boldsymbol{k}\cdot\boldsymbol{x}'}\, \mathcal{L}_\ell(\hat{\boldsymbol{k}}\cdot\hat{\boldsymbol{x}}') - S_\ell. \tag{3.25}$$

The shot-noise contribution to the multipole power spectrum estimate is given by

$$S_\ell = \frac{2\ell+1}{2\, I_{\rm norm}} \int_{V_{\rm s}} n_{\rm exp}(\boldsymbol{x})\, (1+\alpha_{\rm ran})\, {w_{\rm FKP}}^2(\boldsymbol{x})\, \mathcal{L}_\ell(\hat{\boldsymbol{k}}\cdot\hat{\boldsymbol{x}}')\, \mathrm{d}^3x\,. \tag{3.26}$$

As $S_\ell \ll S$ for multipoles of order $\ell > 0$, the shot-noise correction is negligible for multipoles other than the monopole (Beutler *et al.*, 2014a; Gil-Marín *et al.*, 2015d). In that case, the estimator can be written as

$$P_\ell(k) = \int_{\rm bin} \widehat{F}(\boldsymbol{k}) \left[\widehat{F}_\ell(\boldsymbol{k})\right]^* \mathrm{d}\hat{\boldsymbol{k}} - S\, \delta^{\rm K}_{\ell 0}, \tag{3.27}$$

where $\delta^{\rm K}_{\ell 0}$ is the Kronecker delta ensuring that the shot-noise contribution is only subtracted from the monopole. The multipole moments of the weighted density contrast field are given by

$$\widehat{F}_\ell(\boldsymbol{k}) \equiv \frac{2\ell+1}{2} \int_{V_{\rm s}} F(\boldsymbol{x})\, \mathrm{e}^{-\mathrm{i}\boldsymbol{k}\cdot\boldsymbol{x}}\, \mathcal{L}_\ell(\hat{\boldsymbol{k}}\cdot\hat{\boldsymbol{x}})\, \mathrm{d}^3x\,. \tag{3.28}$$

This definition can be further decomposed into integrals over the number density fields of galaxies and randoms,

$$\widehat{F}_\ell(\boldsymbol{k}) = \frac{2\ell+1}{2\sqrt{I_\mathrm{norm}}}\left[\widehat{n_{\mathrm{obs}\,\ell}}(\boldsymbol{k}) - \alpha_\mathrm{ran}\,\widehat{n_{\mathrm{ran}\,\ell}}(\boldsymbol{k})\right], \tag{3.29}$$

where I_norm is the normalization constant already defined in equation (3.18),

$$\widehat{n_{\mathrm{obs}\,\ell}}(\boldsymbol{k}) = \int_{V_\mathrm{s}} n_\mathrm{obs}(\boldsymbol{x})\, w_\mathrm{FKP}(\boldsymbol{x})\, \mathrm{e}^{-\mathrm{i}\boldsymbol{k}\cdot\boldsymbol{x}}\, \mathcal{L}_\ell(\hat{\boldsymbol{k}}\cdot\hat{\boldsymbol{x}})\, \mathrm{d}^3x \quad \text{and} \tag{3.30}$$

$$\widehat{n_{\mathrm{ran}\,\ell}}(\boldsymbol{k}) = \int_{V_\mathrm{s}} n_\mathrm{ran}(\boldsymbol{x})\, w_\mathrm{FKP}(\boldsymbol{x})\, \mathrm{e}^{-\mathrm{i}\boldsymbol{k}\cdot\boldsymbol{x}}\, \mathcal{L}_\ell(\hat{\boldsymbol{k}}\cdot\hat{\boldsymbol{x}})\, \mathrm{d}^3x\,. \tag{3.31}$$

For simplicity, we have absorbed the FKP weights into the transformation. As the evaluation of these integrals corresponds to a single sum, the computation complexity is reduced significantly.

The approximative LoS recovery will eventually break down for galaxy pairs at low redshifts and wide separation angles resulting in a bias that is only significant for multipoles higher than the quadrupole (Samushia *et al.*, 2015). Since we are analysing a high-redshift sample in this thesis with a monopole-dominated wedge signal, we expect this bias to be negligible for our clustering wedge estimate.

The Yamamoto-Blake estimator is regularly used to measure the PS anisotropies of state-of-the art galaxy surveys. Until recently, equation (3.28) was computed as a direct sum over the galaxies and randoms. For example, Beutler *et al.* (2014a) estimates the power spectrum multipoles from the BOSS DR11 CMASS sample in this way. Later in this section, we discuss the recently developed FFT estimator for power spectrum multipoles, which reduces the computation costs significantly with respect to the traditional method.

3.2.3 The estimator for power spectrum wedges

We now extend the Yamamoto-Blake estimator to the clustering wedges in Fourier space defined in equation (3.4). First, the weighted wedge overdensity field is defined as

$$\widehat{F}^{\mu_2}_{\mu_1}(\boldsymbol{k}) \equiv \frac{1}{(\mu_2-\mu_1)\sqrt{I_\mathrm{norm}}}\left[\widehat{n_{\mathrm{obs}}}^{\mu_2}_{\mu_1}(\boldsymbol{k}) - \widehat{n_{\mathrm{ran}}}^{\mu_2}_{\mu_1}(\boldsymbol{k})\right], \tag{3.32}$$

where the wedge projections of the number density of galaxies and randoms are given by

$$\widehat{n_{\mathrm{obs}}}^{\mu_2}_{\mu_1}(\boldsymbol{k}) = \int_{V_\mathrm{s}} n_\mathrm{obs}(\boldsymbol{x})\, w_\mathrm{FKP}(\boldsymbol{x})\, \Theta^{\mu_2}_{\mu_1}(\hat{\boldsymbol{k}}\cdot\hat{\boldsymbol{x}})\, \mathrm{e}^{-\mathrm{i}\boldsymbol{k}\cdot\boldsymbol{x}}\, \mathrm{d}^3x \quad \text{and} \tag{3.33}$$

$$\widehat{n_{\mathrm{ran}}}^{\mu_2}_{\mu_1}(\boldsymbol{k}) = \int_{V_\mathrm{s}} n_\mathrm{ran}(\boldsymbol{x})\, w_\mathrm{FKP}(\boldsymbol{x})\, \Theta^{\mu_2}_{\mu_1}(\hat{\boldsymbol{k}}\cdot\hat{\boldsymbol{x}})\, \mathrm{e}^{-\mathrm{i}\boldsymbol{k}\cdot\boldsymbol{x}}\, \mathrm{d}^3x\,. \tag{3.34}$$

Again, the FKP weights are taken into the transformation. Here $\Theta^{\mu_2}_{\mu_1}(\mu)$ is the top-hat function for the range $\mu_1 \le \mu \le \mu_2$. Our estimator for the wedge power spectrum is then given by

$$P^{\mu_2}_{\mu_1}(\boldsymbol{k}) = \widehat{F}(\boldsymbol{k})\,\left[\widehat{F}^{\mu_2}_{\mu_1}(\boldsymbol{k})\right]^* - S^{\mu_2}_{\mu_1}(\boldsymbol{k}). \tag{3.35}$$

Just like the usual Yamamoto-Blake estimator, this estimator assumes the distant-observer approximation ('moving-LoS' method).

The shot-noise term $S_{\mu_1}^{\mu_2}(\boldsymbol{k})$ is given by

$$S_{\mu_1}^{\mu_2}(\boldsymbol{k}) = \frac{1}{(\mu_2 - \mu_1)\, I_{\mathrm{norm}}} \int_{V_\mathrm{s}} n_{\mathrm{exp}}(\boldsymbol{x})\, (1 + \alpha_{\mathrm{ran}})\, {w_{\mathrm{FKP}}}^2(\boldsymbol{x})\, \Theta_{\mu_1}^{\mu_2}\left(\frac{\boldsymbol{k}\cdot\boldsymbol{x}_j}{|\boldsymbol{k}|\,|\boldsymbol{x}|}\right) \mathrm{d}^3x\,, \tag{3.36}$$

corresponding to the multipole shot-noise term defined in equation (3.26). This estimate will be modified due to the systematic errors affecting the BOSS survey in Section 3.3.3.

3.2.4 The Yamamoto-FFT estimator

Even though the computing time of the estimator has been significantly reduced by adopting the distant-observer approximation, time efficiency is still a concern as the power spectrum wedges must be estimated for thousands of mock realizations (cf. Section 3.5). As shown recently by Bianchi *et al.* (2015) and Scoccimarro (2015), the Yamamoto-Blake estimator can be sped up significantly by use of multiple fast Fourier transforms. The Legendre polynomials $\mathcal{L}_\ell(\mu)$ can be expressed as a series of products $\mu^\ell = (\hat{\boldsymbol{x}}\cdot\hat{\boldsymbol{k}})^\ell$, so that the $\hat{\boldsymbol{x}}$ and $\boldsymbol{k}$ components can be factored out. The higher-order weighted density fields $\widehat{F}_\ell(\boldsymbol{k})$ of equation (3.28) can be written as (Bianchi *et al.*, 2015; Scoccimarro, 2015)

$$\widehat{F}_2(\boldsymbol{k}) = \frac{3}{2}\sum_{i,j} \hat{\boldsymbol{k}}_i\, \hat{\boldsymbol{k}}_j\, \widehat{Q}_{ij}(\boldsymbol{k}) - \frac{1}{2}\widehat{F}(\boldsymbol{k}) \quad \text{and} \tag{3.37}$$

$$\widehat{F}_4(\boldsymbol{k}) = \frac{35}{8}\sum_{i,j,k,l} \hat{\boldsymbol{k}}_i\, \hat{\boldsymbol{k}}_j\, \hat{\boldsymbol{k}}_k\, \hat{\boldsymbol{k}}_l\, \widehat{Q}_{ijkl}(\boldsymbol{k}) - \frac{15}{4}\widehat{F}_2(\boldsymbol{k}) + \frac{3}{8}\widehat{F}(\boldsymbol{k}), \tag{3.38}$$

where the Fourier transforms of the following tensors enter,

$$Q_{ij}(\boldsymbol{x}) = \hat{\boldsymbol{x}}_i\, \hat{\boldsymbol{x}}_j\, F(\boldsymbol{x}) \quad \text{and} \quad Q_{ijkl}(\boldsymbol{x}) = \hat{\boldsymbol{x}}_i\, \hat{\boldsymbol{x}}_j\, \hat{\boldsymbol{x}}_k\, \hat{\boldsymbol{x}}_l\, F(\boldsymbol{x}). \tag{3.39}$$

Due to the symmetries of the $Q_{\cdot}$ tensors, the calculation of $\hat{F}_2(\boldsymbol{k})$ needs six more FFTs in addition to the one of the original FKP estimator, calculating $\hat{F}_4(\boldsymbol{k})$ needs 15 additional transforms. Because of the low computational costs of FFTs, even for large grid sizes, the computing time is negligible compared to the original Yamamoto-Blake estimator.

Unfortunately, μ^ℓ products cannot be factored out from the top-hat kernels $\Theta_{\mu_1}^{\mu_2}(\mu)$ used in the estimator for clustering wedges defined in equation (3.35) and thus a FFT scheme does not apply directly to this estimator. However, the clustering wedges can be calculated from the multipoles using the transformation law in equation (3.8).

In foresight that we have to perform the measurement on thousands of mock realizations, we adopt the Yamamoto-FFT scheme for wedges indirectly. We truncate the power spectrum multipole series at the hexadecapole due to the very poor signal-to-noise of higher order multipoles (Yoo & Seljak, 2015; Grieb *et al.*, 2016a) and the fact that perturbation theory does not predict significant $P_\ell(k)$ at scales $k \lesssim 0.25\ h\,\mathrm{Mpc}^{-1}$ for $\ell \geq 6$ (Taruya *et al.*, 2011; Kazin *et al.*,

2012). From the monopole, quadrupole, and hexadecapole measurement, the clustering wedges are estimated as

$$P_{\mu_1}^{\mu_2}(k) = \sum_{\ell \in \{0,2,4\}} P_\ell(k)\, T_{n\ell}, \tag{3.40}$$

using the *transformation matrix* $\boldsymbol{T}$. The elements of this matrix are given by $T_{n\ell} = \bar{\mathcal{L}}_{\ell,\mu_1,\mu_2}$, where $\bar{\mathcal{L}}_{\ell,\mu_1,\mu_2}$ is the wedge-averaged Legendre polynomial as given by equation (3.9).

The agreement of the estimator with the one given by equation (3.35) is shown for the measurements of three power spectrum wedges from a CMASS-like catalogue in Section 3.5.3.

3.3 Observational systematics for the BOSS survey

Clustering analysis on previous releases of BOSS used two separate galaxy catalogues, LOWZ ($0.15 \leq z \leq 0.43$) and CMASS ($0.43 \leq z \leq 0.7$). A short overview of the results from DR9 (Ahn *et al.*, 2012) to DR12 (Alam *et al.*, 2015a) was given in Section 1.4.

In this thesis and in a set of companion papers led by Anderson *et al.* (2016, *in prep.*), the DR12 *combined sample* ($0.2 \leq z \leq 0.75$) based on the concatenation of the two previous catalogues (Reid *et al.*, 2016) is analysed, increasing the effective cosmic volume to $V_{\rm eff} = 7.4\,{\rm Gpc}^3$. This final sample is tuned for optimal estimation of the two-point clustering statistics. As discussed later in more detail, an additional 1000 deg^2 of 'early' data has been included in the low-redshift part of the catalogue that was not present in previous releases of the LOWZ sample.

3.3.1 Incompleteness of a galaxy survey due to observational systematics and corrective weights

The number density of galaxies observed in BOSS, as in any realistic survey, is affected by survey systematics and thus not correspond to the underlying number density of the sample. Systematic effects originating from the targeting and observing strategies affect the galaxy sample that is given by to observed and spectroscopically classified galaxies. Thus also the clustering signal that is observed from the sample can be biased due to these effects. Hence, these effects are corrected for by applying corrective weights to the galaxy catalogue.

- The angular size of a spectroscopic fibre is 62", which prevents to observe two galaxies close by with a single observational plate ('fibre collisions'). A weight $w_{\rm fc} \geq 1$ is defined to account for targets that could not be associated with a fibre, but belong to the same class of targets than a near-by observed one (which gets up-weighted by unity). However, it is possible to observe two close-by galaxies because of multiple observational plates for the same pointing.
- In a similar way, $w_{\rm rf} \geq 1$ is used to up-weight a near-by galaxy of the same target type in case of a failure of the pipeline that determines the spectroscopic redshift.

These first two weights are combined into the *counting weight*[3], $w_c = w_{fc} + w_{rf} - 1$.

Further, the target density of the CMASS sample is affected by the local stellar density and seeing (Ross *et al.*, 2012; Anderson *et al.*, 2014b; Reid *et al.*, 2016).

- A weight w_{star} based on the stellar density around a galaxy and the galaxies' surface brightness corrects for this systematic effect.
- Another systematic weight, w_{see}, corrects for the effect on the target density due to the seeing conditions during the photometric observations.

These later two weights together assign a *systematic weight*, $w_{sys} = w_{star}\, w_{see}$, to each galaxy.

It should be noted that the systematic weights are normalized such that they average to one over the whole sky. To incorporate the 'early' data, the survey is decomposed into several patches. Thus, the weights of each patch need to be normalized by the average w_{sys} of that region,

$$w_{sys} \mapsto \frac{w_{sys}}{\langle w_{sys} \rangle_{subsample}}. \tag{3.41}$$

The final weight, $w_{tot}(\boldsymbol{x}_i)$, of a galaxy at position $\boldsymbol{x}_i$ is given by

$$w_{tot}(\boldsymbol{x}_i) = w_{sys}(\boldsymbol{x}_i)\, w_c(\boldsymbol{x}_i) = w_{star}(\boldsymbol{x}_i)\, w_{see}(\boldsymbol{x}_i)\, [w_{fc}(\boldsymbol{x}_i) + w_{rf}(\boldsymbol{x}_i) - 1]\,. \tag{3.42}$$

Due to the weighting, the effective number of galaxies,

$$N_{gal,eff} = \sum_{i=1}^{N_{gal}} w_{tot}(\boldsymbol{x}_i). \tag{3.43}$$

is larger than the number of galaxies in the catalogue, N_{gal},

3.3.2 Details of the selection function, the completeness, and the veto mask

In order to characterize the angular selection function Φ_{ang} of the BOSS survey, the BOSS footprint is split into sectors that correspond to the union of spherical polygons defined by a unique intersection of spectroscopic tiles. The survey completeness, C, defined as the fraction of targets in a sector that are accounted for by observed galaxies including the weighting, is treated as uniform within a sector (Reid *et al.*, 2016, table 1). The left-hand panel of Figure 3.3 shows the footprint of the survey, indicating each pointing of the survey with a circle whose colour represents the sector completeness C.

The whole survey selection is described by the set of random points, which sample the survey volume roughly 50 times more densely than the galaxies ($N_{ran} \simeq 50\, N_{gal,eff}$). Within the

[3] w_c is also denoted as 'completeness weight' in the literature, but we want to avoid misunderstandings with the definition of the sector completeness, so we use the name 'counting weight'.

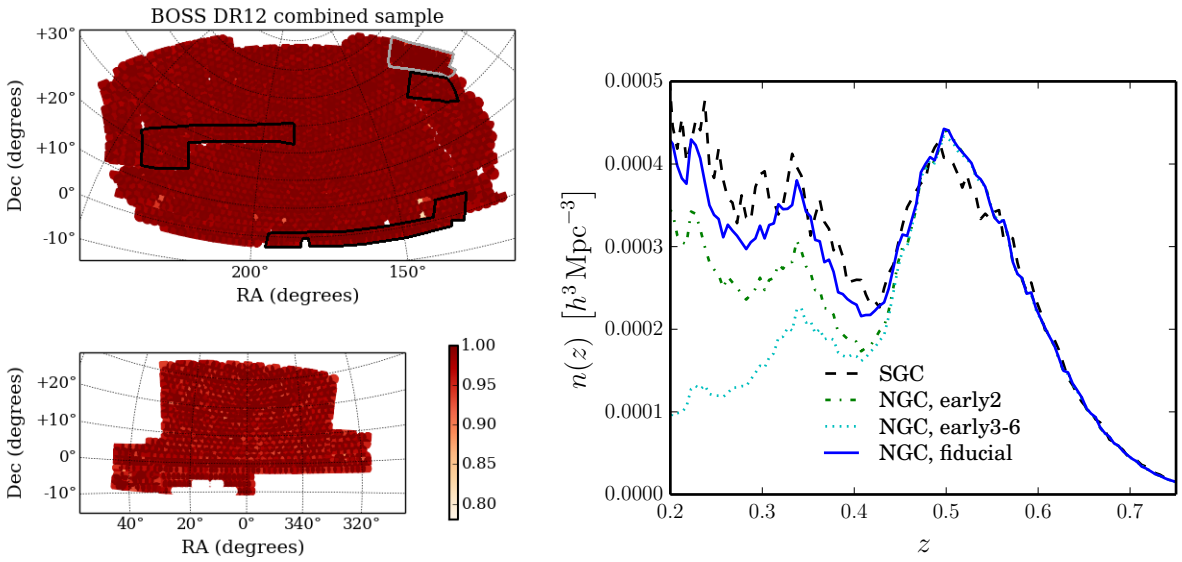

Figure 3.3 – *Left-hand panel:* The BOSS DR12 footprint of the NGC and SGC subsamples with circles indicating the different pointings of the telescope. The sector completeness is indicated by the colour of the circle. The 'early' regions in the Northern hemisphere are indicated by a gray ('early2') and black ('early3-6') edging. *Right-hand panel:* The (radial) selection function of the different patches of the BOSS combined sample.

geometrical boundaries of the survey, certain small regions remain where galaxies could not have been observed, such as the centre posts of the observational plates or the surroundings of a bright star. Despite the small angular size of each individual 'masked' region, they are not randomly distributed across the sky and sum to a non-negligible area. Thus, they are excluded from any analysis by the use of veto masks removing points of the random catalogue that fall within these masked regions (details in Reid *et al.*, 2016).

Besides the footprint and mask, the decomposition into patches is relevant for the selection function of the survey. The fiducial part of the Northern galactic cap (NGC) of LOWZ was targeted with the same selection criteria as the Southern galactic cap (SGC), but the targets in the Northern 'early patches' have been identified erroneously using slightly different criteria. These patches are the BOSS chunks 2 ('early2') and chunks 3–6 ('early3-6'), which both have been targeted using differently faulty selection criteria. Starting with chunk 7, the correct target selection algorithm was applied. As described in Reid *et al.* (2016), the early patches can be included in the catalogue by taking into account the deviations of the radial selection functions $n(z)$ for each patch. The SGC sample does not include early regions and thus the fiducial SGC is the full Southern sample. The individual selection functions of each patch are shown in the right-hand panel of Figure 3.3. The NGC subsample is comprised of the different patches in the North; the NGC and SGC subsamples are combined to form the full final catalogue.

This combined sample is analysed in two wide, non-overlapping redshift bins — referred to as 'low' ($0.2 \leq z < 0.5$) and 'high' ($0.5 \leq z < 0.75$) — while consistency checks are performed with an overlapping, 'intermediate' redshift bin ($0.4 \leq z < 0.6$). The definitions of the redshift

Table 3.1 – The effective redshifts, volumes, and number densities of the three redshift bins defined for the combined sample. The volumes $V_{\rm eff}$ (in units of $h^{-3}\,{\rm Gpc}^3$) and number densities $n_{\rm eff}$ (in units of $h^3\,{\rm Mpc}^{-3}$) are given for the different regions of the survey individually, computed in the fiducial cosmology defined in Table 3.2. The LOWZ and CMASS redshift ranges are given for comparison.

Bin	Redshift range	$z_{\rm eff}$	Patch	$V_{\rm eff}$	$n_{\rm eff}$
low	$0.2 \leq z \leq 0.5$	0.38	NGC, fid.	0.721	0.00032
			NGC, early2	0.014	0.00029
			NGC, early3-6	0.086	0.00025
			SGC	0.317	0.00035
intermediate	$0.4 \leq z \leq 0.6$	0.51	NGC, fid.	0.824	0.00034
			NGC, early2	0.018	0.00033
			NGC, early3-6	0.119	0.00033
			SGC	0.351	0.00033
high	$0.5 \leq z \leq 0.75$	0.61	NGC, fid.	0.782	0.00026
			NGC, early2	0.017	0.00026
			NGC, early3-6	0.116	0.00026
			SGC	0.332	0.00025
For comparison:					
LOWZ	$0.2 \leq z \leq 0.43$	0.32	NGC	0.425	0.00029
			SGC	0.189	0.00031
CMASS	$0.43 \leq z \leq 0.7$	0.57	NGC	1.153	0.00028
			SGC	0.555	0.00028

ranges are given in Table 3.1, listing also the effective redshifts, volumes, and number densities for the different patches of each bin (see Reid *et al.*, 2016, equation 52).

The effective data-to-randoms ratio $\alpha_{\rm ran}$ is defined by

$$\alpha_{\rm ran} \equiv \left(\sum_i^{N_{\rm gal}} w_{\rm tot}(\boldsymbol{x}_i)\, w_{\rm FKP}(\boldsymbol{x}_i)\right)\left(\sum_j^{N_{\rm ran}} w_{\rm FKP}(\boldsymbol{x}_j)\right)^{-1} \tag{3.44}$$

This choice ensures that the spatial average of the FKP density contrast $F(\boldsymbol{x})$ over the survey volume is $\langle F(\boldsymbol{x})\rangle = 0$. Note that Beutler *et al.* (2014a) and other works leave the FKP weight $w_{\rm FKP}$ out of the definition of $\alpha_{\rm ran}$, which should not change the result.

We now use the random catalogue to derive the normalization given by equation (3.18) by expressing the survey integral as a sum over the set of random points using equation (3.13) and the relation $\int_{V_{\rm s}} {\rm d}^3\boldsymbol{r}\, n_{\rm ran}(\boldsymbol{x})\, f(\boldsymbol{x}) \to \sum_j^{N_{\rm ran}} f(\boldsymbol{x}_i)$, which is valid for any smooth $f(x)$. This transformation yields

$$I_{\rm norm} = \alpha_{\rm ran} \sum_j^{N_{\rm ran}} n_{\rm exp}(\boldsymbol{x}_j)\, {w_{\rm FKP}}^2(\boldsymbol{x}_j). \tag{3.45}$$

3.3.3 Modified shot noise estimate

The shot-noise estimate in equation (3.17) does not account for deviations from a Poisson distributed galaxy and random sample. As a sample with the characteristics of a BOSS LSS sample does not need to have pure Poisson noise, a modification of this estimate is required to take into account the presence of systematic weights and deviations from the pure Poisson case due to the exclusion effect from fibre collisions. The latter arises because a good fraction of pairs that are angularly close by are excluded from the sample as no spectroscopic fibre could be assigned to one of the partners. The neighbour galaxy that is up-weighted using $w_{\mathrm{fc}}(\boldsymbol{x})$ as described in Section 3.3.1 does not have to be radially related to the omitted galaxy. The modified shot noise is calculated using the phenomenological treatment described in Gil-Marín *et al.* (2015a, App. A): if all galaxies that are combined to a fibre collision group were actually at the same redshift, i.e., all fibre collision pairs happen to be 'true pairs', the shot noise is given by[4]

$$S_{\mathrm{tp}} = \frac{1}{I_{\mathrm{norm}}} \int_{V_{\mathrm{s}}} n_{\mathrm{exp}}(\boldsymbol{x})\, {w_{\mathrm{FKP}}}^2(\boldsymbol{x}) \, \left(w_{\mathrm{sys}}(\boldsymbol{x}) + \alpha_{\mathrm{ran}}\right) \, \mathrm{d}^3x \,. \tag{3.46}$$

This is the only relation used in Beutler *et al.* (2014a). If, however, fibre collision pairs are only angularly close but separated in redshift, i.e., 'false pairs', the shot noise is given by[5]

$$S_{\mathrm{fp}} = \frac{1}{I_{\mathrm{norm}}} \int_{V_{\mathrm{s}}} n_{\mathrm{exp}}(\boldsymbol{x})\, {w_{\mathrm{FKP}}}^2(\boldsymbol{x}) \, \left(w_{\mathrm{tot}}(\boldsymbol{x}) + \alpha_{\mathrm{ran}}\right) \, \mathrm{d}^3x \,. \tag{3.47}$$

In reality, we expect to have a mixture of true and false pairs, so we expect

$$S_{\mathrm{final}} = f_{\mathrm{tp}}\, S_{\mathrm{tp}} + (1 - f_{\mathrm{tp}})\, S_{\mathrm{fp}} \tag{3.48}$$

for a given true pair fraction f_{tp}, which we assume to be $f_{\mathrm{tp}}^{\mathrm{fid}} \equiv \frac{1}{2}$ in agreement with Gil-Marín *et al.* (2015a) where tests against the PTHALO mock catalogues (Manera *et al.*, 2012) find a similar value.

Applying the same transformation to convert the integrals into sums as in the case of the normalization constant I_{norm}, we need to account for the different noise contributions from the clustered data and the unclustered randoms in equations (3.46) and (3.47). Thus, we choose to split the calculation accordingly into two sums, one corresponding to the systematic-weight affected part and the another one for the α_{ran}-part of the equations above. For the former, we have to take into account that we sum over weighted 'galaxies', each associated with a varying

[4] In regions with less chance to detect a galaxy, $w_{\mathrm{sys}} > 1$, the number of auto-pairs drops by ${w_{\mathrm{sys}}}^2$. The detected galaxies $N(\boldsymbol{x})$ are modelled as Poisson point process and the observed (effective) field is a (weighting) function of this process, $\langle n_{\mathrm{obs}} \rangle = w_{\mathrm{sys}}(\boldsymbol{x})\, \langle N(\boldsymbol{x}) \rangle = n_{\mathrm{exp}}(\boldsymbol{x})$. Thus, $\langle n_{\mathrm{obs}}(\boldsymbol{x})\, n_{\mathrm{obs}}(\boldsymbol{x}') \rangle = w_{\mathrm{sys}}(\boldsymbol{x})\, w_{\mathrm{sys}}(\boldsymbol{x}')\, \langle N(\boldsymbol{x})\, N(\boldsymbol{x}') \rangle = n_{\mathrm{exp}}(\boldsymbol{x})\, n_{\mathrm{exp}}(\boldsymbol{x}')\, [1 + \xi(\boldsymbol{x} - \boldsymbol{x}')] + n_{\mathrm{exp}}(\boldsymbol{x})\, w_{\mathrm{sys}}(\boldsymbol{x})\, \delta_{\mathrm{D}}(\boldsymbol{x} - \boldsymbol{x}')$ in this case.

[5] If effective galaxies (artificially) come in pairs, $w_{\mathrm{c}} = 2$, the number of auto-pairs (of pairs) drops by this factor squared. The detected galaxy pairs are modelled as Poisson point process $\tilde{N}(\boldsymbol{x})$ and the observed (effective) field is a (weighting) function of this process, $\langle n_{\mathrm{obs}} \rangle = w_{\mathrm{c}}(\boldsymbol{x})\, \langle \tilde{N}(\boldsymbol{x}) \rangle = n_{\mathrm{exp}}(\boldsymbol{x})$. Thus, $\langle n_{\mathrm{obs}}(\boldsymbol{x})\, n_{\mathrm{obs}}(\boldsymbol{x}') \rangle = w_{\mathrm{c}}(\boldsymbol{x})\, w_{\mathrm{c}}(\boldsymbol{x}')\, \langle \tilde{N}(\boldsymbol{x})\, \tilde{N}(\boldsymbol{x}') \rangle = n_{\mathrm{exp}}(\boldsymbol{x})\, n_{\mathrm{exp}}(\boldsymbol{x}')\, [1 + \xi(\boldsymbol{x} - \boldsymbol{x}')] + n_{\mathrm{exp}}(\boldsymbol{x})\, w_{\mathrm{c}}(\boldsymbol{x})\, \delta_{\mathrm{D}}(\boldsymbol{x} - \boldsymbol{x}')$ in this case.

finite volume element $w_{\rm tot}(\boldsymbol{x})\, n^{-1}_{\rm exp}(\boldsymbol{x})$. Hence, the conversion for the terms involving $w_{\rm sys}(\boldsymbol{x})$ and $w_{\rm tot}(\boldsymbol{x})$ — represented generally by $w_{\cdot}(\boldsymbol{x})$ below — is done by

$$\int_{V_{\rm s}} n_{\rm exp}(\boldsymbol{x})\, {w_{\rm FKP}}^2(\boldsymbol{x})\, w_{\cdot}(\boldsymbol{x})\, \mathrm{d}^3x \;=\; \sum_{\rm sample} w_{\rm tot}(\boldsymbol{x})\, {w_{\rm FKP}}^2(\boldsymbol{x})\, w_{\cdot}(\boldsymbol{x}). \tag{3.49}$$

This leads to a final estimate of the shot noise given by

$$S_{\rm final} = \frac{1}{I_{\rm norm}}\Bigg[f_{\rm tp} \sum_{\rm sample} {w_{\rm FKP}}^2(\boldsymbol{x})\, w_{\rm tot}(\boldsymbol{x})\, w_{\rm sys}(\boldsymbol{x}) + (1-f_{\rm tp}) \sum_{\rm sample} {w_{\rm FKP}}^2(\boldsymbol{x})\, {w_{\rm tot}}^2(\boldsymbol{x}) + \alpha^2_{\rm ran} \sum_{\rm randoms} {w_{\rm FKP}}^2(\boldsymbol{x})\Bigg]. \tag{3.50}$$

This separation of pairs by $f_{\rm tp}$ for the shot noise affects also the FKP weights as discussed in Section 3.3.4. In the case of the estimator for clustering wedges in equation (3.35), we use $S^{\mu_2}_{\mu_1}(\boldsymbol{k}) = S_{\rm final}$, neglecting anisotropies in the shot-noise estimate the same way as for the Yamamoto-Blake estimator in equation (3.27) for multipoles.

Due to the phenomenological nature of this treatment, we expect that the true shot noise can deviate from the estimate of equation (3.50). Variations from the assumption of pure Poisson shot noise are discussed in several recent studies (Casas-Miranda *et al.*, 2002; Seljak *et al.*, 2009; Hamaus *et al.*, 2010; Manera & Gaztanaga, 2011; Baldauf *et al.*, 2013). An incomplete shot-noise treatment can cause systematic biases on cosmological parameters. Thus, we include an additional shot-noise term N (see Section 5.1) as a free parameter to our modelling in order to capture any remaining residual shot-noise contribution. This parameter is marginalized over in the BAO+RSD analysis.

3.3.4 Modified FKP weights

The estimator for the power spectrum described in Section 3.2 weights each galaxy with the FKP weight $w_{\rm FKP}(\boldsymbol{x})$ in order to minimize the variance of the estimate. This extra weight was given in equation (3.15) assuming that the expected power spectrum amplitude $P_{\rm FKP}$ is constant and that $\alpha_{\rm ran} \ll 1$. Next we derive the optimal weighting in presence of systematic weights and fibre collisions extending the work in Beutler *et al.* (2014a), who derived a simpler result based on the shot-noise estimate in equation (3.46), ignoring the second shot-noise contribution in equation (3.47).

Following Feldman *et al.* (1994), the error of the power spectrum estimation for a given measurement bin centred around k can be expressed as

$$\sigma^2_P(k) \simeq \frac{1}{V_k} \int \mathrm{d}^3k\, |P(\boldsymbol{k})Q(\boldsymbol{k}) + S_{\rm final}|^2, \tag{3.51}$$

where V_k is the volume of the measurement bin, a spherical shell in k-space, and $Q(\boldsymbol{k})$ is the window function as given by equation (3.21). The shot noise contribution $S_{\rm final}$ follows our

treatment of the fibre collisions in equation (3.50). Here, we neglect the shot noise of the survey window as it is suppressed by $\alpha_{\rm ran}^2 \lll 1$.

Performing the same steps as in the derivation in Beutler *et al.* (2014a, appendix A), we write the fractional variance of the power spectrum as

$$\left(\frac{\sigma_P(k)}{P(k)}\right)^2 = \frac{1}{V_k}\int \left|Q(\boldsymbol{k}') + \frac{S_{\rm final}}{P(\boldsymbol{k})}\right|^2 \mathrm{d}^3k' \tag{3.52}$$

$$= \frac{\int {w_{\rm FKP}}^4(\boldsymbol{x})\, f(\boldsymbol{x})\, \mathrm{d}^3x}{\left[\int {w_{\rm FKP}}^2(\boldsymbol{x})\, g(\boldsymbol{x})\, \mathrm{d}^3x\right]^2}, \tag{3.53}$$

where the integration space was transformed using Parseval's theorem, introducing two functions $f(\boldsymbol{x})$ and $g(\boldsymbol{x})$ defined as

$$f(\boldsymbol{x}) \equiv \left| n_{\rm exp}^2(\boldsymbol{x}) + \frac{n_{\rm exp}(\boldsymbol{x})\left[f_{\rm tp}\, w_{\rm sys}(\boldsymbol{x}) + (1-f_{\rm tp}) w_{\rm tot}(\boldsymbol{x}) + \alpha_{\rm ran}\right]}{P(k)}\right|^2 \quad \text{and} \tag{3.54}$$

$$g(\boldsymbol{x}) \equiv n_{\rm exp}^2(\boldsymbol{x}), \tag{3.55}$$

respectively. Perturbing the weight $w_{\rm FKP}(\boldsymbol{x}) \rightarrow w_{\rm FKP}(\boldsymbol{x}) + \delta w(\boldsymbol{x})$ yields

$$\left(\frac{\sigma_P(k)}{P(k)}\right)^2 \simeq \frac{\int {w_{\rm FKP}}^4(\boldsymbol{x})\left[1 + 4\frac{\delta w(\boldsymbol{x})}{w_{\rm FKP}(\boldsymbol{x})}\right] f(\boldsymbol{x})\, \mathrm{d}^3x}{\left|\int {w_{\rm FKP}}^2(\boldsymbol{x})\left[1 + 2\frac{\delta w(\boldsymbol{x})}{w_{\rm FKP}(\boldsymbol{x})}\right] g(\boldsymbol{x})\, \mathrm{d}^3x\right|^2} \tag{3.56}$$

As proven in Beutler *et al.* (2014a, appendix A) by a Taylor expansion around $\delta w(\boldsymbol{x}) = 0$, the optimal weight has to satisfy

$$\frac{\int {w_{\rm FKP}}^3(\boldsymbol{x})\, f(\boldsymbol{x})\, \delta w(\boldsymbol{x})\, \mathrm{d}^3x}{\int {w_{\rm FKP}}^4(\boldsymbol{x})\, f(\boldsymbol{x})\, \mathrm{d}^3x} = \frac{\int w_{\rm FKP}(\boldsymbol{x})\, g(\boldsymbol{x})\, \delta w(\boldsymbol{x})\, \mathrm{d}^3x}{\int {w_{\rm FKP}}^2(\boldsymbol{x})\, g(\boldsymbol{x})\, \mathrm{d}^3x}. \tag{3.57}$$

The solution is given by $w_{\rm FKP}(\boldsymbol{x}) \propto \sqrt{g(\boldsymbol{x})/f(\boldsymbol{x})}$, where we insert the two functions given in equations (3.54) and (3.54). Further simplification yields

$$w_{\rm FKP}(\boldsymbol{x}) \propto \frac{1}{n_{\rm exp}(\boldsymbol{x}) + \left[f_{\rm tp}\, w_{\rm sys}(\boldsymbol{x}) + (1-f_{\rm tp}) w_{\rm tot}(\boldsymbol{x}) + \alpha_{\rm ran}\right]/P(\boldsymbol{k})}. \tag{3.58}$$

Neglecting the last term in the square brackets because of $\alpha_{\rm ran} \ll 1$ and using the simplifying approximation of a constant expected power spectrum amplitude, $P(\boldsymbol{k}) = P_{\rm FKP} = \text{const}$, we find that

$$w_{\rm FKP} = \frac{1}{f_{\rm tp}\, w_{\rm sys}(\boldsymbol{x}) + (1-f_{\rm tp})\, w_{\rm tot}(\boldsymbol{x}) + \bar{n}(\boldsymbol{x})\, P_{\rm FKP}} \tag{3.59}$$

is the minimum-variance weight for our case. Here, $f_{\rm tp}$ is the true pair fraction fiducially set to $f_{\rm tp} = 0.5$ as in the final shot-noise estimate of equation (3.50). In the case of $f_{\rm tp} = 1$, we recover the result presented in Beutler *et al.* (2014a, equation A.18), while setting $w_{\rm sys}(\boldsymbol{x}) = 1$ and $w_{\rm tot}(\boldsymbol{x}) = 1$ gives the standard FKP result of equation (3.15).

3.3.5 Details of the implementation of the clustering wedges estimator using the Yamamoto-FFT scheme

Our implementation of the Yamamoto-FFT estimator for the power spectrum multipoles up to the hexadecapole is mostly based on code written in C/C++ and uses the FFTW[6] library, which is one of the most common choices for a FFT library. Before applying the FFTs, the real-space version of equation (3.32) is calculated on a mesh using 1200^3 grid cells applying the triangular-shaped cloud (TSC) scheme to assign galaxies and randoms to the cells. The side length of the grid is 4000 h^{-1} Mpc. After the FFT, the mass-assignment scheme is corrected for by using an approximative, non-iterative version of the anti-aliasing correction introduced in Jing (2005). Montesano *et al.* (2010, appendix A) show that dividing each Fourier mode by the corrective term $C_1(\boldsymbol{k})$ given in Jing (2005, equation 20),

$$C_1^{\mathrm{TSC}}(\boldsymbol{k}) = \prod_i \left[1 - \sin^2\left(\frac{\pi\, k_i}{2\, k_{\mathrm{N}}}\right) - \frac{2}{15}\sin^4\left(\frac{\pi\, k_i}{2\, k_{\mathrm{N}}}\right)\right], \tag{3.60}$$

where k_{Ny} is the Nyquist frequency of the grid, yields a more precise power spectrum estimate than dividing by the Fourier transform of the mass assignment function (e.g. Angulo *et al.*, 2008). This C_1 scheme applied here was also used in Jeong & Komatsu (2009, studies on N-body simulations) and Montesano *et al.* (2012, cosmological implications of the BOSS DR7 power spectrum).

The final measurements are obtained by averaging the multipole estimates of equation (3.27) over spherical shells in k-space as

$$P_\ell(k) = \frac{1}{V_k}\int_{\mathrm{bin}} P_\ell(\boldsymbol{k})\,\mathrm{d}\hat{\boldsymbol{k}} = \frac{1}{N_{\mathrm{modes}}(k)} \sum_{k-0.5\,\Delta k \le |k| < k+0.5\,\Delta k} P_\ell(\boldsymbol{k}), \tag{3.61}$$

where V_k is the shell volume and $N_{\mathrm{modes}}(k)$ is the number of $\boldsymbol{k}$ modes contained in that shell. We define wave-number bins with $\Delta k = 0.005\ h\,\mathrm{Mpc}^{-1}$ from $k_{\mathrm{min}} = 0\ h\,\mathrm{Mpc}^{-1}$ to $k_{\mathrm{max}} = 0.25\ h\,\mathrm{Mpc}^{-1}$. Thus each bin is significantly larger than the fundamental mode of the grid, $k_{\mathrm{fund}} = 1.57 \times 10^{-3}\ h\,\mathrm{Mpc}^{-1}$. Also, k_{max} is always smaller than the Nyquist frequency of the grid, $k_{\mathrm{Ny}} = 0.942\ h\,\mathrm{Mpc}^{-1}$ and thus we can expect the error from aliasing to be less than 0.01% (Sefusatti *et al.*, 2015). The central wave-numbers are denoted as k_i in the following.

Post-processing steps, such as the conversion to clustering wedges, are performed using Python scripts. We consider configurations of two and three bins in μ. For simplicity and consistency with the analysis of two clustering wedges in configuration space (Kazin *et al.*, 2012, 2013; Sánchez *et al.*, 2013, 2014), the transverse and line-of-sight projections are labelled $P_\perp(k_i) \equiv P_0^{0.5}(k_i)$ and $P_\parallel(k_i) \equiv P_{0.5}^{1}(k_i)$, respectively. If three wedges are used, we denote the projections as $P_{\mathrm{3w,1}}$ to $P_{\mathrm{3w,3}}$ and the μ ranges are defined accordingly. For general references, we label the power spectrum wedges as $P_A(k_i)$ and combine all measurement bins into a single vector $\boldsymbol{P}^{\mathrm{obs}} = (P_A(k_i))$.

[6] http://www.fftw.org/

3.4 The window function effect

A non-trivial survey geometry biases the power spectrum estimator presented in Section 3.2. For scales of sizes close to or larger than the distances between the boundaries of the survey, the measured power spectrum is suppressed as the modes within the survey fail to resolve the perturbations at their full length. This effect can be described with a convolution of a theoretical prediction $P^{\rm theo}(\boldsymbol{k})$ with a window function as in equation (3.19). As already done in Gil-Marín *et al.* (2015d), we omit the term from the integral constraint (Beutler *et al.*, 2014a, section 5.2) due to its negligible effect for large-volume surveys such as BOSS,

$$P^{\rm obs}(\boldsymbol{k}) = \int Q(\boldsymbol{k}-\boldsymbol{k}')\, P^{\rm theo}(\boldsymbol{k}')\, {\rm d}^3k' \,. \tag{3.62}$$

The estimator of the window function $Q(\boldsymbol{k})$ was given in equation (3.21).

The isotropic power spectra measurements of the LRG, LOWZ and CMASS samples in DR5 to DR10/DR11 (Percival *et al.*, 2007a; Reid *et al.*, 2010; Montesano *et al.*, 2012; Anderson *et al.*, 2013, 2014b) defined an isotropic survey window function as the average of $|W(k)|^2 \equiv Q(\boldsymbol{k})$ over spherical shells in k-space. In order to take the anisotropies of the power spectrum correctly into account, multipole window functions were introduced in Beutler *et al.* (2014a, section 5.1). The large-scale suppression of power is stronger for higher-order multipoles due to the lack of resolution for wide angles. The multipole window function for the DR11 and DR12 BOSS samples are discussed in Beutler *et al.* (2014a) and Gil-Marín *et al.* (2015d), respectively.

For our Fourier space analysis, we extend the formalism of the multipole window function to clustering wedges. Consistently with our measurement method using the Yamamoto-FFT estimator, the wedge window functions are derived from estimates of the multipole window function (Beutler *et al.*, 2014a, equation 33),

$$|W(k,k')|^2_{\ell L} = 2{\rm i}^{\ell}(-{\rm i})^L\,(2\ell+1)\sum_{ij,i\neq j}^{N_{\rm ran}} w_{\rm FKP}(\boldsymbol{x}_i)\, w_{\rm FKP}(\boldsymbol{x}_j) \times j_\ell(k|\Delta\boldsymbol{x}|)\, j_L(k'|\Delta\boldsymbol{x}|)\, \mathcal{L}_\ell(\hat{\boldsymbol{x}}_{\rm mid}\cdot\hat{\boldsymbol{x}})\, \mathcal{L}_L(\hat{\boldsymbol{x}}_{\rm mid}\cdot\hat{\boldsymbol{x}}), \tag{3.63}$$

where $\Delta\boldsymbol{x} = \boldsymbol{x}_i - \boldsymbol{x}_j$, $\boldsymbol{x}_{\rm mid} = (\boldsymbol{x}_i + \boldsymbol{x}_j)/2$, and $j_\ell(x)$ represents the spherical Bessel function of order ℓ. Due to its immense computation time, this double sum was restricted to a subset of ca. 65,000 randoms. We performed a convergence test and did not find improvement if a larger subset of randoms is used.

The multipole window functions are subsequently transformed to wedge window functions by use of the matrix $\boldsymbol{T}$ that transforms multipoles to wedges as in equation (3.40),

$$|W(k,k')|^2_{{\rm 3w},nm} = \sum_{\ell,L\in\{0,2,4\}} T_{n\ell}\, T^{-1}_{Lm}\, |W(k,k')|^2_{\ell L}, \tag{3.64}$$

where T^{-1}_{Lm} are the elements of the inverse transformation matrix, $\boldsymbol{T}^{-1}$. For two wedges, only the monopole and quadrupole are used to generate $|W(k,k')|^2_{{\rm 2w},nm}$ in order to ensure that the transformation matrix is non-singular.

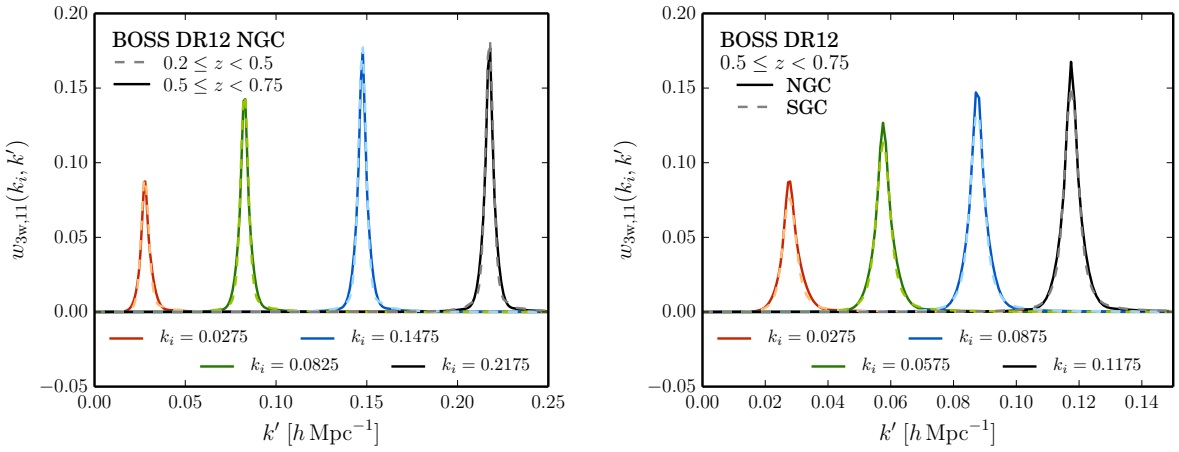

Figure 3.4 – The window matrix for the most-perpendicular wedge of the DR12 combined sample, $w_{3w,11}(k_i, k')$. The left-hand panel shows the dependency of $w_{3w,11}$ on the redshift range (low redshift bin dashed, high redshift bin solid) and the mean k_i (given in $h\,\mathrm{Mpc}^{-1}$) of the output bin. In the right-hand panel, the different window matrices for the two galactic caps of the survey are plotted (NGC solid, SGC dashed) for the high-redshift bin and lower output k_i than in the first panel.

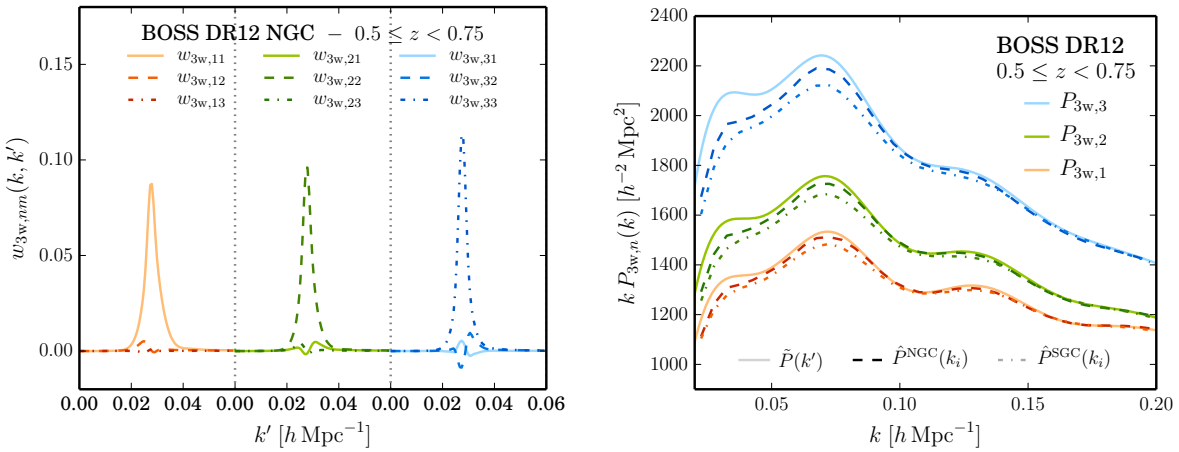

Figure 3.5 – *Left-hand panel:* The window matrix elements $w_{3w,11}(k_i, k')$ describe the contributions of the different input wedges to the output wedges, shown here for the wavenumber bin $k_i = 0.0275$ in the high-redshift bin (from left to right, the x-axis is split into repeating intervals for better visibility). *Right-hand panel:* The effect of the window matrix $w_{3w,nm}$ for the DR12 combined sample on the Fourier space wedges in the high redshift bin. The solid lines are the theoretical predictions $\tilde{P}_{3w,n}(k')$ (using the model described in Chapter 5 for best-fitting ΛCDM parameters), and the dashed (dash-dotted) lines corresponds to the prediction convolution with the window function, $\hat{P}_{3w,n}(k_i)$, for the North (South) galactic cap.

We apply a forward approach to compare model predictions for the power spectrum wedges to the measurements, by convolving the theoretical predictions $\tilde{P}_{3\mathrm{w},n}$ with the estimate for the window function, as a deconvolution can amplify the noise in the measurement. In order to reduce the computation time, the convolution is described by a window matrix multiplication. The normalized window matrix $\boldsymbol{M}$ is precomputed, with elements $w_{3\mathrm{w},nm}(k_i,k')$ given by

$$w_{3\mathrm{w},nm}(k_i,k') = W_{k_i}^{-1}\, w_{k'}\, |W(k_i,k')|^2_{3\mathrm{w},nm}\, (k')^2. \tag{3.65}$$

Here, the input wavenumbers k' and their weights $w_{k'}$ are determined using the Gauss-Legendre quadrature. The normalization W_{k_i} is chosen such that $\sum_{n,m=1}^{3} \sum_{k'} w_{3\mathrm{w},nm}(k_i,k') = 1$ for each k_i.

The final prediction for the power spectrum wedge vector, $\boldsymbol{P}^{\mathrm{pred}} = (\hat{P}_{3\mathrm{w},n}(k_i))$, is then given by

$$\boldsymbol{P}^{\mathrm{pred}} = \boldsymbol{M} \cdot \boldsymbol{P}^{\mathrm{theo}}, \qquad \hat{P}_{3\mathrm{w},n}(k_i) = \sum_{k'} w_{3\mathrm{w},nm}(k_i,k')\, \tilde{P}_{3\mathrm{w},m}(k'), \tag{3.66}$$

where $\boldsymbol{P}^{\mathrm{theo}} = (\tilde{P}_{3\mathrm{w},n}(k'))$ are model predictions for the wedges of the underlying power spectrum at the input wavenumbers k'.

To illustrate the features of the window matrix, we plot its elements for the most-perpendicular wedge, $w_{3\mathrm{w},11}(k_i,k')$, using different configurations in Figure 3.4. In the left-hand panel, we show that the window matrices for the low and high redshift bin do not significantly differ. Further, this plots shows the narrow width of the window function around each k_i, as well as the fast convergence of the normalized amplitude to an asymptotic height. In the right-hand panel of the same figure, it can be seen that the window matrices for North and South have a slightly different normalization due to the smaller volume of the South, but otherwise follow the same trends with k_i and k'.

In the left-hand panel of Figure 3.5, the cross- and auto-contributions of the three power spectrum wedges are shown for $k_i = 0.0275$ for the high-redshift bin. This plot illustrates that the cross-talking induced by the anisotropic window matrix is non-negligible for the most-parallel wedge. The right-hand panel of the same figure shows the convolved power spectrum for the Northern (NGC) and Southern (SGC) galactic cap versus the theoretical input power spectrum (taken from the best-fitting parameters of a ΛCDM model) to emphasize that the power suppression induces by the survey geometry is stronger for the SGC. In these two plots, only the results for the high redshift bin are presented, but the conclusions are the same for the other redshift bins.

While this thesis has been prepared, an alternative technique to account for the anisotropic window function effect was published (Wilson *et al.*, 2015). The advantage of this alternative method is the faster computation of the convolution by using 1D FFTs. In its original formulation, this technique does not account for wide-angle effects. This technique can be extended to wide surveys such as BOSS (private communication with F. Beutler), but due to the sufficient performance achieved by the precomputation of the window matrix, the benefit from switching to this new technique is small.

Table 3.2 – The sets of cosmology parameters used in this thesis and for the BOSS DR12 combined sample analysis (Anderson *et al.*, 2016, *in prep.*). All cosmologies are flat ΛCDM, so that $\Omega_\Lambda = 1 - \Omega_M$. Except for the 'template' cosmology, $\Omega_c h^2$ can be derived from $\Omega_c h^2 = \Omega_M h^2 - \Omega_b h^2$. For the template cosmology, there is a massive neutrino component in addition, $\Omega_\nu h^2 = 0.00064$ (corresponding to $\sum m_\nu = 0.06$ eV) — just as for the *Planck* 2015 reference ΛCDM cosmology (Adam *et al.*, 2015).

Name	Ω_M	h	$\Omega_b h^2$	σ_8	n_s
Fiducial	0.31	0.676	0.022	0.8	0.97
QPM	0.29	0.7	0.02247	0.8	0.97
Patchy	0.307115	0.6777	0.02214	0.8288	0.96
Minerva	0.285	0.695	0.02104	0.828	0.9632
Template	0.315298	0.6726	0.022204	0.828	0.964817

3.5 Synthetic galaxy catalogues for the BOSS samples

Synthetic catalogues that mimic the clustering properties of the BOSS LSS samples serve as basis to infer the covariance matrix for the fits of the clustering measurements on the DR12 combined sample. In order to fulfil this function, these catalogues incorporate the full survey geometry (i.e., they share the same angular and radial selection function) and the most important observational systematics — see Section 3.3 and Reid *et al.* (2016) — such as the veto masks and fibre collisions. A precise estimate of the covariance matrix requires a large number of mock catalogues, so that mass generation of hundreds to thousands of realizations is crucial. As accurate modelling of the gravitational dynamics only needs to be achieved in the quasi-linear regime, solving the large-scale dynamical evolution can rely on fast, approximate gravity solvers to generate large-scale halo catalogues. These haloes are subsequently populated with synthetic galaxies by use of phenomenological small-scale models that are calibrated on a few N-body simulations. The performance of a wide variety of mock halo and galaxy catalogue generators have been compared in Chuang *et al.* (2015). Also, our estimator for Fourier space wedges is tested on such mock catalogues.

Within the BOSS collaboration, two sets of mock catalogues mimicking the DR12 combined sample were constructed by separate teams using different tools, allowing for additional tests for systematic effects on the final constraints coming from the covariance matrix. Both sets of DR12 mocks feature a large number of realizations to overcome the sample noise in the precision matrix estimate (see the discussion of the clustering likelihood evaluation in Section 4.1.2). These efforts reflect the increasing need for the generation of accurate and reliable mock catalogues since the creation of the PThalos mocks for DR9 (Manera *et al.*, 2012, 2015).

As the two sets of mocks are generated assuming cosmological parameters different than the 'fiducial' ones, these values are compared against each other in Table 3.2.

3.5.1 MultiDark-Patchy mocks

The set of MultiDark-Patchy (Kitaura *et al.*, 2015, 2016) mocks are based on the Patchy (Kitaura *et al.*, 2014) recipe to generate mock halo catalogues. In a first step, the Augmented Lagrangian Perturbation Theory (ALPT; Kitaura & Hess, 2013) formalism is used to generate a DM density

and velocity field, splitting the Lagrangian displacement field (cf., Section 2.4.1) into a large-scale component, which is derived by 2LPT, and a small-scale component that is modelled by the spherical collapse approximation. The initial conditions are generated with cosmological parameters that are matched to the BIG-MULTIDARK N-body simulations (Klypin *et al.*, 2014). These parameters are given as 'PATCHY' in Table 3.2.

The halo density field is then modelled using perturbation theory and nonlinear stochastic biasing with parameters calibrated against the fully non-linear simulations (Rodríguez-Torres *et al.*, 2015). The second step populates the haloes with galaxies by halo abundance matching between the BOSS DR12 combined sample and simulations using HADRON (Zhao *et al.*, 2015). The clustering of the PATCHY catalogues reproduce the BOSS DR12 two- and three-point statistics (Rodríguez-Torres *et al.*, 2015). The survey selection is applied to a light-cone interpolation of the galaxy population at 10 different intermediate redshifts (SUGAR; see Rodríguez-Torres *et al.*, 2015). A set of 2045 realizations exists from which we obtain the covariance matrix discussed in Section 4.5 for the fits of the clustering model to the data.

3.5.2 QPM mocks

An alternative set of mock catalogues are based on a technique known as quick-particle-mesh (QPM; White *et al.*, 2014). This method uses a low-resolution particle mesh code to generate the large-scale dark matter density field from initial conditions that have been created using the cosmological parameters given as 'QPM' in Table 3.2. In a second step, sophisticated post-processing of the proto-haloes in that density field makes use of halo occupation distribution (HOD) modelling[7] to ensure that the small-scale clustering of the BOSS DR12 data is matched by that of the mocks. The combined-sample QPM mocks vary the HOD parameters over the redshift in order to create a more realistic survey sample from the fixed simulation output at $z = 0.55$. Three sets of 1000 realizations each were constructed for the DR12 LOWZ, CMASS, and combined samples.

The CMASS realizations are used to verify the FFT estimator in Section 3.5.3 and for the covariance matrix for the RSD challenge fits (cf., Section 5.2.2). Later, the QPM combined sample covariance matrix is used as an alternative to the PATCHY covariance matrix as a simple consistency check for systematics in the covariance estimate (see Section 4.5.2).

3.5.3 Verification of the FFT estimator

As described in Section 3.2, we estimate the power spectrum wedges by transforming the results of the Yamamoto-FFT multipole estimator (Bianchi *et al.*, 2015; Scoccimarro, 2015) using the transformation matrix given in equation (3.40). In order to verify that this does not give biased results compared to the direct estimate by means of the analogy of the Yamamoto-Blake estimator for power spectrum multipoles as given in equation (3.35), we compare these two estimators on the QPM mocks described in Section 3.5.2 for the DR12 CMASS samples in a version where fibre collisions have not been simulated to focus on the galaxy clustering only.

[7] The HOD technique is described in more details in Section 4.3, where it is used to generate galaxy catalogues from the set of MINERVA simulations.

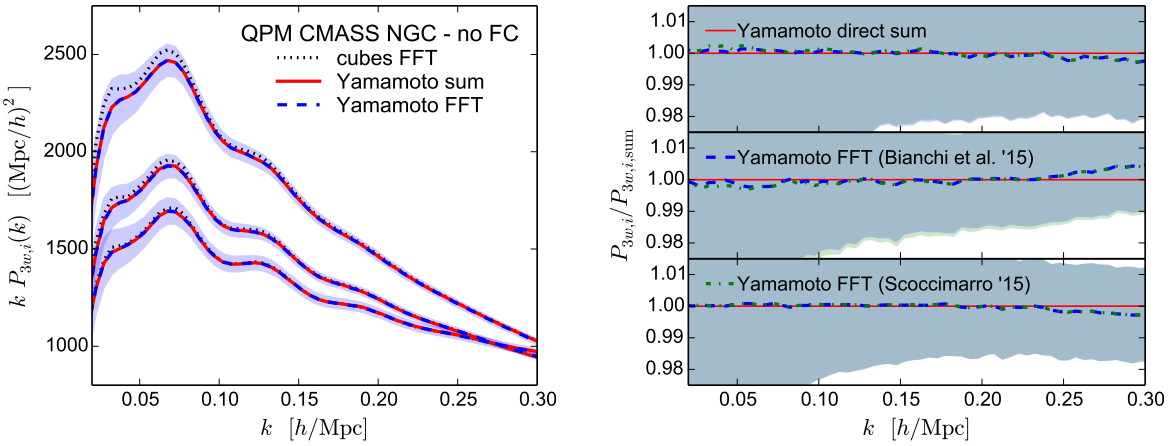

Figure 3.6 – *Left-hand panel:* Comparison of the mean power spectrum wedges of 1000 QPM DR12 CMASS mocks from the Yamamoto-Blake direct-sum estimator given in equation (3.35) against the Yamamoto-FFT estimator of Bianchi *et al.* (2015) and Scoccimarro (2015). The shaded region is the dispersion of the estimated power spectra of the individual mocks. *Right-hand panel:* The ratio of these power spectra to highlight the insignificance of the deviations.

As shown in Figure 3.6, no significant deviations between the direct-sum and FFT estimated power spectra wedges can be identified at the scales of interest ($|\Delta P_{3\mathrm{w},n}(k)|/P_{3\mathrm{w},n} \lesssim .5\%$ for $k \lesssim 0.25\ h\,\mathrm{Mpc}^{-1}$). Further, we test whether the simplification proposed in Scoccimarro (2015), reducing the number of FFTs per realization from 1+6+15 to 7, has a comparable performance than the full version. Especially, the accuracy of the estimators with respect to the mean and dispersion across the catalogues is relevant. Our comparison shows that the mean wedges are almost exactly the same, but the Scoccimarro-estimated intermediate wedge has a slightly smaller dispersion than the Bianchi-estimated one. As the method used in Scoccimarro (2015) is not completely compatible with the Yamamoto-Blake estimator, we use the approach of Bianchi *et al.* (2015) in this work. None the less, the RSD analysis should not be affected from deviations in the dispersion because the covariance is estimated from the mock catalogues in the same way as the data.

3.6 The Fourier space clustering wedges of the BOSS DR12 combined sample

In Figure 3.7, the three power spectrum wedges of the Northern (NGC, left-hand panels) and Southern galactic cap (SGC, right-hand panels) of the combined sample are plotted for the low (high) redshift bin in the upper (lower) panels. The measurements are shown with error bars corresponding to the diagonal entries of the covariance matrix obtained from the PATCHY mock catalogues. All measurements, on the data and the mocks, are consistently performed assuming the fiducial cosmology of the BOSS DR12 analysis (Anderson *et al.*, 2016, *in prep.*), whose matter density fraction is very close to the *Planck* 2013 (Ade *et al.*, 2014c) and 2015 (Ade *et al.*, 2015)

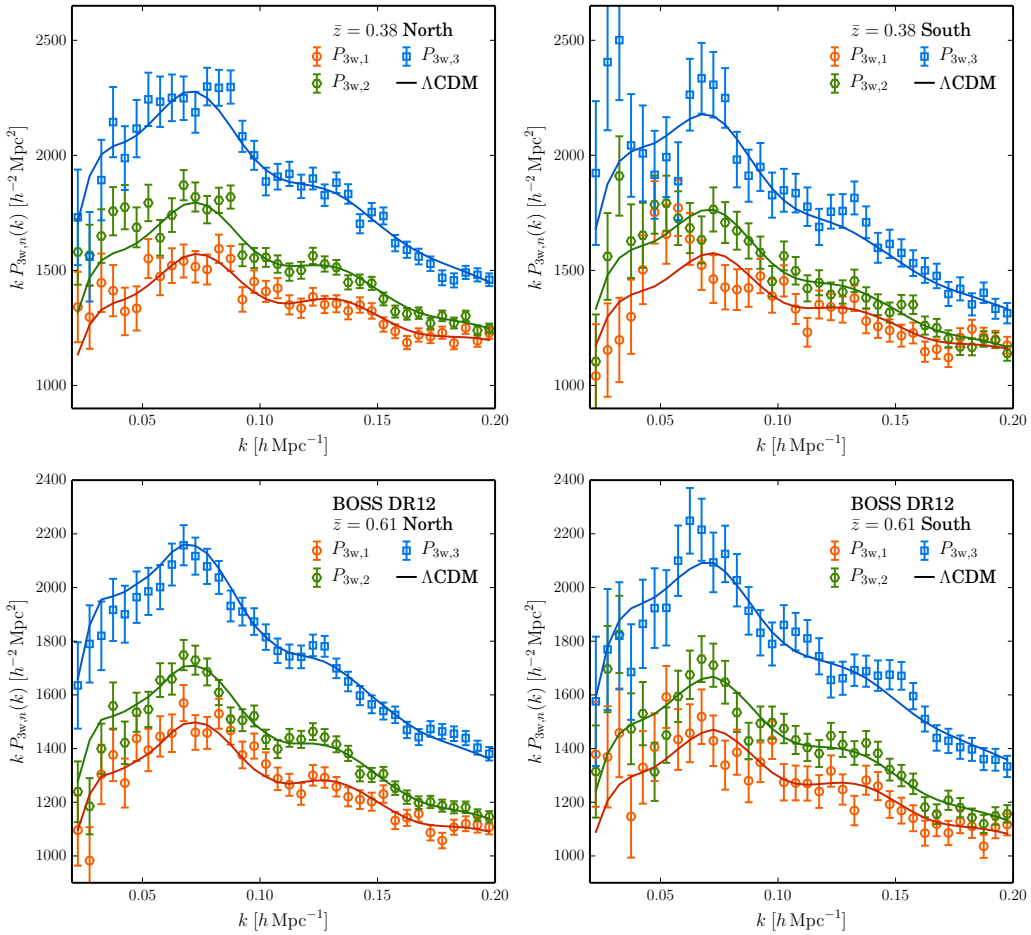

Figure 3.7 – The power spectrum wedges for NGC and SGC of the BOSS DR12 combined sample in the low (upper) and high (lower panel) redshift bin defined in Table 3.1. Error bars are derived as the square root of the diagonal entries of PATCHY covariance matrix (see Section 4.5.1). The model prediction is the best-fit ΛCDM model using the maximum-likelihood parameters of a combined fit of the *Planck* 2015 CMB observations and BOSS DR12 Fourier space wedges. The low redshift bin fits used separate bias, RSD, and shot noise parameters for NGS (left-hand panels) and SGC (right-hand panels), whereas the high bin used only one set of nuisance parameters.

central values. The full set of parameters for the fiducial cosmology is listed in Table 3.2.

In the same figure, also the model predictions for the full shape of the clustering wedges obtained with the techniques described in Section 5.1 are shown (solid lines). The model parameters are based on the maximum-likelihood values of a combined fit of a ΛCDM cosmology to the BOSS DR12 clustering wedges of the low and high redshift bins in Fourier space and the *Planck* 2015 CMB observations. For the low redshift bin, we use two different sets of nuisance parameters (the bias and RSD parameters and the additional shot noise) to account for the fact that the NGC and SGC samples might contain two slightly different galaxy population at low redshifts as discussed later in Section 3.6.2.

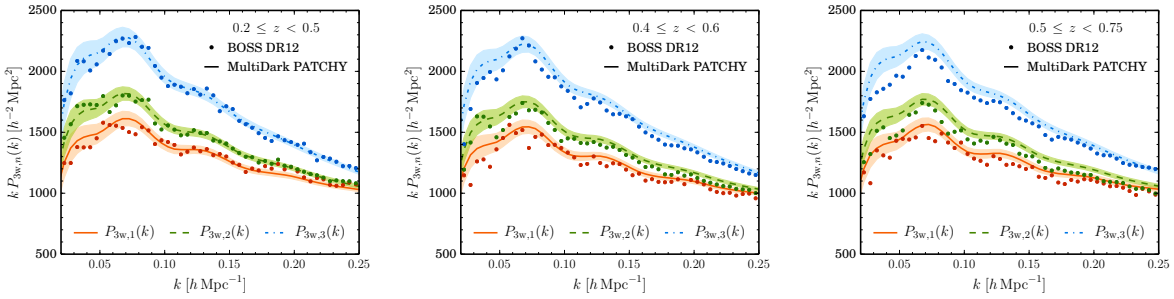

Figure 3.8 – MultiDark PATCHY power spectrum wedges compared against the BOSS DR12 combined sample for the low (left-hand panel), intermediate (centre panel) and high (right-hand panel) redshift bin. These measurements correspond to 2045 full survey (combining NGC and SGC) mocks and have been performed assuming the fiducial cosmology.

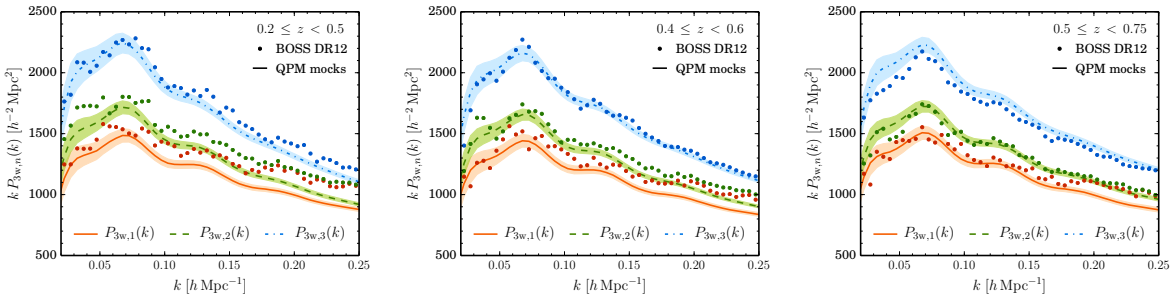

Figure 3.9 – QPM power spectrum wedges compared against the BOSS DR12 combined sample for the low (left-hand panel), intermediate (centre panel) and high (right-hand panel) redshift bin. These measurements correspond to 1000 full survey (combining NGC and SGC) mocks and have been performed assuming the fiducial cosmology.

3.6.1 Galaxy clustering comparison between the data and the mocks

For consistency, the power spectrum measurements from the BOSS DR12 combined sample and the mock realizations are performed in the fiducial cosmology as defined in Table 3.2. Thus the fiducial distances in the measurements are different from the true distances in the underlying synthetic galaxy samples. The relevant distance quantities such as $D_\mathrm{A}(z)$ and $H(z)$ are compared later in Table 5.1.

Here, we compare the clustering measurements in Fourier space on the mocks with the data. The mean power spectrum wedges derived from the PATCHY mocks show very good agreement with the clustering of the DR12 combined sample as shown by the comparison in Figure 3.8. This agreement becomes slightly worse the higher the redshift is, but as the modelling of the full characteristics of a galaxy survey such as BOSS is a great challenge, deviations can be expected.

The QPM mocks described in Section 3.5.2 are an alternative set of synthetic survey catalogues used for comparison tests. In Figure 3.9, the mean and dispersion of the QPM power spectrum wedges are compared against the measurements on the BOSS DR12 combined sample for the low (left-hand panel) and the high redshift bin (right-hand panel) and the agreement is found to be worse than for the PATCHY mocks. Other than the larger dispersion of the PATCHY

mocks (discussed later in Section 4.5.3), the larger number of realizations, the better agreement of the PATCHY clustering with the data, and the improved modelling of the redshift evolution in the PATCHY mocks are reasons for the choice of the PATCHY mocks as reference for the covariance estimate. The covariance matrices obtained from the PATCHY and QPM mocks are discussed in Section 4.5.

In the BOSS DR12 LOWZ and CMASS analyses (Gil-Marín *et al.*, 2015d,c; Cuesta *et al.*, 2015), only minor differences were found in the covariance matrices obtained from the QPM and PATCHY mocks (in particular, QPM predicts a larger high-k dispersion of the power spectrum monopole). However, no significant effect from interchanging the covariances was found for BAO and RSD fits on the data.

3.6.2 The clustering properties of the NGC and SGC subsamples

Due to small differences in the photometry between the two galactic caps, the combined sample of BOSS does not have a unique selection function. As there are also erroneously targeted 'early regions', the sample is split into patches with their own selection function $n(z)$, which were shown in Figure 3.3. Thus, there is no guarantee that the galaxy populations of the different regions fully correspond to each other. As part of the Fourier space analysis presented in this thesis, the clustering properties of the individual subsamples are compared, focussing on hemispherical subsamples that combine the patches in each of the two galactic caps of the survey (NGC and SGC).

In Figure 3.10, we show the power spectrum monopole for each subsample with error bars derived from the diagonal of the PATCHY covariance matrix (see Section 4.5.1) for the low (left-hand panels) and high (right-hand panels) redshift bins. The centre panels show the $P_0(k)$ up to a wavenumber of $k_{\rm max} = 0.3\,h\,{\rm Mpc}^{-1}$, the lower panels show the ratio of SGC power spectrum to the NGC power spectrum. The upper panel shows the selection functions for the different subsamples, excluding the early regions in the North.

The comparison of the measured power spectrum monopole, $P_0(k)$, of the NGC and SGC subsamples of the final catalogue with the predicted NGC–SGC dispersion from the PATCHY mocks shows significant tension for the low redshift bin, while the differences in the high redshift bin are consistent with the sample variance of the mocks. In terms of the power spectrum monopole, the SGC clustering in the low redshift bin shows a 4% amplitude mismatch.

As discussed in more detail in Ross *et al.* (2016, *in prep.*), the discrepancy can be solved by taking into account the colour shifts between SDSS DR8 photometry (Aihara *et al.*, 2011) in the North and South that have been identified by Schlafly & Finkbeiner (2011). These corrections affect the LOWZ SGC colour cut on $c_{\parallel}$ (Reid *et al.*, 2016, equation 9),

$$r_{\rm cmod} < 13.5 + c_{\parallel,{\rm corr}}/0.3, \quad \text{where} \quad c_{\parallel,{\rm corr}} = c_{\parallel} - 0.015 \tag{3.67}$$

and the CMASS SGC colour cuts on $d_{\perp}$ (Reid *et al.*, 2016, equations 13 and 14),

$$\begin{aligned} &d_{\perp,{\rm corr}} > 0.55 \quad \text{and} \\ &i_{\rm cmod} < \min\left(19.86 + 1.6(d_{\perp,{\rm corr}} - 0.8), 19.9\right), \quad \text{where} \\ &d_{\perp,{\rm corr}} = d_{\perp} - 0.0064. \end{aligned} \tag{3.68}$$

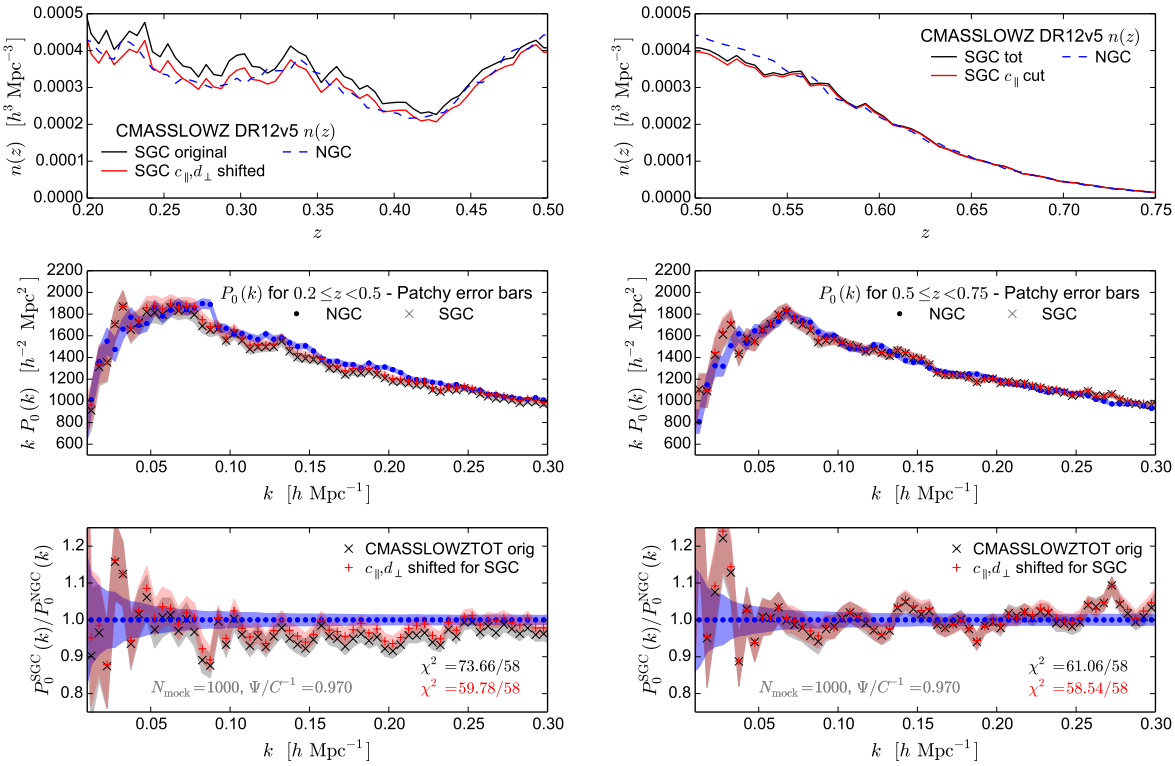

Figure 3.10 – The number density (upper panels) and power spectrum monopole (centre panels) for the NGC (blue) and SGC (black lines) subsamples of the combined sample in the low (left-hand panels) and high (right-hand panels) redshift bins. Error bars (shaded area) are derived from the Patchy mocks. The red line corresponds to a corrected SGC sample taking the colour shifts between SDSS photometry in the North and South into account (for more details, see Ross *et al.*, 2016, *in prep.*). The lower panels shows the $P_0(k)$ ratio to highlight the deviations between the samples in the two hemispheres.

The selection function and power spectrum monopole of the corrected SGC subsample are overplotted in Figure 3.10. The SGC $n(z)$ is reduced by 10% at low redshifts and the amplitude mismatch in $P_0(k)$ is lowered to a level that is consistent with the North. The corrected SGC result is still below the one of NGC for most wavenumber bins, but as the window function induces a correlation between the bin, only the analysis of the log likelihood χ^2, defined later in equation (4.4), can quantify the level of consistency. Thus, apart from the difference vector, the co-added NGC and SGC precision matrix is needed,

$$\boldsymbol{\psi}^P_{\rm diff} = (1+D)\left[\boldsymbol{C}^{P_0}_{\rm diff}\right]^{-1}, \quad \text{where} \quad \boldsymbol{C}^{P_0}_{\rm diff} = \boldsymbol{C}^{P_0}_{\rm NGC} + \boldsymbol{C}^{P_0}_{\rm SGC}, \tag{3.69}$$

The covariance matrices were obtained from 1000 Patchy realizations and has been corrected for sampling noise using the correction factor in equation (4.5), $(1 + D)$, that is given in the figure. The likelihood, the precision matrix, and the correction factors are discussed in more detail in Section 4.1.2.

This analysis shows that the low-redshift NGC–SGC difference in the corrected sample is of the order of what can be expected for this number of measurement bins. Further, the

high redshift bin also shows slightly increased consistency, even though it was already in good agreement in the original sample.

These results on the shifts of $n(z)$ and $P_0(k)$ are in very good agreement with results presented in Ross *et al.* (2012) for the configuration space DR9 CMASS analysis, which did not find any significant change in the galaxy clustering after correcting for the shifted photometry. Further tests on the DR12 combined sample in configuration space (Ross *et al.*, 2016, *in prep.*) show the same trends as seen in Fourier space, but the amplitude mismatch is not a significant change as the relative errors bars are much larger for the correlation function.

We see this analysis as good evidence that the NGC and SGC subsamples probe slightly different galaxy populations for redshifts lower than $z \leq 0.5$. As a consequence, we describe the two parts of the low redshift sample with two different bias, RSD, and shot noise parameters when modelling the power spectrum wedges (see Chapter 5). Using 'gRPT+RSD' fits of the PATCHY mocks as those described in Section 5.2.3, we find that this assumption does not weaken the constraining power for AP and growth parameters in BAO+RSD fits.

4

Covariance Matrices

> "Complicating the noise issue is the fact that one person's noise is another person's signal. [...] [T]he signals one astronomer was seeking were considered so much noise in the eyes of another."
>
> Cole (1998)

Inference of cosmological information from large-scale structure observations relies on an estimate for the covariance of the measurements. In order not to spoil the precision of the cosmological observations, also the covariance matrix needs to be accurately estimated. The covariance matrices associated with galaxy clustering are usually obtained from a *brute-force* production of hundreds or thousands of synthetic realizations (called 'mocks') using fast approximate schemes for the gravitational evolution and formation of overdense structures. As the cosmological observations are evaluated at quasi-linear scales, the clustering covariance is not measured with full non-linear simulations as this would be computationally too expensive. However, the covariance estimates from the mock method is affected by noise due to the finite number of realizations as discussed in Section 4.1. This results in a biased estimate for the inverse of the covariance matrix, which leads to biased estimates of the obtained constraints (Taylor *et al.*, 2013; Dodelson & Schneider, 2013; Percival *et al.*, 2014; Taylor & Joachimi, 2014). Pushing the number of mock realizations to the regime of a couple of thousands can ameliorate this inaccuracy.

To validate the model of the redshift-space galaxy clustering described in sections 2.4.4 to 2.4.6, working with N-body simulations is a necessary step in order to verify how well the clustering two-point statistics are described in the mildly non-linear regime. An improved accuracy at small scales is beneficial for cosmologial fits as the number of modes increase with the third power of maximum wavenumber of the fitting range. In general, only a few realizations of the expensive N-body simulations are available, so that the data covariance matrix can only be predicted with a low signal-to-noise ratio. Even more so for a number of measurement bins that is of the same order or larger than the number of realizations, in which case the obtained covariance matrix cannot be inverted to estimate the precision matrix (cf., Section 4.1.2). For this

case, a theoretical framework for the modelling of anisotropic clustering covariance, relying on the assumption of a Gaussian likelihood for the two-point statistics, is presented in Section 4.2. These predictions are compared against the results from the set of 100 MINERVA simulations in Section 4.4. The simulations are described in Section 4.3.

Alternatively, the covariance can be estimated with methods that work on a small number of independent realizations, or even only one. Examples of such methods are bootstrap and jackknife. The latter technique will be used in this work to estimate the error on the covariance. In the context of clustering covariance estimates, Hamilton *et al.* (2006) uses a reshuffling scheme for the phases of a periodic simulation to estimate the power spectrum covariance from a single realization and a similar resampling was used by Schneider *et al.* (2011).

Parametric models of the covariance matrix model the broad features with smooth analytical functions depending on free parameters that are calibrated against a smaller number of simulations (Pearson & Samushia, 2015). The noise in the obtained covariance matrix can also be reduced by means of a shrinkage estimation (Pope & Szapudi, 2008) or covariance tapering (Paz & Sanchez, 2015).

As the modelling of the survey systematics such as the selection function and the fibre collisions are very non-trivial, the BOSS clustering working group bases their clustering analyses on two large sets of mock catalogues that are used also for further checks for systematic of the modelling apart from the estimate of the covariance matrix. The covariance matrices obtained from these mocks are described in Section 4.5.

The complexity of the covariance estimation increases further if the dependence of the covariance on the cosmological model is to be analysed as well (e.g., for the BAO covariance, Labatie *et al.*, 2012). As the main aim of this thesis are the cosmological fits to the BOSS DR12 clustering, only the most relevant aspects of the estimation of the covariance matrix are presented in this thesis.

4.1 Covariance matrix estimates from sets of mock simulations and their noise properties

4.1.1 The data covariance matrix

For this section, we assume that the measurement vector $\boldsymbol{P}^{\mathrm{obs}} = (P_A(k_i))$ has elements $P_A(k_i) \equiv P_A^i$ that can denote power spectrum (PS) wedges or multipoles, measured at wavenumber bins centred at k_i. Analogously, the quantities $\xi_A(r_i) \equiv \xi_A^i$ denote measurements of two-point correlation function (2PCF) wedges or multipoles in separation bins centred at r_i.

Usually the covariance matrix $\boldsymbol{C}^P$ is estimated from a set of N_{m} mock measurements, denoted ${}^{(n)}P_A^i$, where $n \in \{1, \ldots, N_{\mathrm{m}}\}$, so that[1]

$$C^P_{ABij} = \frac{1}{N_{\mathrm{m}} - 1} \sum_n \left({}^{(n)}P_A^i - \langle P_A^i \rangle \right) \left({}^{(n)}P_B^j - \langle P_B^j \rangle \right). \tag{4.1}$$

[1]The 2PCF covariance matrix $\boldsymbol{C}^\xi = \left(C^\xi_{ABij}\right)$ is likewise estimated from mock measurements ${}^{(n)}\xi_A^i$.

Table 4.1 – The correction factors of equation (4.5) for the precision matrices of our configuration of measurement bins and numbers of realizations used to estimate the covariance matrix of the anisotropic clustering in configuration space (bins of seperation distance s) and Fourier space (bins of wavenumber k). The first set of configurations is used for the covariance matrices of the MINERVA simulations in Section 4.4; in this case except for the large configuration space bins, the covariance matrix is singular due to $N_\mathrm{b} \geq N_\mathrm{m} - 2$ or noise-dominated as $D \geq 0.5$. The second set of configurations is used for the covariances matrices of the BOSS DR12 combined sample discussed in Section 4.5.

N_m	Space	Unit	k_min/ s_min	k_max/ s_min	Δk/ Δs	#(k_i)/ #(s_i)	#(wedges)/ #(multipoles)	N_b	D
100	k	$h\,\mathrm{Mpc}^{-1}$	0	0.25	0.005	50	3	150	–
					0.010	25	3	75	0.7677
100	s	$h^{-1}\,\mathrm{Mpc}$	0	180	5	36	3	108	–
					15	12	3	36	0.3737
1000	k	$h\,\mathrm{Mpc}^{-1}$	0.02	0.2	0.005	36	3	108	0.1091
2045	k	$h\,\mathrm{Mpc}^{-1}$	0.02	0.2	0.005	36	3	108	0.0533

Here, the mean over all simulations is given by

$$\langle P_A^i \rangle = \frac{1}{N_\mathrm{m}} \sum_n {}^{(n)}P_A^i. \tag{4.2}$$

4.1.2 The clustering likelihood and the precision matrix

Assuming that the Fourier transform of the density contrast $\widehat{\delta}(\boldsymbol{k})$, as defined in equation (2.32), is a Gaussian random field, the Fourier modes $|\hat{\delta}(\boldsymbol{k})|^2$ follow a Rayleigh distribution (see e.g. Kalus *et al.*, 2016). In the following, we assume that the number of Fourier modes observed is large enough to validate the assumption that the power spectrum follows a multi-variate Gaussian distribution with fixed covariance.[2]

We denote a point in the parameter space of a theoretical clustering model as $\boldsymbol{\zeta} \in \mathcal{X}$ and the model predictions as $\boldsymbol{P}^\mathrm{pred}(\boldsymbol{\zeta}) = \left(\hat{P}_A(k_i)\right)$. Given that the covariance matrix $\boldsymbol{C}^P$ is known exactly and fixed, we can compute the likelihood of a model prediction for the clustering statistic, $\boldsymbol{P}^\mathrm{pred}$ or $\boldsymbol{\xi}^\mathrm{pred}$, using its inverse, the *precision matrix*, $\boldsymbol{\psi}^P$, by[3]

$$\mathscr{L}\left(\boldsymbol{\zeta} \mid \boldsymbol{P}^\mathrm{obs}, \boldsymbol{\psi}^P\right) = \frac{|\boldsymbol{\psi}^P|}{\sqrt{2\pi}} \exp\left[-\frac{1}{2}\chi^2(\boldsymbol{P}^\mathrm{pred}(\boldsymbol{\zeta}), \boldsymbol{P}^\mathrm{obs}, \boldsymbol{\psi}^P)\right]. \tag{4.3}$$

[2]Deviations from the Gaussianity of the angular power spectrum likelihood have recently been analysed (Sun *et al.*, 2013; Kalus *et al.*, 2016) and it was shown that constraints on primordial non-Gaussianity are affected by the negligence of the non-Gaussian contribution. The logarithm of the spatial power spectrum was found to be closer to a Gaussian random variable at large scales than the power spectrum itself by Ross *et al.* (2013). In this work, we consider the assumption of a Gaussian likelihood as sufficient for quasi-linear scales (Manera *et al.*, 2012; Ross *et al.*, 2013). Further, we neglect the dependence of the covariance on cosmological parameters as suggested by Carron (2013).

[3]For the 2PCF likelihood, replace the $\boldsymbol{P}^\mathrm{pred}$, $\hat{P}_A^i$, $\boldsymbol{P}^\mathrm{obs}$, P_A^i, and $\boldsymbol{\psi}^P$ by $\boldsymbol{\xi}^\mathrm{pred}$, $\hat{\xi}i_A^i$, $\boldsymbol{\xi}^\mathrm{obs}$ and ξ_A^i, and $\boldsymbol{\psi}^\xi$.

Table 4.2 – The correction factors for the parameter constraints as given by equation (4.6) for our configuration of measurement bins, numbers of realizations used to estimate the covariance matrix, and number of fitting parameters. $k_{\rm min}$ and $k_{\rm max}$ are given in units of $h\,{\rm Mpc}^{-1}$.

$N_{\rm m}$	$k_{\rm min}$	$k_{\rm max}$	$N_{\rm b}$	$N_{\rm p}$ (z-bin)	M
1000	0.02	0.2	108	8 (int,high)	1.0494
1000	0.02	0.2	108	13 (low)	1.0439
2045	0.02	0.2	108	8 (int,high)	1.0231
2045	0.02	0.2	108	13 (low)	1.0206

Here, the *log-likelihood* or χ^2 function is given by

$$\begin{aligned}\chi^2(\boldsymbol{P}^{\rm pred},\boldsymbol{P}^{\rm obs},\boldsymbol{\psi}^P) &= \left(\boldsymbol{P}^{\rm obs}-\boldsymbol{P}^{\rm pred}\right)^{\rm T}\cdot\boldsymbol{\psi}^P\cdot\left(\boldsymbol{P}^{\rm obs}-\boldsymbol{P}^{\rm pred}\right)\\ &= \sum_{A,B}\sum_{i,j}\left(P_A^i-\hat{P}_A^i\right)\psi^P_{ABij}\left(P_B^j-\hat{P}_B^j\right),\end{aligned} \tag{4.4}$$

where ψ^P_{ABij} are the elements of the precision matrix $\boldsymbol{\psi}^P$.

This likelihood is usually explored using Monte Carlo Markov chains to estimate the constraints in the parameter space $\mathcal{X}$. This technique is further discussed in Appendix A.

If the exact covariance matrix is not known, but estimated using equation (4.1), the noise in $(\boldsymbol{C}^P)^{-1}$ must be considered as a potential systematic. Then, the likelihood of equation (4.3) has to be marginalized over the distribution of the uncertainties in $(\boldsymbol{C}^P)^{-1}$. In the case in which ${}^{(n)}P_A^i$ are Gaussian random samples, the inverse covariance matrices follow an inverse Wishart distribution with the true precision matrix $\boldsymbol{\psi}^P$. In most analyses however, $(\boldsymbol{C}^P)^{-1}$ is used to replace the exact inverse covariance $\boldsymbol{\psi}^P$, resulting in known biases of the parameter estimates that must be corrected for (see e.g. Kaufman, 1967; Taylor *et al.*, 2013; Dodelson & Schneider, 2013; Percival *et al.*, 2014; Taylor & Joachimi, 2014). In this work, this bias is accounted for by the usual rescaling (Hartlap *et al.*, 2007),

$$\boldsymbol{\psi}^P = (1-D)\,\boldsymbol{C}^{P^{-1}}, \quad \text{where} \quad D=\frac{N_{\rm b}+1}{N_{\rm m}-1}, \tag{4.5}$$

where $N_{\rm b}$ is the totbal number of bins in the measurements $P_A(k_a)$. Thus, the smaller the number of realizations, $N_{\rm m}$, the larger these corrections are; in the extreme case of $N_{\rm b}\geq N_{\rm m}-2$, the covariance matrix $\boldsymbol{C}^P$ becomes singular.

In addition, the effect of the noise propagates to the parameter constraints, so that the obtained variance of each parameter needs to be rescaled by (Percival *et al.*, 2014)

$$M=\sqrt{\frac{1+B\,(N_{\rm b}-N_{\rm p})}{1+A+B\,(N_{\rm p}+1)}}, \tag{4.6}$$

where $N_{\rm p}$ is the number of fitting parameters and the two factors A and B are given as

$$A=\frac{2}{(N_{\rm m}-N_{\rm b}-1)\,(N_{\rm m}-N_{\rm b}-4)}, \tag{4.7}$$

$$B=\frac{N_{\rm m}-N_{\rm b}-2}{(N_{\rm m}-N_{\rm b}-1)\,(N_{\rm m}-N_{\rm b}-4)}. \tag{4.8}$$

As only a limited set of synthetic catalogues — the MINERVA HOD samples discussed in Section 4.3 — is available for the model testing in Section 5.2, a smooth and non-singular estimate of the covariance matrix by theoretical modelling of the data covariance and its inverse is derived in Section 4.2.

Our model does not take the survey selection function into account so that for the final BOSS sample we base the covariance estimate on the sets of mocks described in Section 4.5. As these sets are large, the correction factors for the covariance of the $P_{3\mathrm{w},i}(k)$ measurements and the fitted parameters, listed in Tables 4.1 and 4.2, respectively, are small despite the large number of measurement bins used.

4.2 Theoretical Gaussian covariance matrices for tests of redshift-space clustering models

The theoretical framework presented in this section relies on the Gaussian approximation for the likelihood, which was found to be sufficient for clustering experiments in the linear and quasi-linear regime (Manera *et al.*, 2012). This work was published in Grieb *et al.* (2016a) and all figures and tables in this section and most of the text are borrowed from this paper. The theoretical modelling of the anisotropic clustering covariance has not been studied in detail, in contrast to the covariance of the angle-averaged clustering statistics (Feldman *et al.*, 1994; Smith *et al.*, 2008; Sánchez *et al.*, 2008) or the covariance of angular 2-point statistics (Crocce *et al.*, 2011). Our theoretical estimate aims at the model verification using synthetic catalogues with periodic boundary conditions, giving explicit formulae for the covariance of the multipoles as well as clustering wedges of the redshift-space galaxy PS and 2PCF for cubic mock catalogues. For RSD and BAO studies, usually distance scales between 30 and 180 $h^{-1}\,\mathrm{Mpc}$ and wavenumbers between 0.02 and 0.2 $h\,\mathrm{Mpc}^{-1}$ are considered as relevant (corresponding to the quasi-linear regime of gravitational evolution). The accuracy of the theoretical estimates is validated with the MINERVA simulations. The incorporation of the effects of a non-trivial survey geometry (described by the angular and radial selection of galaxies) is left for future work, which is discussed in Section 4.4.4. Also no supersurvey modes have been taken into account for the modelling of the clustering covariance, in agreement with the absence of those modes in our simulations.[4]

4.2.1 Modelling of the covariance of galaxy two-point clustering measurements

Fourier space: the power spectrum covariance

The assumption made for the likelihood $\mathscr{L}$ of the clustering statistics given by equation (4.3) — that the 2D power spectrum follows a Gaussian distribution — leads to the following relation

[4] Besides other effects, supersurvey modes alter the local clustering amplitude σ_8 (and thus the zero mode of the initial conditions) of a realization in a stochastic way. Such effects can be modelled using the 'separate-universe' approach (Sirko, 2005; Wagner *et al.*, 2015).

for the PS mode-by-mode covariance (see Feldman *et al.*, 1994, for the monopole),

$$\mathrm{Cov}\left[P(\boldsymbol{k}),P(\boldsymbol{k}')\right] = \frac{2\,(2\pi)^3}{V_\mathrm{s}}\delta_\mathrm{D}(\boldsymbol{k}-\boldsymbol{k}')\left[P(k,\mu)+S\right]^2, \tag{4.9}$$

where V_s is the volume of the sample and S is a shot-noise contribution that takes into account that the discrete galaxy positions of a given survey are sampled by a Poisson point process as discussed in Section 3.2.1. In the case of a periodic box, the volume is given by $V_\mathrm{s} = L^3$, where L is the side length of the box, and the shot noise is estimated from the inverse of the average number density, $S = \bar{n}^{-1}$. For a survey with a selection function given by a random catalogue with varying number density, the effective volume has to be estimated from the window function (Bernstein, 1994; de Putter *et al.*, 2012) and the shot noise as in equation (3.17). The Dirac delta function reflects the independence of Fourier modes for a random field with statistical translational invariance and in the absence of gravitational mode coupling. The anisotropy of the PS is taken into account by the dependency of $P(k,\mu)$ on the LoS parameter.

This ansatz for the covariance neglects the trispectrum contribution (Scoccimarro *et al.*, 1999) and the supersample covariance (SSC; also called *beat coupling*). The modelling of these effects is beyond the scope of this thesis and, thus, their analysis is left to potential future improvements of the modelling that are discussed in Section 4.4.4.

The theoretical covariance matrix for binned anisotropic PS measurements is obtained by averaging per-mode equations such as (4.9) over the number of independent Fourier modes $\boldsymbol{k}$ that contribute to each wavenumber bin. Just as in Section 3.3.5, we assume the bins to be centred at k_i with width Δk so that their volume is $V_{k_i} = 4\pi[(k_i+\Delta k/2)^3 - (k_i-\Delta k/2)^3]/3$. The bin-average is easily performed by integration in spherical coordinates, (k,θ,φ), so that $\delta_\mathrm{D}(\boldsymbol{k}-\boldsymbol{k}') = \delta_\mathrm{D}(k-k')\delta_\mathrm{D}(\theta-\theta')\delta_\mathrm{D}(\varphi-\varphi')/(2\pi k^2\sin\theta)$, and making use of the following relation:

$$\begin{aligned}\frac{1}{V_{k_i}}\int_{V_{k_i}}\mathrm{d}^3k\,\frac{1}{V_{k_j}}\int_{V_{k_j}}\mathrm{d}^3k'\;\mathrm{Cov}\left[P(\boldsymbol{k}),P(\boldsymbol{k}')\right] &= \frac{2\,(2\pi)^5}{V_{k_i}\,V_{k_j}\,V_\mathrm{s}}\int_{k_i-\Delta k/2}^{k_i+\Delta k/2}k^2\,\mathrm{d}k\int_{k_j-\Delta k/2}^{k_j+\Delta k/2}(k')^2\,\mathrm{d}k' \\ &\times\int_{-\pi/2}^{\pi/2}\sin(\theta)\,\mathrm{d}\theta\int_{-\pi/2}^{\pi/2}\sin(\theta')\,\mathrm{d}\theta'\,\frac{\delta_\mathrm{D}(k-k')\delta_\mathrm{D}(\theta-\theta')}{2\pi k^2\sin(\theta)}\left[P(k,\cos(\theta))+S\right]^2.\end{aligned} \tag{4.10}$$

Multipole expansion of the power spectrum covariance. A useful definition is the multipole expansion of the per-mode covariance given by

$$\sigma^2_{\ell_1\ell_2}(k) \equiv \frac{(2\ell_1+1)\,(2\ell_2+1)}{V_\mathrm{s}}\int_{-1}^{1}\left[P(k,\mu)+S\right]^2\mathcal{L}_{\ell_1}(\mu)\,\mathcal{L}_{\ell_2}(\mu)\,\mathrm{d}\mu. \tag{4.11}$$

The normalization was chosen such that the pre-factor of $\sigma^2_{00}(k)$ is the usual $2/V_\mathrm{s}$ for an isotropic PS.

Replacing $P(k,\mu)$ by its multipole expansion, $P(k,\mu) = \sum_\ell P_\ell(k)\mathcal{L}_\ell(\mu)$, we find

$$\sigma^2_{\ell_1\ell_2} = \frac{(2\ell_1+1)\,(2\ell_2+1)}{V_\mathrm{s}} \sum_{\ell_3=0}^{\infty}\sum_{\ell_4=0}^{\ell_3} \left[P_{\ell_4}(k) + S\,\delta_{\ell_4 0}\right]\left[P_{\ell_3-\ell_4}(k) + S\,\delta_{(\ell_3-\ell_4)0}\right] \times \int_{-1}^{1} \mathcal{L}_{\ell_1}(\mu)\,\mathcal{L}_{\ell_2}(\mu)\,\mathcal{L}_{\ell_4}(\mu)\,\mathcal{L}_{\ell_3-\ell_4}(\mu)\,\mathrm{d}\mu. \quad (4.12)$$

At this point, we use the expansion of a product of two Legendre polynomials by use of Wigner $3j$-symbols (Rotenberg *et al.*, 1959),[5]

$$\mathcal{L}_{\ell_1}(\mu)\mathcal{L}_{\ell_2}(\mu) = \sum_{\ell=|\ell_1-\ell_2|}^{\ell_1+\ell_2} A^{\ell}_{\ell_1\ell_2}\,\mathcal{L}_\ell(\mu), \quad \text{where} \quad A^{\ell}_{\ell_1\ell_2} \equiv (2\ell+1)\begin{pmatrix}\ell_1 & \ell_1 & \ell\\ 0 & 0 & 0\end{pmatrix}^2 \quad (4.13)$$

and the orthogonality of the $\mathcal{L}_\ell(x)$, yielding

$$\int_{-1}^{1} \mathcal{L}_{\ell_1}(\mu)\mathcal{L}_{\ell_2}(\mu)\mathcal{L}_{\ell_4}(\mu)\mathcal{L}_{\ell_3-\ell_4}(\mu)\,\mathrm{d}\mu = 2\sum_{\ell=\max(|\ell_1-\ell_2|,|2\ell_4-\ell_3|)}^{\min(\ell_1+\ell_2,\ell_3)} \frac{A^{\ell}_{\ell_1\ell_2}}{2\ell+1}\frac{A^{\ell}_{\ell_4(\ell_3-\ell_4)}}{2\ell+1}. \quad (4.14)$$

Inserting this back into the expression in equation (4.11) gives

$$\sigma^2_{\ell_1\ell_2}(k) = \frac{2\,(2\ell_1+1)\,(2\ell_2+1)}{V_\mathrm{s}} \sum_{\ell_3=0}^{\infty}\sum_{\ell_4=0}^{\ell_3} \left[P_{\ell_4}(k) + S\,\delta_{\ell_4 0}\right]\left[P_{\ell_3-\ell_4}(k) + S\,\delta_{(\ell_4-\ell_3)0}\right] \times \sum_{\ell=\max(|\ell_1-\ell_2|,|2\ell_4-\ell_3|)}^{\min(\ell_1+\ell_2,\ell_3)} \frac{A^{\ell}_{\ell_1\ell_2}}{2\ell+1}\frac{A^{\ell}_{\ell_4(\ell_3-\ell_4)}}{2\ell+1}, \quad (4.15)$$

where $\delta_{\ell 0}$ reflects the fact that the shot noise contributes only to terms with the power spectrum monopole.

Covariance of power spectrum multipoles. First, we consider PS Legendre moments measured in the wavenumber bins defined above. Their theoretical covariance matrix $C_{\ell_1\ell_2 ij}$ can be

[5] An alternative expression for the product of two Legendre polynomials can be found in Bailey (1933),

$$A^{\ell_1+\ell_2-2\ell}_{\ell_1\ell_2} = \frac{2\ell_1+2\ell_2-4\ell+1}{2\ell_1+2\ell_2-2\ell+1}\frac{G_{\ell_1-\ell}\,G_\ell\,G_{\ell_2-\ell}}{G_{\ell_1+\ell_2-\ell}},$$
$$\text{where} \quad G_\ell \equiv \frac{\prod_{p=1}^{2\ell-1} p}{\ell!}.$$

This expansion has been used recently in Wilson *et al.* (2015) for an FFT-based treatment of the window function effect, cf. Section 3.4.

obtained by the following integration over the bins:

$$\mathrm{Cov}\left[P^i_{\ell_1}, P^j_{\ell_2}\right] = \frac{(2\ell_1+1)\,(2\ell_2+1)}{V_{k_i}\,V_{k_j}} \times \int_{V_{k_i}}\int_{V_{k_j}} \mathrm{Cov}\left[P(\boldsymbol{k}), P(\boldsymbol{k}')\right]\,\mathcal{L}_{\ell_1}(\cos(\theta))\,\mathcal{L}_{\ell_2}(\cos(\theta'))\,\mathrm{d}^3k'\;\mathrm{d}^3k\,. \quad (4.16)$$

This equation expressed in spherical coordinates as in equation (4.10) reads

$$\mathrm{Cov}\left[P^i_{\ell_1}, P^j_{\ell_2}\right] = \frac{2\,(2\ell_1+1)\,(2\ell_2+1)\,(2\pi)^4}{V_{k_i}V_{k_j}\,V_\mathrm{s}} \int_{k_i-\Delta k/2}^{k_i+\Delta k/2} k^2\,\mathrm{d}k \int_{-1}^{1} \mathrm{d}\mu\,\left[P(k,\mu)+S\right]^2\,\mathcal{L}_{\ell_1}(\mu)\,\mathcal{L}_{\ell_2}(\mu), \quad (4.17)$$

where we already evaluated the Dirac delta functions. Using the definition of $\sigma^2_{\ell_1\ell_2}$, the bin-averaged PS multipole covariance $C^P_{\ell_1\ell_2}(k_i,k_j) \equiv \mathrm{Cov}\left[P^i_{\ell_1}, P^j_{l_2}\right]$ yields

$$C^P_{\ell_1\ell_2}(k_i,k_j) = \frac{2\,(2\pi)^4}{V^2_{k_i}}\delta_{ij} \int_{k_i-\Delta k/2}^{k_i+\Delta k/2} \sigma^2_{\ell_1\ell_2}(k)\,k^2\,\mathrm{d}k. \quad (4.18)$$

This expression was already given in Taruya *et al.* (2010, Appendix C), but was not averaged over wavenumber bins. They used these terms up to $\ell \leq 2$ using the linear input power spectrum without validation.

Using the expansion of equation (4.15), the monopole covariance is found to be given by

$$C^P_{00}(k_i,k_j) = \frac{4\,(2\pi)^4}{V^2_{k_i}\,V_\mathrm{s}}\delta_{ij} \sum_\ell \frac{1}{2\ell+1} \int_{k_i-\Delta k/2}^{k_i+\Delta k/2} k^2\,\left[P_\ell(k)+S\,\delta_{\ell 0}\right]^2\,\mathrm{d}k. \quad (4.19)$$

This shows that the naive guess that the monopole covariance would only be given by the monopole power spectrum term, $(P_0(k)+S)^2$, is not correct. Instead, the monopole covariance has contributions from all higher-order multipoles. In the same way, equation (4.18) shows that the covariance of higher-order multipoles does not vanish — even though the input power spectrum is only modelled up to $\ell = 4$ (see Section 4.3.3) — as lower-order covariance terms contribute as well, always dominated by the monopole covariance term. This is discussed also in Yoo & Seljak (2015, appendix A) and will be important later on as well.

Covariance of power spectrum wedges. Second, we consider clustering wedges $P^{\mu_2}_{\mu_1}(k)$ as defined by equation (3.4). We denote the measurement of $P^{\mu+\Delta\mu}_{\mu}$ in the wavenumber bin centred around k_i as P^i_μ. Then, the integration over the wavenumber bins can be written as

$$\mathrm{Cov}\left[P^i_\mu, P^j_{\mu'}\right] = \frac{(2\pi)^2}{V_{k_i}\,V_{k_j}\,(\Delta\mu)^2} \int_{k_i-\Delta k/2}^{k_i+\Delta k/2} k^2 \int_{k_j-\Delta k/2}^{k_j+\Delta k/2} (k')^2 \times \int_{\mu\leq|\tilde{\mu}|\leq\mu+\Delta\mu}\int_{\mu'\leq|\tilde{\mu}'|\leq\mu'+\Delta\mu} \mathrm{Cov}\left[P(\boldsymbol{k}), P(\boldsymbol{k}')\right]\;\mathrm{d}\tilde{\mu}\,\mathrm{d}\tilde{\mu}'\,\mathrm{d}k'\,\mathrm{d}k, \quad (4.20)$$

using an integration scheme similar to equation (4.10), restricted to the volume of each wedge, $\Delta\mu\, V_{k_i}$. The evaluation of the Dirac delta functions in $\mathrm{Cov}[P(\boldsymbol{k}), P(\boldsymbol{k}')]$ yields the theoretical covariance of the bin-averaged wedges, $C^P_{\mu\mu'}(k_i, k_j) \equiv \mathrm{Cov}\left[P^i_\mu, P^j_{\mu'}\right]$ to be given by

$$C^P_{\mu\mu'}(k_i, k_j) = \frac{4\,(2\pi)^4}{V_{k_i}^2\, V_\mathrm{s}\,(\Delta\mu)^2}\delta_{ij}\,\delta_{\mu\mu'}\int_{k_i-\Delta k/2}^{k_i+\Delta k/2} k^2\,\mathrm{d}k\int_{\mu}^{\mu+\Delta\mu}\left[P(k,\tilde{\mu})+S\right]^2\,\mathrm{d}\tilde{\mu}, \tag{4.21}$$

where $\delta_{\mu\mu'}$ reflects that the wedges are discrete and non-intersecting. An additional factor of 2 comes from the fact that the symmetry in $\mu \to -\mu$ has been used to simplify the integration over the μ range into a single contiguous interval.

In contrast to the multipoles, different Fourier space wedges are not correlated in our linear Gaussian theory, even after integration over the wavenumber bin.

Configuration Space: the 2PCF Covariance

First, the covariance of the (unbinned) 2PCF multipole moments is derived from the results in Fourier space. The Fourier inverse of equation (2.37) yields

$$\mathrm{Cov}\left[\xi_{\ell_1}(\boldsymbol{s}), \xi_{\ell_2}(\boldsymbol{s}')\right] = \frac{1}{(2\pi)^6}\int \mathrm{d}^3k \int \mathrm{d}^3k'\ \mathrm{Cov}\left[P_{\ell_1}(\boldsymbol{k}), P_{\ell_2}(\boldsymbol{k}')\right]\ \mathrm{e}^{\mathrm{i}\boldsymbol{k}\cdot\boldsymbol{s}}\,\mathrm{e}^{\mathrm{i}\boldsymbol{k}'\cdot\boldsymbol{s}'}, \tag{4.22}$$

where the covariance of the power spectrum multipoles is given by

$$\mathrm{Cov}\left[P_{\ell_1}(\boldsymbol{k}), P_{\ell_2}(\boldsymbol{k}')\right] = (2\pi)^3\delta_\mathrm{D}(\boldsymbol{k}-\boldsymbol{k}')\,\sigma^2_{\ell_1\ell_2}(k), \tag{4.23}$$

using the definition of the per-mode multipole covariance as in equation (4.11).

The resulting expression for the covariance of 2PCF multipoles is

$$\mathrm{Cov}\left[\xi_{\ell_1}(s), \xi_{\ell_2}(s')\right] = \frac{1}{(2\pi)^3}\int \sigma^2_{\ell_1\ell_2}(k)\,\mathrm{e}^{\mathrm{i}\boldsymbol{k}\cdot\boldsymbol{s}}\,\mathrm{e}^{\mathrm{i}\boldsymbol{k}\cdot\boldsymbol{s}'}\,\mathrm{d}^3k\,, \tag{4.24}$$

which can be simplified by use of the same transformation as in equation (3.6) as

$$\mathrm{Cov}\left[\xi_{\ell_1}(s), \xi_{\ell_2}(s')\right] = \frac{\mathrm{i}^{\ell_1+\ell_2}}{2\pi^2}\int_0^\infty \sigma^2_{\ell_1\ell_2}(k)\,j_{\ell_1}(ks)\,j_{\ell_2}(ks')\,k^2\,\mathrm{d}k. \tag{4.25}$$

This equation was already given in an almost identical form by White *et al.* (2015), but the authors did not explicitly include the shot-noise contribution that enters $\sigma^2_{\ell_1\ell_2}(k)$.

The covariance of the 2PCF multipoles. The bin-averaged 2PCF multipole covariance matrix, $C^\xi_{\ell_1\ell_2}(s_i, s_j) \equiv \mathrm{Cov}\left[\xi^i_{\ell_1}, \xi^j_{l_2}\right]$ is then given by the volume average over the distance bin around s_i with volume $V_{s_i} = 4\pi\left(s^3_{i,\mathrm{max}} - s^3_{i,\mathrm{min}}\right)/3$. This bin average is necessary in order not to overestimate the 2PCF covariance (Cohn, 2006; Sánchez *et al.*, 2008). The volume average is absorbed in the bin-averaged spherical Bessel functions defined by

$$\bar{\jmath}_\ell(ks_i) \equiv \frac{4\pi}{V_{s_i}}\int_{s_i-\Delta s/2}^{s_i+\Delta s/2} s^2\,j_\ell(ks)\,\mathrm{d}s. \tag{4.26}$$

Thus, the elements of the resulting covariance matrix can be written as

$$C^{\xi}_{\ell_1\ell_2}(s_i, s_j) = \frac{\mathrm{i}^{\ell_1+\ell_2}}{2\pi^2} \int_0^\infty k^2\, \sigma^2_{\ell_1\ell_2}(k)\, \bar{\jmath}_{\ell_1}(ks_i)\, \bar{\jmath}_{\ell_2}(ks_j)\, \mathrm{d}k. \tag{4.27}$$

This relation shows that the configuration space multipoles pick up the same 'mixing' contributions to their covariance as the power spectrum multipoles, but in addition all wavenumbers k with non-vanishing power are mixed as well by the integration over the Bessel functions.

The covariance of the 2PCF wedges. We consider 2PCF clustering wedges as defined in equation (3.7) and denote the measurement of $\xi^{\mu+\Delta\mu}_{\mu}$ in the distance bin around s_i by ξ^i_μ. Using the relation between wedges and Legendre moments given in equation (3.8), the covariance of the configuration space wedges is given by

$$\begin{aligned}\mathrm{Cov}\left[\xi^i_\mu, \xi^j_{\mu'}\right] = \frac{1}{V_{s_i}\, V_{s_j}\, (\Delta\mu)^2} \int_{s_i-\Delta s/2}^{s_i+\Delta s/2} s^2\, \mathrm{d}s \int_{s_j-\Delta s/2}^{s_j+\Delta s/2} (s')^2\, \mathrm{d}s' \int_{\mu_1}^{\mu_2} \mathrm{d}\tilde{\mu} \int_{\mu'}^{\mu'+\Delta\mu} \mathrm{d}\tilde{\mu}' \\ \times \sum_{\ell_1,\ell_2} \mathrm{Cov}\left[\xi_{\ell_1}(s), \xi_{\ell_2}(s')\right]\, \mathcal{L}_{\ell_1}(\mu)\, \mathcal{L}_{\ell_2}(\mu').\end{aligned} \tag{4.28}$$

By inserting the covariance of the multipoles from equation (4.27), the covariance of the 2PCF clustering wedges, $C^{\xi}_{\mu\mu'}(s_i, s_j) \equiv \mathrm{Cov}\left[\xi^i_\mu, \xi^j_{\mu'}\right]$, is found to be

$$C^{\xi}_{\mu\mu'}(s_i, s_j) = \sum_{\ell_1,\ell_2} \frac{\mathrm{i}^{\ell_1+\ell_2}}{2\pi^2} \bar{\mathcal{L}}_{\ell_1,\mu}\, \bar{\mathcal{L}}_{\ell_2,\mu'} \int_0^\infty k^2\, \sigma^2_{\ell_1\ell_2}(k)\, \bar{\jmath}_{\ell_1}(ks_i)\, \bar{\jmath}_{\ell_2}(ks_j)\, \mathrm{d}k, \tag{4.29}$$

where the wedge-averaged Legendre polynomials $\bar{\mathcal{L}}_{\ell,\mu_1,\mu_2}$ are given by equation (3.9).

4.3 The Minerva simulations and synthetic HOD catalogues

The theoretical covariance matrix discussed in this chapter is verified on quasi-linear scales using a set of N-body simulations. The volume of each realization is large enough so that the anisotropic galaxy clustering can be measured with a signal-to-noise and precision comparable to present-day galaxy redshift surveys. The haloes of the simulations have been populated with galaxies by use of the halo occupation distribution (HOD; Peacock & Smith, 2000; Scoccimarro *et al.*, 2001; Berlind & Weinberg, 2002) technique in order to mimick the clustering statistics of real surveys such as BOSS. Besides the covariance tests, these simulations are used to validate the clustering model of Chapter 5. For that purpose, the covariance matrix is obtained with the theoretical description of this chapter as the covariance matrix estimated from the data cannot be inverted due to the small number of realizations.

Table 4.3 – The parameters of the HOD model of equations (4.30) to (4.32) defining our 'CMASS-like' galaxy sample at $z = 0.57$. All masses are in units of $h^{-1}\,\mathrm{M}_\odot$.

Parameter	$\log_{10}(M_{\min})$	$\log_{10}(M_0)$	$\log_{10}(M_1')$	$\sigma_{\log_{10} M}$	α
Value	13.07	13.1	14.2	0.347	0.8

4.3.1 The Minerva N-body simulations

The Minerva simulations are a set of 100 dark matter-(DM)-only realizations obtained using the N-body technique described in Section 2.4.3. We run this set of simulations using the N-body code Gadget[6] (Springel, 2005). Each realization uses 1000^3 DM particles in a cubic box of side length 1500 h^{-1} Mpc with periodic boundary conditions. The simulations were started at redshift $z_{\mathrm{ini}} = 63$ using 2LPT[7] initial conditions (Scoccimarro, 1998; Crocce *et al.*, 2006, cf., Section 2.4.1) based on an input power spectrum computed using Camb (Lewis *et al.*, 2000, see also Section 2.3.1). In order to remove transients in the clustering sourced by the initial distribution of particles, the initial positions have been obtained from a 'glass-like' distribution of points (Baugh *et al.*, 1995; White, 1994; L'Huillier *et al.*, 2014). The cosmological parameters for these simulations are given in Table 3.2 and are chosen to match the best-fitting ΛCDM model of the WMAP9 + BOSS DR9 $\xi(r)$ analysis (Sánchez *et al.*, 2013, Table I). The positions and velocities of the DM particles were stored for five output redshifts $z \in \{2.0, 1.0, 0.57, 0.3, 0\}$, jointly with the halo positions and velocities found by a friends-of-friend halo finder applied with the standard linking length equal to 0.2 of the mean inter-particle separation. The halo mass resolution is $m_{\min} = 2.67{\times}10^{12}\ h^{-1}\,\mathrm{M}_\odot$. In a post-processing step, SubFind (Springel *et al.*, 2001, section 4.2) was run to generate the final halo catalogues for each realization and output redshift. The mean halo mass function for $z = 0.57$ is plotted in the upper part of Figure 4.1.

4.3.2 The Minerva HOD galaxy catalogues

In order to generate a galaxy catalogue comparable to the CMASS sample of BOSS, we populated the haloes and subhaloes of each simulation with galaxies according to an HOD model with suitable parameters. In such HOD models the average number N of synthetic galaxies in haloes of mass M is given by the mean occupation function $N(M)$. This function is parametrized as in Zheng *et al.* (2007),

$$\langle N(M)\rangle = \langle N_{\mathrm{cen}}(M)\rangle + \langle N_{\mathrm{sat}}(M)\rangle, \tag{4.30}$$

decomposing the number of galaxies into contributions from central and satellite galaxies. The contribution to the mean occupation function by the centrals is given by

$$\langle N_{\mathrm{cen}}(M)\rangle = \frac{1}{2}\left[1 + \mathrm{erf}\left(\frac{\log M - \log M_{\min}}{\sigma_{\log M}}\right)\right], \tag{4.31}$$

[6]The latest public release is Gadget-2 which is available at http://www.gadgetcode.org/.

[7]A 2LPT code for generating initial conditions is available at http://cosmo.nyu.edu/roman/2LPT/.

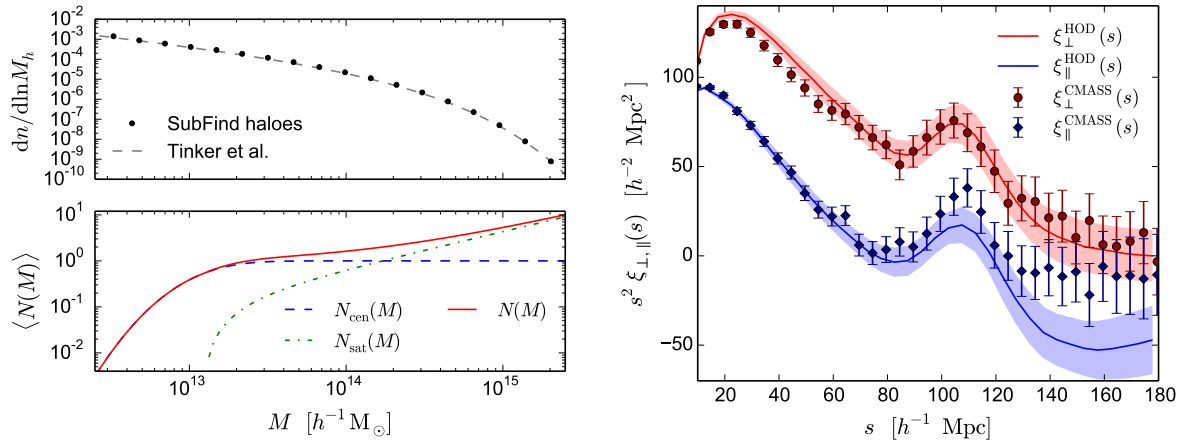

Figure 4.1 – *Upper left-hand panel:* the mean halo mass function of the SubFind output for our Minerva snapshots at $z = 0.57$ (black points) and the prediction (gray dashed line) based on the recipe of Tinker *et al.* (2008). *Lower left-hand panel:* the mean galaxy occupation function as defined in equation (4.30), $\langle N(M)\rangle$ (red solid line), and its decomposition into central (blue dashed line) and satellite components (green dotted line) for the parameters given in Table 4.3. *Right-hand panel:* Comparison of the 2PCF clustering wedges $\xi_\perp^{\rm HOD}(s)$ and $\xi_\parallel^{\rm HOD}(s)$ of our HOD sample (red and blue solid lines, respectively, standard deviation over our 100 realizations indicated by the filled region) compared with the corresponding measurements from the CMASS sample of BOSS DR11 (transverse wedge: circles, parallel wedge: diamonds) by Sánchez *et al.* (2014).

modelling the scatter between the galaxy luminosity and mass with a smooth cut-off at masses of $M_{\rm min}$ described by an error function with relative scale $\sigma_{\log M}$. Te satellites contribution is set to

$$\langle N_{\rm sat}(M)\rangle = \langle N_{\rm cen}(M)\rangle \left(\frac{M - M_0}{M_1'}\right)^\alpha , \tag{4.32}$$

so that only haloes already populated by a central galaxy have satellites assigned to them. The number of satellite galaxies is sampled with a Poisson distribution with the mean set by equation (4.32) where the cut-off mass scale is M_0, the normalization mass scale is M_1', and the power-law slope is α. The positions and velocities of satellite galaxies are drawn from random DM particles associated with the host halo, whereas the position and velocity of the central galaxy are derived from the most-bounded DM particle of the halo.

The Minerva galaxy catalogues are generated at a redshift of $z = 0.57$, the mean redshift of the BOSS CMASS sample, using the HOD parameters given in Table 4.3. The resulting mean galaxy occupation function is shown in the lower left-hand panel of Figure 4.1. The final synthetic galaxy catalogues have a mean galaxy density of $\bar{n} \approx 4 \times 10^{-4}\ h^3\,{\rm Mpc}^{-3}$ and a linear bias of $b \simeq 2$ relative to the DM density field of the simulations. Using the ratio of the redshift- and real-space monopole of the HOD sample at linear separation scales, we find the Kaiser factor (cf., Section 2.4.2) to be $S = 1.28$, in perfect agreement with its theoretical prediction given by the growth-rate factor of equation (2.64) for the Minerva cosmology, $f(z = 0.57) = 0.76$, and the linear galaxy bias of the synthetic sample. The agreement between the anisotropic clustering of the HOD galaxy sample and the CMASS sample of BOSS DR11 is shown in the right-hand

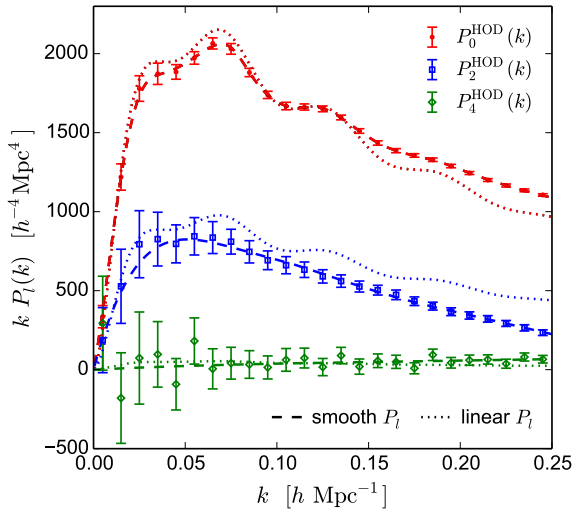

Figure 4.2 – Comparison of the mean power spectrum multipoles of our HOD sample (points) with the PS multipoles, $P_l^{\rm lin}(k)$ (dotted lines), of the linear-theory predictions given by equation (4.33), and the smoothed interpolation, $P_l^{\rm smooth}(k)$ (dashed lines). Both the linear and smoothed multipoles are taken as input for linear and non-linear predictions of the Gaussian covariance.

panel of Figure 4.1 comparing the 2PCF clustering wedges of both samples.

4.3.3 The LoS-dependent power spectrum

The theoretical prediction for the covariance matrix relies on an estimate for the anisotropic power spectrum, which ideally is also given by a theoretical recipe. As the simplest case, we assume a linear prediction for the 2D galaxy power spectrum where redshift-space anisotropies are caused by the linear Kaiser effect (Kaiser, 1987, see also Section 2.4.2),

$$P^{\rm lin}(k,\mu) = b^2 P_{\rm L}(k)\,(1+\beta^2\mu^2)^2, \tag{4.33}$$

where $P_{\rm L}(k)$ is the linear matter power spectrum (cf., Section 2.3.1) predicted by CAMB for the redshift of the sample, $z_{\rm eff} = 0.57$, and b is the linear galaxy bias. With these assumptions, the only non-vanishing PS multipoles — the Legendre moments $P_\ell(k)$ of the anisotropic power spectrum as defined in equation (3.3) — are the monopole, quadrupole, and hexadecapole.

Figure 4.2 shows the mean PS monopole, quadrupole and hexadecapole measured from the MINERVA simulations. The linear theory definition of equation (4.33), shown by the dotted lines, gives an inadequate description of the anisotropic galaxy power spectrum in the quasi-linear regime. To improve upon this description we performed a smoothing spline interpolation of our mean PS multipole measurements, $P_l^{\rm smooth}(k)$, shown by the dashed lines in Figure 4.2, to create a noiseless non-linear power spectrum that can be used for covariance predictions,

$$P^{\rm smooth}(k,\mu) = P_0^{\rm smooth}(k) + P_2^{\rm smooth}(k)\,\mathcal{L}_2(\mu) + P_4^{\rm smooth}(k)\,\mathcal{L}_4(\mu). \tag{4.34}$$

For the estimation of the smoothing length, we take the measured dispersion of the PS multipoles into account. The BAO wiggles in the smoothed quadrupole have been slightly damped by this procedure but, due to the small signal-to-noise ratio of the BAO feature in the quadrupole, this does not affect the predicted covariance.

In the same way as the linear model of equation (4.33), this ansatz also has only monopole, quadrupole and hexadecapole contributions by definition. Higher-order multipoles are negligible for $k \lesssim 0.25\ h\,\mathrm{Mpc}^{-1}$. In the following, we will use these two power spectrum models for the analysis and validation of our Gaussian covariance predictions (referred to as 'lin' and 'smooth', respectively).

4.4 Validation of the Gaussian prediction for the covariance matrix

In this section, the agreement between the theoretical covariance prediction and the results from the Minerva simulations described in Section 4.3 is discussed. Specifically, the Gaussian covariance prediction of Section 4.2.1 is verified on quasi-linear scales up to the uncertainty found in the estimates from the simulations to show that the predictions are precise enough to allow performance test of clustering+RSD models in Section 5.2.

In order to compare the theoretical predictions with the noisy estimates from the Minerva simulations, we chose two different binning configurations: one leading to an invertible covariance matrix (in case of multipoles up to the hexadecapole or three clustering wedges) denoted 'large' and one appropriate for fitting of CMASS-like measurements (for which the data covariance matrix obtained from 100 catalogues is singular) denoted 'small'. These binning choices, together with the resulting number of bins and the corresponding correction factors $(1 - D)$ as defined by equation (4.5) are listed in Table 4.1.

As the measurements of the redshift-space two-point clustering from the cubic simulations assume a global plane-parallel LoS along one of the axis of the simulation box ('distant-observer approximation'), the LoS is assumed to be along on the axes of the box ($i \in \{1, 2, 3\}$) and the LoS parameter is simply given by $\mu = k_i/|\boldsymbol{k}|$. Thus, the tensors $Q_\cdot$ defined in equation (3.39) are not needed to derive the power spectrum multipoles, $P_\ell(\boldsymbol{k})$ in equation (3.27), and one single FFT is sufficient for the estimator.[8] In order to reduce the level of noise in the mean and covariance of the measurements, we measure the two-point statistic of every realization three times by assuming the LoS to be parallel to each of the three different axes and then average the results.

Due to this averaging over the three LoS axes, the error on the covariance cannot easily be predicted analytically. Thus, we measure the error on the covariance matrix $\boldsymbol{C}^P$ as *jackknife* estimate from the same set of mock measurements,[9]

$$\left(\Delta C^P_{xyij}\right)^2 = \frac{N_\mathrm{m} - 1}{N_\mathrm{m}} \sum_m \left({}^{(m)}C^P_{xyij} - C^P_{xyij}\right)^2, \tag{4.35}$$

[8] Likewise, the estimator for the configuration space multipoles and wedges (Landy & Szalay, 1993) also simplifies as the volume of the wavenumber and separation distance bins can be easily calculated numerically so that no randoms have to be used. The configuration space measurements used for this thesis and the publication (Grieb *et al.*, 2016a) have been measured by Ariel Sánchez using his well-tested code (Sánchez *et al.*, 2013, 2014).

[9] The error on the covariance matrix of all configuration space measurements, C^ξ_{xyij}, are obtained in an analogous way.

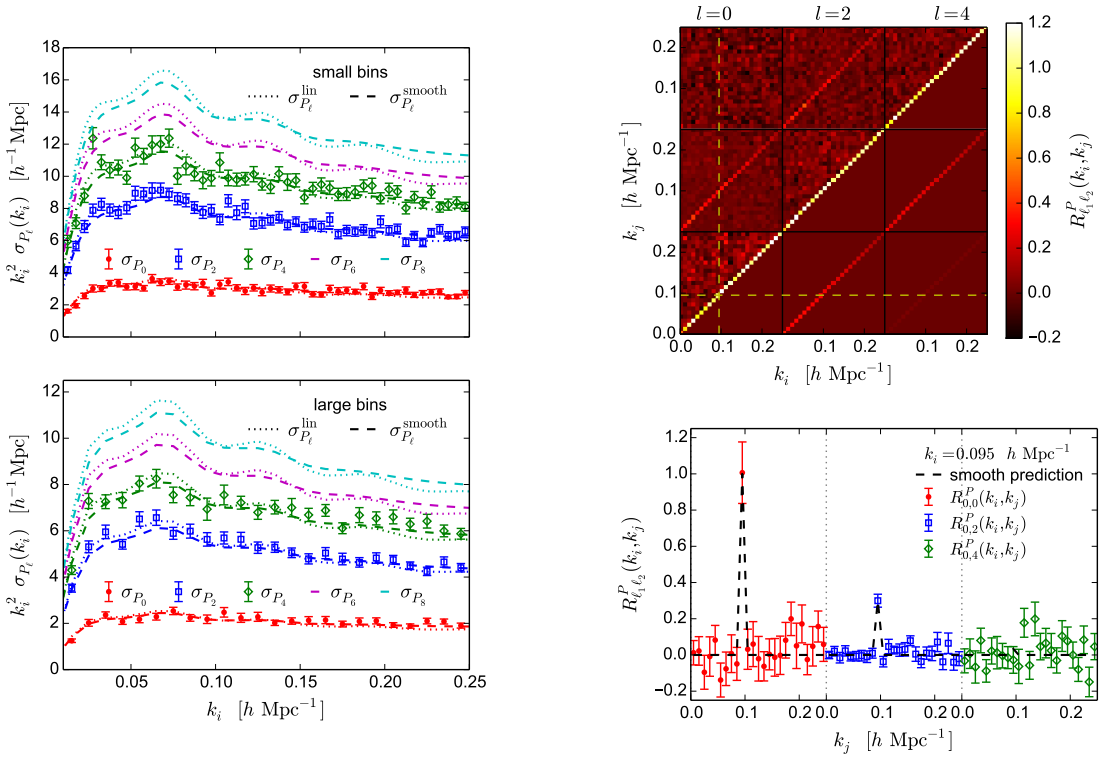

Figure 4.3 – *Left-hand panels:* Comparison of the dispersion of the PS multipoles, $\sigma_{P_\ell}(k_i)$, of our HOD realizations (points) with the Gaussian predictions from equation (4.18) for the small (upper panel) and large (lower panel) binning schemes. The dotted lines were derived using the linear model of equation (4.33), while the dashed lines correspond to the smoothed non-linear recipe of equation (4.34). *Upper right-hand panel:* The full correlation matrix of the PS multipoles, $R^P_{\ell_1\ell_2}(k_i,k_j) = C^P_{\ell_1\ell_2}(k_i,k_j)[\sigma_{P^{\rm smooth}_{\ell_1}}(k_i)\,\sigma_{P^{\rm smooth}_{\ell_2}}(k_j)]^{-1}$ (normalized by the theoretical prediction), shows a dominant diagonal and a significant cross-correlation between monopole and quadrupole (shown here: large binning). *Lower right-hand panel:* Cut through the correlation matrix for $\ell_1 = 0$ at $k_i = 0.095\ h\,{\rm Mpc}^{-1}$. The correlation contamination from physical effects not accounted for by our model and from noise is at the 15% level and well within the error bars.

where ${}^{(m)}C^P_{xyij}$ is the covariance estimate based on leaving out the mth realization,

$$ {}^{(m)}C^P_{xyij} = \frac{1}{N_{\rm m}-1}\sum_{n\neq m}\left({}^{(n)}P^i_x - \langle P^i_x\rangle\right)\left({}^{(n)}P^j_y - \langle P^j_y\rangle\right). \tag{4.36} $$

We checked that the jackknife estimate of the error on the covariance matrix for the case of a single LoS axis is in close agreement with the theoretical prediction given in Taylor *et al.* (2013).

4.4.1 Fourier-space covariance

The predicted covariance of the PS multipoles is compared against the data covariance measured from our 100 simulations in Figure 4.3. The dispersion of PS multipoles given by $\sigma^P_\ell(k_i) \equiv [C^P_{\ell\ell}(k_i,k_i)]^{1/2}$ for the small (large) binning setup is shown in the upper (lower) left-hand panel.

The error bars in these plots are given by $\Delta\sigma^P_\ell(k_i) \equiv [\Delta C^P_{\ell\ell}(k_i,k_i)]^{1/2}$, where $\Delta C^P_{\ell\ell}(k_i,k_i)$ is obtained with the jackknife estimator given in equation (4.35). The theoretical prediction is given for $\ell \leq 8$, but we measured $P_\ell(k)$ only for $\ell \leq 4$ due to the increasing noise.

The differences between linear and non-linear predictions (shown as dotted and dashed lines, respectively) are small for the dispersion of the monopole and quadrupole. For the hexadecapole, however, the dispersion is slightly overpredicted (underpredicted) for lower (higher) k by the linear theory curve, while a better match is obtained with the prediction from the smoothed multipole measurements. The predicted dispersion σ_{P_ℓ} is shown to increase with larger ℓ in both cases; this trend continues for higher-order multipoles as illustrated by the plotted predictions for σ_{P_6} and σ_{P_8} shown in Figure 4.3.

The measurements of the off-diagonal terms $C^P_{\ell_1,\ell_2}(k_i,k_j)$ suffer from low signal-to-noise and hence show larger relative scatter than the dispersion terms. To highlight the full covariance properties, we define the correlation matrix for PS multipoles as

$$R^P_{\ell_1\ell_2}(k_i,k_j) = C^P_{\ell_1\ell_2}(k_i,k_j)\,\left[\sigma_{P^{\rm smooth}_{\ell_1}}(k_i)\,\sigma_{P^{\rm smooth}_{\ell_2}}(k_j)\right]^{-1}. \tag{4.37}$$

Note that we normalized the data covariance by the theoretical dispersion obtained from the smooth non-linear power spectrum, $\sigma_{P^{\rm smooth}_\ell}$, in order to avoid further noise contamination.

The upper right-hand panel of Figure 4.3 represents the data correlation matrix (upper triangular part) and the theoretical prediction (lower triangular part) by colour; the lower right-hand panel shows a cut through this matrix. As the differences in our linear and non-linear modelling are much smaller than the variations in the measurements we find equally good agreement between the two predictions and our simulation data. The level of unaccounted data correlation in the off-diagonal terms is up to 20%, but this is most likely due to noise contamination as the error bars are of this size as well. Because of the scatter, we cannot identify additional contributions not included in our Gaussian ansatz in our covariance measurements. The noise level for the monopole is larger than for the higher-order multipoles due to the averaging over the LOS directions as this procedure reduces the noise of the RSD contributions but not the one of the real-space matter clustering.

Assuming three PS wedges, we label the covariance between the n-th and m-th wedge as $C^P_{3{\rm w},n,m}(k_i,k_j)$ and the dispersion as $\sigma^P_{3{\rm w},n}(k_i) \equiv [C^P_{3{\rm w},n,n}(k_i,k_i)]^{1/2}$ for clarity. For the case of two clustering wedges, we use the labels $\perp$ and $\parallel$. Figure 4.4 compares the predicted covariance of two (upper panels) and three (lower panels) wedges to the data covariance measured from our 100 realizations for the small (left-hand panels) and large (right-hand panels) binning configuration. In the linear-theory predictions, the BAO peaks and troughs in the dispersion are not as damped as in the data, especially for the most parallel wedges. Further, using linear theory the high-k dispersion of the intermediate and most perpendicular wedge is underpredicted ($k \gtrsim 0.15\ h$/Mpc). The agreement can be improved by use of the theory curves from the smoothed non-linear power spectrum.

We complete the PS wedge covariance analysis by showing the full correlation matrix compared to the non-linear prediction in Figure 4.5. Here we restrict the analysis to the 3-wedges case for brevity; the 2-wedges correlation matrix has similar properties. As described in Section 4.2.1, the predicted cross-correlation $C^P_{3{\rm w},n,m}(k_i,k_j)$ vanishes for $n \neq m$ or $k_i \neq k_j$. The data

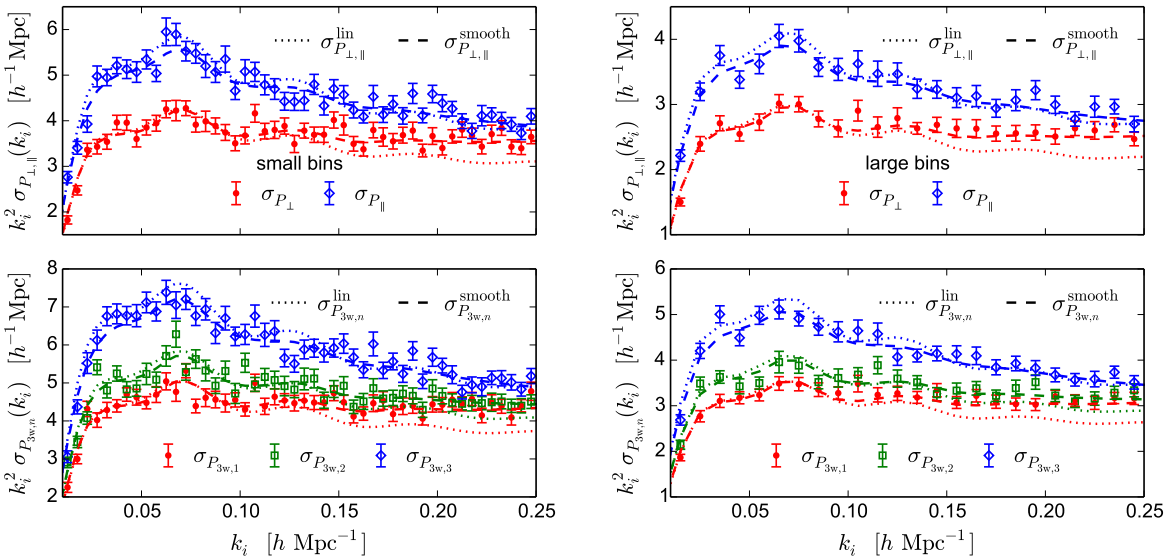

Figure 4.4 – Comparison of the dispersion of the PS wedges of our HOD realizations (points) for the small (left-hand panels) and large (right-hand panels) binning configuration with the Gaussian predictions from equation (4.21) for the linear (dotted lines) and smoothed non-linear (dashed lines) input power spectra. The upper and lower panels show the cases of two wedges, $\sigma_{P_{\perp,\parallel}}(k_i)$, and three wedges, $\sigma_{P_{3{\rm w},n}}(k_i)$, respectively.

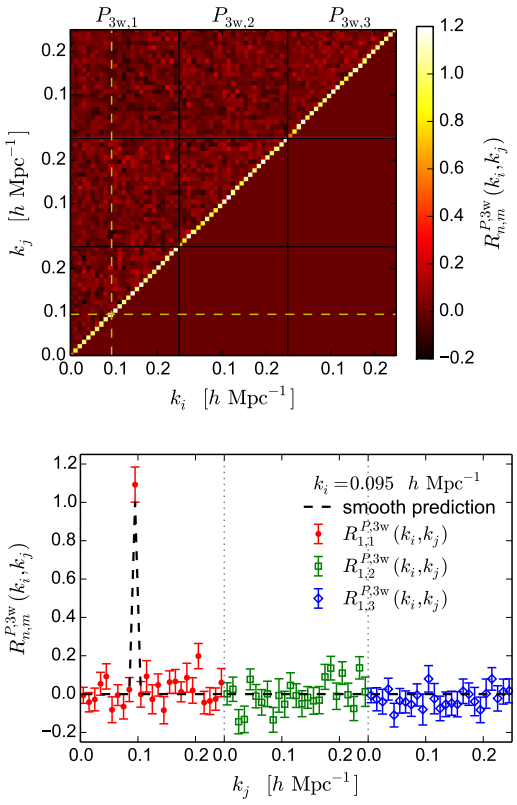

Figure 4.5 – *Upper panel:* The full correlation matrix of the PS wedges, $R_{3{\rm w},n,m}(k_i,k_j) = C^P_{3{\rm w},n,m}(k_i,k_j)[\sigma_{P^{\rm smooth}_{3{\rm w},n}}(k_i)\,\sigma_{P^{\rm smooth}_{3{\rm w},m}}(k_j)]^{-1}$, shows a dominant diagonal and no significant cross-correlation between wedges (shown here: large binning scheme). *Lower panel:* Cut through the correlation matrix for the most transverse wedge, $\xi_{3{\rm w},1}$, at $k_i = 0.095\ \ h\,{\rm Mpc}^{-1}$. The correlation contamination from physical effects not accounted for by our model and from noise is at the 15% level (same level as the error bars).

correlation matrix,

$$R_{3\mathrm{w},n,m}(k_i,k_j) = C^{P}_{3\mathrm{w},n,m}(k_i,k_j)\left[\sigma_{P^{\mathrm{smooth}}_{3\mathrm{w},n}}(k_i)\,\sigma_{P^{\mathrm{smooth}}_{3\mathrm{w},m}}(k_j)\right]^{-1}, \tag{4.38}$$

again normalized by the non-linear theoretical prediction, shows a level of unaccounted cross-correlation of up to 15%. As for the multipoles, this is most likely noise contamination and the scatter cannot be associated with any systematic deviations from our Gaussian model as the error bars estimated with the jackknife method are also of this size.

4.4.2 Configuration-space covariance

In configuration space, the covariance matrix is not dominated by the diagonal entries. The dispersion of the 2PCF multipoles, given by $\sigma^{\xi}_{\ell}(s_i) \equiv [C^{\xi}_{\ell\ell}(s_i,s_i)]^{1/2}$, contains the scaling of the covariance with scale. In the left-hand panels of Figure 4.6, the predicted dispersion of the 2PCF multipoles is compared to the data dispersion measured from our 100 simulations for the small (upper panel) and large (lower panel) binning setup. The difference between linear and non-linear predictions for the multipole covariance is negligible compared to the deviations between the measurements and the theory estimates. Those deviations are largely due to the low number of realizations and the fact that the Fourier transform to configuration space translates uncorrelated modes into highly correlated measurements of the binned anisotropic 2PCF. In contrast to the power spectrum case, the dispersion of higher-order multipole moments of the correlation function does not increase with ℓ. In fact, the left-hand panels of Figure 4.6 show that σ_{ξ_6} and σ_{ξ_8} follow a trend that is very similar in shape and amplitude to the quadrupole and hexadecapole dispersions.

The correlation between measurement bins is best illustrated by the full information encoded in the correlation matrix, which is defined in an analogous way to the case of PS multipoles,

$$R^{\xi}_{\ell_1\ell_2}(s_i,s_j) = C^{\xi}_{\ell_1\ell_2}(s_i,s_j)\left[\sigma_{\xi^{\mathrm{smooth}}_{\ell_1}}(s_i)\,\sigma_{\xi^{\mathrm{smooth}}_{\ell_2}}(s_j)\right]^{-1}, \tag{4.39}$$

using the non-linear prediction to normalize the matrix without introducing more noise. Cross-covariance terms, $C^{\xi}_{\ell_1\ell_2}(s_i,s_j)$, show a large scatter due to the low signal-to-noise of our measurements. We find that the differences in our linear and non-linear modelling are much smaller than the scatter in the measurements and thus conclude agreement between the different predictions and data on an equally good level.

In the upper right-hand panel of Figure 4.6, we show the structure in the data correlation matrix (upper triangular part) next to the theoretical prediction (lower triangular part). For a better visualization of the level of correlation, the lower panel shows a cut through the matrix. The prediction for the monopole, quadrupole and hexadecapole correlation is in very good agreement with the measurements, which show a slow decline of the correlation away from the diagonal of the matrix. We see however that the data cross-correlations between different multipole moments (especially between monopole and hexadecapole) are noisy, but the measured decline of correlation away from the diagonals of the sub-matrices is followed by the predictions.

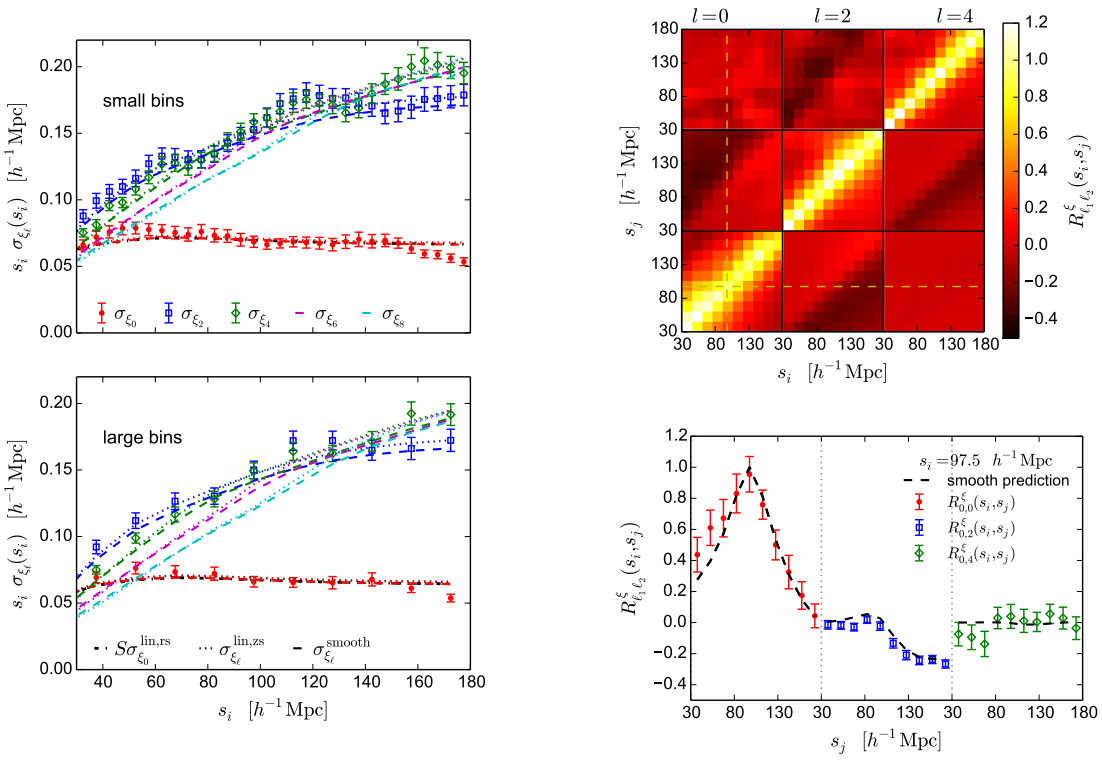

Figure 4.6 – *Left-hand panels:* Comparison of the dispersion of the 2PCF multipoles, $\sigma_{\xi_\ell}(s_i)$, of our HOD realizations (points) with the Gaussian predictions from equation (4.27) for the small (upper panel) and large (lower panel) binning configuration. The dotted and dashed lines correspond to the linear and smoothed non-linear input power spectra, respectively. In addition, we show the prediction of the real-space covariance as given in Sánchez *et al.* (2008), rescaled by the linear Kaiser factor $S = 1.28$ as dot-dashed black line. This curve cannot be distinguished from the Gaussian prediction for the monopole given in this work. *Upper right-hand panel:* In the full correlation matrix of the 2PCF multipoles, $R^{\xi}_{\ell_1\ell 2}(s_i,s_j) = C^{\xi}_{\ell_1\ell_2}(s_i,s_j)[\sigma_{\xi^{\rm smooth}_{\ell_1}}(s_i)\,\sigma_{\xi^{\rm smooth}_{\ell_2}}(s_j)]^{-1}$ (normalized by the theoretical prediction), shown here for the large binning, we see a high level of cross-correlation which is only slowly declining away from the main diagonals and the diagonals of the monopole-quadrupole and quadrupole-hexadecapole sub-matrices. The monopole and the hexadecapole are not correlated. *Lower right-hand panel:* Cut through the correlation matrix for $\ell_1 = 0$ at $s_i = 112.5\ h^{-1}\,\mathrm{Mpc}$. Although the correlation curves inferred from our simulations are noisy, they follow the same trends as out our theoretical predictions.

As for PS wedges, we label the covariance between the n-th and m-th 2PCF wedge as $C^{\xi}_{3\mathrm{w},n,m}(s_i,s_i)$ and the dispersion as $\sigma^{\xi}_{3\mathrm{w},n}(s_i) \equiv [C^{\xi}_{3\mathrm{w},n,n}(s_i,s_i)]^{1/2}$. In the case of two wedges only, we label each one with a subscript $\perp$ or $\parallel$.

In Figure 4.7, we plot the predicted dispersion of two (upper panels) and three (lower panels) wedge measurements in configuration space compared to the data dispersion measured from the Minerva simulation for the small (left-hand panels) and large (right-hand panels) binning configuration. In all cases, there is no significant difference between the linear and the non-linear predictions. The estimate from linear theory is always slightly larger than the estimate from the smoother interpolation of the measured power spectrum multipoles, but this difference is much smaller than the deviation between theory and data.

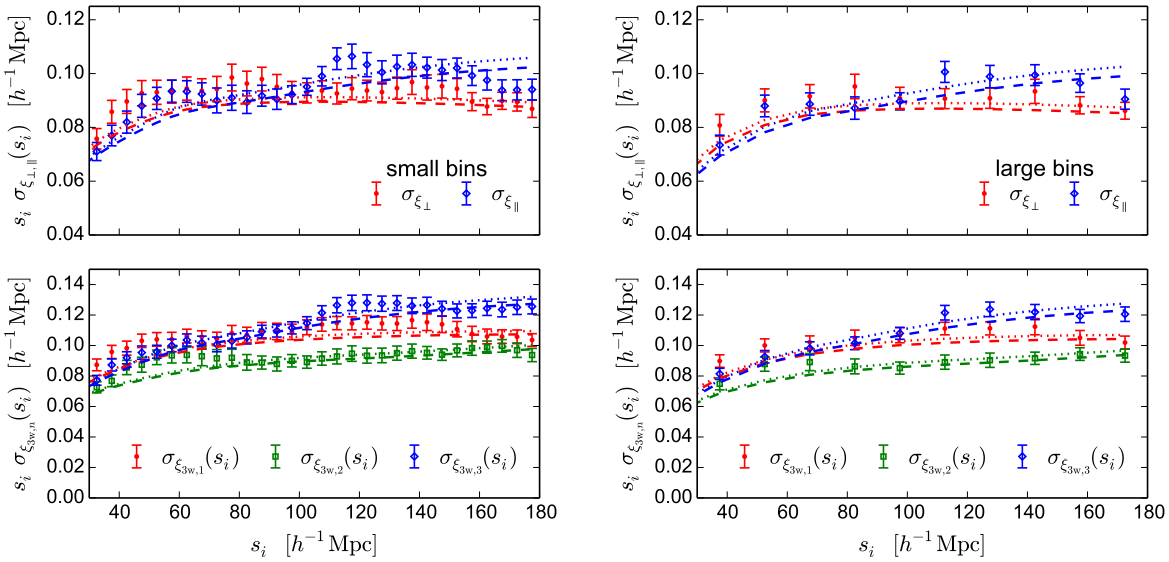

Figure 4.7 – Comparison of the dispersion of the 2PCF wedges of our HOD realizations (points) for the small (left-hand panels) and large (right-hand panels) binning configuration with the Gaussian predictions from equation (4.29). The dotted and dashed lines correspond to the linear and smoothed non-linear input power spectra, respectively. The upper and lower panels show the cases of two wedges, $\sigma_{\xi_{\perp,\parallel}}(s_i)$, and three wedges, $\sigma_{\xi_{3w,n}}(s_i)$, respectively.

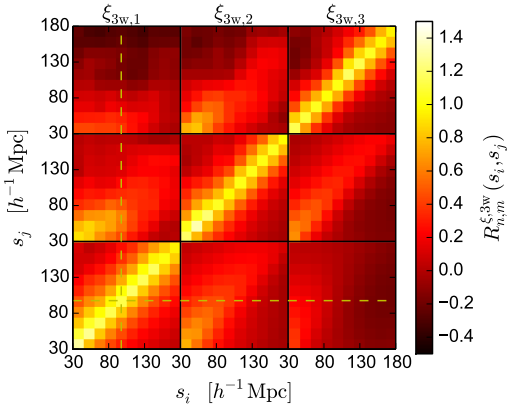

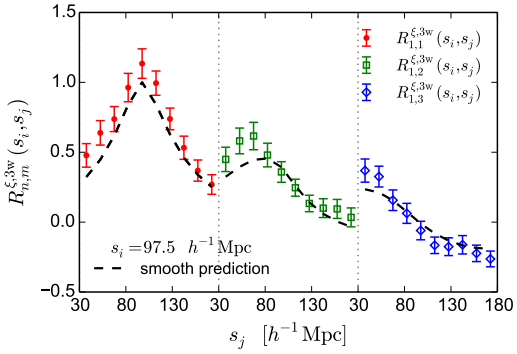

Figure 4.8 – *Upper panel:* The full correlation matrix of the 2PCF wedges, $R^{\xi}_{3w,n,m}(s_i,s_j) = C^{\xi}_{3w,n,m}(s_i,s_j)[\sigma_{\xi^{\mathrm{smooth}}_{3w,n}}(s_i)\,\sigma_{\xi^{\mathrm{smooth}}_{3w,m}}(s_j)]^{-1}$ (normalized by the theoretical prediction), is dominated by a high level of correlation between different wedges and distance bins (shown here for the large binning configuration). *Lower panel:* Cut through the correlation matrix for the most transverse wedge, $\xi_{3w,1}$, at $s_i = 112.5\ h^{-1}$ Mpc. Although the data cross-correlations are noisy, they are well described by our theoretical prediction (the significant correlation of the covariance is discussed in the text).

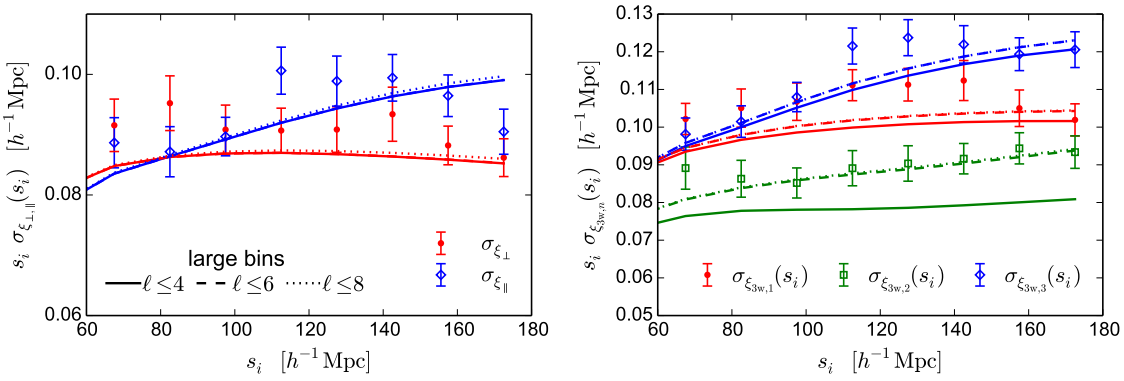

Figure 4.9 – Convergence of the dispersion of two configuration space wedges (left-hand panel) and three wedges (right-hand panel) with the multipole order included in equation (4.29). For two wedges, the sum can be safely truncated after $\ell = 4$ without changing the results on a significant level. In case of three wedges, the convergence at an appropriate level is reached by including terms up to $\ell = 6$.

The cross-correlation for 2PCF wedges is as significant as for the configuration-space multipoles. In analogy to the discussion on the Fourier space wedges, we define the correlation matrix for 2PCF wedges as $R^{\xi}_{3\mathrm{w},n,m}(s_i, s_j) = C^{\xi}_{3\mathrm{w},n,m}(s_i, s_j)[\sigma_{\xi^{\mathrm{smooth}}_{3\mathrm{w},n}}(s_i)\ \sigma_{\xi^{\mathrm{smooth}}_{3\mathrm{w},m}}(s_j)]^{-1}$, normalized by the non-linear theoretical prediction. We show the full correlation matrix compared to the non-linear prediction in Figure 4.8. Again, we restrict our discussion to the case of three wedges for brevity. The correlation matrix for two 2PCF wedges has similar properties. As the Fourier transformation mixes independent Fourier modes, the covariance $C^{\xi}_{3\mathrm{w},n,m}(s_i, s_j)$ only decays slowly with increased separation between the distance bins and ranges of the LOS parameter. The data correlation (upper panel of Figure 4.8) shows good overall agreement between the theoretical prediction (lower triangular part) and our measurement (upper triangular part). The plotted full matrix shows also that the cross-correlation structure for 2PCF wedges is more complex than for 2PCF multipoles. For better visualization, we show a cut through the matrix in the lower panel of Figure 4.8. We find differences between our measurements and the theoretical predictions of up to 20%, which is a bit higher than for the multipole case. As for the previous cases, these discrepancies are most likely due to noise contamination and the level of noise is very similar for different cuts through the matrix. The model under- or overpredicts the data over wide ranges of pair separations because the noise in the covariance is as correlated as the 2PCF itself. Hence, we are not able to test for deviations from of our Gaussian ansatz with the number of realizations at hand.

The prediction for the dispersion of 2PCF wedges in Figure 4.7 and the covariance matrix in Figure 4.8 are based on the sum over ℓ_1 and ℓ_2 in equation (4.29), including contributions up to $\ell \leq 6$. We argue that this is enough to reach an appropriate accuracy by analysing the convergence of the wedge covariance for the large binning scheme. For this, we first evaluate the sum including all terms up to the hexadecapole, and then successively add the $\ell = 6$ and $\ell = 8$ contributions. As shown in Figure 4.9, the two wedge dispersion is converged after including only those contributions up to $\ell \leq 4$; the dispersion for three wedges needs only to

also include $\ell = 6$ in the sum in order to achieve convergence at an appropriate level.

As already discussed in Section 4.2.1, the most significant shortcoming of our model for the analysed sample of N-body simulations is the neglected trispectrum contribution, which is only relevant for scales in the non-linear regime. In order to validate extensions to the Gaussian model that include the trispectrum contribution at the quasi-linear scales, which are of interest for model verification, we would need a much larger set of N-body simulations to reduce the level of noise in the covariance.

As a final test, we analyse whether our model for the monopole covariance has improved over the simplifying assumptions used by Sánchez *et al.* (2008), where the Gaussian real-space covariance from linear theory has been rescaled by the Kaiser factor for linear RSD. This model defines the monopole covariance in real-space as follows:

$$C_{0,0}^{\xi,\mathrm{lin,rs}}(s_i, s_j) = \frac{1}{\pi^2 V_\mathrm{s}} \int_0^\infty \left[b\, P_\mathrm{L}(k) + S\right]^2 \bar{\jmath}_\ell(k s_i)\, \bar{\jmath}_\ell(k s_j)\, k^2\, \mathrm{d}k, \tag{4.40}$$

From this, the z-space covariance is estimated to be $C_{0,0}^{\xi,\mathrm{lin,zs}}(s_i, s_j) = S^2\, C_{0,0}^{\xi,\mathrm{lin,rs}}(s_i, s_j)$, where $S = 1 + \frac{2}{3}\beta + \frac{1}{5}\beta^2$. As shown in Figure 4.6, this simple ansatz gives already an excellent description of the covariance of the redshift-space 2PCF monopole, even though the anisotropy of the input power spectrum has been neglected. However, any RSD or BAO fit using anisotropic clustering measurements would need to take the higher-order multipoles into account, which can only be done by the formulae presented in this work.

Additional tests indicate that the discrepancy between the simplified monopole recipe in equation (4.40) and the full Gaussian model presented in Section 4.2.1 depends on the bias. While there is a negligible difference for the highly biased HOD galaxy sample analysed here (where $b \simeq 2$), the covariance of an under-biased tracer sample ($b \lesssim 1$, similar $\bar{n}$) is only correctly modelled taking the full anisotropy of the input power spectrum into account.

4.4.3 Validation of the precision matrix

Evaluation of the Gaussian likelihood via the χ^2 function given in equation (4.4) needs an estimate of the inverse of the covariance matrix, the precision matrix. As pointed out in Section 4.1.2, the covariance matrix $\boldsymbol{C}^\xi$ estimated from an ensemble of realizations is affected by noise, resulting in a biased estimate of the precision matrix. This bias can be removed by the rescaling of the inverse covariance matrix as given by equation (4.5), using the correction factors $(1 - D)$ (Hartlap *et al.*, 2007).

The level of noise is quite high in our case due to the small number of realizations and large number of measurements bins, preventing extensive tests of the precision matrix. Thus, here the focus of this section is on the validation of the covariance matrix. The inverse data covariance matrix from our set of simulations is only discussed for binning schemes that do not yield a singular covariance matrix or a precision matrix dominated by noise. Thus, we require $D < 0.5$ for the correction factors listed in Table 4.1. Using three wedges or multipole orders, this requirement is only fulfilled for the 'large' scheme in configuration space ($\Delta s = 15\ h^{-1}\,\mathrm{Mpc}$, and 12 bins per wedge/multipole measurement). For brevity, we only discuss the multipole

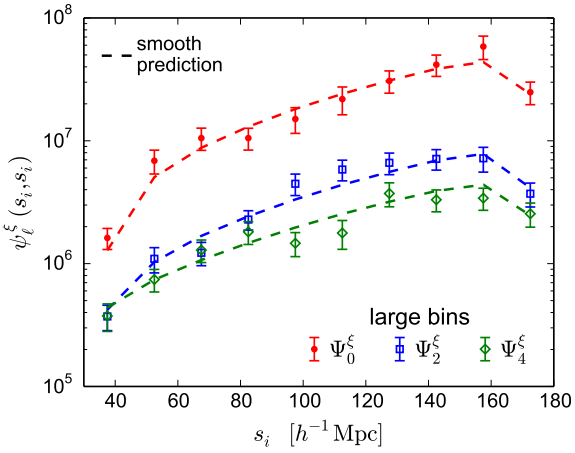

Figure 4.10 – The diagonal entries of the bias-corrected inverse data covariance matrix $\boldsymbol{\psi}^\xi$, defined in equation (4.5), of the configuration space multipole measurements and their error bars, which have been determined with the jackknife method. The dashed lines show the theoretical prediction for the inverse of the theoretical covariance matrix using the smoothed input power spectrum. These results were obtained using the distance range 30 h^{-1} Mpc $\leq s \leq$ 180 h^{-1} Mpc with bin sizes of $\Delta s = 10\ h^{-1}$ Mpc

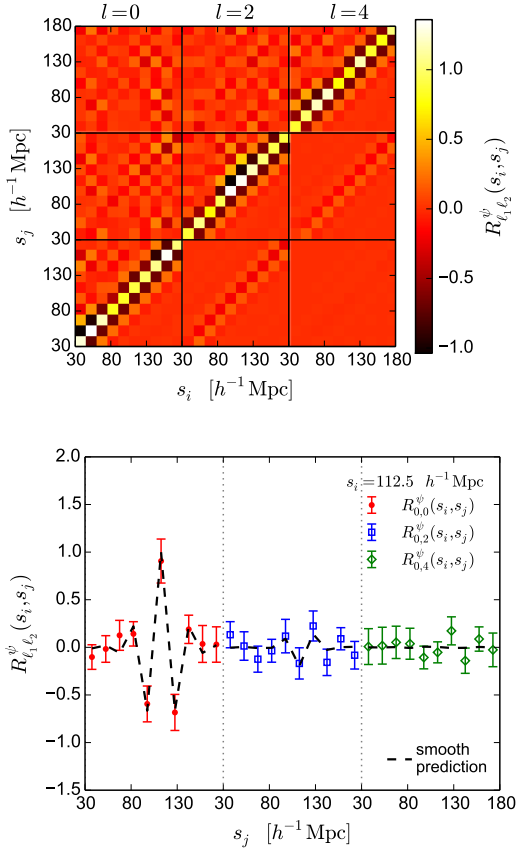

Figure 4.11 – *Upper panel*:: The full precision matrix of the 2PCF multipoles, obtained as bias-corrected inverse data covariance matrix and normalized by the theoretical prediction, $R^\psi_{\ell_1\ell_2}(k_i,k_j) = \psi^\xi_{\ell_1\ell_2}(s_i,s_j)[\psi^\xi_{\mathrm{smooth},\ell_1\ell_1}(s_i,s_i)\,\psi^\xi_{\mathrm{smooth},\ell_2\ell_2}(s_j,s_j))]^{-1/2}$. The structure is more complex than for the correlation matrix due to sign-changing off-diagonal terms. The diagonals of the sub-matrices, the 'mixing terms', show a mirrored structure. *Lower panel:* Cut through the precision matrix for $\ell_1 = 0$ at $s_i = 112.5\ h^1$ Mpc. The contamination from physical effects or noise not accounted for by our modelling is within the error bars which are very large due to the inversion of a noise-contaminated covariance matrix. The precision matrix was measured with distance bins in the range 30 h^{-1} Mpc $\leq s \leq$ 180 h^{-1} Mpc using a bin size of $\Delta s = 10\ h^{-1}$ Mpc

results, $\boldsymbol{\psi}^\xi_\ell = (1-D)\,[\boldsymbol{C}^\xi_\ell]^{-1}$, where $\boldsymbol{C}^\xi_\ell$ has elements $C_{\ell_1\ell_2}(s_i,s_j)$. Further, the axis-averaging of the measurements of the redshift-space two-point statistics is abandoned because equation (4.5) would need to be modified in that case.

In analogy to the covariance notation, we write the elements of the precision matrix $\boldsymbol{\psi}^\xi_\ell$ as

$\psi^{\xi}_{\ell_1\ell_2}(s_j, s_j)$. The theoretical prediction, $\psi^{\xi}_{\mathrm{smooth},\ell_1\ell_2}(s_j, s_j)$, is obtained from the Gaussian prediction for the multipole covariance using the smoothed input power spectrum (and by setting $D = 0$ in equation (4.5) due to the absence of sampling noise). Here we focus only on the non-linear prediction for illustration. The prediction from the linear input power spectrum is very similar, as already discussed in Section 4.4.

The measured and predicted diagonal entries of the precision matrix are shown in Figure 4.10. The error bars are determined with the jackknife technique. For each jackknife estimate, the inverse covariance matrix is rescaled using a modified correction factor D accounting for the removed realization by replacing $N_\mathrm{m} \rightarrow N_\mathrm{m} - 1$. Due to the fact that the covariance matrix is only poorly determined, the errors on the precision matrix are very large (up to ca.20% after the application of the correction factor). Within these errors, the measurements do not show significant deviations from the model predictions $\psi^{\xi}_{\mathrm{smooth}}$.

The accuracy of the modelling for the off-diagonal terms is analysed by plotting the full precision matrix normalized by the theoretical prediction,

$$R^{\psi}_{\ell_1\ell_2}(k_i, k_j) = \psi^{\xi}_{\ell_1\ell_2}(s_i, s_j) \left[\psi^{\xi}_{\mathrm{smooth},\ell_1\ell_1}(s_i, s_i)\, \psi^{\xi}_{\mathrm{smooth},\ell_2\ell_2}(s_j, s_j))\right]^{-\frac{1}{2}}, \tag{4.41}$$

in the upper panel of Figure 4.11. In order to better visualize the complex structure a cut through this matrix is shown in the lower panel. The sub-diagonal entries are negative and 'mirror' the diagonal entries. A similar structure is found for terms mixing the monopole and quadrupole as well as the quadrupole and hexadecapole entries. Further away from the block diagonals, the structure is noise-dominated and deviations between data and theory are largely below the noise level.

4.4.4 Outlook to the theoretical prediction of the anisotropic clustering covariance for real surveys

The aim of this work is limited to predictions of the anisotropic clustering covariance on quasi-linear scales in order to be able to perform the validation of the clustering+RSD modelling on a limited set of large-volume N-body realizations as done in Section 5.2. Further work is needed to incorporate the beat coupling with supersurvey modes and the contributions from the connected trispectrum part of the covariance that arises due to non-linear evolution (Scoccimarro *et al.*, 1999). These effects have been neglected here due to the absence of supersurvey modes (supersample covariance; SSC) in the N-body realizations and the restrictions to quasi-linear scales ($k \lesssim 0.2\ h\,\mathrm{Mpc}^{-1}$, $s \gtrsim 40\ h^{-1}\,\mathrm{Mpc}$). In order to validate a model for the influence of the supersurvey response on the covariance on the anisotropic clustering covariance, an similar analysis to the work in de Putter *et al.* (2012), Takada & Hu (2013), and Li *et al.* (2014) is required, which is beyond the scope of the work published in Grieb *et al.* (2016a) and this thesis. The effect of beat coupling of smaller scales with supersurvey modes can be estimated, for example, by use of the separate universe response (Li *et al.*, 2014). Further, the fact that the local density estimate is obtained in the presence of power on scales larger than the survey size affects the power spectrum covariance of real surveys in the same manner as SSC, but the net effect only makes up 10% of the original beat-coupling effect (de Putter *et al.*, 2012). The

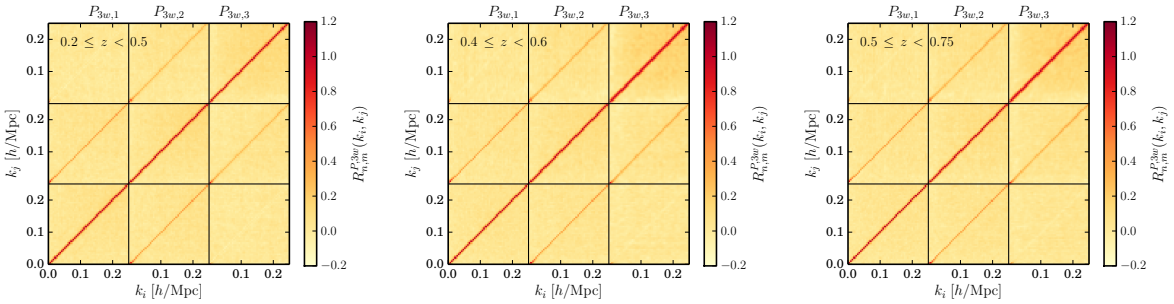

Figure 4.12 – Correlation matrix of the MultiDark Patchy power spectrum wedges for the low (left-hand panel), intermediate (centre panel) and high (right-hand panel) redshift bin. As in Figure 3.8 before, NGC and SGC have been combined for this measurement for simplicity.

contribution of the two latter effects to the PS covariance has been shown to become important at non-linear scales $k \gtrsim 0.1\ h\,\mathrm{Mpc}^{-1}$ for redshift zero (de Putter *et al.*, 2012; Takada & Hu, 2013; Li *et al.*, 2014).

The mode coupling in the standard trispectrum term due to non-linear gravitational evolution is subdominant compared to SSC, but adds to it creating a plateau in the signal-to-noise ratio of the matter power spectrum in the mildly non-linear regime and beyond (Carron *et al.*, 2015). Recently, O'Connell *et al.* (2015) presented a way to take into account non-Gaussian contributions to the anisotropic 2PCF covariance matrix for a CMASS-like survey.

We expect careful modelling to be more important the more complex the analysed galaxy sample is, and the deeper in the non-linear regime the clustering probe advances. The Gaussian model derived here can easily be extended to account for the dependence of the covariance on cosmological parameters by varying the input power spectrum. A second near-future extension can be the theoretical modelling of the clustering covariance of surveys with non-trivial geometry; see de Putter *et al.* (2012) for the analytical treatment of the survey window in case of the covariance of isotropic clustering measurements.

4.5 Data covariance matrices for the BOSS combined sample from mock catalogues

As current theoretical predictions of the anisotropic clustering covariance cannot take into account the observational systematics of the BOSS survey with the required accuracy, the covariance matrix for the analysis of the BOSS DR12 combined sample is estimated from large sets of mock catalogues. The reference matrix is obtained from the Patchy set of mocks that have been described in section Section 3.5.1. An alternative set of mocks, the QPM mocks introduced in Section 3.5.2, are used to cross-check the reference covariance matrix.

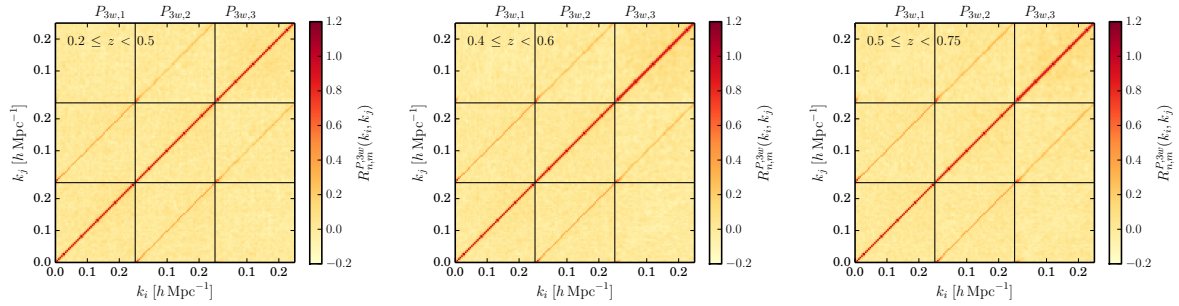

Figure 4.13 – Correlation matrix of the QPM power spectrum wedges for the low (left-hand panel), intermediate (centre panel) and high (right-hand panel) redshift bin. As in Figure 3.9 before, NGC and SGC have been combined for this measurement for simplicity.

4.5.1 The Patchy covariance and precision matrix

The very good agreement of the mean Patchy power spectrum wedges with the clustering of the DR12 combined sample was discussed in Section 3.6.1. The elements of the Patchy covariance matrix are estimated from the $N_\mathrm{m} = 2045$ mocks using equation (4.1). For a better visualization of the structure in the covariance matrix, the correlation matrix is plotted in Figure 4.12. In contrast to the definitions in Section 4.4, the data covariance is normalized by its own diagonal terms,

$$R^P_{3\mathrm{w},n,m}(s_i,s_j) = C^P_{3\mathrm{w},n,m}(s_i,s_j)[\sigma_{P_{3\mathrm{w},n}}(s_i)\,\sigma_{P_{3\mathrm{w},m}}(s_j)]^{-1}, \tag{4.42}$$

as no theoretical prediction is available. Further, the SNR with which the diagonal terms, $\sigma_{P_{3\mathrm{w},n}}(s_i) = [C^P_{3\mathrm{w},n,n}(s_i,s_i)]^{1/2}$, are estimated is much better than for the covariance measured on the Minerva catalogues (due to the larger number of realizations). The effect of the window function, discussed earlier in Section 3.4, introduces a correlation between neighbouring bins and wedges that can be seen as non-vanishing sub-diagonal entries. Especially in the correlations for the most-parallel wedge in the high-redshift bin, cross-covariance between all bins is increased by fibre collisions between galaxy pairs close in angular separation (which happens more often for the CMASS sample than for LOWZ, Reid *et al.*, 2016). The different levels of variance for the different wedges and galactic hemispheres are discussed in Section 4.5.3.

When the precision matrix obtained from the Patchy reference covariance matrix is used for χ^2 evaluations during BAO+RSD fits, we use the correction factor $(1-D)$ as defined by equation (4.5) given in Table 4.1 for $N_\mathrm{m} = 2045$; the rescaling factors for errors on fitted parameter are given in Table 4.2.

4.5.2 The QPM covariance and precision matrix

The QPM covariance matrix used for cross-checks is likewise estimated using equation (4.1) from the 1000 realizations. Again, the full covariance structure is better shown by the correlation matrix for three power spectrum wedges, $R^{P,3\mathrm{w}}_{n,m}(k_i,k_j)$, as defined in equation (4.42). This matrix is plotted in Figure 4.13. Qualitatively, neighbouring wavenumber bins and wedges are

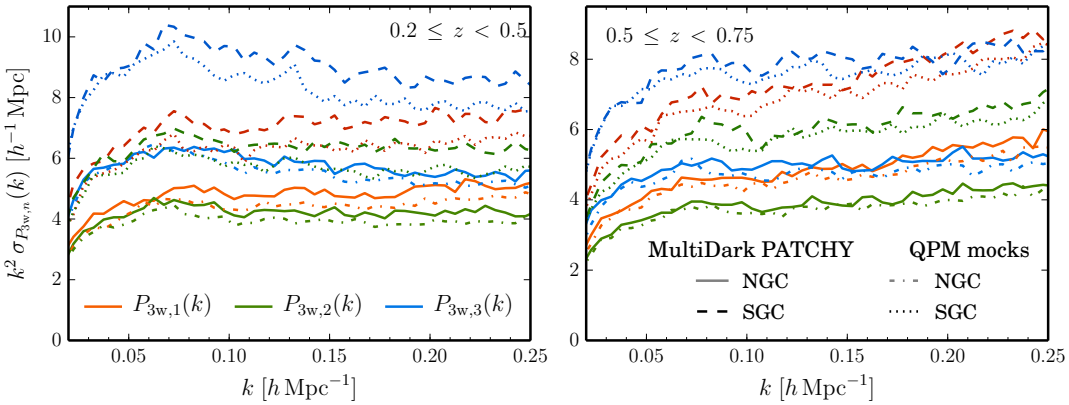

Figure 4.14 – Dispersion of the QPM and MultiDark Patchy power spectrum wedges for the low (upper panel) and high (lower panel) redshift bin, separating the two galactic caps.

correlated due to the effect of the window function on a similar level than in the Patchy covariance estimate.

When the QPM covariance matrix is used for clustering measurements on the NGC and SGC subsamples separately, we use the correction factor $(1-D)$ given in Table 4.1 for $N_\mathrm{m} = 1000$. If the χ^2 function as given by equation (4.4) is evaluated for the precision matrix obtained from the covariance of measurements combining the galactic hemispheres (such as the covariance of the difference between the galactic caps), we need to take into account that the NGC and SGC subsamples of the QPM mocks are correlated by a factor $r^2 = V^2_\mathrm{shared}/(V_\mathrm{NGC}\,V_\mathrm{SGC}) = 0.014$. Thus, we split the realizations in two independent subsets where the first subset is given by the NGC of the first 500 mocks and the SGC of the last 500 mocks and the other subset has the remaining realizations. The covariance matrices are calculated for each subset and then averaged; the inverse of the averaged covariance matrix is rescaled by a modified Hartlap *et al.* (2007)-factor as used for the DR11 mocks which have an even more significant overlap between the subsamples (Percival *et al.*, 2014),

$$\boldsymbol{\psi} = \left(1 - \frac{1+r^2}{2}\,D\right)\,\boldsymbol{C}^{-1}, \tag{4.43}$$

where D is given by equation (4.5) using $N_\mathrm{m} = 500$ to account for the number of independent realizations in each subset.

4.5.3 Comparison of the clustering dispersion of the two set of mocks

In Figure 4.14, we plot the power spectrum wedges dispersion measured separately for each of the two galactic caps from the two sets of mocks. The South has ca. 40% of the North's volume and thus its dispersion is ca. 1.6 times larger. The power spectrum dispersion obtained from the Patchy mocks, due to their larger matter density parameter Ω_M, is slightly larger than the one derived from the alternative QPM mocks, especially in the low redshift bin (upper panel).

In the high bin, the trend with k is stronger. Thus, the choice to use the PATCHY mocks for the reference covariance matrix also represents the more 'conservative' option, besides the good arguments that the number of realizations is larger, the agreement of the measured two-point clustering between the PATCHY mocks and the data is better, and the more advanced modelling of the redshift evolution.

5

Modelling the redshifts-space galaxy clustering

"If you want to make an apple pie from scratch, you must first create the universe."

Carl Sagan

Modelling the redshift-space galaxy clustering is the key element to obtain accurate cosmological constraints from galaxy samples. As described in Section 2.4.7, the BAO signal in the galaxy correlation function can be seen as a broad peak at the sound horizon scale of about 100 h^{-1} Mpc. Thus, this feature is located in the quasi-linear regime and, therefore, it provides us with a very robust probe of the expansion history of the Universe. However, non-linearities distort this feature, even more so in redshift space. The model discussed in this chapter specifically addresses redshift-space distortions. Section 5.1 contains a brief summary of the modelling recipes used to generate model predictions, describing the tools and the underlying methods, that were developed by my collaborators Martín Crocce, Román Scoccimarro, and Ariel Sánchez. My contribution to the modelling effort was the validation of the model in Fourier space. In this first section, the full parameter space of the model is presented and the meaning of each parameter summarized. The verification of the redshift-space clustering model and comparative performance tests on the challenge and combined sample mock catalogues described in Section 5.2 are a main part of the scientific work described in this thesis. Section 5.2.1 presents the verification of the modelling bases on the Minerva N-body simulations. The results of the RSD fits on the BOSS challenge mocks are discussed in Section 5.2.2. Finally, Section 5.2.3 presents the verification with the Patchy mocks mimicking the full characteristics of the final BOSS sample.

5.1 The theoretical model for Fourier space wedges

An accurate model of the redshift-space galaxy clustering statistics is needed in order to have a framework for full-shape fits that is competitive with BAO distance measurements on reconstructed density fields. To meet the requirements in accuracy, a new full-shape model derived

Table 5.1 – The sound horizon scale $r_s(z_d)$ at the drag redshift and the angular diameter distances $D_A(z_{eff})$ and Hubble parameters $H(z_{eff})$ for the cosmologies specified in Table 3.2 at the effective redshifts z_{eff} of the ranges defined in Table 3.1.

Cosmology \ Value [unit]	$r_s(z_d)$ [Mpc]	z_{eff} [−]	$D_A(z_{eff})$ [Mpc]	$H(z_{eff})$ [km s^{-1} Mpc^{-1}]
Fiducial	147.78	0.38	1108.9	82.92
		0.51	1312.8	89.61
		0.61	1433.0	95.21
MINERVA	148.49	0.57	1363.5	93.71
QPM	147.13	0.38	1076.7	84.93
		0.51	1276.9	91.50
		0.61	1395.3	97.00
PATCHY	147.66	0.38	1106.9	83.00
		0.51	1310.9	89.66
		0.61	1431.0	95.45
Template	147.34	0.38	1112.1	82.79
		0.51	1316.3	89.54
		0.61	1436.3	95.18

from Renormalized Perturbation Theory (denoted as 'gRPT') and a Gaussian streaming model for redshift-space distortions (Scoccimarro, 2004) is used in this work. In order to account for non-linear gravitational dynamics in the model prediction for the matter power spectrum, this approach is based on the theoretical framework of RPT, which was described in Section 2.4.4. The redshift-space galaxy clustering statistics are derived from the matter clustering signal by use of a bias model that considers non-linear and non-local contributions. In redshift-space, the galaxy density field has contributions from the velocity field, which requires a non-linear RSD model even for the largest scales. These two aspects of the modelling were discussed in Section 2.4.5 and Section 2.4.6, respectively. The aim of this section is to describe the parameter set used in modelling in order to prepare the discussion of the RSD fits in Chapter 6. Three companion papers (Grieb *et al.*, 2016b; Salazar-Albornoz *et al.*, 2016; Sánchez *et al.*, 2016, *in prep.*) will make use of this model to infer cosmological implications from the BOSS DR12 combined sample. The model, that is dubbed 'gRPT+RSD' in this thesis, will be described in more detail in Blas *et al.* (2016, *in prep.*; non-linear gravitational dynamics) and Sánchez *et al.* (2016, *in prep.*; modelling of the galaxy bias and RSD, details of the implementation).

5.1.1 Modelling the Alcock-Paczynski distortion

The results obtained with the 'gRPT+RSD' model rely on a prediction for the linear-theory input power spectrum. When the parameters of the underlying cosmological model are not varied, this prediction is computed using a fixed 'template' cosmology. The model predictions are given in terms of the power spectrum monopole, quadrupole, and hexadecapole ($P_\ell^{\mathrm{model}}(k)$

for $\ell \in \{0, 2, 4\}$), which are combined in the full anisotropic (2D) power spectrum prediction,

$$P^{\text{model}}(k,\mu) = P_0^{\text{model}}(k) + P_2^{\text{model}}(k)\,\mathcal{L}_2(\mu) + P_4^{\text{model}}(k)\,\mathcal{L}_4(\mu). \tag{5.1}$$

Due to the Alcock-Paczynski (AP) effect described in Section 2.4.7, geometrical distortions arise from a mismatch in the assumed and true cosmology. This effect is modelled with two *distortion parameters* $q_\perp$ and $q_\parallel$ that describe the rescaling, in Fourier space, of the wavenumbers transverse, $k_\perp$, and parallel, $k_\parallel$, to the LoS direction,

$$q_\perp \equiv \frac{k_\perp^{\text{fid}}}{k_\perp} \quad \text{and} \quad q_\parallel \equiv \frac{k_\parallel^{\text{fid}}}{k_\parallel}, \tag{5.2}$$

where $k_\perp^{\text{fid}}$ and $k_\parallel^{\text{fid}}$ are the observed wavenumbers assuming the fiducial cosmology.

Then, the distorted theoretical prediction for the power spectrum wedges is given by

$$\tilde{P}_{\mu_1}^{\mu_2}(k^{\text{fid}}) = \frac{q^{-3}}{\mu_2 - \mu_1} \int_{\mu_1}^{\mu_2} P^{\text{model}}(k(k^{\text{fid}},\mu^{\text{fid}}),\mu(k^{\text{fid}},\mu^{\text{fid}}))\,\mathrm{d}\mu^{\text{fid}}, \tag{5.3}$$

where the integrand has the following rescaled parameters:

$$k(\mu^{\text{fid}},k^{\text{fid}}) \equiv k^{\text{fid}} \sqrt{q_\parallel^{-2}\,(\mu^{\text{fid}})^2 + q_\perp^{-2}\,[1-(\mu^{\text{fid}})^2]} \tag{5.4}$$

$$\mu(\mu^{\text{fid}},k^{\text{fid}}) \equiv \mu^{\text{fid}}\,q_\parallel^{-1}\left(q_\parallel^{-2}\,(\mu^{\text{fid}})^2 + q_\perp^{-2}\left[1-(\mu^{\text{fid}})^2\right]\right)^{-1/2}. \tag{5.5}$$

The scaling of the power spectrum with $q^{-3} \equiv q_\perp^{-1}\,q_\parallel^{-2}$ is due to the volume distortion from the AP effect.

In a BAO distance measurement (cf., Section 2.3.2), the angular diameter distance $D_{\text{A}}(z)$ and Hubble parameter $H(z)$ are measured relative to the sound horizon scale at the drag redshift, $r_{\text{s}}(z_{\text{d}})$, of the template. The distortion parameters $q_\perp$ and $q_\parallel$ of equation (5.2) only take the geometric effect into account. Thus, results that are comparable across different analyses (using different templates) can be obtained by defining a second set of *Alcock-Paczynski parameters*, which also include an additional rescaling of the angular-diameter distance $D_{\text{A}}(z)$ and the Hubble parameter $H(z)$ by the fiducial sound horizon scale, $r_{\text{s}}^{\text{fid}}(z_{\text{d}})$,

$$\alpha_\perp \equiv \frac{D_{\text{A}}(z)}{D_{\text{A}}^{\text{fid}}(z)}\frac{r_{\text{s}}^{\text{fid}}(z_{\text{d}})}{r_{\text{s}}(z_{\text{d}})} \quad \text{and} \quad \alpha_\parallel \equiv \frac{H^{\text{fid}}(z)}{H(z)}\frac{r_{\text{s}}^{\text{fid}}(z_{\text{d}})}{r_{\text{s}}(z_{\text{d}})}. \tag{5.6}$$

These ratios are defined using the conventional units Mpc and $\mathrm{km\,s^{-1}\,Mpc{-}1}$ for $D_{\text{A}}(z)$ and $H(z)$ respectively. In our implementation of the model, the wavenumbers k are in units of $h\,\mathrm{Mpc}^{-1}$. Thus, the distortion and AP parameters are related by

$$\alpha_\perp = q_\perp \frac{r_{\text{s}}^{\text{fid}}(z_{\text{d}})}{r_{\text{s}}(z_{\text{d}})}\frac{h^{\text{fid}}}{h} \quad \text{and} \quad \alpha_\parallel = q_\parallel \frac{r_{\text{s}}^{\text{fid}}(z_{\text{d}})}{r_{\text{s}}(z_{\text{d}})}\frac{h^{\text{fid}}}{h}. \tag{5.7}$$

The cosmological distances entering these parameters, $D_{\text{A}}(z)$, $H(z)$, and $r_{\text{s}}(z_{\text{d}})$, are listed in Table 5.1 for the different cosmologies used in this work.

Table 5.2 – The set of parameters that define the parameter space $\mathcal{X}$ of our full-shape fits with the 'gRPT+RSD' model. BAO+RSD fits use the distortion, growth, bias, RSD, shot-noise, and optionally the power spectrum amplitude parameters. Fits for the cosmological interference use the bias, RSD, and shot-noise parameters, besides the parameters of cosmological model and the nuisance parameters of the complementary cosmological probes. All parameters have a flat prior which is uniform within the given limits and zero outside.

Parameter	Function	Unit	Prior limits	Starting Point	Step size
		Bias parameters			
$b_1\sigma_8$	Linear bias	–	0.5–9	1.9	0.06
$b_2\sigma_8$	Second-order bias	–	(−4)–4	0	0.06
γ_3^-	Non-local bias	–	(−3)–3	1	0.04
		RSD parameter			
$a_{\rm vir}$	FoG kurtosis	–	0.2–10	2	0.06
		Shot-noise parameter[§]			
N	Extra shot noise	$h^{-3}\,{\rm Mpc}^3$	(−1800)–1800	1000	50
		Power spectrum amplitude parameter[¶]			
$A_{\rm p}$	Modulations of σ_8^2	–	(−0.9)–1.1	1	0.01
		Distortion parameters			
$q_\perp$	$k_\perp$ rescaling	–	0.5–1.5	1	0.02
$q_\parallel$	$k_\parallel$ rescaling	–	0.5–1.5	1	0.04
		Growth parameter			
$f\,\sigma_8$	Growth-rate factor	–	0–3	0.47	0.04

[§] In the case of the low-redshift bin, N is varied within −1000–1000, starting at 600, as the Poisson shot-noise estimate is also smaller.

[¶] $A_{\rm p}$ is varied in the tests on Minerva, but not for final fits on the real and mock combined sample, as it was found that fixing the power spectrum amplitude is not relevant for the final BAO+RSD constraints.

For comparison with isotropic BAO distance observations, we define the angle-averaged AP parameter α as

$$\alpha \equiv \left(\alpha_\perp^2\,\alpha_\parallel\right)^{1/3}, \quad \text{so that} \quad \alpha = \frac{D_{\rm V}(z)}{D_{\rm V}^{\rm fid}(z)}\,\frac{r_{\rm s}^{\rm fid}(z_{\rm d})}{r_{\rm s}(z_{\rm d})}, \tag{5.8}$$

where the angle-averaged distance $D_{\rm V}(z)$ is given by equation (2.106).

5.1.2 Details of the implementation and summary of the final set of model parameters

We perform two kinds of analyses with the Fourier space wedges, the conventional BAO+RSD fits using a fixed 'template' cosmology (denoted as 'RSD-type full-shape fits' in the following) and 'cosmological full-shape fits', in which the predictions assuming a given cosmological model with varying parameters are compared directly with the observed clustering wedges.

Originally, our model is defined to keep the non-local contributions to the galaxy bias up to those terms corresponding to second-order Lagrangian bias (cf. Section 2.4.5). However, tests of the modelling with simulations showed that fixing the γ_3 coefficient to the local Lagrangian prediction of equation (2.91) yields less accurate results than marginalizing over a free γ_3 pa-

rameter. Thus, this coefficient is fitted to the data in agreement with studies that show that Eulerian bias is not necessarily compatible to local Lagrangian bias in the non-linear regime (Matsubara, 2011).

For BAO+RSD fits, the input power spectrum is kept fixed, modelling variations of the cosmology with the distortion parameters, the power spectrum amplitude A_p, and the growth rate f, all varied as free parameters. The full parameter space $\mathcal{X}$ for the model verification tests on Minerva and the challenge mocks consists of 9 parameters,

$$\zeta = (q_\perp,\, q_\parallel,\, f\,\sigma_8,\, b_1\,\sigma_8,\, b_2,\, \gamma_3^-,\, a_\mathrm{vir},\, A_\mathrm{p},\, N)^\mathrm{T} \in \mathcal{X}, \tag{5.9}$$

following the usual convention to express final results in terms of $b_1\,\sigma_8$, and $f\,\sigma_8$. A_p modulates the clustering amplitude σ_8 by a rescaling of the underlying linear-theory prediction for the power spectrum. b_1 and b_2 are the local and quadratic local bias factors of the expansion defined in equation (2.85). As described in Section 2.4.5, b_2 is an effective parameter that also takes up contributions from higher-order local bias parameters as the scale-dependency of the quadratic bias has been neglected in our modelling. In our modelling of the non-local galaxy bias, only γ_3^- is varied as a free parameter, while γ_2 is set by the local Lagrangian relation given in equation (2.91). The parameters that affect the redshift-space anisotropies are the growth rate f and a_vir, which is a parameter that corresponds to the kurtosis of the velocity dispersion distribution modelled by the FoG function F_vir of equation (2.99). Finally, we account for deviations from a pure Poisson shot noise with a free, constant, and additive shot-noise contribution N to all power spectrum wedges.

We explore this parameter space using the Markov chain Monte Carlo (MCMC) technique as described in Appendix A.2. Our implementation of 'gRPT+RSD' takes a few seconds to compute the predicted power spectrum wedges $\tilde{P}_{3\mathrm{w},n}(k,\mu)$, $n \in \{1,2,3\}$, from the input power spectrum $P_\mathrm{lin}(k)$. In order to decrease the computing time for each model prediction, precomputed look-up tables are rescaled by the amplitude parameter in an approximative way to emulate variations of σ_8 of the order of several %. Thus, recalculating the power spectrum wedges from a modified $A_\mathrm{p}\,P_\mathrm{lin}(k)$ takes a fraction of a second. Later in Section 5.2.1, we show that this parameter does not affect the RSD-type full-shape fits for the Minerva simulations. Hence, we do not include this parameter in the BAO+RSD fits to the synthetic Patchy catalogues. For these tests and the cosmological fits of Chapter 6, CosmoMC[1] (Lewis & Bridle, 2002, see also Appendix A.3) was used.

In case of the cosmological full-shape fits, the full model predictions must be computed from the power spectrum given by the cosmological parameters for each point in the parameter space that is evaluated.

As discussed in Appendix A.2, the choice of the prior distribution can have an influence on the accuracy of the obtained parameter constraints. We choose flat priors on all parameters given by the limits listed in Table 5.2. Careful analysis of our results makes us confident that they are not affected by applying a too restrictive choice of limits or allowing for variations in a too wide range. The chains are considered converged if the Gelman-Rubin convergence criterion (Gelman & Rubin, 1992) as defined in equation (A.20) satisfies $\hat{R} - 1 < 0.02$.

[1] http://cosmologist.info/cosmomc/

5.2 Verification of the model

The 'gRPT+RSD' model was comprehensively tested on a large set of full N-body simulations. In Section 5.2.1 we present test on the performance of the model by applying it to the power spectrum wedges measured from the MINERVA HOD catalogues described in Section 4.3.2.

The BOSS collaboration chose to validate the performance of the different BAO+RSD measurement techniques used in the DR12 analysis by means of a set of 'challenge' mocks. These results are used to quantify the systematic biases for the obtained BAO distance and growth measurements. We describe our results of the mock challenge analysis in Section 5.2.2.

The challenge mocks only model the CMASS sample. In order to test the model on artificial catalogues that match the clustering of the full combined sample, the set of PATCHY mocks are fitted in Section 5.2.3. These fits also serve as a basis for the estimation of the cross covariance between the results obtained from different analysis approaches that are applied in the BOSS galaxy clustering working group. This estimate is needed to generate the consensus distance and growth measurements of (Anderson *et al.*, 2016, *in prep.*).

5.2.1 Performance tests for the redshift-space clustering modelling on the MINERVA HOD catalogues

The MINERVA HOD catalogues described in Section 4.3.2 have similar clustering properties as the BOSS combined sample and are obtained from full N-body simulations. Thus, they represent a suitable test case to validate the modelling of the Fourier space wedges in redshift space. For this test, we use the recipe for the theoretical covariance matrix for clustering wedges in Fourier space presented in Section 4.2.

In the left-hand panel of Figure 5.1, we show the best-fit model of the power spectrum wedges compared to the mean MINERVA HOD measurements. For this fit, we chose $k_{\rm min} = 0.01\ h\,{\rm Mpc}^{-1}$ and $k_{\rm max} = 0.2\ h\,{\rm Mpc}^{-1}$ and match the cosmology of the template power spectrum to the underlying cosmology of the N-body simulations (listed as 'Minerva' in Table 3.2). The dispersion over the realisations, indicated by the error bars, is much larger than the deviations between the model and the measurement at all scales. This agreement even extends into the non-linear regime outside the fitting range.

In order to validate the best wavenumber range for which the model provides the tightest unbiased estimates of the distortion and growth parameters, we used the 'gRPT+RSD' model to perform RSD-type full-shape fits on the mean measurements of the MINERVA HOD power spectrum wedges using two and three clustering wedges with a varying upper limit $k_{\rm max}$ for the fitting range. The results, shown in the right-hand panel of Figure 5.1, are in excellent agreement with the correct values of distortion parameters and $f\,\sigma_8(\bar{z})$ for the case of three wedges. The marginalized confidence intervals of the distortion parameters are not exactly centred on the expectation values, which we find is due to the fact that the additional shot noise parameter N is strongly correlated with most other bias and RSD nuisance parameters, and also shows small trends with the distortion parameters and $f\,\sigma_8$. Since the deviations are

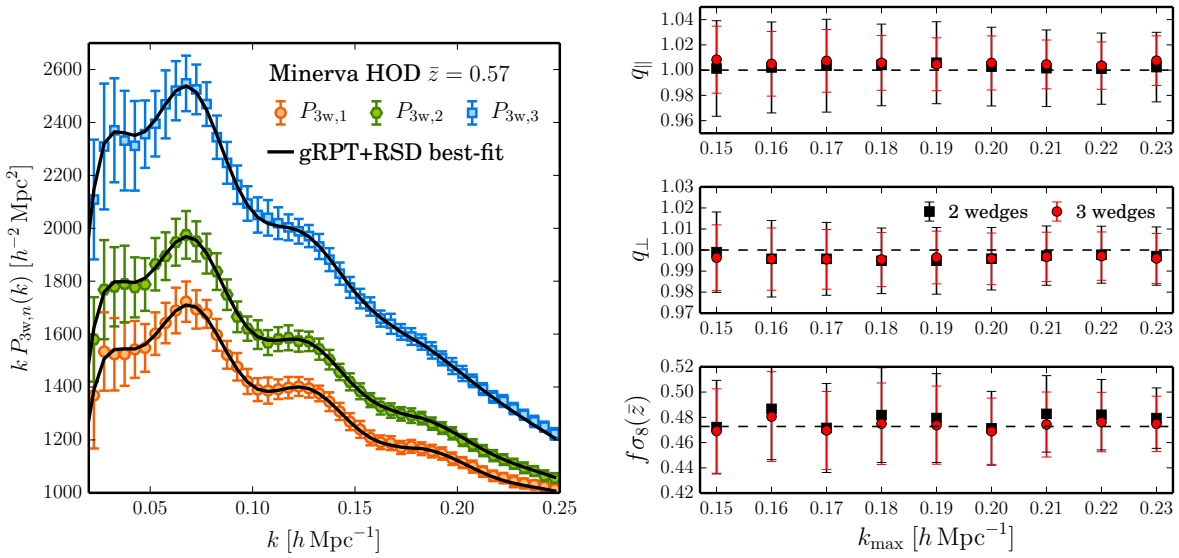

Figure 5.1 – *Left-hand panel:* Best-fitting 'gRPT+RSD' model to the mean power spectrum wedges of the Minerva HOD sample using $k_{\min} = 0.01\ h\,\mathrm{Mpc}^{-1}$ and $k_{\max} = 0.2\ h\,\mathrm{Mpc}^{-1}$. The cosmology was fixed, i.e., $q_\parallel = q_\perp = 1$, $f\,\sigma_8(\bar{z}) = 0.473$ (cf., Minerva in Table 3.2). *Right-hand panel:* Marginalized results for $q_\parallel$, $q_\perp$, and $f\,\sigma_8(\bar{z})$ from 'gRPT+RSD' model fits to the mean Fourier space wedges of the Minerva HOD samples using different fitting ranges $0.01\ h\,\mathrm{Mpc}^{-1} \leq k_i \leq k_{\max}$. The fits using three wedges (red) has significantly smaller error bars than for two wedges.

Table 5.3 – The results for $q_\parallel$, $q_\perp$, and $f\,\sigma_8(\bar{z})$ from RSD-type full-shape 'gRPT+RSD' fits to the mean and individual Minerva measurement using two and three Fourier space wedges fitting wavenumbers in the range $0.01\ h\,\mathrm{Mpc}^{-1} \leq k_i \leq 0.2\ h\,\mathrm{Mpc}^{-1}$. The measurements were obtained either assuming the true Minerva cosmology or the fiducial cosmology of the BOSS DR12 analysis (whose parameters are listed in Table 3.2). Mean chain results are given as the weighted mean and standard deviation of the burn-in removed Markov chains. The best-fit parameters of the 100 individual fits are given by the weighted average of each individual Markov chain; here we report the mean and standard deviation of the best-fit parameters.

Configuration	Param.	Mean chains	Individual	True Value
Two wedges,	$q_\perp$	0.996 ± 0.015	0.996 ± 0.016	1.000
Minerva	$q_\parallel$	1.003 ± 0.032	1.005 ± 0.033	1.000
cosmology	$f\,\sigma_8(\bar{z})$	0.471 ± 0.030	0.482 ± 0.035	0.473
Three wedges	$q_\perp$	0.996 ± 0.013	0.995 ± 0.013	1.000
Minerva	$q_\parallel$	1.006 ± 0.022	1.007 ± 0.023	1.000
cosmology	$f\,\sigma_8(\bar{z})$	0.469 ± 0.027	0.469 ± 0.028	0.473
Two wedges,	$q_\perp$	1.005 ± 0.016	1.005 ± 0.016	1.010
fiducial	$q_\parallel$	1.025 ± 0.034	1.026 ± 0.034	1.020
cosmology	$f\,\sigma_8(\bar{z})$	0.472 ± 0.030	0.485 ± 0.037	0.473
Three wedges,	$q_\perp$	1.006 ± 0.013	1.005 ± 0.013	1.010
fiducial	$q_\parallel$	1.027 ± 0.023	1.028 ± 0.024	1.020
cosmology	$f\,\sigma_8(\bar{z})$	0.471 ± 0.028	0.471 ± 0.028	0.473

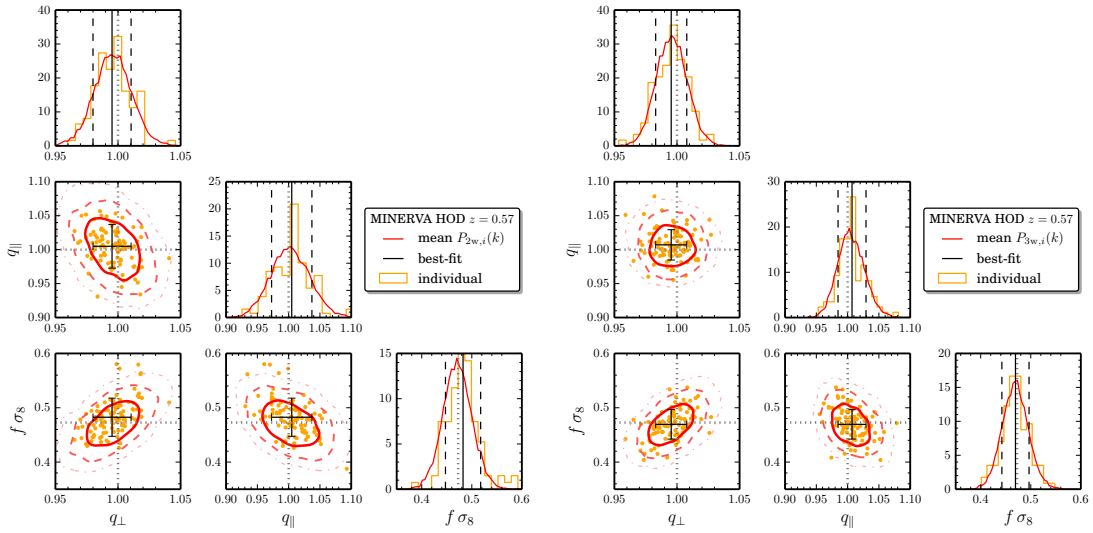

Figure 5.2 – Marginalized results for $q_\parallel$, $q_\perp$, and $f\,\sigma_8(\bar{z})$ from RSD-type full-shape 'gRPT+RSD' fits to the mean (red) and individual (orange) MINERVA HOD measurement of two (left-hand panel) and three (right-hand panel) Fourier space wedges fitting a wavenumber range $0.01\ h\,\mathrm{Mpc}^{-1} \leq k_i \leq 0.2\ h\,\mathrm{Mpc}^{-1}$. As the plotting ranges are chosen to be the same for all plots, it can easily be seen that the three-wedges constraints are a little tighter than the results from the two-wedges fits, especially for $q_\parallel$ as the degeneracy between $q_\parallel$ and $q_\perp$ has been broken by including a third angle-dependent projection. The expected parameters are indicated as dotted lines in the histograms. They are recovered by the mean results of the fits.

much smaller than the statistical error for a single MINERVA volume,[2] we do not take it into account for the RSD analyses in the following.

In Figure 5.2, we show the corresponding marginalized histograms and 2D contours of confidence levels of 68%, 95%, and 99% for the parameters $q_\parallel$, $q_\perp$, and $f\,\sigma_8(\bar{z})$ from the fits to MINERVA. The left-hand panel shows the two-wedges results, while the right-hand panel corresponds to the fits using three wedges. The dispersion of the individual fits (orange histograms) is in good agreement with the marginalized posterior distributions obtained from the mean measurement; all small fraction of 'outliers', especially for high $f\,\sigma_8$, disappears by including a third wedge into the measurement configuration. In this case, we find perfect agreement between the confidence levels derived from the chains and the disperion of the individual best-fit results and expect them both to be unbiased estimates of the real uncertainty.

For the real data, the true cosmology is unknown and a fiducial cosmology has to be assumed. Hence, we test whether assuming a different cosmology for the measurement of the power spectrum wedges, the fiducial cosmology for the BOSS DR12 analysis listed in Table 3.2, could bias the results. In Table 5.1 we compare the fits of the RSD-type full-shape fits using the true MINERVA and the fiducial cosmology. The distortion and growth parameters are recovered with very similar accuracies in both measurement cosmologies for two and three wedges.

Due to the increased constraining power of the analyses with three wedges over using two

[2]The volume of a single MINERVA realization, $V = (1500\ h^{-1}\,\mathrm{Mpc})^3$, is roughly equivalent to the effective volume of the full BOSS combined sample, cf., Table 3.1.

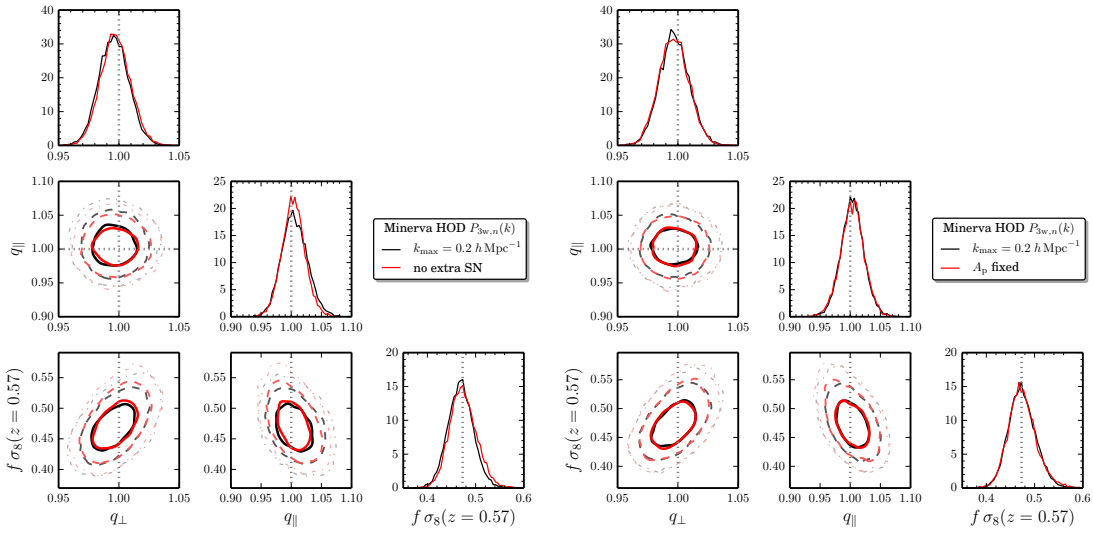

Figure 5.3 – Marginalized results for $q_\parallel$, $q_\perp$, and $f\,\sigma_8(\bar{z})$ from 'gRPT+RSD' fits to the mean MINERVA HOD measurement of three Fourier space wedges fitting a wavenumber range $0.01\ h\,\mathrm{Mpc}^{-1} \leq k_i \leq 0.2\ h\,\mathrm{Mpc}^{-1}$. The expected parameters are indicated as dotted lines in the histograms. *Left panel:* Overplotted in red are fits where the additional shot noise term N is fixed to zero (thus, only the Poisson shot noise estimate is subtracted from all Fourier space wedges measurements). The small systematic biases on these three parameters that were found for the standard parameter space are decreased by this configuration indicating that these biases result from unavoidable correlations between the nuisance parameters and the three cosmological ones. *Right panel:* Overplotted in red are fits where the power spectrum amplitude parameter A_p is fixed to zero (here, $N = 0$ for both fits). This does not have any effect on the constraints of the three cosmological parameters.

wedges only, from now on we will present results obtained using $P_{3\mathrm{w},n}(k)$ only. Exceptions are RSD challenge analysis in Section 5.2.2 and the consistency tests on the data discussed in Section 6.1.1.

Modelling robustness for extra shot noise and power spectrum amplitude variations

Testing for systematics induced by the varying shot-noise and amplitude parameters, we show the marginalized 1D histograms and 2D contours of the parameters $q_\parallel$, $q_\perp$, and $f\,\sigma_8(\bar{z})$, derived from BAO+RSD fits to the three Fourier space wedges using the 'gRPT+RSD' model in Figure 5.3. Here, we use the mean measurement of the power spectrum wedges of the MINERVA HOD galaxy samples, fitting wavenumber bins in the range $0.01\ h\,\mathrm{Mpc}^{-1} \leq k_i \leq 0.2\ h\,\mathrm{Mpc}^{-1}$. In the left panel, we show that fixing the extra shot noise to zero, $N = 0$, results in constraints that are less biased with respect to the true values of these parameters (indicated by the dotted lines). Thus, the minor deviations found in the recovered distortion parameters are likely due to correlations between the nuisance and cosmological parameters. However, this systematic cannot be avoided as the additional shot noise term is required in the full-shape fits to real and mock samples with the observational systematics of BOSS to account for deviations from pure Poisson noise (cf., Section 3.3.3). N absorbs also a constant stochastic 'shot-noise' term in the modelling of the redshift-space galaxy bias that has been neglected in Section 2.4.6.

Table 5.4 – The set of synthetic galaxy catalogues used in BOSS RSD challenge. The cosmological density parameter Ω_M and h have only been revealed after the submission of the 'blind' results. Of the challenge N series (synthetic CMASS NGC sample), a set of 84 realizations was generated. For the periodic boxes, only a single realization exists for each type. All samples are snapshots at a fixed redshift $\bar{z}$.

Name	Type	Ω_M	h	$\bar{z}$	HOD
A	periodic box	0.306	0.6777	0.5617	standard
B	periodic box	0.306	0.6777	0.5617	high bias
C	periodic box	0.27	0.7	0.441	velocity bias
D	periodic box	0.286	0.7	0.5	standard
E	periodic box	0.286	0.7	0.5	velocity bias
F	periodic box	0.306	0.6777	0.5617	assembly bias
G	periodic box	0.306	0.6777	0.5617	assembly bias
N series	cut sky (CMASS NGC)	0.286	0.7	0.5	standard

In linear theory, there is a perfect degeneracy between the growth rate f and the clustering amplitude σ_8. We test if this is also true for the RSD-type full-shape fits with the 'gRPT+RSD' model, where the amplitude of the input power spectrum A_p is used to model variations of σ_8. Hence, the recovered distortion and growth parameters, especially the constraints on the combination $f\,\sigma_8$, are compared for the cases of a free amplitude A_p and a fixed one (where $A_p = 1$). Completely fixing the shape and amplitude of the template power spectrum is preferred as it simplifies the calculation of the model predictions. In the standard configuration for the MINERVA RSD fits, we vary A_p by 10%. The right panel of Figure 5.1 shows that keeping A_p fixed does not change the constraints on the three cosmological parameters, $q_\parallel$, $q_\perp$, and $f\,\sigma_8$. Thus, the A_p parameter is not used in the RSD-type full-shape fits of the power spectrum wedges obtained from the PATCHY catalogues in Section 5.2.3.

5.2.2 Results for the BOSS RSD challenge catalogues

Within the BOSS collaboration, special attention is paid to perform stringent cross checks of the different modelling and measurement techniques used in the BOSS DR12 analysis of the combined sample, especially for those approaches that are combined to obtain the BOSS DR12 consensus constraints (Anderson *et al.*, 2016, *in prep.*). Hence the performance of the various full-shape approaches are compared in an RSD-fit challenge on large-volume synthetic catalogues to check for (unknown) systematics and the consistency of the results from the different analysis techniques. The results from all contributing method will be discussed and compared against each other in Tinker *et al.* (2016, *in prep.*).

The first part of the challenge was based on the analysis of six different HOD galaxy samples constructed out of large-volume N-body simulations. Apart from standard HOD parameters, other non-standard cases, including velocity or assembly bias, are considered. The simulations correspond to ΛCDM cosmologies with slightly different density parameters (see the list in Table 5.4). In Figure 5.4, the final results from fitting two (orange diamonds) and three (green pentagons) Fourier-space wedges measured from the first five challenge boxes are shown. For

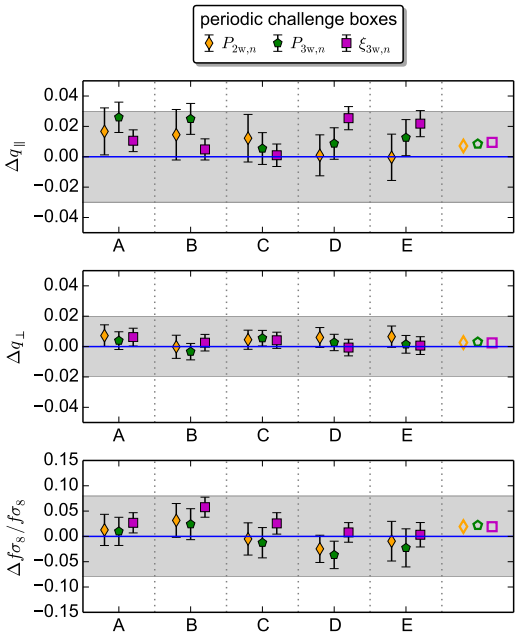

Figure 5.4 – Marginalized results for $q_\parallel$, $q_\perp$, and $f\,\sigma_8(\bar{z})$ from 'gRPT+RSD' model fits to the clustering-wedges measurement of the periodic challenge boxes A–E listed in Table 5.4, fitting wavenumber bins in the range $0.01\ h\,\mathrm{Mpc}^{-1} \leq k_i \leq 0.2\ h\,\mathrm{Mpc}^{-1}$. The measurements are obtained from averaging over the possible three LoS directions assuming a plane-parallel redshift-space geometry. Shown are the final results from two (orange) and three (green) Fourier-space wedges, compared with the results obtained from three configuration-space wedges (magenta, Sánchez *et al.*, 2016, *in prep.*). The empty symbols are an systematic error indicator summed over all periodic boxes (see text) and the shaded gray band shows the statistical error that is expected for the constraints obtained from DR12 combined sample in the high-redshift bin.

Table 5.5 – Results of the distortion and growth parameters from RSD-type full-shape fits with the 'gRPT+RSD' model to the Fourier-space wedges of the periodic challenge boxes listed in Table 5.4, fitting wavenumber bins in the range $0.01\ h\,\mathrm{Mpc}^{-1} \leq k_i \leq 0.2\ h\,\mathrm{Mpc}^{-1}$. Δx denotes the deviation between the best-fit result, obtained as mean of the MCMC simulation, and the expected value, while σ_x is the standard deviation found from the chains (for $x \in \{q_\parallel, q_\perp, f\,\sigma_8\}$). For the boxes A–E, an axis-averaged measurement was performed to reduce the sampling noise of the reshift-space power spectrum. As only a single realization exists for each box type, the results are none the less variance-limited for the normal and averaged measurements.

	Two wedges						Three wedges					
Box	$\Delta q_\parallel$	$\sigma_{q_\parallel}$	$\Delta q_\perp$	$\sigma_{q_\perp}$	$\Delta f\,\sigma_8$	$\sigma_{f\,\sigma_8}$	$\Delta q_\parallel$	$\sigma_{q_\parallel}$	$\Delta q_\perp$	$\sigma_{q_\perp}$	$\Delta f\,\sigma_8$	$\sigma_{f\,\sigma_8}$
	Normal measurements											
A	0.021	0.014	0.007	0.008	0.034	0.031	0.027	0.009	0.004	0.006	0.031	0.028
B	0.021	0.014	−0.003	0.008	0.049	0.033	0.028	0.010	−0.006	0.006	0.044	0.032
C	0.033	0.017	−0.005	0.007	0.068	0.039	0.029	0.013	−0.005	0.006	0.037	0.036
D	−0.002	0.017	0.006	0.007	0.070	0.035	0.005	0.012	0.002	0.006	0.049	0.034
E	−0.008	0.017	0.006	0.007	0.085	0.044	0.009	0.014	−0.000	0.007	0.070	0.046
F	0.024	0.014	0.002	0.008	0.016	0.032	0.033	0.009	−0.002	0.006	−0.014	0.038
G	0.018	0.015	−0.008	0.008	0.034	0.034	0.028	0.011	−0.004	0.007	0.017	0.038
	Axis-averaged											
A	0.017	0.015	0.007	0.007	0.013	0.031	0.026	0.010	0.004	0.006	0.010	0.028
B	0.015	0.017	0.000	0.008	0.032	0.034	0.025	0.011	−0.003	0.006	0.024	0.031
C	0.012	0.016	0.005	0.007	−0.005	0.032	0.005	0.011	0.006	0.006	−0.012	0.030
D	0.001	0.014	0.006	0.007	−0.025	0.027	0.001	0.011	0.003	0.006	−0.037	0.028
E	0.000	0.016	0.007	0.007	−0.009	0.040	0.013	0.012	0.001	0.006	−0.023	0.038

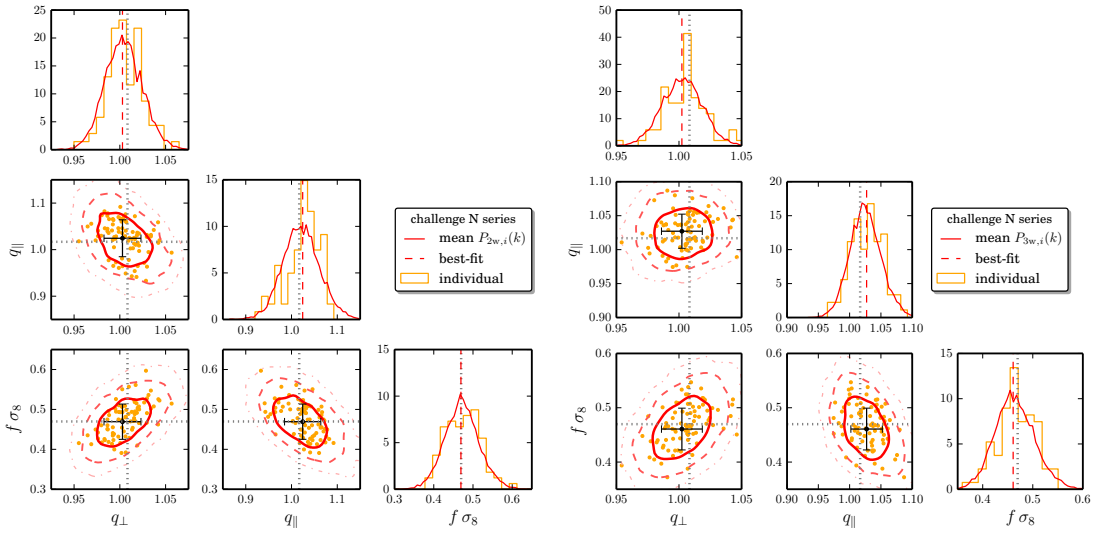

Figure 5.5 – Marginalized results for $q_\parallel$, $q_\perp$, and $f\,\sigma_8(\bar{z})$ from 'gRPT+RSD' model fits to the mean challenge N series measurement of two (left-hand panel) and three (right-hand panel) Fourier space wedges fitting wavenumbers in the range $0.02\ h\,\mathrm{Mpc}^{-1} \leq k_i \leq 0.2\ h\,\mathrm{Mpc}^{-1}$. The mean chain parameters are indicated as dashed red lines in the histograms and as a filled black circle with the standard deviation as errors in the 2D plots. The best-fit parameters for each of the 84 individual mock measurements are indicated as orange dots in the 2D plots. Their histogram is plotted over the mean chain histogram in fainter colors. The results using two wedges is similarly accurate but less precise (please note the different plotting ranges); just as for the MINERVA fits in Figure 5.2, the $q_\perp$–$q_\parallel$ degeneracy has been broken in the three-wedges results of this CMASS-like sample. In addition to the MINERVA case, this sample is affected by the survey selection function and, thus, the window function effect has been taken into account.

comparison, we also plot the results obtained from fitting three configuration-space wedges (magenta squares Sánchez *et al.*, 2016, *in prep.*). For this test, the redshift-space clustering measurements were performed by averaging the measurements obtained from taking the three different axes as LoS direction, in order to reduce the sampling noise of the reshift-space power spectrum. The precision is probed by the standard deviation of the results, $\sigma_x = \langle (x - \langle x \rangle)^2 \rangle^{1/2}$ ($x \in \{\Delta q_\perp, \Delta q_\parallel, \Delta f\,\sigma_8 / f\,\sigma_8\}$), which are indicated by the empty symbols in Figure 5.4. The Fourier space results reach the same level of precision as the configuration space results; the deviations from the true values are always much smaller than the statistical errors that are expected for the high-redshift bin of the DR12 combined sample (which are indicated by the shaded gray band in the plot). The accuracy cannot be tested with this limited set of realizations as sample variance prevents the analysis of a systematic bias. The high values of the $q_\parallel$ results from the periodic boxes A, B, F, G ($> 1\sigma$) do not indicate a failure of the model as these catalogues are obtained using different HOD implementations from the same underlying N-body realization. In fact, the small dispersion between these results shows the consistency of the modelling with respect to the failure of the model assumptions such as assembly and velocity bias.

The second part of the challenge are the 'N series' samples, a set of 84 synthetic catalogues mimicking the DR12 CMASS NGC subsample (dubbed 'cut-sky' mocks). They are designed

Table 5.6 – The results for $q_\parallel$, $q_\perp$, and $f\,\sigma_8(\bar{z})$ from RSD-type full-shape 'gRPT+RSD' fits to the mean and individual N series measurement using two and three Fourier space wedges fitting wavenumbers in the range $0.02\ h\,\mathrm{Mpc}^{-1} \leq k_i \leq 0.2\ h\,\mathrm{Mpc}^{-1}$. The measurements were obtained assuming the fiducial cosmology of the BOSS DR12 analysis (cf., Table 3.2), which is different from the true N series cosmology (cf., Table 5.4). Mean chain results are given as the weighted mean and standard deviation of the burn-in removed Markov chains. The best-fit parameters of the 84 individual fits are given by the weighted average of each individual Markov chain; here we report the mean and standard deviation of the best-fit parameters.

Configuration	Param.	Mean chains	Individual	True value
Two wedges	$q_\perp$	1.004 ± 0.021	1.006 ± 0.020	1.008
	$q_\parallel$	1.021 ± 0.041	1.025 ± 0.037	1.017
	$f\,\sigma_8(\bar{z})$	0.472 ± 0.045	0.475 ± 0.043	0.470
Three wedges	$q_\perp$	1.002 ± 0.017	1.005 ± 0.017	1.008
	$q_\parallel$	1.026 ± 0.026	1.027 ± 0.025	1.017
	$f\,\sigma_8(\bar{z})$	0.464 ± 0.040	0.468 ± 0.038	0.470

to allow for tests of a systematic bias in the obtained parameter confidence levels as they are all generated from N-body simulations assuming the same cosmological parameter (which are close to the Minerva cosmology). The catalogues are obtained with a standard HOD model (again with similar parameters to those of the Minerva HOD). As the full survey geometry is modelled, the window matrix prescription of Section 3.4 was used to take the selection function into account in the fits (in contrast to the Minerva performance tests in Section 5.2.1). Figure 5.5 shows the marginalized constraints from the N series fits in Fourier space. In agreement with the results obtained from Minerva, using three wedges (right-hand panels) improves the contraints by breaking the degeneracy between the distortion parameters $q_\perp$ and $q_\parallel$ that is present in the 2D constraints obtained from two wedges (left-hand panels). The results and expected values are listed in Table 5.6. We obtain results that are in good agreement with those inferred from Minerva, but the deviations of the mean $\alpha_\perp$ and $\alpha_\parallel$ results from the true values are a little larger than those seen for Minerva. Tests of the scale-dependency of the results (by varying k_{min}) do not show evidence for any systematic effect on the RSD fits induced by the window matrix treatment (which has a stronger effect on larger scales). Any deviations seen are significantly smaller than the statistical uncertainty obtained from a single realization.

5.2.3 Model validation with the Patchy synthetic catalogues

The Patchy mocks, described in Section 3.5.1, are used to measure the consistency and covariance between the different approaches used to analyse the BOSS DR12 combined sample. In contrast to the Minerva simulations, these mocks provide a test case on the full redshift range of the combined sample and take the survey geometry and observing systematic of BOSS into account. The power spectrum wedge measurements of the Patchy mocks are fitted in the three redshift bins defined in Table 3.1 using the window function convolution of the model wedges described in Table 3.4. For consistency with the treatment of the data, two different sets of bias, RSD, and shot-noise parameters are assumed for the low-redshift bin to account for the two potentially different galaxy populations, as discussed in Section 3.6.2. Further, we fix the

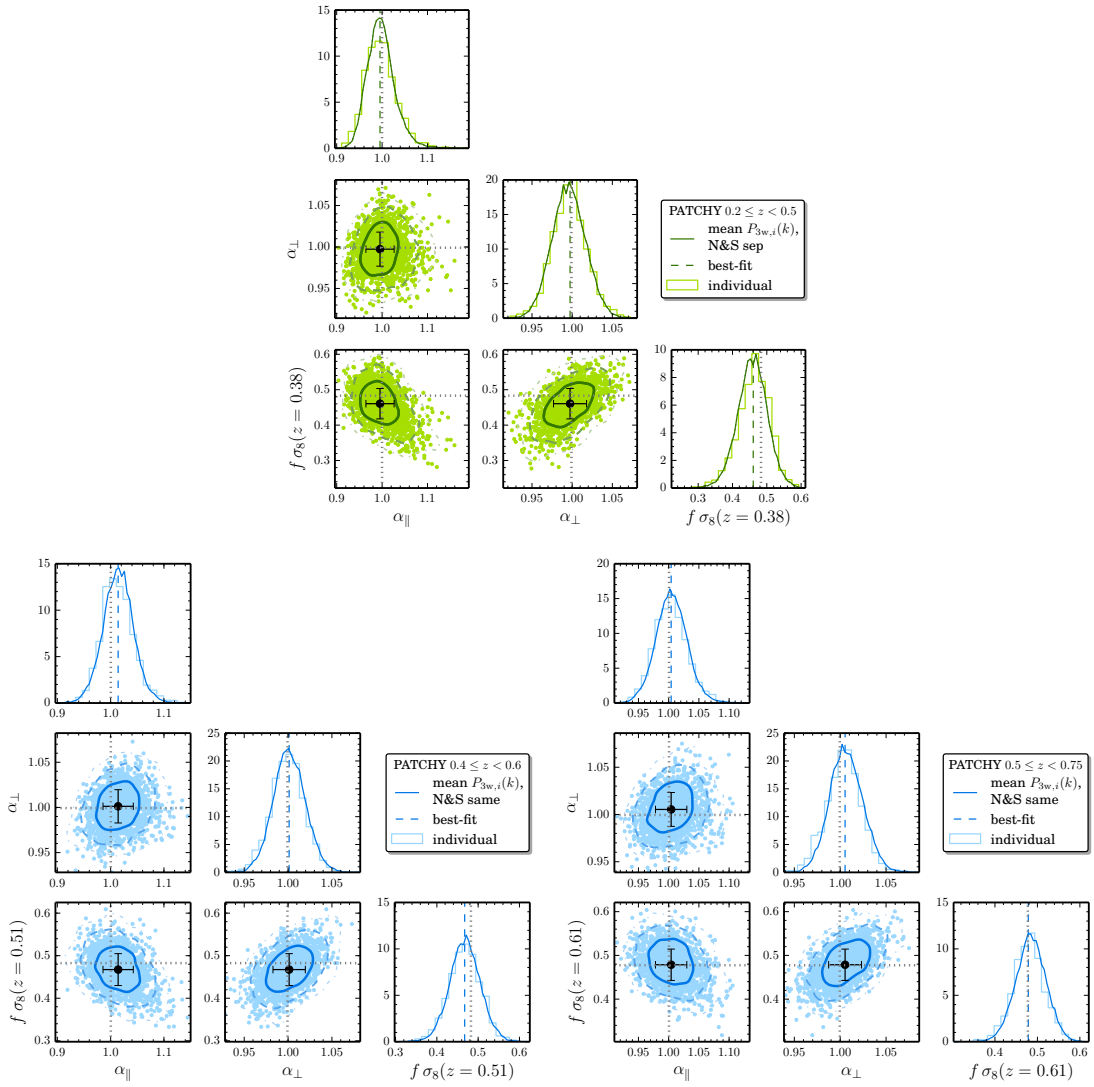

Figure 5.6 – Marginalized results for $\alpha_\parallel$, $\alpha_\perp$, and $f\,\sigma_8(\bar{z})$ from 'gRPT+RSD' model fits to the mean PATCHY measurement of three Fourier space wedges in the low (left-hand panel), intermediate (centre panel), and high (right-hand panel) redshift bins fitting wavenumbers in the range $0.02\ h\,\mathrm{Mpc}^{-1} \leq k_i \leq 0.2\ h\,\mathrm{Mpc}^{-1}$. The mean chain parameters are indicated as dashed lines in the histograms and as a filled circle with the standard deviation as errors in the 2D plots. The best-fit parameters for each of the 2045 individual mock measurements are shown as dots in the 2D plots. In the plots on the diagonals of each panels, the histogram of best-fit parameters (fainter colors) is plotted over the histogram of the posterior sample obtained from Markov chain for the mean measurments (darker colors). The results for the different redshift bins are very similar and no statistically relevant systematic biases are found (however, $f\,\sigma_8(\bar{z})$ in the low-redshift part of the sample is underestimated by roughly $.5\sigma$, see discussion in the text). The low redshift bin fits used separate bias, RSD, and shot noise parameters for NGS and SGC, whereas the other two bins used only one set of nuisance parameters.

power spectrum amplitude parameter A_p, as suggested by the tests of Section 5.2.1, reducing in this way the parameter space to 8 variables for the intermediate and high redshift bins, and 13 for the low redshift bin. As described in Section 4.1.2, the obtained parameter uncertainties

Table 5.7 – The results for $\alpha_\parallel$, $\alpha_\perp$, and $f\,\sigma_8(\bar{z})$ from 'gRPT+RSD' model fits to the mean and individual PATCHY measurement of three Fourier space wedges in all three redshift bins fitting wavenumbers in the range $0.02\ h\,\mathrm{Mpc}^{-1} \leq k_i \leq 0.2\ h\,\mathrm{Mpc}^{-1}$. Mean chain results are given as the weighted mean and standard deviation of the burn-in removed Markov chains. The best-fit parameters of the 2045 individual fits are given by the weighted average of each individual Markov chain; here we report the mean and standard deviation of the best-fit parameters. The results for the different redshift bins are very similar and no statistically relevant systematic biases are found (however, $f\,\sigma_8(\bar{z})$ in the low-redshift part of the sample is underestimated by roughly $.5\sigma$, see discussion in the text). The low redshift bin fits used separate bias, RSD, and shot noise parameters for NGS and SGC, whereas the other two bins used only one set of nuisance parameters.

Bin	Param.	Mean chains	Individual	True value
Low	$\alpha_\perp$	0.996 ± 0.021	0.996 ± 0.023	0.999
	$\alpha_\parallel$	0.998 ± 0.031	0.998 ± 0.037	1.000
	$f\,\sigma_8(\bar{z})$	0.458 ± 0.044	0.462 ± 0.048	0.483
Intermediate	$\alpha_\perp$	1.002 ± 0.019	0.999 ± 0.020	0.999
	$\alpha_\parallel$	1.014 ± 0.029	1.014 ± 0.031	1.000
	$f\,\sigma_8(\bar{z})$	0.468 ± 0.038	0.467 ± 0.039	0.483
High	$\alpha_\perp$	1.007 ± 0.019	0.004 ± 0.020	1.000
	$\alpha_\parallel$	1.005 ± 0.026	1.004 ± 0.028	1.001
	$f\,\sigma_8(\bar{z})$	0.484 ± 0.036	0.479 ± 0.038	0.478

must be rescaled by the correction factors M of equation (4.6) in order to account for the impact of sampling noise on the covariance matrix. These rescaling factors are given in Table 4.2 for $N_\mathrm{m} = 2045$.

The constraints on $\alpha_\parallel$, $\alpha_\perp$, and $f\,\sigma_8(\bar{z})$ for the fits to the mean and individual PATCHY measurements are given in Table 5.7. The 2D contours and 1D histograms of the marginalized results for all three bins are shown in Figure 5.6, overplotting the individual results as 2D scatter plot and 1D histogram in lighter colours. The mean and dispersion measured for the best-fit values of the 2045 individual measurements (listed in the 'Individual' column) are in very good agreement with the 68% confidence region (given by the mean and error in the 'Mean chains' column) of the fit to the mean measurement.

In order to decide whether the deviations between the mean best-fit results and the true values are statistically relevant and need to be treated as a systematic error (especially the underestimated $f\,\sigma_8(\bar{z})$ in the low redshift bin), we discuss these deviations in terms of the statistical error. We denote a measurement bias as $\Delta x \equiv x_\mathrm{fit} - x_\mathrm{exp}$, where x_fit is the mean marginalized parameter of the MCMC chains for the mean measurements and x_exp is the theoretical prediction for the measured quantity. The largest systematic deviations are found for $f\,\sigma_8(\bar{z})$ in the low redshift bin ($\Delta f\,\sigma_8 \approx 0.5\,\sigma_{f\,\sigma_8}$) and for $\alpha_\parallel$ in the intermediate bin ($\Delta\alpha_\parallel \approx 0.5\,\sigma_{\alpha_\parallel}$), but these are never much larger than half of the statistical error (denoted here as σ_x) for one realization.

Scale dependency of the results

In order to test whether the window function introduces any systematic bias into our analysis, we test the scale-dependency of the results of the 'gRPT+RSD' fits to the Fourier space wedges. By varying k_min, we exclude the regime at the low end of the wavenumber range from the

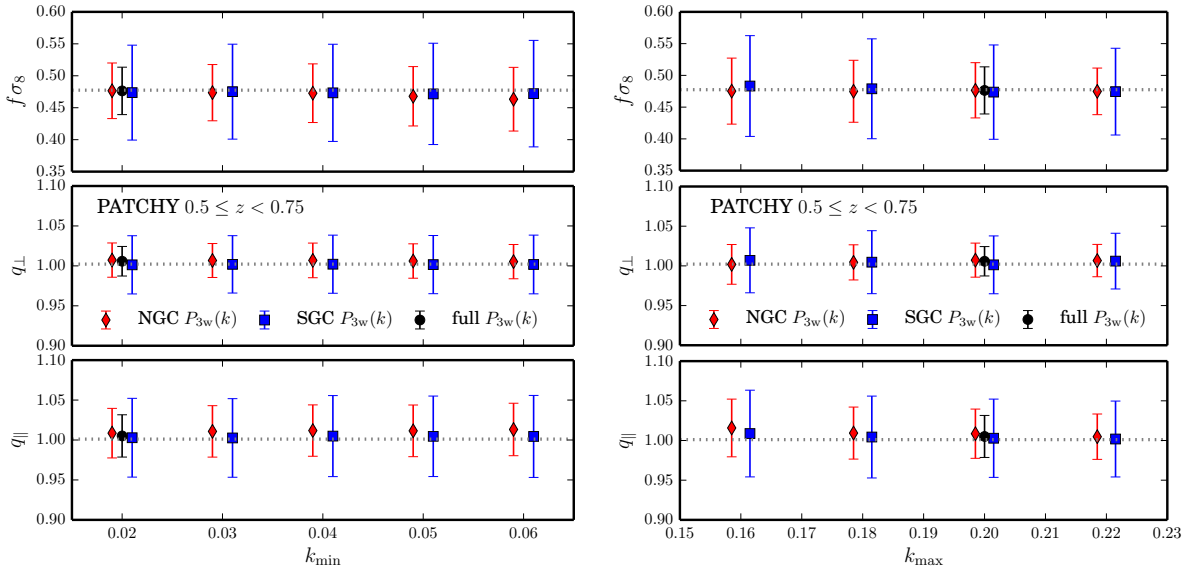

Figure 5.7 – Marginalized results for $q_\parallel$, $q_\perp$, and $f\,\sigma_8(\bar{z})$ from 'gRPT+RSD' model fits to the mean PATCHY measurement of three Fourier space wedges in the high redshift bin fitting wavenumbers in the range $k_{\rm min} \leq k_i \leq k_{\rm max}$. The results from fits to the SGC subsample are marked by red diamonds, the NGC results by blue squares. For the fiducial fitting range, $k_{\rm min} = 0.02\ h\,{\rm Mpc}^{-1}$ and $k_{\rm max} = 0.2\ h\,{\rm Mpc}^{-1}$, the results from combining NGC and SGC (describing both subsamples with the same nuisance parameters) are shown as black dots. No systematic trend with $k_{\rm min}$ (upper panel) or $k_{\rm max}$ (lower panel) can be identified. Not shown here are the results on the low and intermediate redshift bin, which also do not show indications of a scale-dependency.

analysis where the window function effect is more important. An incomplete treatment of the window function effect can be expected to result in a trend of the cosmological results with $k_{\rm min}$. As shown in the upper panel of Figure 5.7, there is no dependency of the BAO+RSD results for the mean PATCHY $P_{3{\rm w},n}(k)$ measurements on $k_{\rm min}$ (we only present the high redshift bin in this plot, but the results for the other two redshift bins show a similar behaviour). Thus, we are confident that our window matrix formalism does not induce any systematic bias into our analysis.

In a similar analysis, we test for a scale-dependency of the cosmological parameters due to inaccuracies of our clustering model for the (approximative) non-linear evolution of the clustering obtained from the PATCHY catalogues. We perform RSD-type full-shape fits with varying $k_{\rm max}$ and find consistent results, free of systematic trends with $k_{\rm max}$, even when smaller scales than our fiducial fitting range are including in the analysis (see lower panel of Figure 5.7). This is consistent with the results obtained from the fully non-linear MINERVA simulations in which non-linearities could be more pronounced that for the PATCHY mocks. For reasons of brevity, again only the case of the high redshift bin has been shown as illustration. For the other two redshift bins, a scale-dependency of the result can be excluded at the same level.

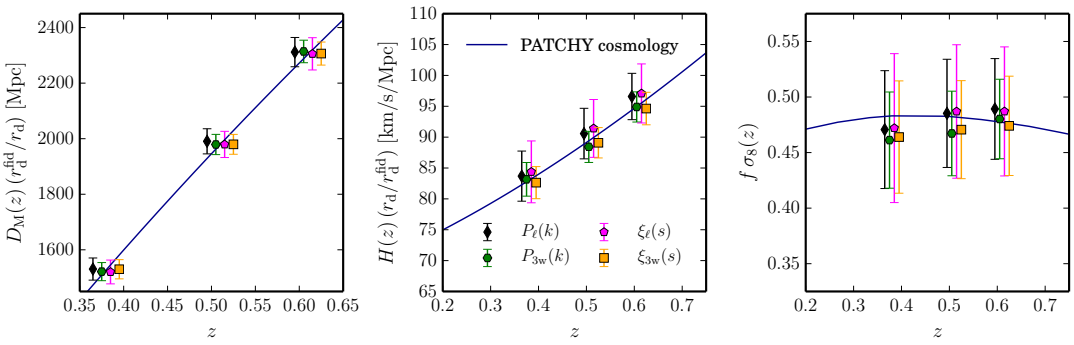

Figure 5.8 – Mean results for the $D_M(z)\,\left[r_s^{fid}(z_d)/r_s(z_d)\right]$, $H(z)\,\left[r_s(z_d)/r_s^{fid}(z_d)\right]$, and $f\,\sigma_8(\bar{z})$ best-fit values from BAO+RSD fits to the individual PATCHY measurements in the three redshift bins. The error bars indicated the dispersion across the 1000 realizations that are included in this comparison. The results from the different approaches within the BOSS collaboration — PS multipoles (Beutler *et al.*, 2016b, *in prep.*), PS wedges (this thesis), 2PCF multipoles (Satpathy *et al.*, 2016, *in prep.*), and 2PCF wedges (Sánchez *et al.*, 2016, *in prep.*) — are compared against the predictions for the PATCHY cosmology. The constraints obtained from all techniques are in excellent agreement with each other. The confidence regions obtained by fitting the clustering wedges with the 'gRPT+RSD' model are the most precise. For better visibility, the results are shifted by an offset in z.

Comparison of the results within the BOSS collaboration

The different clustering analysis techniques that contribute to the final BOSS DR12 consensus measurement (Anderson *et al.*, 2016, *in prep.*) are PS multipoles (Beutler *et al.*, 2016b, *in prep.*), PS wedges (this thesis and Grieb *et al.*, 2016b, *in prep.*), 2PCF multipoles (Satpathy *et al.*, 2016, *in prep.*), and 2PCF wedges (Sánchez *et al.*, 2016, *in prep.*). In order to derive a consensus measurement, the covariance between the results obtained with these approaches is estimated from the respective results on a subset of the first 1000 PATCHY mocks. The comparison of the methods is shown in Figure 5.8 where the BAO distance and growth measurements, $D_M(z)\,\left[r_s^{fid}(z_d)/r_s(z_d)\right]$, $H(z)\,\left[r_s(z_d)/r_s^{fid}(z_d)\right]$, and $f\,\sigma_8(\bar{z})$, are compared against the predictions for the PATCHY cosmology. Good consistency is found between the individual confidence regions; the methods using the 'gRPT+RSD' model (i.e., clustering wedges in configuration and Fourier space) provide the tightest constraints.

The generated cross-analysis covariance matrix will be discussed in (Anderson *et al.*, 2016, *in prep.*). As the cross-correlation between the measurements is below unity, it is beneficial to combine the different analysis techniques into a consensus constraint. This constraint will be dominated by the 'gRPT+RSD' results, but the other approaches will increase the precision and the accuracy (as minor systematics of an individual technique can be compensated by the others).

6

Cosmological implications of the BOSS DR12 Fourier-space clustering wedges

"In a nutshell, the universe is 4% visible, 23% undetectable and 73% unimaginable. Welcome to the cosmos, full of mass you can measure but not manhandle, driven by a force you can infer but not explain."

Tim Radford

In this chapter, the clustering wedges measured from the final combined sample of BOSS in Fourier space are used to infer constraints in a cosmological context. Thus, this chapter contains the main results of this thesis. The BAO distance and growth fits to the power spectrum wedges of each redshift bin separately are discussed in Section 6.1. A comparison with the results of the corresponding configuration space analysis and other complementary approaches for the clustering analysis on the DR12 combined sample can be found in Section 6.2. Section 6.3 lists the additional cosmological dataset used in the derivation of cosmological constraints from the clustering measurements. Implications for various cosmological parameter spaces (including the standard model and its most important extensions, as described in Section 6.4) from our measurements in combination with *Planck* and SN Ia data are discussed in Section 6.5.

6.1 RSD-type full-shape measurements of the BAO distance and growth using Fourier-space wedges

In this section, we present the anisotropic BAO and RSD constraints derived from the full-shape clustering analysis of the BOSS DR12 combined sample as 'single-probe' measurement (assuming a *Planck* 2015 input power spectrum, whose parameters are listed as 'template' in Table 3.2). For this analysis, the three power spectrum wedges of the combined sample are fit-

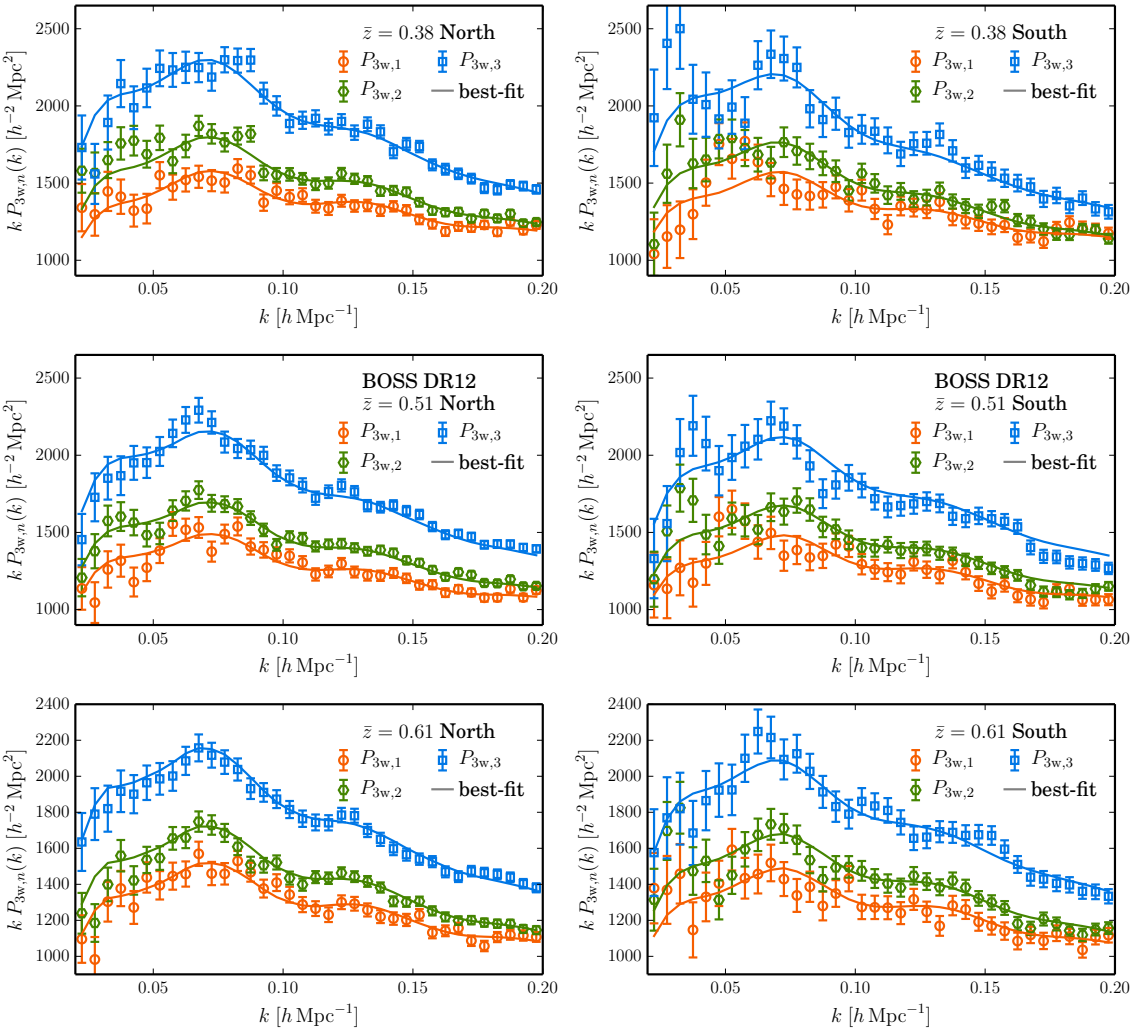

Figure 6.1 – The power spectrum wedges for NGC and SGC of the combined sample in the low (upper) and high (lower panel) redshift bin defined in Table 3.1. Error bars are derived as the square root of the diagonal entries of Patchy covariance matrix (see Section 4.5.1). The model prediction are for the maximum-likelihood BAO+RSD parameters using a best-fit *Planck* 2015 input power spectrum. The low redshift bin fits used separate bias, RSD, and shot noise parameters for NGC (left panels) and SGC (right panels), whereas the intermediate and high bins used only one set of nuisance parameters.

ted using the 'gRPT+RSD' model, whose implementation is described in Chapter 5.[1] The power spectrum wedges of the Northern (NGC) and Southern (SGC) galactic cap of the combined sample are plotted in Figure 6.1. The solid lines show the model predictions corresponding to the maximum-likelihood parameters from BAO+RSD fits to each redshift bin using an input power spectrum based on the best-fit *Planck* 2015 cosmological parameters. The model predictions

[1]Unless stated otherwise, all results in this section have been obtained by fitting the fiducial wavenumber range $0.02\,h\,\mathrm{Mpc}^{-1} \leq k \leq 0.2\,h\,\mathrm{Mpc}^{-1}$ using the reference covariance matrix obtained from the Patchy mock catalogues (see Section 4.5.1).

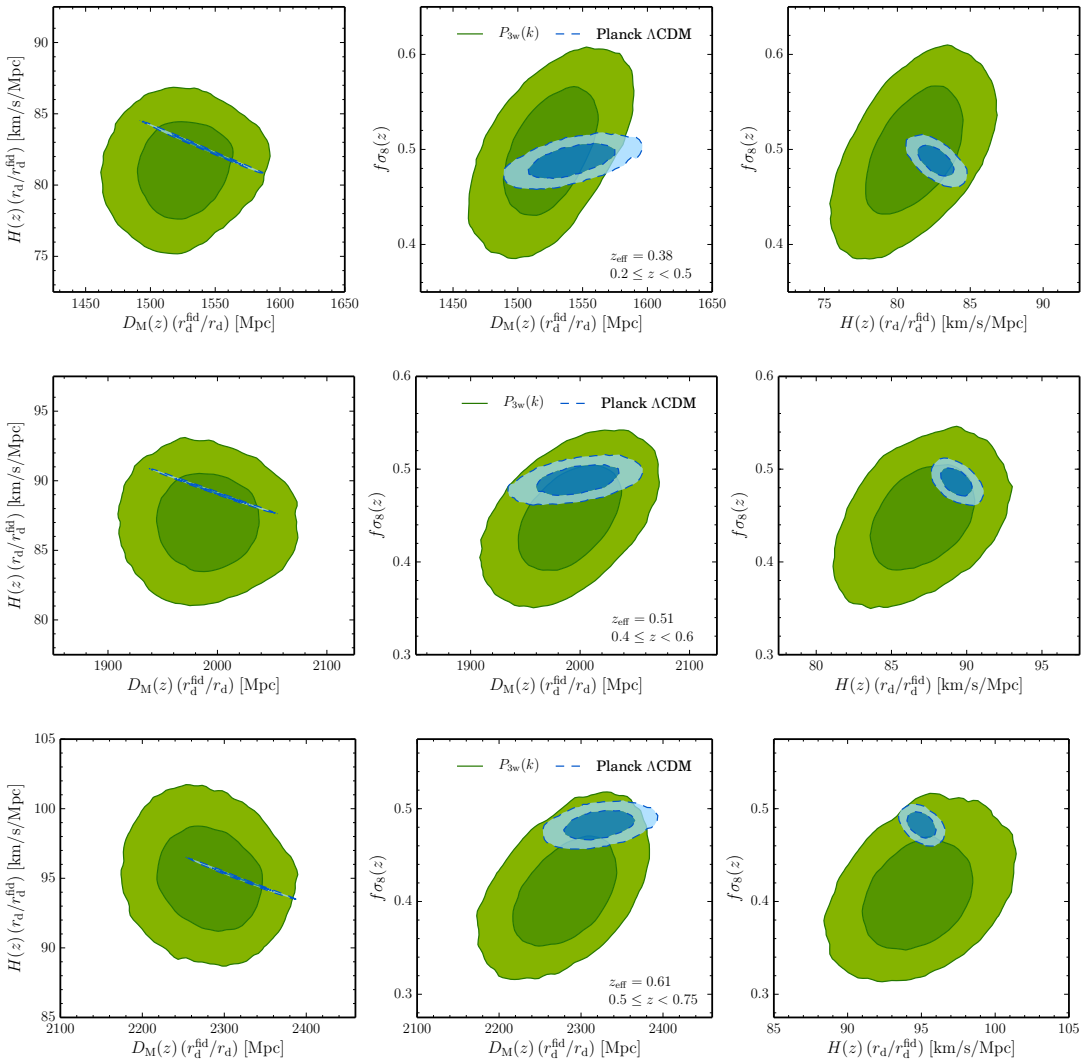

Figure 6.2 – The regions of 68% and 95% confidence level (CL) in the marginalized 2D posteriors of the comoving transverse distance and the sound horizon ratio, $D_{\rm M}(z)\,\left[r_{\rm s}^{\rm fid}(z_{\rm d})/r_{\rm s}(z_{\rm d})\right]$, the Hubble parameter and the sound horizon ratio, $H(z)\,\left[r_{\rm s}(z_{\rm d})/r_{\rm s}^{\rm fid}(z_{\rm d})\right]$, and the growth parameter $f\,\sigma_8(\bar{z})$ from BAO+RSD fits to the DR12 combined sample in the low (upper panel), intermediate (middle panel), and high redshift bin (lower panel). For these MCMC-estimated contours plotted in green, three power spectrum have been fitted in the wavenumber range $0.02\ h\,{\rm Mpc}^{-1} \leq k \leq 0.2\ h\,{\rm Mpc}^{-1}$ using the covariance from 2045 PATCHY mocks. The low redshift bin fits used separate bias, RSD, and shot noise parameters for NGC (left panels) and SGC (right panels), whereas the results in the high redshift bin were obtained using only one set of nuisance parameters. These measurements represent the main results of this thesis. For comparison, the theoretical predictions for the standard cosmological model (ΛCDM) from the *Planck* 2015 TT+lowP (Ade *et al.*, 2015) observations are overplotted as blue confidence regions.

Table 6.1 – The results of the BAO+RSD fits to the DR12 combined sample in terms of the comoving transverse distance and the sound horizon ratio, $D_{\rm M}(z)\ \left[r_{\rm s}^{\rm fid}(z_{\rm d})/r_{\rm s}(z_{\rm d})\right]$, the Hubble parameter and the sound horizon ratio, $H(z)\ \left[r_{\rm s}(z_{\rm d})/r_{\rm s}^{\rm fid}(z_{\rm d})\right]$, and the growth rate parameter $f\,\sigma_8(\bar{z})$. We also give the ratio of the angle-averaged BAO distance and fiducial sound horizon scale, $D_{\rm V}(z)/r_{\rm s}^{\rm fid}$, and the Alcock-Paczynski parameter $F_{\rm AP}(z)$ as these are usually used for cosmological inferences with CosmoMC (Lewis & Bridle, 2002). For these fits, three power spectrum have been fitted in the wavenumber range $0.02\ h\,{\rm Mpc}^{-1} \leq k \leq 0.2\ h\,{\rm Mpc}^{-1}$ using the covariance matrix from 2045 Patchy mocks. Besides the mean values from the chains, we given the limits for a confidence level of 68 % (and 95% in parenthesis).

Parameter	Unit	Low	Intermediate	High
$f\,\sigma_8(\bar{z})$	–	$0.498^{+0.044}_{-0.045}\ \left(^{+0.088}_{-0.090}\right)$	$0.448 \pm 0.038\ \left(^{+0.076}_{-0.078}\right)$	$0.409 \pm 0.040\ \left(^{+0.086}_{-0.077}\right)$
$D_{\rm M}(z)\ \left[\frac{r_{\rm d}^{\rm fid}}{r_{\rm d}}\right]$	Mpc	$1525 \pm 24\ \left(^{+52}_{-51}\right)$	$1990 \pm 32\ (\pm 66)$	$2281^{+42}_{-43}\ \left(^{+83}_{-88}\right)$
$H(z)\ \left[\frac{r_{\rm d}}{r_{\rm d}^{\rm fid}}\right]$	$\mathrm{km\,s^{-1}\,Mpc^{-1}}$	$81.2^{+2.2}_{-2.3}\ \left(^{+4.6}_{-4.7}\right)$	$87.0^{+2.3}_{-2.4}\ \left(^{+4.7}_{-4.8}\right)$	$94.9 \pm 2.5\ \left(^{+5.3}_{-5.1}\right)$
$D_{\rm V}(z)/r_{\rm s}^{\rm fid}$	–	$10.04 \pm 0.14\ \left(^{+0.27}_{-0.29}\right)$	$12.92 \pm 0.18\ \left(^{+0.37}_{-0.38}\right)$	$14.60 \pm 0.24\ \left(^{+0.46}_{-0.48}\right)$
$F_{\rm AP}(z)$	–	$0.413 \pm 0.014\ \left(^{+0.028}_{-0.029}\right)$	$0.578 \pm 0.018\ \left(^{+0.035}_{-0.038}\right)$	$0.722 \pm 0.022\ \left(^{+0.044}_{-0.045}\right)$

were convolved with the window matrix (see Section 3.4). In the low redshift bin, we use two different sets of nuisance parameters for the bias and RSD model to account for the fact that, as discussed in Section 3.6.2, the NGC and SGC samples might contain two slightly different galaxy population at low redshifts. For the high redshift bin, the NGC–SGC difference in the model prediction results only from the different window matrices.

The BAO+RSD fits are performed using the Markov chain Monte Carlo (MCMC) technique by means of a modified version of CosmoMC (Lewis & Bridle, 2002), adapted to compute our 'gRPT+RSD' model predictions as described in Sánchez *et al.* (2016, *in prep.*). As described in Section 5.1.2, the parameter space $\mathcal{X}$ for our RSD-type full-shape fits comprises of 8 free parameters for the intermediate and high redshift bin and 13 for the low redshift bin. The results of the fits are given by the posterior distribution statistics taken from the chains as discussed in Appendix A.2.2. Using the definitions of the AP parameters in equation (5.6) and the fiducial distances given in Table 5.1, the results are expressed in terms of the combinations, $D_{\rm M}(z)\ \left[r_{\rm s}^{\rm fid}(z_{\rm d})/r_{\rm s}(z_{\rm d})\right]$, $H(z)\ \left[r_{\rm s}(z_{\rm d})/r_{\rm s}^{\rm fid}(z_{\rm d})\right]$, and $f\,\sigma_8(\bar{z})$. The 68% and 95% confidence levels (CL) of the two-dimensional posterior distributions of these parameters for fits of the BOSS DR12 power spectrum wedges are show as green contours in Figure 6.2 (the panels correspond to the low, intermediate, and high redshift bin from top to bottom). The resulting confidence intervals (1- and 2-sigma) of all redshift bins are listed in Table 6.1. The blue contours correspond to the ΛCDM predictions from the *Planck* 2015 TT+lowP (Ade *et al.*, 2015) measurements (in the following labelled as *Planck* predictions). We find excellent consistency of these measurements given our errors.

As BAO distance measurements are often expressed in terms of ratio of the angle-averaged distance and the fiducial sound horizon scale, $D_{\rm V}(z)/r_{\rm s}^{\rm fid}$ and the Alcock-Paczynski parameter $F_{\rm AP}(z)$, we give these derived quantities as well in Table 6.1. The 2D posterior contours of these parameters, together with $f\,\sigma_8(\bar{z})$, can be more accurately described by a Gaussian approximation than those for $D_{\rm M}(z)$, $H(z)$ and $f\,\sigma_8(\bar{z})$. Thus, this combination of parameters will be used

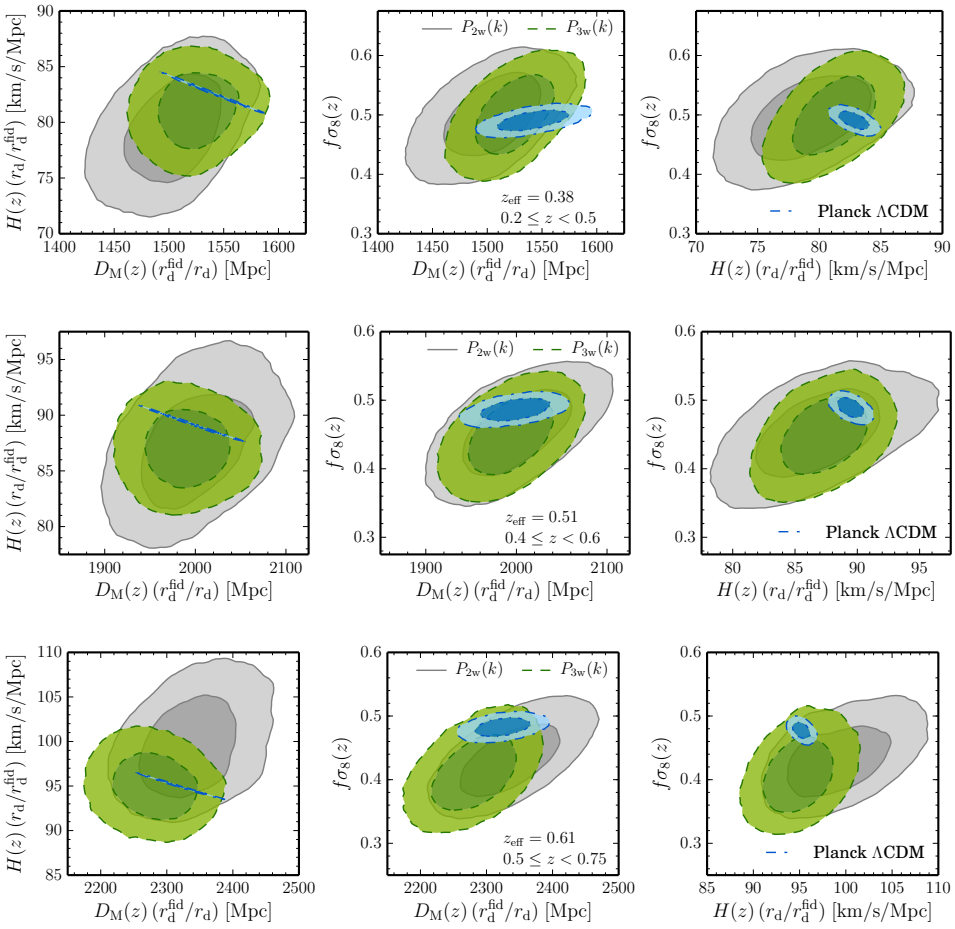

Figure 6.3 – The 2D posteriors of the comoving transverse distance and the sound horizon ratio, $D_M(z)\left[r_s^{fid}(z_d)/r_s(z_d)\right]$, the Hubble parameter and the sound horizon ratio, $H(z)\left[r_s(z_d)/r_s^{fid}(z_d)\right]$, and the growth parameter $f\,\sigma_8(\bar{z})$ from BAO+RSD fits to the DR12 combined sample in the low (upper panel), intermediate (centre panel), and high (lower panel) redshift bin. For this fit, two (gray contours) and three (green contours) power spectrum wedges have been fitted in the wavenumber range $0.02\,h\,\mathrm{Mpc}^{-1} \leq k \leq 0.2\,h\,\mathrm{Mpc}^{-1}$ using the reference covariance matrix obtained from PATCHY mocks (corresponding to the chosen number of wedges).

to derive the RSD consensus constraints in Anderson *et al.* (2016, *in prep.*) (see also the comparison the the results obtained from other analysis techniques that have been applied within the BOSS collaboration in Section 6.2.2).

6.1.1 Internal consistency checks

In this section, we test our BOSS DR12 BAO+RSD measurements presented in the previous section, for robustness against various potential sources of systematics, such as the set of mocks used to obtain the covariance matrix, the galaxy population discrepancies between the NGC and SGC subsamples described in Section 3.6.2, and effects indicated by the scale-dependency of the results.

Robustness with respect to the number of clustering wedges

A change in the number of wedges requires an adoption of the covariance matrix and window matrix, accordingly. Thus, changing the number of wedges serves as an comprehensive test for the robustness of the measurements; however, the changed information content has to be taken into account when results are compared.

In Figure 6.3, we compare the regions of 68% and 95% CL from the geometric and growth measurements obtained from a BAO+RSD fit to two (gray contours) and three (green contours) power spectrum wedges using the same wavenumber range $0.02\ h\,\mathrm{Mpc}^{-1} \leq k \leq 0.2\ h\,\mathrm{Mpc}^{-1}$ and the corresponding reference covariance matrix obtained from PATCHY mocks. As already seen in the tests performed on the MINERVA catalogues discussed in Section 5.2.1, the constraints from two wedges have a stronger degeneracy in the $D_\mathrm{M}(z)$–$H(z)$ parameter plane that is broken when using three wedges. This results in tighter confidence intervals obtained for the Hubble parameter, while the angular diameter distance constraints improve less significantly. As the constrained region along the $D_\mathrm{M}(z)$–$H(z)$ degeneracy using two clustering wedges prefers lower values for both quantities than the three-wedges results in the low redshift bin, but higher values in the high redshift bin, it is no surprise that the two- and three-wedges confidence regions are centred on each other for the overlapping intermediate bin.

The overall picture shows good consistency between the two measurement configurations, justifying the choice of using the three-wedges case as main result of this work and to use them for the combination with other cosmological probes.

Validity of the covariance matrix from the mocks

As a test of the robustness of the full-shape results, we perform cross-checks by repeating the RSD-type full-shape fits with the alternative QPM covariance matrices described in Section 4.5.2. Due to the larger fiducial volume of the PATCHY mocks (corresponding to the larger density parameter Ω_M), the volume of the PATCHY mocks is smaller than for the QPM mocks. As the variance of the power spectrum is inversely proportional to the volume, we expect slightly tighter constraints for using the QPM matrix.

As shown in Figure 6.4, the contours of 68% and 95% CL for combinations of the parameters $D_\mathrm{M}(z)\ \left[r_\mathrm{s}^\mathrm{fid}(z_\mathrm{d})/r_\mathrm{s}(z_\mathrm{d})\right]$, $H(z)\ \left[r_\mathrm{s}(z_\mathrm{d})/r_\mathrm{s}^\mathrm{fid}(z_\mathrm{d})\right]$, and $f\,\sigma_8(\bar{z})$ obtained from BAO+RSD fits using the same data and the two different covariance matrices are in good agreement with each other (plotted are the low and high redshift bin in the top and bottom panel, respectively; the results for the intermediate bin are similar). However, the 68% and 95% confidence regions are slightly smaller in the QPM case for the low redshift bin.

We check for potential inconsistencies between the statistical errors for the distance and growth measurements obtained from the set of PATCHY mocks and the errors measured on the data. Figure 6.5 shows the distribution of errors on $\alpha_\parallel$, $\alpha_\perp$, and $f\,\sigma_8(\bar{z})$ obtained from the BAO+RSD fits using the 2045 individual PATCHY measurements of the power spectrum wedges in the low, intermediate and high redshift bin (from the upper to lower panel). The error of the fit to the mean measurement of the power spectrum wedges is indicated by a dashed vertical line. For comparison, the size of the marginalized constraints of the DR12 combined sample fits are

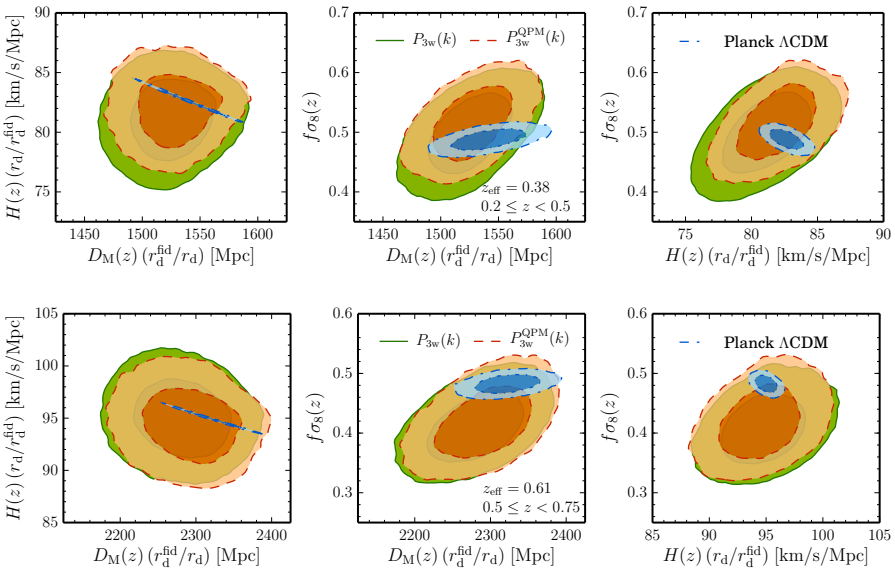

Figure 6.4 – The 68% and 95% CL regions of the 2D posteriors of the comoving transverse distance and the sound horizon ratio, $D_M(z)\left[r_s^{fid}(z_d)/r_s(z_d)\right]$, the Hubble parameter and the sound horizon ratio, $H(z)\left[r_s(z_d)/r_s^{fid}(z_d)\right]$, and the growth parameter $f\,\sigma_8(\bar{z})$ from BAO+RSD fits to the DR12 combined sample in the low (upper panel) and high (lower panel) redshift bin. For these fits, three power spectrum wedges have been fitted in the wavenumber range $0.02\ h\,\mathrm{Mpc}^{-1} \leq k \leq 0.2\ h\,\mathrm{Mpc}^{-1}$ using the reference PATCHY (green) and the alternative QPM (orange) covariance matrix.

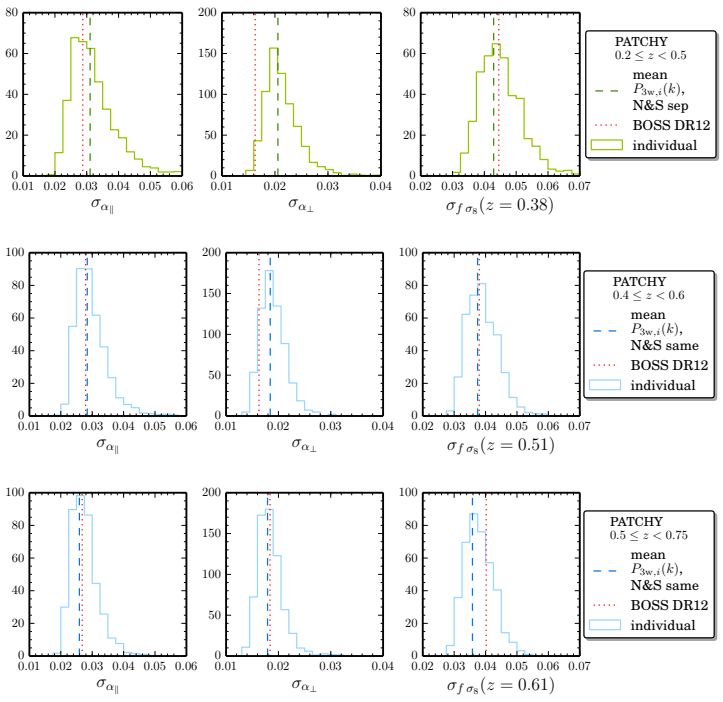

Figure 6.5 – Histograms of the marginalized error on $\alpha_\parallel$, $\alpha_\perp$, and $f\,\sigma_8(\bar{z})$ from 'gRPT+RSD' model fits to the individual measurement of three Fourier space wedges of 2045 PATCHY mocks in the low (left-hand panel), intermediate (centre panel), and high (right-hand panel) redshift bins fitting wavenumbers in the range $0.02\ h\,\mathrm{Mpc}^{-1} \leq k_i \leq 0.2\ h\,\mathrm{Mpc}^{-1}$. The error of the fits to the mean measurement is shown by vertical line. For comparison, the error from the BAO+RSD fits to the real data has been included by a red dashed line.

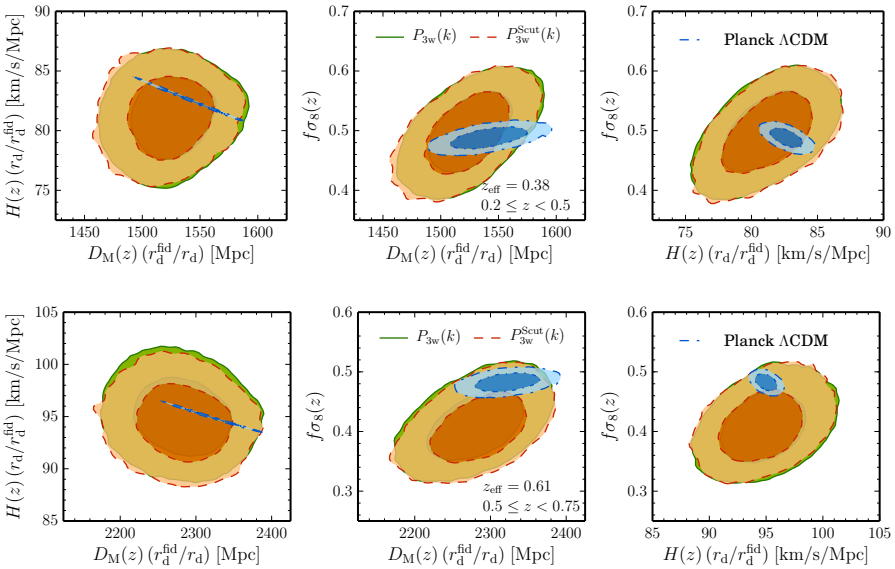

Figure 6.6 – The 68% and 95% CL contours of the 2D posteriors of the comoving transverse distance and the sound horizon ratio, $D_M(z)\left[r_s^{fid}(z_d)/r_s(z_d)\right]$, the Hubble parameter and the sound horizon ratio, $H(z)\left[r_s(z_d)/r_s^{fid}(z_d)\right]$, and the growth parameter $f\,\sigma_8(\bar{z})$ from BAO+RSD fits to the DR12 combined sample (green) and the colour-corrected version (orange, see discussions in Section 3.6.2) in the low (upper) and high (lower panel) redshift bin. For these fits, three power spectrum wedges have been fitted in the wavenumber range $0.02\ h\,\mathrm{Mpc}^{-1} \leq k \leq 0.2\ h\,\mathrm{Mpc}^{-1}$ using the PATCHY covariance matrix.

indicated by a dotted red line. In most cases, the errors obtained from the data are close to the peak of the distribution, except for the error on the low-redshift $\alpha_\perp$, which is in the lower tail of the error distribution on PATCHY mocks. Thus, we conclude that the errors from the data are largely consistent with the distribution of errors measured from PATCHY.

Robustness with respect to photometric colour shifts

As discussed in Section 3.6.2, differences in the photometric calibration in the two galactic hemispheres of the BOSS surveys might have led to slightly different galaxy populations probed by the NGC and SGC subsamples. Here we present the robustness of our main results with respect to these discrepancies by repeating the RSD+BAO fits with the SGC subsample replaced by the colour-corrected one. In Figure 6.6 we show the constraints on $D_M(z)\left[r_s^{fid}(z_d)/r_s(z_d)\right]$, $H(z)\left[r_s(z_d)/r_s^{fid}(z_d)\right]$, and $f\,\sigma_8(\bar{z})$ from BAO+RSD fits to the DR12 combined sample (green) and the colour-corrected version (orange) in the low (upper) and high (lower panel) redshift bin; the results in the intermediate bin are similar. The difference in the 2D posteriors are negligible, as the differences in the galaxy populations are correctly absorbed into the nuisance parameters of the bias model.

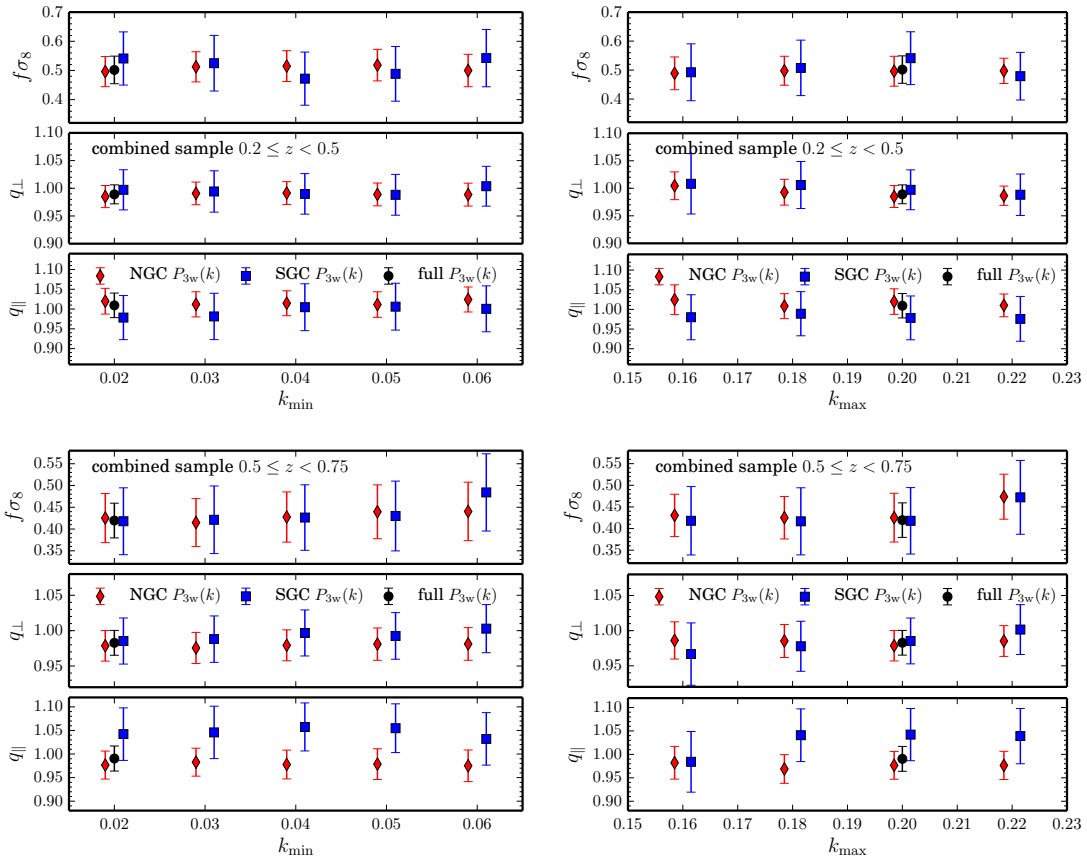

Figure 6.7 – *Left panels:* Marginalized results for $q_\parallel$, $q_\perp$, and $f\,\sigma_8(\bar{z})$ from 'gRPT+RSD' model fits to the DR12 combined sample measurement of three Fourier space wedges in the low (upper panels) and high redshift bins (lower panels) fitting wavenumbers in the range $k_{\rm min} \leq k_i \leq 0.2\ h\,{\rm Mpc}^{-1}$. The results from fits to the SGC are marked by red diamonds, the NGC results in blue squares. For the fiducial fitting range, $k_{\rm min} = 0.02\ h\,{\rm Mpc}^{-1}$, the results from combining NGC and SGC (describing both subsamples with the same nuisance parameters) are shown as black dots. Some deviations are expected from the negligence of some modes by tighter fitting ranges and no systematic trend with $k_{\rm min}$ can be identified.
Right panels: Marginalized results for $q_\parallel$, $q_\perp$, and $f\,\sigma_8(\bar{z})$ from the same fits of a wavenumber range $0.02\ h\,{\rm Mpc}^{-1} \leq k_i \leq k_{\rm max}$. Some deviations are expected from the negligence of some modes by tighter fitting ranges and no systematic trend with $k_{\rm max}$ can be identified.

Robustness of the BAO+RSD fits with respect to k ranges

In this subsection, we test the robustness of the BAO+RSD fits to $P_{{\rm 3w},i}(k)$ of the NGC and SGC with respect to variations of the wavenumber limits of the fitting range. By varying $k_{\rm min}$ we exclude scales that could be affected by an inaccurate treatment of the window function and/or other large-angle systematics of the survey, such as residuals from the stellar-density or seeing correction (cf., Section 3.3.1).

In the left panels of Figure 6.7, we show the results obtained by varying $k_{\rm min}$ from 0.02 to $0.06\ h\,{\rm Mpc}^{-1}$ to exclude the largest scales where these effects have the biggest impact. Due to sample variance, the inclusion of more almost uncorrelated large-scale Fourier modes is

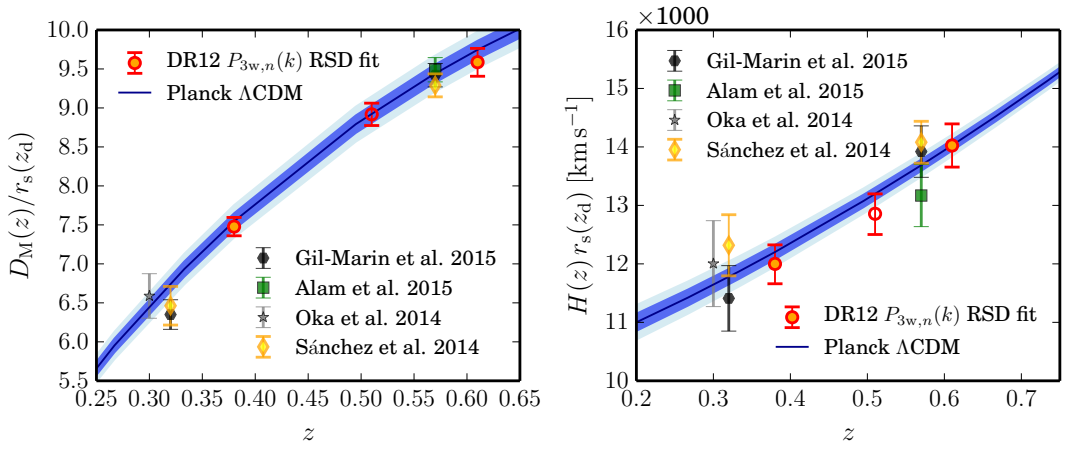

Figure 6.8 – The measurements of the comoving transverse distance over the sound horizon scale, $D_M(z)\,r_s^{-1}(z_d)$ (left-hand panel), and the Hubble parameter times the sound horizon scale, $H(z)\,r_s(z_d)$ (right-hand panel), in the three different redshift bins. The intermediate result has an empty marker in order to indicate the correlation with the results of two outer redshift bins, which are independent from each other. The *Planck* ΛCDM predictions are shown as blue bands where the darker (lighter) shaded region indicates the 1-sigma (2-sigma) region. See text for the references to the previous full-shape measurements on BOSS samples.

expected to change the results smoothly and would lead to small changes of the results with respect to k_{min}. Taking this into account, no trends of parameter constraints with k_{min} can be identified with worrying systematic effects. The variations we see can be expected from sample variance and no trends can be found in the obtained constraints.

In addition, we vary k_{max} to check whether our model fails to correctly describe the non-linearity of the data at some point in the quasi-linear regime (which could be exceptionally large compared to the non-linear evolution of the MINERVA simulations, on which the model was validated, see Section 5.2.1). In the range from $k_{max} = 0.16\ h\,\mathrm{Mpc}^{-1}$ to $0.22\ h\,\mathrm{Mpc}^{-1}$ plotted in the right panels of Figure 6.7, we again see shifts as expected as more information is included in the analysis. No clear signalling of a failure of the model is found up to the fiducial $k_{max} = 0.2\ h\,\mathrm{Mpc}^{-1}$. Thus, we are confident that our model can accurately describe the non-linear clustering seen in the data.

6.2 Comparison within the BOSS collaboration

6.2.1 Comparison with previous results

In order to verify the consistency with previous RSD-type full-shape measurements on the BAO distance and the growth rate, and to show the improvement in precision that our results represent, we here compare our main constraints to the most recent BAO+RSD analyses on the LOWZ and CMASS samples of BOSS DR11 and DR12.

Our measurements of the combinations $D_M(z)\,r_s^{-1}(z_d)$ and $H(z)\,r_s(z_d)$ in the three redshift

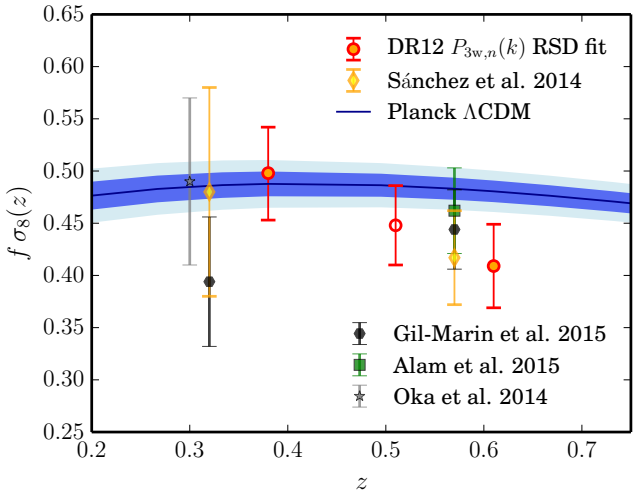

Figure 6.9 – The $f\,\sigma_8(\bar{z})$ measurements in the three different redshift bins. The intermediate result has an empty marker in order to indicate the correlation with the results of two outer redshift bins, which are independent from each other. The *Planck* ΛCDM predictions are shown as blue bands where the darker (lighter) shaded region indicates the 1-sigma (2-sigma) region. See text for the references to the previous growth measurements on BOSS samples.

bins (of which the intermediate one is not independent from the other two) are compared against *Planck* ΛCDM predictions and previous results from BOSS samples in Figure 6.8. The predecessor full-shape measurements are taken from the analysis of the Sloan DR7 LRG sample (Oka *et al.*, 2014, CF multipoles), the clustering wedges (Sánchez *et al.*, 2014, CF wedges) and the most-recent (Alam *et al.*, 2015b, CF multipoles) analysis of the DR11 CMASS sample, and the DR12 LOWZ and CMASS samples (Gil-Marín *et al.*, 2015d, PS multipoles). For the transverse distance (left-hand panel), our results are in perfect agreement with previous BOSS measurements and the Planck ΛCDM predictios; the improvement mostly corresponds to a better splitting of the redshift bins with effective volume giving a much better handle on the low-redshift distance. Similarly, the Hubble parameter (right-hand panel) is better constrained at low redshifts by our measurements compared to previous results

In Figure 6.9, we compare our $f\,\sigma_8(\bar{z})$ measurements in all three redshift bins with previous results of the same BOSS analyses as before. Again, all results are completely consistent to each other, with the LOWZ measurement of Gil-Marín *et al.* (2015d) being inconsistent with our low-redshift measurement at roughly 1σ. Differences of this order are not a surprise as our low-z measurement probes a larger volume than the LOWZ sample due to the extended redshift range. However, we measured a value of $f\,\sigma_8(\bar{z})$ lower than the *Planck* ΛCDM prediction by roughly 1σ in the high-redshift bin. This is consistent with recent CMASS measurements (Sánchez *et al.*, 2014, see also the broader discussion of previous BOSS results in Section 1.4.1).

6.2.2 Comparison with other analysis approaches applied to the BOSS DR12 combined sample

In Anderson *et al.* (2016, *in prep.*), the results presented here are combined with the companion full-shape analyses on the BOSS DR12 combined sample in Beutler *et al.* (2016b, *in prep.*, PS multipoles), Sánchez *et al.* (2016, *in prep.*, CF wedges), and Satpathy *et al.* (2016, *in prep.*, CF multipoles). As shown in Figure 6.10, all four approaches show excellent consistency between

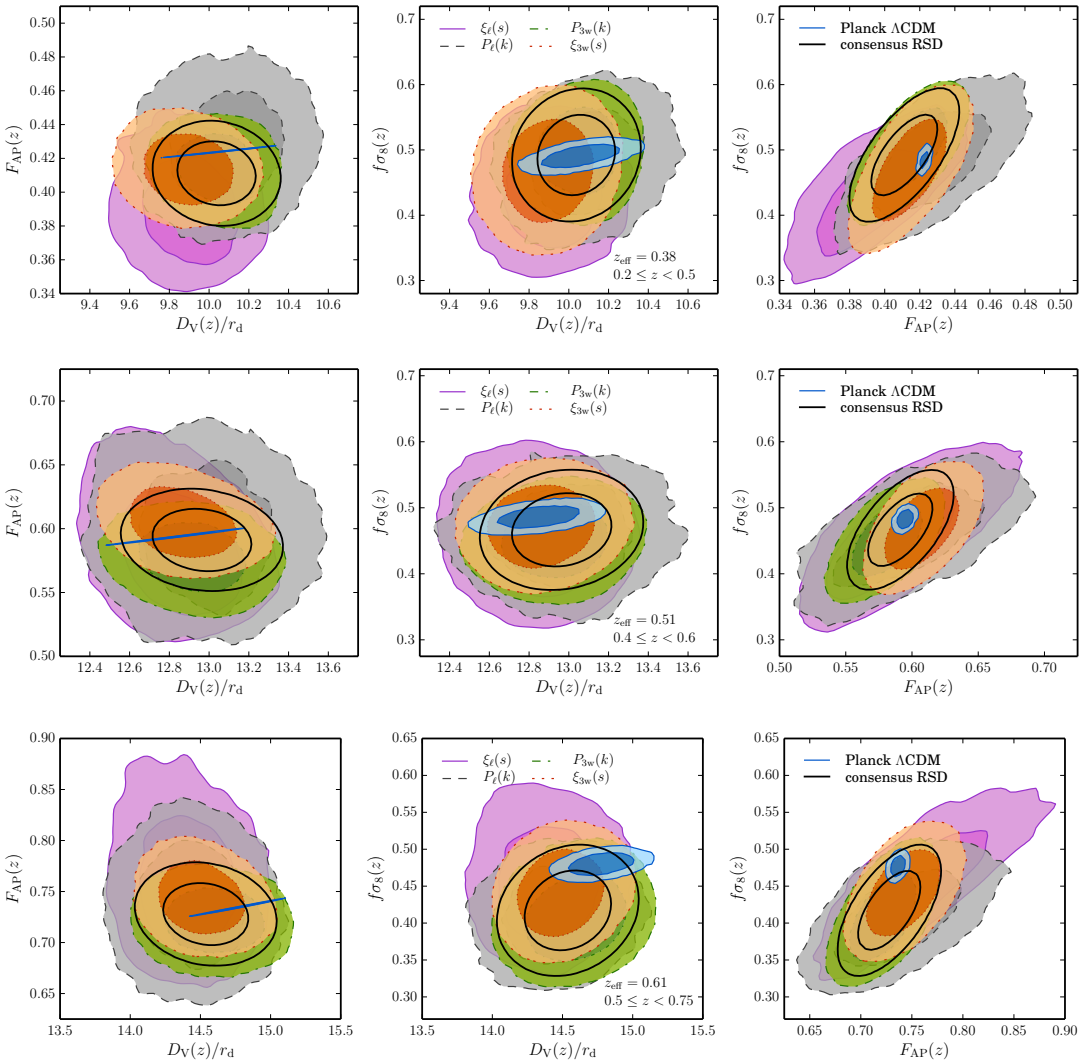

Figure 6.10 – The comparison of the 68% and 98% confidence regions in the marginalized 2D posteriors of the angle-averaged comoving distance over the sound horizon scal, $D_{\rm V}(z)\, r_{\rm s}^{-1}(z_{\rm d})$, the Alcock-Paczynski parameter, $F_{\rm AP}(z)$, and the growth parameter $f\,\sigma_8(\bar{z})$ from BAO+RSD fits to the DR12 combined sample in the low (upper panel), intermediate (middle panel), and high redshift bin (lower panel). The contours plotted in green are the fits to the three power spectrum fitted in the wavenumber range $0.02\ h\,{\rm Mpc}^{-1} \le k \le 0.2\ h\,{\rm Mpc}^{-1}$ (whose marginalized constraints on the alternative BAO+RSD parameters $D_{\rm A}(z)$, $H(z)$, and $f\,\sigma_8(\bar{z})$ are presented in Figure 6.2). The other constraints are the companion RSD analysis in Beutler *et al.* (2016b, *in prep.*, PS multipoles, black), Sánchez *et al.* (2016, *in prep.*, CF wedges, orange), and Satpathy *et al.* (2016, *in prep.*, CF multipoles, magenta). The black ellipses are the 68% and 95% confidence levels of the consensus measurements in Anderson *et al.* (2016, *in prep.*), which combine these measurements in a single set of constraints. For comparison, the theoretical ΛCDM predictions from *Planck* observations are overplotted as blue confidence regions.

each other at a level that can be expected from the cross-analysis covariance on the PATCHY fits (cf. Anderson *et al.*, 2016, *in prep.*; and also Section 5.2.3) indicating that no individual BAO+RSD fitting approach is affected by systematics that are unaccounted for. The 'gRPT+RSD' fits to clustering wedges yield the tightest constraints for the distance and growth parameters in all redshift bins.

The confidence regions of the Fourier space multipoles (Beutler *et al.*, 2016b, *in prep.*) are larger due to the smaller wavenumber range probed ($k < 0.15\ h\,\mathrm{Mpc}^{-1}$ for monopole and quadrupole, the hexadecapole is only fitted up to $0.1\ h\,\mathrm{Mpc}^{-1}$) as their modelling approach has less accuracy in the non-linear regime than ours. The results by Satpathy *et al.* (2016, *in prep.*) show consistency with the trends of our results from the restriction to two clustering wedges (see Figure 6.3), as their CLPT fits only include the 2PCF monopole and quadrupole.

Using the PATCHY covariance between the individual results, the consensus constraints are estimated by combining the results from the different approaches into a single set of constraints. This procedure assumes Gaussianity of the posterior distributions, which we find to be given at an appropriate level for each technique. The consensus constraints correctly take the covariance between the different measurements and parameters into account, resulting in final constraints that are tighter and make maximal use of the cosmological information in the data. Ideally, the combined RSD measurements also compensates for residual systematics of the different approaches (which must be minor, as the consistency check shows).

For the final consensus value presented in Anderson *et al.* (2016, *in prep.*), the full-shape measurements are combined with the post-reconstruction BAO-only measurements of Ross *et al.* (2016, *in prep.*, CF multipoles) and Beutler *et al.* (2016a, *in prep.*, PS multipoles). As density-field reconstruction improves the BAO distance constraints significantly — especially resulting in more precise measurements of $D_\mathrm{V}(z)\,r_\mathrm{s}^{-1}(z_\mathrm{d})$, — also the other derived parameters such as $f\,\sigma_8(\bar{z})$ benefit from a tighter constrained full parameter space. As the DR12 combined catalogue represents the largest galaxy sample currently available, the consensus constraints are the most precise and most accurate BAO+RSD measurement obtained to date.

6.3 Additional cosmological data sets

A redshift survey such as BOSS probes the geometry of the Universe and the growth of structure on a limited redshift range. Thus, the cclustering measurements mostly constrain the cosmological parameters that are sensitive to the late-time evolution of the Universe. In order to obtain the tightest possible cosmological constraints, the BAO+RSD or full-shape measurement must be combined with complementary cosmological probes, most importantly CMB observations, to determine the sound horizon at the drag epoch.

In this thesis, the cosmological information in the full-shape of the power spectrum wedges of the DR12 combined sample in the low and high redshift bin, modelled with the non-linear redshift-space clustering recipe 'gRPT+RSD' described in Chapter 5, is analysed. We dub our method the cosmological full-shape analysis, in order to distinguish it from the conventional BAO+RSD analysis that combines the anisotropic BAO distance and growth rate measurements with other cosmological probes using an approximative Gaussian prior obtained from the BAO+

Table 6.2 – The parameters and priors of the cosmological standard model and its extensions used in this work. All parameters have a flat prior which is uniform within the given limits and zero outside. If no prior limits and step size are given, the corresponding parameter was fixed.

Parameter	Function	Unit	Prior limits	Starting Point	Step size
		ΛCDM (flat, standard ν)			
$\Omega_b\, h^2$	Baryon density	—	0.005–0.1	0.0221	0.0001
$\Omega_c\, h^2$	CDM density	—	0.001–0.99	0.12	0.0005
$100\, \theta_{MC}$	Acoustic scale	—	0.5–10	1.0411	0.0002
τ	Optical depth to re-ionization	—	0.01–0.8	0.09	0.005
n_s	Scalar spectral tilt	—	0.8–1.2	0.96	0.002
$\ln(10^{10}\, A_s)$	Primordial perturbation amplitude	—	2–4	3.1	0.001
w	Linear EoS for DE	—	—	−1	—
Ω_K	Curvature component	—	—	0	—
$\sum m_\nu$	Neutrino mass	eV	—	0.06	—
N_{eff}	Eff. #(relativistic DoF)	—	—	3.046	—

RSD fits that used a fixed power spectrum. This other method is dubbed RSD-type full-shape fit in this thesis.

Besides our full-shape measurements, we use the temperature and low-ℓ polarization measurements obtained from the *Planck* mission (denoted as *Planck* 2015 TT+lowP, Ade *et al.*, 2015) of the *Planck* 2015 release (Adam *et al.*, 2015). We will see that *Planck*+BOSS DR12 is a very powerful cosmological probe and that including other cosmological observations in the analysis only adds little information, with the exception of supernovae of type Ia, which probe the cosmic expansion history at low redshifts via the luminosity distance scale. Hence, we make use of the joint analysis of the SDSS-II and SNLS supernova samples (JLA; Betoule *et al.*, 2014). In order to avoid a complicated systematic error budget and measurements that are correlated with the ones described above, we abstain from including other cosmological probes such as weak lensing or Ly-α forest BAO measurements.

6.4 Cosmological parameter spaces

The standard cosmological model is the 6-parameter ΛCDM model introduced in Section 1.1. It assumes that the Universe has flat spatial hypersurfaces and that its energy budget comprises of (pressureless) cold dark matter, baryonic non-relativistic matter, relativistic radiation, and Dark Energy modelled as a cosmological constant (corresponding to vacuum energy). Just as for the template cosmology, see Table 3.2, and the standard cosmological interpretation of the *Planck* CMB observations in Adam *et al.* (2015), we assume that the relativistic radiation in the ΛCDM Universe consists of a neutrino background with $\Omega_\nu h^2 = 0.00064$ besides the photon background. This corresponds to a fixed sum over the neutrino masses of $\sum \mu_\nu = 0.06\,\mathrm{eV}$. The most precise cosmological observations are very consistent with this standard paradigm (Ade *et al.*, 2015; Anderson *et al.*, 2014b).

The parameters of the ΛCDM parameter space are listed in Table 6.2. The extensions to this

Table 6.3 – The parameters and priors of the extensions to the standard cosmological model used in this work. This list contains only the modifications with respect to the base parameters listed in Table 6.2. All parameters have a flat prior which is uniform within the given limits and zero outside.

Parameter	Function	Unit	Prior limits	Starting Point	Step size
	wCDM (linear equation of state for DE)				
w	Linear EoS for DE	—	(-3)–(-0.3)	-1	0.06
	w_0w_aCDM (CPL parametrization for DE)				
w_0	Zero-point of the CPL EoS for DE	—	(-3)–(-0.3)	-1	0.06
w_a	Slope of the CPL EoS for DE	—	(-2)–2	0	0.5
	ΛCDM + γ (modified gravity)				
γ	Growth modification	—	0–3	0.55	0.1
	wCDM + γ (linear EoS for DE, modified gravity)				
w	Linear EoS for DE	—	(-3)–(-0.3)	-1	0.06
γ	Growth modification	—	0–3	0.55	0.1
	K-ΛCDM (curvature, standard ν)				
Ω_K	Curvature component	—	(-0.3)–0.3	0	0.02
	K-wCDM (curvature, linear EoS for DE)				
Ω_K	Curvature component	—	(-0.3)–0.3	0	0.02
w	Linear EoS for DE	—	(-3)–(-0.3)	-1	0.06
	ΛCDM + massive neutrinos (free $\sum m_\nu$)				
$\sum m_\nu$	Neutrino mass	eV	0–2	0.06	0.05
	$N_{\rm eff}$-ΛCDM (free #(relativistic DoF))				
$N_{\rm eff}$	Eff. #(relativistic DoF)	—	0.05-10	3.046	0.04
	wCDM + massive neutrinos (linear EoS for DE, free $\sum m_\nu$)				
$\sum m_\nu$	Neutrino mass	eV	0–2	0.06	0.05
w	Linear EoS for DE	—	(-3)–(-0.3)	-1	0.06
	$N_{\rm eff}$-ΛCDM + massive neutrinos (free $\sum m_\nu$ and #(rel. DoF))				
$\sum m_\nu$	Neutrino mass	eV	0–2	0.06	0.05
$N_{\rm eff}$	Eff. #(relativistic DoF)	—	0.05-10	3.046	0.04

parameter space that are analysed in this thesis are listed in Table 6.3. Besides the cosmological parameters in these lists, the full parameter space $\mathcal{X}$ for our cosmological fits contains the nuisance parameters of the set of cosmological probes included in the analysis. For the full-shape fits including the measurements of the BOSS DR12 clustering wedges, the additional nuisance parameters are the bias, RSD, and shot-noise parameters listed in Table 5.2. All these parameter tables contain the priors (assumed to be flat within the given range) and the step sizes of our exploration of the parameter spaces using the cosmological MCMC code CosmoMC. In addition to the given prior limits, H_0 was enforced to be in the range $20\,\mathrm{km\,s^{-1}\,Mpc^{-1}} \leq H_0 \leq 100\,\mathrm{km\,s^{-1}\,Mpc^{-1}}$. More details on how CosmoMC can be used for cosmological interference are given in Appendix A.3. The *Planck* and JLA modules are taken from the official release (version of July 2015), while the implementation of the 'gRPT+RSD' model described in Chapter 5 is addressed in greater detail in (Sánchez *et al.*, 2016, *in prep.*). The parameter spaces were explored

Table 6.4 – Mean and standard deviation of the most-relevant model parameters for fits using the cosmological standard model and usual extensions to it. The fits include at least the *Planck* 2015 TT+lowP data, which are successively combined with the power spectrum wedges $P_{3w}(k)$ of the BOSS DR12 low and high redshift bins and the JLA SN Ia data. Given are the 1-sigma and 2-sigma (in parenthesis) intervals. The constraints for curvature extensions are listed in Table 6.5, those for neutrino extensions in Table 6.6.

Parameter	*Planck* 2015	+ BOSS DR12 $P_{3w}(k)$	+ JLA SN Ia
	ΛCDM (flat, standard ν)		
Ω_M	$0.315 \pm 0.014\ \left(^{+0.030}_{-0.027}\right)$	$0.312^{+0.008}_{-0.009}\ \left(^{+0.015}_{-0.019}\right)$	$0.311^{+0.009}_{-0.010}\ \left(^{+0.015}_{-0.019}\right)$
h	$0.673^{+0.011}_{-0.010}\ (\pm 0.021)$	$0.675^{+0.007}_{-0.006}\ \left(^{+0.014}_{-0.011}\right)$	$0.676^{+0.007}_{-0.006}\ \left(^{+0.014}_{-0.011}\right)$
	wCDM (linear equation of state for DE)		
Ω_M	$0.205^{+0.054}_{-0.051}\ \left(^{+0.146}_{-0.060}\right)$	$0.306^{+0.014}_{-0.015}\ \left(^{+0.028}_{-0.030}\right)$	$0.307^{+0.011}_{-0.012}\ \left(^{+0.021}_{-0.022}\right)$
w	$-1.55^{+0.32}_{-0.30}\ \left(^{+0.66}_{-0.43}\right)$	$-1.029^{+0.070}_{-0.054}\ \left(^{+0.117}_{-0.139}\right)$	$-1.019^{+0.048}_{-0.039}\ \left(^{+0.079}_{-0.090}\right)$
	w_0w_aCDM (CPL parametrization for DE)		
w_0	$-1.44^{+0.47}_{-0.45}\ \left(^{+0.95}_{-0.72}\right)$	$-1.03 \pm 0.24\ \left(^{+0.48}_{-0.47}\right)$	$-0.98 \pm 0.11\ \left(^{+0.22}_{-0.21}\right)$
w_a	$-0.42^{+1.23}_{-1.15}\ \left(^{+2.15}_{-1.49}\right)$	$-0.06^{+0.77}_{-0.62}\ \left(^{+1.25}_{-1.44}\right)$	$-0.16^{+0.46}_{-0.36}\ \left(^{+0.75}_{-0.87}\right)$
	ΛCDM + γ (modified gravity)		
Ω_M	–	$0.312^{+0.008}_{-0.009}\ \left(^{+0.015}_{-0.019}\right)$	$0.311^{+0.009}_{-0.010}\ \left(^{+0.015}_{-0.019}\right)$
γ	–	$0.52 \pm 0.10\ \left(^{+0.20}_{-0.19}\right)$	$0.52 \pm 0.10\ (\pm 0.19)$
	wCDM + γ (linear EoS for DE, modified gravity)		
w	–	$-1.04^{+0.10}_{-0.07}\ \left(^{+0.15}_{-0.17}\right)$	$-1.02^{+0.06}_{-0.05}\ (\pm 0.10)$
γ	–	$0.56^{+0.12}_{-0.14}\ \left(^{+0.27}_{-0.23}\right)$	$0.54 \pm 0.11\ \left(^{+0.23}_{-0.21}\right)$

using the fast–slow split of cosmological and nuisance parameters, enabling the 'dragging' of the fast parameters along each Metropolis proposal of slow parameters (see Appendix A.2.1 for more details on the Metropolis-Hastings algorithm).

The proposal probability was derived from parameter covariance matrices obtained from the chains itself, updating the proposal matrix as long as $30 > R - 1 > 0.4$ (where R is the Gelman-Rubin convergence parameter that is defined in Appendix A.2.3). The initial proposal matrix has been taken from the corresponding official Planck chains for the probed parameter space (or preliminary previous runs if available). The chains were stopped when they reached $R < 1.02$, which is the usual limit to consider Markov chains as being sufficiently converged to the stationary posterior distribution to allow the determination of robust cosmological constraints.

6.5 Cosmological implications of the combined measurements

Combining the results from our analysis with *Planck* and SN Ia data in cosmological full-shape fits, we infer the regions of 68% and 95% confidence level for the cosmological parameters of the standard model as well as a set of common extensions to it, such as alternative Dark Energy models or non-flat geometries. As many cosmological parameters are correlated for CMB-only constraints, adding low-redshift information on H_0 and Ω_M helps to tighten the marginalized

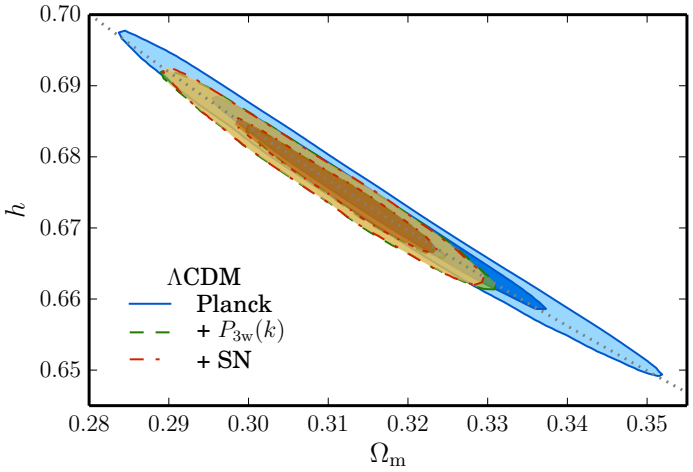

Figure 6.11 – The marginalized 68 and 95 per cent confidence levels (CL) in the Ω_M–h plane for the ΛCDM parameter space from thee *Planck* 2015 TT+lowP (Ade *et al.*, 2015) observations (blue), successively adding the DR12 combined sample $P_{3w,n}(k)$ (green) and JLA SN Ia (Betoule *et al.*, 2014) data (orange). For fitting the three power spectrum wedges a wavenumber range $0.02\ h\,\mathrm{Mpc}^{-1} \leq k \leq 0.2\ h\,\mathrm{Mpc}^{-1}$ and the reference PATCHY covariance matrix were used. The *Planck* confidence contours as well as the combined fits follow the $\Omega_M\,h^3$ degeneracy (Percival *et al.*, 2002) shown as dotted gray line.

constraints of cosmological parameters (e.g. Riess *et al.*, 2011; Amendola & Sellentin, 2016), especially so in extended models such as *w*CDM. The marginalized 68% and 95% CL intervals of the most relevant cosmological parameters for the standard model and the extensions of alternative Dark Energy models are listed in Table 6.4.

6.5.1 The ΛCDM parameter space

The maximum-likelihood model for the combined ΛCDM fit to the *Planck* 2015 data and the BOSS DR12 power spectrum wedges in the low and high redshift bin is shown in Figure 3.7. In all the combined fits, the clustering+RSD parameter space and the fitted wavenumber ranges is the same as for the full-shape fits to individual redshift bins in Section 6.1; here only the independent low and high redshift bins are fitted with separate (low) and equal (high) sets of nuisance parameters for the NGC and SGC subsamples. The resulting constraints on Ω_M and h of the combined *Planck* 2015 plus BOSS DR12 $P_{3w}(k)$ fits (green) are shown in Figure 6.11, compared with the constraints from *Planck* alone (blue). The full-shape BOSS information prefers slightly smaller values for the matter density parameter ($\Omega_M = 0.312^{+0.008}_{-0.009}$) than the *Planck* data alone, while the constraints on the Hubble constant ($h = 0.675^{+0.007}_{-0.006}$) are centred around a similar mean value. All constraints given in the text of this section correspond to the 68% CL. Adding the JLA SN Ia data to the fits does not increase the constraining power (the orange contours obtained from the full combination almost completely overlaps with the green contours). In all the cases analysed, the confidence contours follow a degeneracy along $\Omega_M\,h^3 = \text{const}$ given by equally good fits to the locations and relative heights of the acoustic peaks (Percival *et al.*, 2002). The line given by $\Omega_M\,h^3 = \text{const}$ going through the centre of the CMB-only constraints is indicated by a dotted gray line in the plot. The overall picture shows excellent consistency between the three different probes assuming a ΛCDM cosmology. The agreement between *Planck* and BOSS data could be expected from the outcome of the RSD-type full-shape fits in Section 6.1.

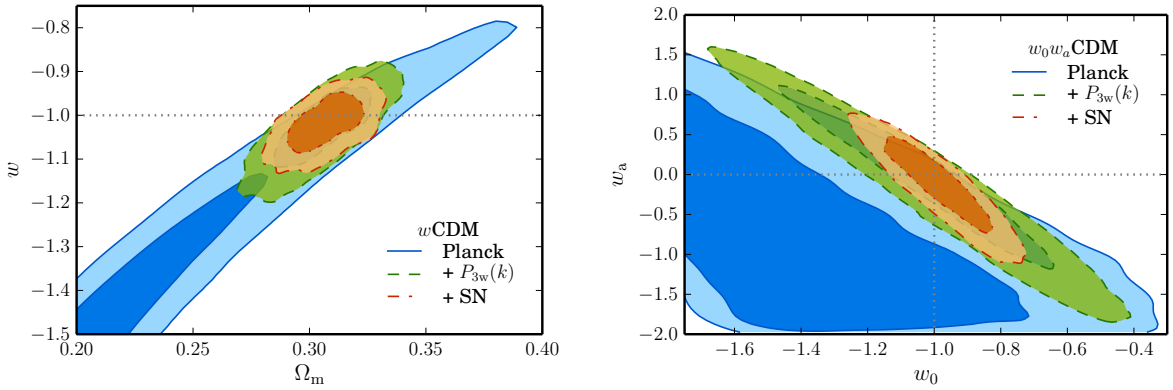

Figure 6.12 – *Left-hand panel:* The 68% and 95% CL in the Ω_M–w parameter plane of the wCDM parameter space from the *Planck* 2015 (blue) fits, successively adding the BOSS DR12 $P_{3w,n}(k)$ (green) and JLA SN Ia (orange) data. *Right-hand panel:* The 68% and 95% CL in the w_0–w_a parameter plane of the w_0w_aCDM parameter space from the *Planck* 2015 (blue) fits, successively adding the BOSS DR12 $P_{3w,n}(k)$ (green) and JLA SN Ia (orange) data.

6.5.2 The wCDM parameter space

The first relaxation of the assumptions of the standard model is to abandon the idea that Dark Energy (DE) can be described by a cosmological constant. As discussed in Section 2.1.3, the simplest model for the equation of state (EoS) of DE is a linear relation,

$$p_{DE} = w_{DE}\,\rho_{DE}, \quad w_{DE} = \text{const.} \tag{6.1}$$

For $w_{DE} = -1$, the ΛCDM model with a cosmological constant is recovered. Consistent with the literature, we denote this extended parameter space as wCDM and use the simple label $w \equiv w_{DE}$ for the EoS parameter of DE, if the context is clear.

As the equation-of-state parameter w is sensitive to the late-time expansion of the Universe, galaxy clustering and supernovae are ideal cosmological probes to constrain Dark Energy, which is not well constrained by CMB data alone. In this last case, w follows a degeneracy with Ω_M and values much below $w = -1$ are preferred, resulting in large 68% CL constraints of $w = -1.55^{+0.32}_{-0.30}$. As shown in the left-hand panel of Figure 6.12, including the power spectrum wedges in the fits results in confidence regions that are centred around the standard ΛCDM value of $w = -1$ within the 68 % CL, $w = -1.029^{+0.066}_{-0.062}$. Including also SN data, the late-time expansion is even better probed so that w is measured to 5% consistency with ΛCDM at 1σ: $w = -1.019^{+0.043}_{-0.045}$.

6.5.3 The w_0w_aCDM parameter space

We use the Chevallier-Polarski-Linder (CPL) parametrization (Chevallier & Polarski, 2001; Linder, 2003) of a time-dependent equation of state for DE as given in equation (2.30):

$$w_{DE}(z) = w_0 + w_a\,(1-a) = w_0 + w_a\frac{z}{1+z}, \tag{6.2}$$

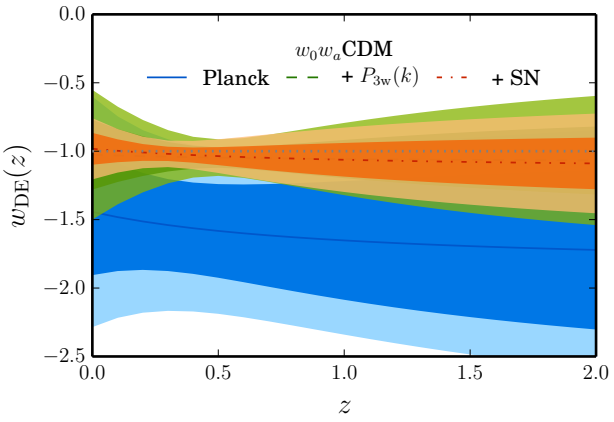

Figure 6.13 – The 68% and 95% CL for the time-dependent equation of state $w_{DE}(z)$ of the wCDM parameter space from the *Planck* 2015 (blue) fits, successively adding the BOSS DR12 $P_{3w,n}(k)$ (green) and JLA SN Ia (orange) data. The error propagation from the constraints on w_0 and w_a was computed with equation (6.4). The low-redshift probes, BOSS DR12 and JLA SN Ia, constrain $w_{DE}(z)$ best at a pivot scale $a_p = (1 + z_p)^{-1}$ roughly given by the effective mean redshift of the probes, $z_p \simeq z_{eff}$.

recovering the ΛCDM model for $w_0 = -1$ and $w_a = 0$.

Again, the constraints on the equation-of-state parameters significantly improve when late-time expansion probes are taken into account. The w_0–w_a parameter plane is practically unconstrained by CMB data alone: a large region roughly below the line $w_a = -3\,(w_0+1)$ is preferred. This plane becomes tightly constrained by including the BOSS DR12 power spectrum wedges, but there remains a degeneracy that follows the line given above, as shown in the right-hand panel of Figure 6.12. The reason is that the combination of *Planck* + BOSS DR12 has the most constraining power on $w_{DE}(z)$ at a 'pivot scale' $z_p \simeq z_{eff}$ (discussed below). In our case, this is at $z_{eff} \approx 0.5$, corresponding roughly to the mean effective redshift of the full combined sample. The degeneracy is further broken by including SN Ia data, resulting in tighter constraints closely centred on the ΛCDM values (the error bars are cut down by half):

$$\left.\begin{aligned} w_0 &= -1.02^{+0.25}_{-0.26} \\ w_a &= -0.06^{+0.70}_{-0.72} \end{aligned}\right\} \quad (\mathit{Planck} + P_{3w}(k)) \qquad \left.\begin{aligned} w_0 &= -0.98 \pm 0.11 \\ w_a &= -0.16 \pm 0.42 \end{aligned}\right\} \quad (+\,\mathrm{SN}) \tag{6.3}$$

In Figure 6.13, we plot the resulting confidence level of the time-dependent equation of state, $w_{DE}(z)$, in the w_0w_aCDM parameter space. The confidence regions around $w_{DE}(z)$ have been computed by propagating the errors on w_0 and w_a as

$$\langle \delta w_{DE}^2 \rangle = \langle \delta w_0^2 \rangle + (1-a)^2 \langle \delta w_a^2 \rangle + 2\,(1-a)\,\langle \delta w_0\, \delta w_a \rangle. \tag{6.4}$$

The error has a minimum at the pivot scale $a_p = (1+z_p)^{-1}$ roughly given by the effective mean redshift probed by the data, $z_p \simeq z_{eff}$. For the combination of *Planck* and BOSS DR12, this is at $z_p \approx 0.5$; the minimal-error constraint at this pivot scale results in the degeneracy in the w_0–w_a parameter plane (shown in the right-hand panel of Figure 6.12) that follows $w_a = -3\,(w_0 + 1)$. Including SN Ia data as well, the pivot redshift moves closer to $z_p \approx 0.3$, resulting in the tighter constraints in the w_0–w_a parameter plane following a slightly shifted line of degeneracy.

We conclude that the final constraints on the EoS parameter of DE are consistent with no evolution of $w_{DE}(z)$, which is well described by a cosmological constant at all redshifts.

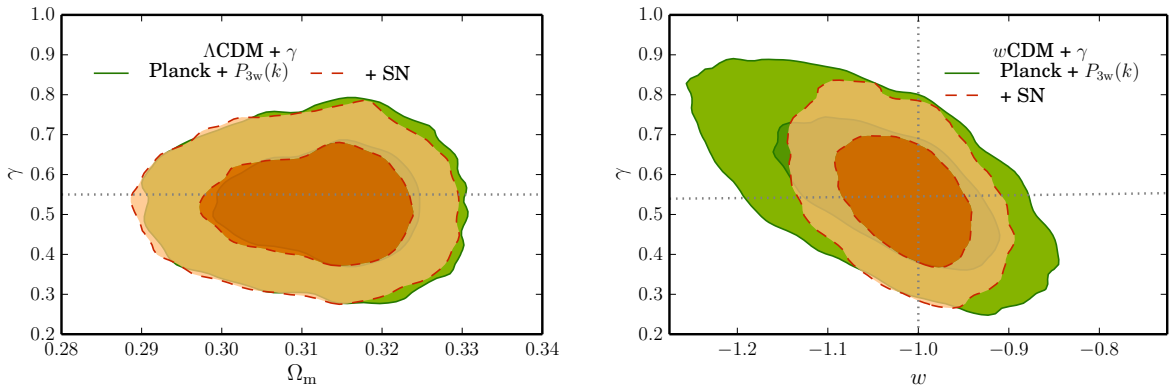

Figure 6.14 – *Left-hand panel:* The 68% and 95% CL in the Ω_M–γ parameter plane of the ΛCDM + γ parameter space from the *Planck* 2015 and BOSS DR12 $P_{3w,n}(k)$ observations (green), and adding JLA SN Ia (orange) data. *Right-hand panel:* The 68% and 95% CL in the w–γ parameter plane of the wCDM + γ parameter space from the *Planck* 2015 and the BOSS DR12 $P_{3w,n}(k)$ observations (green), and adding JLA SN Ia (orange) data. The horizontal dotted line shows the value of the exponent γ depending on the equation-of-state parameter w as given by (2.66).

6.5.4 Probing the growth rate as a test of modified gravity

The growth-rate parameter f depends on the gravitational potential and thus measurements of this quantity via RSD can be used as a probe of the theory of gravity as discussed in Section 2.4.2. The growth rate has the approximate dependency on the matter density parameter Ω_M given by equation (2.66) (Linder & Cahn, 2007; Gong, 2008):

$$f(z) = [\Omega_M(z)]^\gamma \,, \quad \text{where} \quad \gamma \simeq \frac{3(1 - w_{DE})}{5 - 6\, w_{DE}}, \tag{6.5}$$

if the growth of structure is bound to Einstein's general relativity (GR). For the ΛCDM case, $w_{DE} = -1$, the exponent is $\gamma \simeq 0.55$; otherwise, its value only mildly depends on the DE equation of state, w_{DE}.

In order to test for modifications of the fundamental relations of GR, we treat the exponent γ as a free parameter in a ΛCDM background universe (dubbed as ΛCDM + γ parameter space here). In the left-hand panel of Figure 6.14, we plot the regions with a 68 and 95 per cent CL in the Ω_M–γ parameter plane as constrained from the combination of *Planck* and full-shape BOSS DR12 $P_{3w,n}(k)$ observations. The measured CL regions (marginalized over all other parameters, we obtain $\gamma = 0.52 \pm 0.10$) show excellent agreement with the GR value, which is indicated by a horizontal dotted line. As SN Ia do not depend on the growth, their inclusion only results in marginally tighter confidence regions.

This behaviour is different if we allow non-constant DE, as now SN data help to constrain the EoS parameter, $w \equiv w_{DE}$, via the late-time expansion history. The resulting confidence contours in the w–γ parameter plane are shown in the right-hand panel of Figure 6.14. While we obtain $w = -1.04^{+0.08}_{-0.09}$ for the combination of Planck and BOSS DR12 data, the EoS parameter is constrained to $w = -1.02 \pm 0.05$ by the inclusion of SN data (corresponding to the final confidence interval obtained for the plain wCDM model, which is of a similar size). However,

Table 6.5 – Mean and standard deviation of the most-relevant model parameters for fits using curvature extensions of the cosmological standard model. The fits include at least the *Planck* 2015 TT+lowP data, which are successively combined with the power spectrum wedges $P_{3w}(k)$ of the BOSS DR12 low and high redshift bins and the JLA SN Ia data. Given are the 1-sigma and 2-sigma (in parenthesis) intervals.

Parameter	*Planck* 2015	+ BOSS DR12 $P_{3w}(k)$	+ JLA SN Ia
	K-ΛCDM (curvature, standard ν)		
Ω_M	$0.53 \pm 0.10\ (^{+0.25}_{-0.18})$	$0.312 \pm 0.009\ (^{+0.018}_{-0.019})$	$0.311 \pm 0.009\ (^{+0.018}_{-0.019})$
Ω_K	$-0.057 \pm 0.027\ (^{+0.047}_{-0.066})$	$-0.001 \pm 0.003\ (\pm 0.006)$	$-0.001 \pm 0.003\ (\pm 0.006)$
	K-wCDM (curvature, linear EoS for DE)		
Ω_M	$0.49^{+0.28}_{-0.24}\ (^{+0.42}_{-0.32})$	$0.304^{+0.015}_{-0.016}\ (^{+0.029}_{-0.031})$	$0.308 \pm 0.011\ (^{+0.021}_{-0.023})$
Ω_K	$-0.057^{+0.011}_{-0.039}\ (^{+0.049}_{-0.082})$	$-0.002 \pm 0.004\ (^{+0.008}_{-0.007})$	$-0.001^{+0.004}_{-0.003}\ (^{+0.007}_{-0.006})$
w	$-1.36^{+0.77}_{-0.85}\ (^{+1.025}_{-1.44})$	$-1.052^{+0.088}_{-0.071}\ (^{+0.150}_{-0.173})$	$-1.027^{+0.052}_{-0.045}\ (^{+0.092}_{-0.104})$

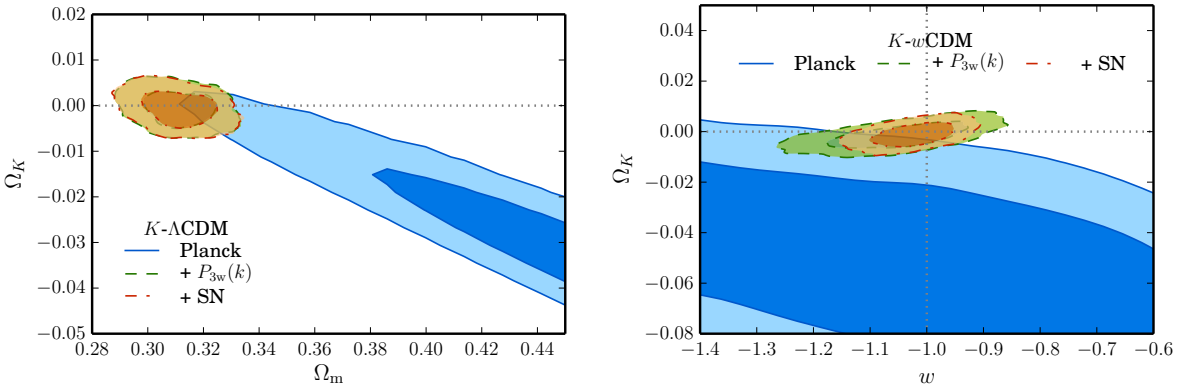

Figure 6.15 – *Left-hand panel:* The 68% and 95% CL in the Ω_M–Ω_K parameter plane of the K-ΛCDM parameter space from the *Planck* 2015 observations (blue), and successively adding BOSS DR12 $P_{3w,n}(k)$ (green) and JLA SN Ia (orange) data. The horizontal dotted line indicates a flat universe, $K = 0$. *Right-hand panel:* The 68% and 95% CL in the w–Ω_K parameter plane of the K-wCDM parameter space from the *Planck* 2015 observations (blue), and successively adding BOSS DR12 $P_{3w,n}(k)$ (green) and JLA SN Ia (orange) data. The vertical dotted line shows the value of the EoS parameter $w = -1$ for a cosmological constant (as in the ΛCDM model).

the exponent γ is only marginally better constrained ($\gamma = 0.56 \pm 0.13$ shrinks to $\gamma = 0.54 \pm 0.11$) as the $P_{3w,n}(k)$ information forces the wCDM model to be close to the ΛCDM case and the w–γ degeneracy of the confidence levels does not follow the $\gamma(w)$ dependency given by equation (2.66), which is shown as the vertical dotted line.

6.5.5 The curvature of the Universe

In a non-flat ΛCDM universe, the curvature constant K tells whether the FLRW metric of equation (2.1) describes a spatial geometry with open (hyperbolic, $K < 0$) or closed (elliptical, $K > 0$) hypersurfaces. The standard case is a flat geometry, $K = 0$. CMB observations alone are not sensitive to the curvature, as the density parameters Ω_M and Ω_K are practically unconstrained due the 'geometric degeneracy' (Efstathiou & Bond, 1999) (as only the angular acoustic scale

is fixed, whose dependency on the cosmological density parameters leaves this degeneracy). Breaking these degeneracies can be achieved with the inclusion of the CMB lensing signal (Ade *et al.*, 2015) or to even higher accuracy with late-time growth constraints such as our BAO+RSD measurements, which place tight constraints on $\Omega_{\rm M}$.

This is shown by the 68% and 95% CL regions in the left-hand panel of Figure 6.15. The addition of the power spectrum wedges results in constraints on the matter density parameter that are of a similar order than for standard ΛCDM fits ($\Omega_{\rm M} = 0.312 \pm 0.009$); the curvature constraints, $\Omega_K = -0.001 \pm 0.003$, prefer a flat universe over cosmologies with a non-zero curvature. These constraints can only be improved at a very modest level from adding SN data.

The geometric degeneracy receives an additional degree of freedom in the K-wCDM parameter space as the EoS parameter $w \equiv w_{\rm DE}$ changes the relation between $\Omega_{\rm M}$, Ω_K and the angular scale of the acoustic peaks. The ΛCDM case ($w = -1$ and $\Omega_K = 0$, indicated by dotted lines) is outside the 95% confidence region for the CMB-only fits. Including our $P_{3{\rm w}}(k)$ data constrains the matter density parameter to $\Omega_{\rm M} = 0.304^{+0.015}_{-0.016}$, leaving a residual degeneracy in the w–Ω_K parameter plane. The statistical error on the DE equation of state ($\approx 8\%$) is only slightly larger than for wCDM fits ($\approx 6.5\%$). Successively adding SN Ia data places a tighter handle on w by probing the late-time expansion history, resulting in constraints in the K-wCDM parameter space in close agreement with the standard ΛCDM model: $\Omega_K = -0.001^{+0.004}_{-0.003}$ and $w = -1.027 \pm 0.049$.

6.5.6 Cosmological constraints on neutrino physics from LSS and CMB observations

Neutrino physics and cosmology

The number and masses of neutrinos play a role in cosmology. Despite the fact that the cosmic neutrino background (CNB) has not been detected yet, there is strong indirect evidence that a see of background neutrinos exists, comparable in number density to the photon background, the CMB. In fact, $n_\nu = (3/11)\, n_\gamma$, so that neutrinos are the most abundant particles in the Universe after the photons. Since neutrinos hardly interact, preventing easy detection or inference on their properties, neutrino physics are an interesting topic both in cosmology and in particle physics. LSS analysis ties in with astroparticle physics as constraints on the sum of neutrino masses can be inferred, in principle, from galaxy clustering and other cosmological probes (Lesgourgues & Pastor, 2012).

Their contribution to the energy density of (relativistic) radiation (if $m_\nu \ll T_\nu$) must be considered. In order to correctly account for neutrino physics in the standard cosmological paradigm, the sum of neutrino masses, $\sum m_\nu$, is taken to be non-zero as the mass-squared differences between neutrino flavours have been detected in neutrino oscillation experiments (e.g., Jelley *et al.*, 2009; Abe *et al.*, 2011, Sudbury Neutrino Observatory and Super-Kamiokande). Also, the neutrino background temperature T_ν is slightly larger than the CMB temperature, due to the energy input from $e^\pm$ annihilation in the early universe. Thus, the effective number of relativistic degrees of freedom, $N_{\rm eff}$, is slightly larger than the number of neutrino flavours. For the standard particle model, postulating electron (ν_e), muon (ν_μ), and tau (ν_τ) neutrinos, this number

is given by $N_{\rm eff} \simeq 3.046$. Neutrinos have often been considered to be massless as the precision of cosmological probes was not sufficient to place constraints on the neutrino physics. Since *Planck* 2013 (Ade *et al.*, 2014c), the cosmological standard model takes the non-zero neutrino masses into account with the assumption of three neutrino of equal mass whose sum adds up to 0.06 eV, which is slightly larger than the current lower bounds from neutrino oscillation experiments (there is no lower bound on the least massive neutrino, so one neutrino mass eigenstate could in principle have a zero mass). The mass-separation scale Δm^2 between two neutrino mass eigenstates is observable with neutrino oscillation experiments. Its detection in two solar neutrino experiments, Super-Kamiokande (SK) and Sudbury Neutrino Observatory (SNO), led to awarding the 2015 Nobel prizes in physics to the heads of these two collaborations, Takaaki Kajita (SK) and Arthur B. McDonald (SNO).

LSS constraints on neutrino physics

The number of flavours in the cosmic relic neutrinos — i.e., primordial neutrinos that decoupled when the Universe was roughly 1 MeV hot, — does have to be limited to the known three lepton flavours. However, the 'bottom-up' scenario of large-scale structure formation can explain the observed cosmic web better than the 'top-down' scenario, which would correspond to a dominant hot dark matter component. Thus, sterile relic neutrinos can only constitute a small fraction of the dark matter component, which is dominated by CDM. The existence of a 'warm' component aside from CDM causes a damping of the small-scale tail of the matter power spectrum as the free-streaming of the sterile particles washes out the gravitational potential wells sourced by clustered CDM. The neutrino constraints from CMB observations follow a complex degeneracy, which can partially be broken by low-redshift probes such as our measurements. Assuming the three standard neutrino flavours, state-of-the art LSS experiments such as the on-going eBOSS survey aim at detecting the sum of neutrino masses indirectly through their impact on the clustering of galaxies (Zhao *et al.*, 2016, section 4.4). Next-generation experiments, such as DESI (Levi *et al.*, 2013), 4MOST (de Jong *et al.*, 2014), PSF (Ellis *et al.*, 2014), and *Euclid* (Laureijs *et al.*, 2011) will be able to constrain the hierarchy of the neutrino mass eigenstates (i.e., determining $\Delta m^2_{12} \lessgtr \Delta m^2_{23}$).

Neutrino physics probed with Fourier space wedges of the BOSS DR12 combined sample and complimentary probes

The CMB constraints from *Planck* 2015 follows a degeneracy of the matter density parameter $\Omega_{\rm M}$ and the sum of neutrino masses $\sum m_\nu$ that is elongated along a line given by the precise measurement of the matter-radiation equality $z_{\rm eq}$ from the CMB. This transition is well constraint by the ratio of the heights of the first and third acoustic peaks. In the upper-left panel of Figure 6.16, the CMB-only constraints in the $\Omega_{\rm M}$–$\sum m_\nu$ parameter plane are shown as blue contours. Marginalized over all other parameters, we obtain $\sum m_\nu < 0.644$ eV (the upper limits in this section are given for 95% CL). The size of the confidence interval could be decreased by including CMB lensing information, as this probes the gravitational potential. In this section, we focus on the improvement of the constraints by adding the BOSS DR12 $P_{\rm 3w}(k)$ data (green

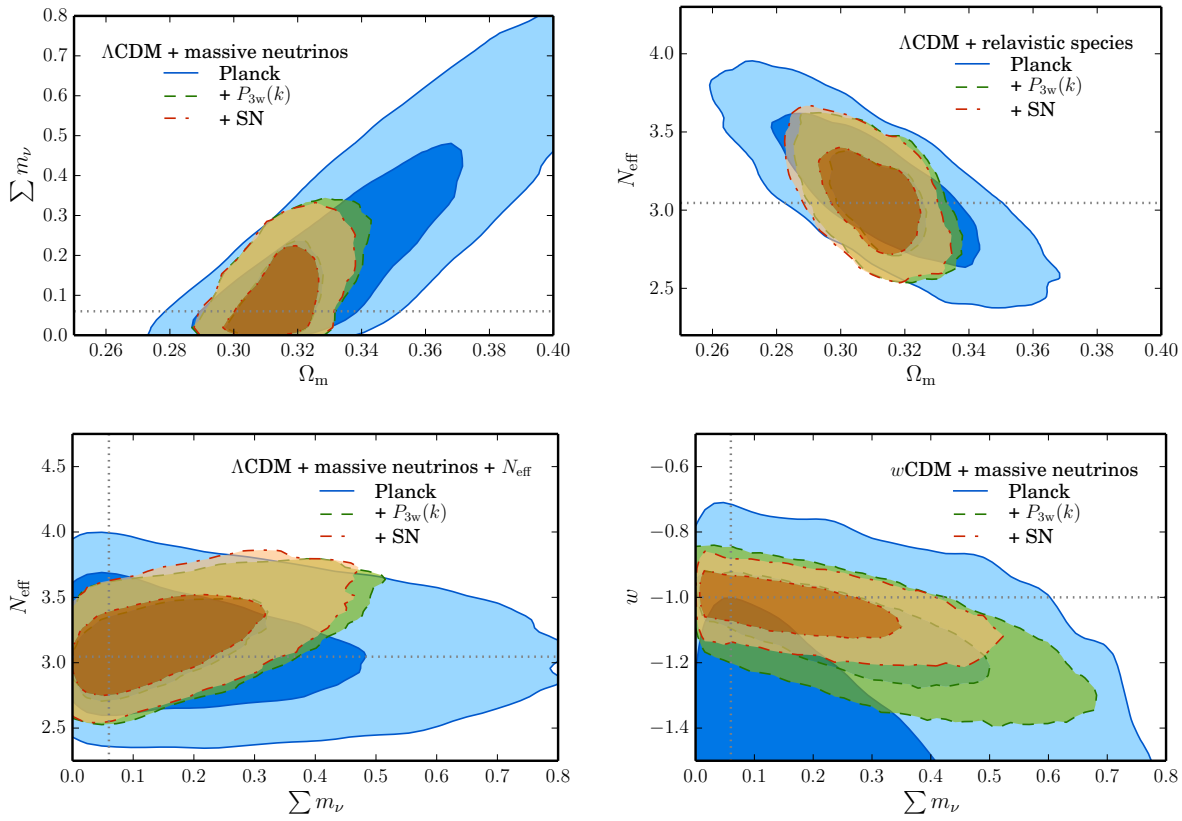

Figure 6.16 – The 68% and 95% CL in the most relevant parameter planes of extensions to the ΛCDM parameter space including massive and sterile neutrinos. *Upper left-hand panel:* The Ω_M–$\sum m_\nu$ parameter plane of the parameter space of ΛCDM extend by varying the sum of neutrino masses showing the confidence regions from the *Planck* 2015 observations (blue), and successively adding BOSS DR12 $P_{3w,n}(k)$ (green) and JLA SN Ia (orange) data. The horizontal dotted line indicates the conventional sum of neutrino masses for the ΛCDM universe, $\sum m_\nu = 0.06\,\mathrm{eV}$. *Upper right-hand panel:* The Ω_M–N_{eff} parameter plane of the N_{eff}-ΛCDM parameter space (allowing for variations in the effective number of relativistic degrees of freedom) with the confidence regions from the same data sets as for the upper left-hand panel. The vertical dotted line shows the value of N_{eff} for the standard model, $N_{eff} = 3.046$. *Lower left-hand panel:* The $\sum m_\nu$–N_{eff} parameter plane of the N_{eff}-ΛCDM parameter space with a varying sum of neutrino masses besides potential modifications of the relativistic degrees of freedom, showing the confidence regions from the same data sets as for the upper left-hand panel. The vertical and horizontal dotted lines indicate the cuts through this parameter plane that correspond to ΛCDM. *Lower right-hand panel:* The $\sum m_\nu$–w parameter plane of the parameter space of wCDM with a varying sum of neutrino masses with the confidence regions from the same data sets as for the upper left-hand panel. The vertical and horizontal dotted lines indicate the cuts through this parameter plane that correspond to ΛCDM.

Table 6.6 – Mean and standard deviation of the most-relevant model parameters for fits using neutrino extensions of the cosmological standard model. In the standard ΛCDM model, massive neutrinos with $\sum m_\nu = 0.06\,\mathrm{eV}$ are including; the effective number of relativistic degrees of freedom corresponding to the radiation and neutrino background is given by $N_{\mathrm{eff}} = 3.046$ The fits include at least the *Planck* 2015 TT+lowP data, which are successively combined with the power spectrum wedges $P_{3\mathrm{w}}(k)$ of the BOSS DR12 low and high redshift bins and the JLA SN Ia data. Given are the 1-sigma and 2-sigma (in parenthesis) intervals.

Parameter	*Planck* 2015	+ BOSS DR12 $P_{3\mathrm{w}}(k)$	+ JLA SN Ia
ΛCDM + massive neutrinos (free $\sum m_\nu$)			
Ω_{M}	$0.34^{+0.031}_{-0.029}\left(^{+0.070}_{-0.044}\right)$	$0.32^{+0.009}_{-0.010}\left(^{+0.022}_{-0.020}\right)$	$0.32^{+0.009}_{-0.010}$ (±0.020)
$\sum m_\nu$	< 0.299 (< 0.644)	< 0.151 (< 0.275)	< 0.143 (< 0.260)
N_{eff}-ΛCDM (free #(relativistic DoF))			
Ω_{M}	$0.312 \pm 0.021\left(^{+0.044}_{-0.042}\right)$	$0.311^{+0.010}_{-0.011}\left(^{+0.020}_{-0.022}\right)$	$0.310^{+0.010}_{-0.011}\left(^{+0.019}_{-0.022}\right)$
N_{eff}	$3.13 \pm 0.32\left(^{+0.066}_{-0.060}\right)$	$3.05^{+0.020}_{-0.024}\left(^{+0.046}_{-0.041}\right)$	$3.08^{+0.021}_{-0.024}\left(^{+0.046}_{-0.042}\right)$
N_{eff}-ΛCDM + massive neutrinos (free $\sum m_\nu$ and #(rel. DoF))			
Ω_{M}	$0.338^{+0.038}_{-0.036}\left(^{+0.168}_{-0.067}\right)$	$0.314^{+0.010}_{-0.012}$ (±0.030)	$0.312^{+0.010}_{-0.011}$ (±0.023)
$\sum m_\nu$	< 0.294 (< 0.641)	< 0.198 (< 0.380)	< 0.192 (< 0.357)
N_{eff}	$3.08 \pm 0.33\left(^{+0.66}_{-0.61}\right)$	$3.18^{+0.25}_{-0.29}\left(^{+0.52}_{-0.51}\right)$	$3.19^{+0.24}_{-0.29}\left(^{+0.55}_{-0.48}\right)$
wCDM + massive neutrinos (linear EoS for DE, free $\sum m_\nu$)			
Ω_{M}	$0.244^{+0.060}_{-0.057}\left(^{+0.168}_{-0.067}\right)$	0.302 ± 0.016 (±0.030)	0.310 ± 0.012 (±0.023)
$\sum m_\nu$	< 0.346 (< 0.697)	$0.28^{+0.17}_{-0.20}$ (< 0.556)	< 0.239 (< 0.416)
w	$-1.65^{+0.38}_{-0.34}\left(^{+0.75}_{-0.62}\right)$	$-1.14^{+0.12}_{-0.10}\left(^{+0.20}_{-0.21}\right)$	$-1.06^{+0.07}_{-0.06}\left(^{+0.11}_{-0.12}\right)$

contours). By tightening the confidence limits on Ω_{M}, the sum of neutrino mass is constrained to an upper limit of $\sum m_\nu < 0.275\,\mathrm{eV}$. Only minor improvement is found by including SN Ia data (orange contours) as these primarily help to constrain h, yielding $\sum m_\nu < 0.260\,\mathrm{eV}$.

The effective number N_{eff} of relativistic DoF in the neutrino sector can also be constrained by CMB and LSS observations. Again, the constraints in the Ω_{M}–N_{eff} parameter plane follow a degeneracy defined by tight constraints on the matter-radiation equality,

$$1 + z_{\mathrm{eq}} = \frac{\Omega_{\mathrm{M}}\, h^2}{(1 + 0.227\, N_{\mathrm{eff}})\, \Omega_{\mathrm{r}}\, h^2}. \tag{6.6}$$

Just as for $\sum m_\nu$, the correlation of the parameter is broken by an indirect measurement of Ω_{M} from the BOSS DR12 analysis. The constraints on the Ω_{M}–N_{eff} parameter plane are shown in the upper right-hand panel of Figure 6.16. Marginalized over all other parameters, we obtain $N_{\mathrm{eff}} = 3.05^{+0.020}_{-0.024}$ (68%), which corresponds to a reduction of the statistical error by a factor of 1.5 compared to $N_{\mathrm{eff}} = 3.12 \pm 0.32$ from CMB data alone. We do not find any improvement in the marginalized constraints nor the FoM for the Ω_{M}–N_{eff} parameter plane from adding the JLA SN Ia data.

The same scenario as described before also applies to the combined parameter space of N_{eff}-ΛCDM + a free $\sum m_\nu$: degeneracies between N_{eff}, $\sum m_\nu$, and Ω_{M} along lines of constant z_{eq} are broken by a handle on Ω_{M} from LSS observations. The 68% and 95% CL contours are shown for the N_{eff}–$\sum m_\nu$ parameter plane in the lower panel of the left-hand side in Figure 6.16.

As the there is a residual degeneracy between $N_{\rm eff}$ and $\sum m_\nu$, the final constraints (*Planck* + $P_{3\rm w}(k)$ + SN) are slightly larger than the for the individual extensions of the parameter space, $\sum m_\nu < 0.357\,\text{eV}$ (98% upper limit) and $N_{\rm eff} = 3.19\pm^{+0.24}_{-0.29}$ (68% CL).

For the last parameter space discussed in this thesis, a wCDM cosmology with a sum of neutrino masses, including SN Ia data significantly improves the constraints. As shown in the lower right-hand panel of Figure 6.16, the $\sum m_\nu$–w parameter plane is hardly constrained by CMB data alone. The information in the DR12 power spectrum wedges can constrain the late-time expansion and thus w, but the remaining freedom along a degeneracy of $\Omega_{\rm M}$ and w also leaves limits on $\sum m_\nu$ that are roughly twice as large as for the ΛCDM case. This results in a 1-sigma signal for the sum of the neutrino masses, $\sum m_\nu = 0.28^{+0.17}_{-0.20}\,\text{eV}$ (68% CL), and also the DE equation-of-state parameter is constrained to an interval that does not contain the ΛCDM value at 68% CL, $w = -1.14^{+0.12}_{-0.10}$. The addition of further information about the local expansion from JLA breaks the remaining freedom and helps to tighten the constraints on $\sum m_\nu$ and w. We obtain $\sum m_\nu < 0.416\,\text{eV}$ (95 % CL) and $w = -1.06^{+0.11}_{-0.12}$ in perfect agreement with a cosmological constant and without the mildest signal of a lower bound of the sum of neutrino masses. The statistical errors obtained correspond to a level less 1.5 times the errors found for each parameter individually in the plain ΛCDM and wCDM cases.

7

Summary and discussion

"All knowledge and understanding of the Universe was no more than playing with stones and shells on the seashore of the vast imponderable ocean of truth."

Isaac Newton

Tremendous efforts are made to infer knowledge about the parameter space of the standard cosmological model and its possible extensions by exhausting the cosmological information available in large-volume galaxy surveys. The research presented in this thesis was performed as a part of the large-scale clustering analysis of the final galaxy sample obtained from BOSS (the DR12 combined galaxy sample). This sample is unprecedented in volume, but the sensitivity of the clustering analysis also depends on the modelling accuracy and other specifications of the measurement and the parameter inference techniques. Anisotropic clustering models were refined in the last decades as new concepts for the non-linear matter clustering and redshift-space distortions were developed, so that their predictive power increased. Hence, full-shape measurements of galaxy clustering have become competitive to distance measurements using the BAO feature as a standard ruler. The precision of such BAO measurements was significantly increased using the linear density-field reconstruction technique.

The clustering analysis of the final BOSS sample relies on both measurement techniques, combining the similar, but not completely redundant approaches into a consensus measurement, which is the variance-weighted average of the individual constraints from each analysis method. Among the few full-shape approaches applied to the data is the Fourier-space analysis of the anisotropic clustering presented in this thesis. Besides cosmological information measured from a geometric distortion of the clustering signal, full-shape fits can also infer the growth rate of large-scale structure. This measurement can be used to constrain possible deviations from the predictions of general relativity.

So far, anisotropic clustering analyses in Fourier space relied on power spectrum multipole measurements. In this work, the concept of clustering wedges was extended to Fourier space to establish a complementary approach to measure clustering anisotropies. The optimal-variance

estimator for Fourier space wedges was defined in analogy to the Yamamoto-Blake estimator as a direct Fourier sum over the galaxies in the sample. However, for reasons of efficient computation, the final measurement of Fourier space wedges were obtained by transforming power-spectrum multipoles estimated using a fast FFT scheme. This method cannot be adapted to the clustering wedges due to their different transformation kernel. The compatibility of the FFT-based and the direct-sum estimator was ensured by tests on synthetic catalogues.

The shot noise and optimal-variance weights of the power spectrum estimator have been revised in order to fully account for all observational systematics of the BOSS survey that cause the galaxy sample to be incomplete. Further, the geometry of the survey reduces the power on scales of the order of the spatial extension of the survey. This effect is described by a window function, with which predictions of the underlying power spectrum are convolved to estimate the observed power spectrum. In this thesis, the modelling of this effect with a window matrix is extended for the application to Fourier space wedges.

For the likelihood analysis of the power spectrum wedges, an estimate of the inverse of the covariance matrix is needed. The data covariance used in full-shape fits of the Fourier-space wedges measured from the BOSS DR12 combined sample is estimated from large sets of synthetic catalogues, the PATCHY and QPM mocks. However, the 'gRPT+RSD' model used in this thesis was validated using a set of 100 full N-body simulations. As the brute-force estimation of the covariance does not produce invertible matrices when applied to sets with such a small number of realizations, a theoretical recipe for the covariance of the anisotropic clustering two-point statistics was needed. In this thesis, explicit formulae for the Gaussian covariance matrix are presented aiming to be sufficiently precise for the model verification. In order to be as general as possible, we looked at the covariance of redshift-space clustering statistics using clustering wedges (i.e., large bins in the LOS parameter) and multipole moments, both in configuration space as well as in Fourier space.

These formulae rely on a model for the input power spectrum. The two different recipes that were tested are, first, a simple model for the redshift-space galaxy power spectrum based entirely on linear theory and, second, a smoothed interpolation of the measurements directly from the simulations. Using both approaches, the covariance model was validated against the set of MINERVA simulations, finding good agreement between the predictions of the Gaussian covariance and the measurements. The theoretical predictions for the covariance of configuration space wedges and multipoles accurately describe the full correlation structure, which is important as measurements of the two-point correlation function are correlated across a wide range of scales (in contrast to Fourier space clustering measurements).

The set of BOSS DR12 mocks were found to approximatively reproduce the clustering of the real data. The effect of noise on the estimate of the inverse of the covariance matrix is small and residual imperfections after the corrective rescaling can be considered negligible.

The synthetic galaxy catalogues obtained from the MINERVA simulations also serve as a test case for the 'gRPT+RSD' clustering model, allowing the determination of the optimal number of wedges and wavenumber range for BAO+RSD fits. We find that the best compromise between sensitivity and accuracy is a configuration of three wedges and a wavenumber range limited by $k_{\mathrm{max}} = 0.2\ h\,\mathrm{Mpc}^{-1}$. Further model performance tests are conducted as part of the BOSS RSD challenge with synthetic catalogues that are specifically designed to detect systematic

biases in the distance and growth measurements obtained from the various approaches for full-shape measurements within the BOSS galaxy clustering working group. Further, the model was validated with the PATCHY mocks as they mimic the entire combined sample by fitting each realization individually. This sample of constraints is used to determine the cross covariance between the results obtained using different full-shape and BAO-only techniques. This estimate is needed to derive the final consensus constraints from the BOSS DR12 combined sample.

Among the different techniques, the full-shape fits of the configuration- and Fourier-space wedges using the 'gRPT+RSD' model have the most constraining power. This is mainly due to the improvements in modelling the non-linear redshift-space distortions, which allow us to include more information from smaller scales than in previous approaches. No significant systematic bias (i.e., of comparable size to the statistical error) was found in any of the rigorous tests on the model.

The Fourier space wedges measured from the BOSS DR12 combined sample in three redshift bins were fitted with the full-shape approach using the 'gRPT+RSD' model in order to derive constraints on the Alcock-Paczynski distortion and the growth rate. The results are in excellent agreement with the analogous outcome in configuration space, and with the findings of the other approaches applied by members of the clustering working group. The 'gRPT+RSD' results are the most precise measurements within the full-shape techniques. The errors were found to be consistent with the distribution of statistical errors on the PATCHY mocks. All tests for systematic errors, such as using a sample corrected for colour shifts between the NGC and SGC imaging, exchanging the PATCHY and QPM covariance matrices, restricting the analysis to only two wedges, and restricting the wavenumber ranges included in the fits to check for a scale-dependency of the results, were negative.

The results from our full-shape fits using Fourier-space wedges are compatible with previous findings on the BOSS LOWZ and CMASS samples, but are significantly more precise due the optimization of the analysis and the improved modelling accuracy. Thus, we are able to infer the most precise parameter constraints for the standard cosmological model and usual extensions, such as modified Dark Energy models, by combining the DR12 full-shape measurements with CMB data from *Planck* (as of 2015) and the joint SN Ia sample (JLA).

7.1 Summary of the cosmological results

First, we summarize the BAO+RSD results on the DR12 combined sample, limiting the discussion to the two non-overlapping outer redshift bins and 68% CL limits.

- The angular diameter distance was constrained to $D_{\rm M}(z_{\rm eff}=0.38)\,(r_{\rm d}^{\rm fid}/r_{\rm d}) = 1525 \pm 24\ h^{-1}\,{\rm Mpc}$ and $D_{\rm M}(z_{\rm eff}=0.61)\,(r_{\rm d}^{\rm fid}/r_{\rm d}) = 2281^{+42}_{-43}\ h^{-1}\,{\rm Mpc}$. This corresponds to a precision of 1.6% and 1.9%, respectively, and is, therefore, of the level of previous CMASS constraints (which probes an effective volume that is by a factor of 1.4 larger than the one of each of the combined sample redshift bins).

- The measured Hubble parameter is $H(z_{\rm eff}=0.38)\,(r_{\rm d}/r_{\rm d}^{\rm fid}) = 81.2^{+2.2}_{-2.3}\,{\rm km\,s^{-1}\,Mpc^{-1}}$ and $H(z_{\rm eff}=0.61)\,(r_{\rm d}/r_{\rm d}^{\rm fid}) = 94.9 \pm 2.5\,{\rm km\,s^{-1}\,Mpc^{-1}}$, corresponding to precisions of 2.8%

and 2.6%. These constraints are significantly more precise than the results obtained from previous analyses.

- The growth rate constraints were determined to be $f\,\sigma_8(z_{\rm eff} = 0.38) = 0.498^{+0.044}_{-0.045}$ and $f\,\sigma_8(z_{\rm eff} = 0.61) = 0.409 \pm 0.040$ (9.0% and 9.7% precision). This is a major improvement for the low-redshift bin (compared to the LOWZ measurements, which were less precise due to the much smaller effective volume), while both results can be considered to be substantially more accurate then previous constraints as intensive model testing ensured the validity of the much improved RSD modelling.

All these measurements are consistent with the ΛCDM predictions from the *Planck* 2015 data at the 1-sigma level.

Combining the full-shape clustering wedges measured from the DR12 combined sample with the *Planck* 2015 and the JLA SN Ia data, we find that ΛCDM is the preferred cosmological model among the variations explored in this thesis.

- Assuming a ΛCDM cosmology, the combined data sets constrain the matter density parameter to $\Omega_{\rm M} = 0.311^{+0.009}_{-0.010}$ and the Hubble constant to $H_0 = 67.6^{+0.7}_{-0.6}\,{\rm km\,s^{-1}\,Mpc^{-1}}$. These values, as well as the statistical errors, are in very good agreement with the results from the *Planck* 2013 + CMASS + LOWZ + SN constraints found in Anderson *et al.* (2014b, using the reconstructed BAO measurement and a different SN Ia sample).

- Relaxing the assumption of a cosmological constant and allowing for a linear EoS with $w_{\rm DE} \neq -1$, we find $w_{\rm DE} = 1.019^{+0.048}_{-0.039}$. This corresponds to a significant improvement over the Planck 2013 + DR11 BAO + SN constraint (Anderson *et al.*, 2014b), which had a 1.5 times larger error, and a minor improvement over the ePlanck + full-shape BOSS + SN constraints obtained in Sánchez *et al.* (2014).

- In the more general CPL parametrization, which allows for a time-dependent EoS for DE, the constraints on the offset and slope of $w_{\rm DE}$ are also more precise by the same factor. In all tested DE models, not even the mildest deviation from ΛCDM was found. $w_{\rm DE} = -1$ is always found to be very well within the 1σ confidence intervals (with the most extreme case being the wCDM model with a free $\sum m_\nu$, where $w_{\rm DE} = -1$ lies close to the edge of the interval).

- Allowing for a modification in the growth rate by varying the exponent γ in $f = [\Omega_{\rm M}(z)]^\gamma$, we measure $\gamma = 0.52 \pm 0.10$ in perfect agreement with GR ($\gamma_{\rm GR} = 0.55$) and with an uncertainty reduced by a factor of 1.5 compared to previous Planck 2013 + full-shape BOSS constraints (Sánchez *et al.*, 2014). The increase of precision in this test for modified gravity was achieved because of the improvements in the RSD modelling, which also resulted in a more precise estimate of f in the RSD-type full-shape fits.

- Any deviation from a flat spatial geometry of the Universe could be measured with a cosmological model that allows for a curvature component. In order to allow for more generous modifications, we also ease the assumptions on DE and constrain the K-wCDM

parameter space in addition to the K-ΛCDM one. The curvature parameter Ω_K is found to be fully consistent with zero in both cases. The total density of the Universe today is only allowed to deviate less than .3% from the critical density at 68% CL (*Planck* + BOSS constraints for K-ΛCDM). The precision of our curvature measurements is of a similar level than for the results obtained in other recent analyses that combined various cosmological probes (Anderson *et al.*, 2014b; Ade *et al.*, 2015).

- The neutrino mass is found to be $\sum m_\nu < 0.260$ eV (95% CL), which does not correspond to an improvement over previous constraints from BOSS, but gives a consistent picture with other recent cosmological analyses such as weak lensing with CFHTLenS (Kitching *et al.*, 2016, $\sum m_\nu < 0.28$ eV at 68 % CL). However, previous indications of positive neutrino masses that add up to larger sum (e.g., Beutler *et al.*, 2014b, measured $\sum m_\nu = 0.35 \pm 0.10$ eV at 68 % CL) cannot be confirmed.

We conclude that the current understanding of the standard cosmological model has thus been further consolidated.

7.2 Outlook

The presented analysis can readily be applied to other data from spectroscopic galaxy-redshift surveys such as WiggleZ (for which the Fourier space wedges might even be measured with a plane-parallel approximation for the individual patches that have a much smaller angular size than a BOSS subsample). However, significant improvements on the cosmological constraints cannot be expected and such an application would primarily represent an cross-check of our analysis and results.

With future galaxy surveys, such as DESI (Levi *et al.*, 2013), 4MOST (de Jong *et al.*, 2014), and PFS (Ellis *et al.*, 2014), the Figure-of-Merit (FoM) of alternative DE parametrizations such as CPL will be drastically increased. Even before these new large surveys are complete, eBOSS results will improve the FoM by a factor of 2–3 (Zhao *et al.*, 2016). It will be especially interesting to decide whether $w_{\rm DE}(z)$ evolves with time with deep future samples that can be split into large-volume bins over a wide redshift range.

Exciting results can be expected from near-future LSS analysis in regard of the neutrino mass, as the current constraints – $\sum m_\nu < 0.143$ eV (68 % CL) in this work – are close to the lower boundary found in neutrino oscillation experiments ($\sum m_\nu \gtrsim 0.06$ eV). If not from eBOSS alone, the combination of different LSS probes (BAO+RSD, weak lensing, cluster counts, Ly-α) might be able not only to detect massive neutrinos (i.e., determine the sum of the neutrino masses to be positive), but also infer the hierarchy of the neutrino masses, which is not asserted yet as particle physics have only detected the mass square differences from neutrino oscillation experiments so far. Parallel to the search for the cosmological signal of massive neutrinos, ongoing beta decay experiments are expected to measure the electron neutrino mass at a precision comparable to current cosmological limits.

For the estimator of clustering wedges, it will be necessary to fully quantify the wide-angle error that is introduced in low-redshift measurements in the Yamamoto-Blake-like estimator

that uses the 'moving-LOS' approximation, which breaks down for low z and large angles (first work on the bias introduced by this approximation was done for power spectrum multipoles in Yoo & Seljak, 2015; Samushia *et al.*, 2015).

The modelling of the redshift-space clustering two-point statistics seems to have converged on a very robust level as the agreement of the RSD results with the BOSS collaboration shows. Further improvement can be expected down the lines of phenomenological models for the pairwise velocity dispersion and the Gaussian and Edgeworth streaming models for RSD (Reid & White, 2011; Uhlemann *et al.*, 2015; Bianchi *et al.*, 2016).

Important for nailing down the systematic error budget is to precisely quantify the error on the covariance matrix from a large set of mocks. In Section 4.4.4, we already discussed the work needed before an estimate of the anisotropic clustering covariance can be given theoretically. Apart from a check of the covariance, an accurate modelling might render the very expensive mass generation of synthetic catalogues unnecessary.

Finally, we want to highlight that with the increased depth of future galaxy surveys fibre collisions might be more important than for BOSS (unless the observing strategy allows for multiple passes). As the current treatment in the analysis has been found not to significantly influence the cosmological constraints, the power spectrum of an underlying sample has not been exactly recovered from a realistic sample yet. There is a field of on-going research in modelling of this effect (Guo *et al.*, 2012), as well as avoiding it in the first place (Makarem *et al.*, 2014), which can be done by allowing multiple passes of each survey sector with faster robotic fibre placements or by relying on IFU units for the spectroscopy.

A

Obtaining cosmological constraints with Markov chain Monte Carlo

> "There is a theory which states that if ever anybody discovers exactly what the Universe is for and why it is here, it will instantly disappear and be replaced by something even more bizarre and inexplicable. There is another theory which states that this has already happened."
>
> Douglas Adams

This first appendix discusses the inference of constraints in the parameter space of the standard cosmological model and its extensions by use of Bayesian statistics and, in particular, the Markov chain Monte Carlo (MCMC) method. The selection and presentation of the aspects addressed here follows the aim to describe how we apply the MCMC method to generate marginalized confidence levels for cosmological parameters. Good reviews on the statistical techniques for Bayesian data analysis in cosmology are Dunkley *et al.* (2005), Verde (2007), and Gelman *et al.* (2013). Following the lines given in these sources, Section A.1 describes the most relevant aspects of Bayesian statistics taking the power spectrum prediction as an illustrative case. In Section A.2, the parameter estimation for a given model by means of MCMC is discussed, again limited to power spectrum models for brevity. This restriction will be lifted in Section A.3, introducing the cosmological parameter inference using CosmoMC from a broad variety of data.

A.1 Bayesian statistics

A.1.1 Probability Theory

In this section, $\mathcal{P}(\boldsymbol{x})$ is a *probability density* on a N_p-dimensional parameter space $\boldsymbol{\zeta} \in \mathcal{X}$ that is normalized such that

$$\int_{\mathcal{X}} \mathcal{P}(\boldsymbol{\zeta})\, \mathrm{d}^{N_\mathrm{p}}\boldsymbol{\zeta} \;=\; 1. \tag{A.1}$$

A conditional probability distribution is written as $\mathcal{P}(\boldsymbol{\zeta}|H)$, meaning the probability of $\boldsymbol{\zeta}$ given the condition H. Quantifying probabilities always relies on a set of hypotheses which are usually hidden in the notation. These hypotheses, H, for instance the assumptions of the model, can be made explicit in the notation by writing the *conditioning rule* as

$$\mathcal{P}(\boldsymbol{x},\boldsymbol{y}|H) = \mathcal{P}(\boldsymbol{x}|\boldsymbol{y},H)\,\mathcal{P}(\boldsymbol{y}|H), \tag{A.2}$$

for a split of the parameter space into the subsets $\boldsymbol{x}$ and $\boldsymbol{y}$. This short introduction only explains parameter estimation using Bayesian statistics, given a model. As model selection, where the hypothesis of probability densities change as the model assumptions change, is not discussed here, we do not make the model assumptions explicit in our notation.

The expectation value and variance of a function $f(\boldsymbol{\zeta})$ given a probability distribution $\mathcal{P}(\boldsymbol{\zeta})$ on $\mathcal{X}$ are given by

$$\langle f\rangle = \int_{\mathcal{X}} f(\boldsymbol{\zeta})\,\mathcal{P}(\boldsymbol{\zeta})\,\mathrm{d}^{N_\mathrm{p}}\zeta \quad \text{and} \tag{A.3}$$

$$\mathrm{var}(f) = \int_{\mathcal{X}} f^2(\boldsymbol{\zeta})\,\mathcal{P}(\boldsymbol{\zeta})\,\mathrm{d}^{N_\mathrm{p}}\zeta \; - \langle f\rangle^2, \tag{A.4}$$

respectively.

A.1.2 Bayes' theorem

For our application, he data is the power spectrum wedges, $\boldsymbol{P}^\mathrm{obs}$. Be $\boldsymbol{\zeta}$ a point in the N_p-dimensional parameter space $\mathcal{X}$ for which the model predictions, $\boldsymbol{P}^\mathrm{pred}(\boldsymbol{\zeta})$, are are computed. The *joint probability distribution* for $\boldsymbol{\zeta}$ and $\boldsymbol{P}^\mathrm{obs}$ is $\mathcal{P}(\boldsymbol{\zeta},\boldsymbol{P}^\mathrm{obs}) = \mathcal{P}(\boldsymbol{\zeta})\,\mathcal{P}(\boldsymbol{P}^\mathrm{obs}|\boldsymbol{\zeta})$ by use of the conditional probability $\mathcal{P}(\boldsymbol{P}^\mathrm{obs}|\boldsymbol{\zeta})$ for a given $\boldsymbol{\zeta}$. Combining this with the reversed conditioning relation $\mathcal{P}(\boldsymbol{\zeta}|\boldsymbol{P}^\mathrm{obs}) = \mathcal{P}(\boldsymbol{\zeta},\boldsymbol{P}^\mathrm{obs})/\mathcal{P}(\boldsymbol{P}^\mathrm{obs})$ yields *Bayes' theorem*,

$$\mathcal{P}(\boldsymbol{\zeta}|\boldsymbol{P}^\mathrm{obs}) = \frac{\mathcal{P}(\zeta)\,\mathcal{P}(\boldsymbol{P}^\mathrm{obs}|\boldsymbol{\zeta})}{\mathcal{P}(\boldsymbol{P}^\mathrm{obs})}, \tag{A.5}$$

where $\mathcal{P}(\boldsymbol{P}^\mathrm{obs})$ is the *evidence* of the data, given by

$$\mathcal{P}(\boldsymbol{P}^\mathrm{obs}) = \int_{\mathcal{X}} \mathcal{P}(\boldsymbol{\zeta})\,\mathcal{P}(\boldsymbol{P}^\mathrm{obs}|\boldsymbol{\zeta})\,\mathrm{d}^{N_\mathrm{p}}\zeta\,. \tag{A.6}$$

As this is a normalization constant, Bayes' theorem is often used to derive the *unnormalized posterior density* $\mathcal{P}(\boldsymbol{\zeta}|\boldsymbol{P}^\mathrm{obs}) \propto \mathcal{P}(\zeta)\,\mathcal{P}(\boldsymbol{P}^\mathrm{obs}|\boldsymbol{\zeta})$ from the *prior distribution* $\mathcal{P}(\boldsymbol{\zeta})$ and the *likelihood*

$$\mathcal{P}(\boldsymbol{P}^\mathrm{obs}|\boldsymbol{\zeta}) = \mathscr{L}\left(\boldsymbol{\zeta} \mid \boldsymbol{P}^\mathrm{obs}, \boldsymbol{\psi}^P\right), \tag{A.7}$$

which in the case of the power spectrum was defined in equation (4.3). This is an example of a likelihood function given by a multivariate Gaussian distribution, depending on the inverse covariance matrix, the precision matrix $\boldsymbol{\psi}^P$, and the difference vector between the model prediction $\boldsymbol{P}^\mathrm{pred}(\zeta)$ and the observation $\boldsymbol{P}^\mathrm{obs}$. The likelihood is often approximated by a Gaussian

probability distribution, especially if the observed data is probing a product of many random variables, for which the central limit theorem guarantees the Gaussianity of the joint probability distribution.

With this theorem, the derivation of parameter constraints given the data, derived from marginalizations of $\mathcal{P}(\boldsymbol{\zeta}|\boldsymbol{P}^{\mathrm{obs}})$, can be calculated from a prior on the parameter that has to be assumed and the likelihood evaluation of the comparison of the model prediction with the data. Bayes' theorem can be seen as the 'update' of the original knowledge on the parameter in the prior (which can be informative, generous, or also completely arbitrary) with the information in the data that is put into the likelihood. The resulting posterior describes the enhanced knowledge on the parameters, compromising between the prior and data information. Of course, the final probability distribution depends on the prior, which thus needs to be chosen carefully. For example, if the prior was chosen too restrictive, the posterior distribution still obeys the restriction and will not reveal full insight in the information contained in the data.

For the power spectrum analysis, *flat priors* were assumed with limits given in Table 5.2. These priors are uniform in the parameters θ_i, $i = 1, \ldots, N_{\mathrm{p}}$, within the limits $[a_i, b_i]$,

$$\mathcal{P}(\boldsymbol{\zeta}) = \prod_{i=1}^{N_{\mathrm{p}}} \mathcal{P}_i(\theta_i), \quad \text{where} \quad \mathcal{P}_i(\theta_i) = \frac{1}{b_i - a_i} \times \begin{cases} 1, & \text{for} \quad a_i \leq \theta_i \leq b_i \\ 0, & \text{otherwise.} \end{cases} \tag{A.8}$$

A.2 Markov chain Monte Carlo

A key principle of the computation of posterior inferences is the simulation of random draws of parameters $\boldsymbol{\zeta}$ for which the posterior is evaluated. The more complex the parameter space is, the more difficult it is to explore it efficiently, as a proper population of the posteriors needs to prefer random draws in 'likely' regions of the parameter space. For instance, the direct evaluation of the posterior on a grid of points in the full parameter space will be useless in most cases in cosmology, where the parameter sets are large, but only small regions are preferred by the data.

A more efficient way are *Markov chain* simulations, also called *Markov chain Monte Carlo*. With this technique, samples $\boldsymbol{\zeta}^i$ are drawn sequentially, with the distribution of the next step only depending on the last drawn value; beginning at a starting point $\boldsymbol{\zeta}^0$, each step $\boldsymbol{\zeta}^i$ is drawn from a transition distribution $\mathcal{P}_{\mathrm{T}}(\boldsymbol{\zeta}^i|\boldsymbol{\zeta}^{i-1})$ that depends on the previous draw $\boldsymbol{\zeta}^{i-1}$. This is the defining principle of a Markovian chain. The transition probability must be constructed such that the Markov chain converges to a unique stationary distribution given by the posterior (which usually can only be computed for a given point but is not known entirely so that it cannot be drawn from directly). Running the Markov chain long enough generates a distribution of points in the parameter space that samples the posterior.

A.2.1 Metropolis-Hastings algorithm

The *Metropolis-Hastings algorithm* (Metropolis *et al.*, 1953; Hastings, 1970) is a specific implementation of the step process in the Markov chain that guarantees by use of an accep-

tance/rejection rule for the transition probability that the stationarity of the chain is reached and that the resulting distribution matches the posterior.

The procedure is defined as described next:

- The starting point $\boldsymbol{\zeta}^0$, for which $\mathcal{P}(\boldsymbol{\zeta}^0|\boldsymbol{P}^{\mathrm{obs}}) > 0$ must be given, is chosen appropriately (usually estimated from a crude approximation of the posterior or an informative prior).
- For any step $i = 1, 2, \ldots$, perform the following steps:
  1. A proposal $\boldsymbol{\zeta}^*$ is sampled from a proposal distribution $\mathcal{P}_{\mathrm{P}}(\boldsymbol{\zeta}^*|\boldsymbol{\zeta}^{i-1})$. Usually, a Gaussian distribution using a good guess of a step size, $\boldsymbol{\sigma}_\zeta$, is used:
  $$\mathcal{P}_{\mathrm{P}}(\boldsymbol{\zeta}^*|\boldsymbol{\zeta}^{i-1}) = \mathcal{N}(\boldsymbol{\zeta}^{i-1}, \boldsymbol{\sigma}_\zeta). \tag{A.9}$$
  2. The acceptance ratio is calculated by
  $$r = \frac{\mathcal{P}(\boldsymbol{\zeta}^*|\boldsymbol{P}^{\mathrm{obs}})\,\mathcal{P}_{\mathrm{P}}(\boldsymbol{\zeta}^{i-1}|\boldsymbol{\zeta}^*)}{\mathcal{P}(\boldsymbol{\zeta}^{i-1}|\boldsymbol{P}^{\mathrm{obs}})\,\mathcal{P}_{\mathrm{P}}(\boldsymbol{\zeta}^*|\boldsymbol{\zeta}^{i-1})} \tag{A.10}$$
  For a symmetric proposal distribution $\mathcal{P}_{\mathrm{P}}(\boldsymbol{x}|\boldsymbol{y}) = \mathcal{P}_{\mathrm{P}}(\boldsymbol{y}|\boldsymbol{x})$ (which is true for a Gaussian distribution), the second ratio is omitted. Further, the transition probability should also only be > 0 if the proposal is included in the prior. Thus, for flat priors as in our case, r reduces to the ratio of the likelihoods, $r = \mathcal{P}(\boldsymbol{P}^{\mathrm{obs}}|\boldsymbol{\zeta}^*)/\mathcal{P}(\boldsymbol{P}^{\mathrm{obs}}|\boldsymbol{\zeta}^{i-1})$.
  3. A simple uniform random variable $x \in [0, 1)$ is drawn and for $x < r$, the step is accepted, $\zeta^i = \zeta^*$, and rejected otherwise. In case of a rejection, the previous step is repeated, $\zeta^i = \zeta^{i-1}$.

It can be shown easily that this method generates a Markov chain with a stationary distribution given by the posterior. The main benefit is that usually the ratio in equation (A.10) can be calculated fast by evaluating the prior and the likelihood at the proposal $\boldsymbol{\zeta}^*$. In case of Gaussian steps (i.e., a symmetric transition probability) and for a Gaussian likelihood given by a χ^2 function as given by equation (4.4), this simplifies to

$$r = \exp\left(\Delta\chi^2\right) \equiv \exp\left(\chi^2(\boldsymbol{\zeta}^*) - \chi^2(\boldsymbol{\zeta}^{i-1})\right), \tag{A.11}$$

where in the illustrative case of our power spectrum model, $\chi^2(\boldsymbol{\zeta}) \equiv \chi^2(\boldsymbol{P}^{\mathrm{pred}}(\boldsymbol{\zeta}), \boldsymbol{P}^{\mathrm{obs}}, \boldsymbol{\psi}^P)$.

The choice of the transition distribution directly relates to the efficiency of the simulations. If steps are chosen too large, the acceptance ratio is very low and the parameter space is not well sampled. Too small steps also prevent a good sampling as larger distances between equiprobable regions cannot be covered fast. Often, a crude approximation of the posterior distribution, especially of the marginalized variance of each parameter, can be used to guess a good step size. The MCMC sampling is also sensitive to re-parametrizations of the model as model parameters can be degenerate preventing an efficient 'walk' through the parameter space. An inappropriately guessed step size can be used to generate a first trial chain whose sampled posterior might not be good enough for the estimation of parameter constraints, but can be used to refine

the step size. The covariance of the sampled parameters of the short, approximate chain can then be used to define decorrelated parameters and refine the step sizes (or alternatively the transition sampling can be chosen to be oriented along the axis of degeneration which can be obtained from the eigenvectors of the parameter covariance matrix). Other issues that need to be considered when a Markov chain is used for parameter estimation are ergodicity of the parameter space and the 'connectedness' of regions of similar likeliness.

A.2.2 Posterior statistics

The points sampled by the Markov chain, ζ^i, $i = 0, \ldots, N_\mathrm{c}$, serve as a sample drawn by the posterior. The marginalized mean and dispersion of a parameter θ_i or a derived function $f(\boldsymbol{\zeta})$ can be obtained using[1]

$$\bar{f} \equiv \langle f \rangle = \frac{1}{N_\mathrm{c} - N_\mathrm{b}} \sum_{i=N_\mathrm{b}}^{N_\mathrm{c}} f(\boldsymbol{\zeta}^i) \quad \text{and} \tag{A.12}$$

$$\sigma_f^2 \equiv \mathrm{var}(f) = \frac{1}{N_\mathrm{c} - N_\mathrm{b} - 1} \sum_{i=N_\mathrm{b}}^{N_\mathrm{c}} \left| f(\boldsymbol{\zeta}^i) - \langle f \rangle \right|^2, \tag{A.13}$$

adopting the convention that $\bar{\theta}_i \equiv \langle f_{\theta_i} \rangle$ and $\sigma_{\theta_i} \equiv \mathrm{var}(f_{\theta_i})$, where $f_{\theta_i}(\boldsymbol{\zeta}) = \theta_i$ just selects the appropriate element in the parameter space.

The estimation of the parameter confidence levels depends on the inverse of the percentile function,

$$P(\hat{f}) = \frac{1}{N_\mathrm{c} - N_\mathrm{b}} \sum_{i=N_\mathrm{b}}^{N_\mathrm{c}} \Theta^\mathrm{H}\left(\hat{f} - f(\boldsymbol{\zeta}^i)\right), \tag{A.14}$$

where $\Theta^\mathrm{H}(x)$ is the Heaviside function. The interval, $[f_\mathrm{min}, f_\mathrm{max}]$, with 68.26% confidence level for a derived parameter $f(\boldsymbol{x})$ is given by the condition $P(f_\mathrm{min}) = 15.87$ and $P(f_\mathrm{max}) = 84.13$. Analogously, the 95.44% CL interval is obtained by $P(f_\mathrm{min}) = 2.28$ and $P(f_\mathrm{max}) = 97.72$. In this work, the CL limits are listed as $\bar{f}^{+f_\mathrm{max}-\bar{f}}_{-(f_\mathrm{min}-\bar{f})}$ — or $\bar{f} \pm \sigma_f$ in case of a symmetric interval $\sigma_f = \bar{f} - f_\mathrm{min} = f_\mathrm{max} - \bar{f}$. Again, the limits for a chain parameter θ_i are given by the same formulas with $f_{\theta_i}(\boldsymbol{\zeta}) = \theta_i$.

Usually, the first N_b steps are removed as the *burn-in* fraction during which stationarity was not yet reached. The burn-in length can be guessed from the coherence length within the chain. Often, a very conservative approach is used by removing a fraction of a third to a half of a long chain.

[1] Note that the notation adopted here uses repeated parameters, $\boldsymbol{\zeta}^i = \boldsymbol{\zeta}^{i-1}$, in case of rejection. Alternatively, as used in our implementation and many other MCMC simulations, such as CosmoMC, the chain elements are not repeated, but provided with a weight that is increased by unity for each rejection.

A.2.3 Convergence criterion

As it is very difficult to estimate whether the sample obtained from a single chain is representative for the posterior or not, multiple chains should be started in parallel (with dispersed starting points). Then, the *convergence* of the chains should be monitored by evaluating the cross-chain variance, the so-called 'mixing' of the chains. Here, we adopt the Gelman-Rubin convergence criterion (Gelman & Rubin, 1992). We assume N_C chains, each having a length of $N_\mathrm{c}^{(j)}$, $j = 1, \ldots, N_\mathrm{C}$, define the mean for each chain and the total mean,

$$\langle {}^{(j)}\zeta \rangle = \frac{1}{N_\mathrm{c}^{(j)}} \sum_{i=1}^{N_\mathrm{c}^{(j)}} {}^{(j)}\zeta^i, \quad \text{and} \quad \langle \zeta \rangle = \frac{1}{N_\mathrm{C}} \sum_{j=1}^{N_\mathrm{C}} \frac{1}{N_\mathrm{c}^{(j)}} \sum_{i=1}^{N_\mathrm{c}^{(j)}} {}^{(j)}\zeta^i. \tag{A.15}$$

The variance between the chains is given by

$$B_n \equiv \frac{1}{N_\mathrm{C} - 1} \sum_{j=1}^{N_\mathrm{C}} \left| \langle {}^{(j)}\zeta \rangle - \langle \zeta \rangle \right|^2, \tag{A.16}$$

while the variance within a chain is

$${}^{(j)}W \equiv \frac{1}{N_\mathrm{c}^{(j)} - 1} \sum_{i=1}^{N_\mathrm{c}^{(j)}} \left| {}^{(j)}\zeta^i - \langle {}^{(j)}\zeta \rangle \right|^2. \tag{A.17}$$

The normal estimator for the variance within all chains,

$$W \equiv \frac{1}{N_\mathrm{C}} \sum_{j=1}^{N_\mathrm{C}} {}^{(j)}W, \tag{A.18}$$

is underestimating the variance of the target distribution if the chains did not yet converge. We can define an estimator of the target variance that gives overestimated results for non-stationary chains by

$$\tilde{W} \equiv \frac{1}{N_\mathrm{C}} \sum_{j=1}^{N_\mathrm{C}} \frac{N_\mathrm{c}^{(j)} - 1}{N_\mathrm{c}^{(j)}} {}^{(j)}W + B_n \left(1 + \frac{1}{N_\mathrm{C}} \right) \tag{A.19}$$

Thus, the Gelman-Rubin ratio defined by

$$\hat{R} \equiv \frac{\tilde{W}}{W} \tag{A.20}$$

is a measure of the stationarity of the chains, which approaches the ideal value of unity from above. Usually, the convergence criterion is given as $\hat{R} - 1$ and chains are considered as converged for $\hat{R} - 1 < 0.02$. We also adopt this convergence rule for our model performance tests in Section 5.2 and the full-shape fits in Section 6.1.

A.3 CosmoMC

CosmoMC (COSMOlogical Monte-Carlo; Lewis & Bridle, 2002) is an MCMC engine for exploring cosmological parameter spaces, written in Fortran, and specifically designed to infer the parameters of cosmological models from CMB observations. The code is widely used among cosmologists and has been revised, extended, and improved by the community. The public code is shared freely, together with additional tools for analysing Monte-Carlo samples and importance sampling.

The matter power spectrum is computed using Camb (Lewis *et al.*, 2000), taking into account BBN, recombination, and re-ionization with additional tools in order to predict the angular power spectrum that is measured from the CMB today, as well as the late-time spatial matter power spectrum as inferred from clustering probes. The code is structured in modules so that extensions can be easily added. Likelihood packages exists for CMB observations, — such as *WMAP* (Bennett *et al.*, 2013), *Planck* (Ade *et al.*, 2014c), ACT (Das *et al.*, 2014), and SPT (Reichardt *et al.*, 2012), — lensing of the CMB (Ade *et al.*, 2014d), SN Ia data, — such as SNLS (Conley *et al.*, 2011), Union (Suzuki *et al.*, 2012), and JLA (Betoule *et al.*, 2014), – galaxy clustering probes (BAO, RSD), Ly-α surveys, galaxy cluster statistics, and many more. The parameters definitions can be done easily with configuration scripts, allowing for flat and Gaussian priors.

By now, CosmoMC has implemented a wide variety of sampling algorithms among which Metropolis-Hastings is only one option. More sophisticated sampling schemes take into account the fact that the effect of some nuisance parameters on the model prediction can be calculated fast, while changing the underlying cosmological parameters requires to recompute the full model. Thus, the parameter space is split into sets of 'fast' and 'slow' parameters (Lewis, 2013), allowing for a more computing-efficient exploration of the parameter space by use of a 'dragging' scheme (Neal, 2005). The convergence tests are based on the Gelman-Rubin $\hat{R}$ statistic defined in equation (A.20).

CosmoMC is the standard exploration tool for the CMB analysis of the *WMAP* and *Planck* teams and is highly optimised to efficiently calculate the CMB temperature and polarization likelihoods, taking care of multi-frequency observations, foreground systematics, the large-/small-scale separation (as they have different sampling distributions; Ade *et al.*, 2014b) of the CMB analysis, and many other aspects that are relevant to get constraints from cosmological data that are as precise as possible.

The analysis of the generated chains (like the marginalizations) can be automated using the getdist package. Also a GUI for visual inspection of the sampled distributions exists.

B

Tables with cosmological constraints

Pumbaa: "Timon, ever wonder what those sparkly dots are up there?"
Timon: "Pumbaa, I don't wonder; I know."
Pumbaa: "Oh. What are they?"
Timon: "They're fireflies that got stuck up in that bluish-black thing."
Pumbaa: "Oh, gee. I always thought they were balls of gas burning billions of miles away."
Timon: "Pumbaa, with you, everything's gas."

The Lion King

In this appendix, the constraints (as 68% and 98% limits) for the full set of parameters for the full-shape fits in Section 6.1 and the concombined measurement fits in Section 6.5 are listed in tables. The parameter spaces are given by the parameters of the 'gRPT+RSD' model as listed in Table 5.2 and the cosmological parameter spaces as listed in Tables 6.2 and 6.3. The listed limits have been derived with the percentile function as discussed in Appendix A.2.2.

B.1 Full-shape measurements of the BAO distance and growth with the DR12 combined sample

Table B.1 – The 68% and 95% limits for the parameters of the full-shape fit to three power spectrum wedges of the DR12 combined sample in the low redshift bin fitted in the wavenumber range $0.02\ h\,\mathrm{Mpc}^{-1} \leq k \leq 0.2\ h\,\mathrm{Mpc}^{-1}$ using the covariance matrix from 2045 PATCHY mocks.

Parameter	68% limits	95% limits
$\alpha_\perp$	0.990 ± 0.016	$0.990^{+0.033}_{-0.032}$
$\alpha_\parallel$	$1.015^{+0.025}_{-0.030}$	$1.015^{+0.059}_{-0.053}$
$f\,\sigma_8$	0.498 ± 0.045	$0.498^{+0.086}_{-0.089}$
b_1^{NGC}	$1.796^{+0.041}_{-0.046}$	$1.796^{+0.089}_{-0.082}$
b_1^{SGC}	1.840 ± 0.053	$1.84^{+0.10}_{-0.10}$
b_2^{NGC}	$-0.16^{+0.37}_{-0.56}$	$-0.16^{+0.94}_{-0.84}$
b_2^{SGC}	0.50 ± 0.62	$0.5^{+1.2}_{-1.2}$
$\gamma_3^{-,\mathrm{NGC}}$	0.54 ± 0.25	$0.54^{+0.50}_{-0.50}$
$\gamma_3^{-,\mathrm{SGC}}$	$1.04^{+0.38}_{-0.33}$	$1.04^{+0.66}_{-0.68}$
$a_{\mathrm{vir}}^{\mathrm{NGC}}$	$4.50^{+1.1}_{-0.96}$	$4.5^{+2.1}_{-2.2}$
$a_{\mathrm{vir}}^{\mathrm{SGC}}$	7.3 ± 1.3	$7.3^{+2.5}_{-2.3}$
N^{NGC}	62 ± 500	—
N^{SGC}	205^{+700}_{-300}	> -661

Table B.2 – The 68% and 95% limits for the parameters of the full-shape fit to three power spectrum wedges of the DR12 combined sample in the intermediate and high redshift bin fitted in the wavenumber range $0.02\ h\,\mathrm{Mpc}^{-1} \leq k \leq 0.2\ h\,\mathrm{Mpc}^{-1}$ using the covariance matrix from 2045 PATCHY mocks.

Redshift bin	Intermediate		High	
Parameter	68% limits	95% limits	68% limits	95% limits
$\alpha_\perp$	0.997 ± 0.016	$0.997^{+0.032}_{-0.032}$	$0.982^{+0.019}_{-0.017}$	$0.982^{+0.035}_{-0.037}$
$\alpha_\parallel$	$1.023^{+0.025}_{-0.029}$	$1.023^{+0.057}_{-0.052}$	0.997 ± 0.027	$0.997^{+0.054}_{-0.052}$
$f\,\sigma_8$	0.448 ± 0.038	$0.448^{+0.074}_{-0.076}$	$0.409^{+0.036}_{-0.042}$	$0.409^{+0.084}_{-0.075}$
b_1	1.919 ± 0.042	$1.919^{+0.084}_{-0.080}$	1.979 ± 0.046	$1.979^{+0.089}_{-0.092}$
b_2	$-0.23^{+0.49}_{-0.94}$	$-0.2^{+1.4}_{-1.2}$	$0.6^{+1.6}_{-1.8}$	$0.6^{+1.9}_{-2.0}$
γ_3^-	1.01 ± 0.27	$1.01^{+0.52}_{-0.52}$	1.01 ± 0.32	$1.01^{+0.63}_{-0.64}$
a_{vir}	$3.6^{+1.5}_{-1.2}$	$3.6^{+2.6}_{-2.9}$	$4.4^{+2.2}_{-1.8}$	$4.4^{+3.2}_{-3.9}$
N	388^{+700}_{-900}	> -686	162^{+500}_{-800}	162^{+1000}_{-1000}

Table B.3 – The 68% and 95% limits for the parameters of the full-shape fit to two power spectrum wedges of the DR12 combined sample in the low redshift bin fitted in the wavenumber range $0.02\ h\,\mathrm{Mpc}^{-1} \leq k \leq 0.2\ h\,\mathrm{Mpc}^{-1}$ using the covariance matrix from 2045 PATCHY mocks.

Parameter	68% limits	95% limits
$\alpha_\perp$	$0.976^{+0.020}_{-0.017}$	$0.976^{+0.038}_{-0.041}$
$\alpha_\parallel$	$1.042^{+0.040}_{-0.044}$	$1.042^{+0.086}_{-0.080}$
$f\,\sigma_8$	0.496 ± 0.047	$0.496^{+0.091}_{-0.095}$
b_1^{NGC}	1.809 ± 0.051	$1.81^{+0.10}_{-0.097}$
b_1^{SGC}	1.848 ± 0.057	$1.85^{+0.11}_{-0.11}$
b_2^{NGC}	$-0.05^{+0.40}_{-0.70}$	$-0.05^{+1.1}_{-0.97}$
b_2^{SGC}	0.44 ± 0.61	$0.4^{+1.2}_{-1.2}$
$\gamma_3^{-,\mathrm{NGC}}$	0.57 ± 0.28	$0.57^{+0.54}_{-0.54}$
$\gamma_3^{-,\mathrm{SGC}}$	$1.02^{+0.39}_{-0.32}$	$1.02^{+0.67}_{-0.70}$
$a_{\mathrm{vir}}^{\mathrm{NGC}}$	$5.4^{+1.6}_{-1.2}$	$5.4^{+3.1}_{-3.4}$
$a_{\mathrm{vir}}^{\mathrm{SGC}}$	$7.77^{+1.7}_{-0.95}$	> 5.42
N^{NGC}	> 62.9	—
N^{SGC}	101^{+600}_{-500}	> -593

Table B.4 – The 68% and 95% limits for the parameters of the full-shape fit to two power spectrum wedges of the DR12 combined sample in the intermediate and high redshift bin fitted in the wavenumber range $0.02\ h\,\mathrm{Mpc}^{-1} \leq k \leq 0.2\ h\,\mathrm{Mpc}^{-1}$ using the covariance matrix from 2045 PATCHY mocks.

Redshift bin	Intermediate		High	
Parameter	68% limits	95% limits	68% limits	95% limits
$\alpha_\perp$	1.001 ± 0.020	$1.001^{+0.042}_{-0.040}$	1.006 ± 0.022	$1.006^{+0.044}_{-0.041}$
$\alpha_\parallel$	$1.026^{+0.037}_{-0.042}$	$1.026^{+0.086}_{-0.082}$	$0.953^{+0.039}_{-0.033}$	$0.953^{+0.067}_{-0.071}$
$f\,\sigma_8$	0.452 ± 0.042	$0.452^{+0.081}_{-0.085}$	$0.433^{+0.035}_{-0.040}$	$0.433^{+0.080}_{-0.072}$
b_1	$1.922^{+0.042}_{-0.049}$	$1.922^{+0.096}_{-0.086}$	1.958 ± 0.043	$1.958^{+0.085}_{-0.081}$
b_2	$-0.22^{+0.46}_{-0.98}$	$-0.2^{+1.5}_{-1.2}$	$0.26^{+0.69}_{-0.99}$	$0.3^{+1.6}_{-1.5}$
γ_3^-	1.01 ± 0.28	$1.01^{+0.54}_{-0.55}$	0.96 ± 0.33	$0.96^{+0.64}_{-0.64}$
a_{vir}	3.4 ± 1.8	< 6.39	< 3.23	< 5.55
N	401^{+600}_{-800}	> -661	-24^{+470}_{-710}	-24^{+1400}_{-1100}

B.2 Combined constraints for the standard cosmological model and some extensions

Table B.5 – The 68% and 95% limits for the parameters of the 'gRPT+RSD' fit to the *Planck* 2015 TT+lowP (Ade *et al.*, 2015) and three power spectrum wedges of the DR12 combined sample in the low and high redshift bin, as well as the fit adding JLA SN Ia data (Betoule *et al.*, 2014), assuming a ΛCDM cosmology in both cases. The DR12 combined sample fit used a wavenumber range of $0.02\ h\,\mathrm{Mpc}^{-1} \leq k \leq 0.2\ h\,\mathrm{Mpc}^{-1}$ and the covariance matrix from 2045 PATCHY mocks. Only basic cosmological and galaxy clustering nuisance parameters are shown.

Data	Planck 2015 + $P_{3\mathrm{w},n}(k)$		+ JLA SN Ia	
Parameter	68% limits	95% limits	68% limits	95% limits
$\Omega_\mathrm{b}\,h^2$	0.02221 ± 0.00020	$0.02221^{+0.00041}_{-0.00040}$	0.02222 ± 0.00021	$0.02222^{+0.00041}_{-0.00041}$
$\Omega_\mathrm{c}\,h^2$	$0.1192^{+0.0016}_{-0.0011}$	$0.1192^{+0.0024}_{-0.0030}$	$0.1191^{+0.0016}_{-0.0012}$	$0.1191^{+0.0024}_{-0.0029}$
$100\,\theta_\mathrm{MC}$	1.04090 ± 0.00043	$1.04090^{+0.00085}_{-0.00083}$	1.04092 ± 0.00044	$1.04092^{+0.00087}_{-0.00084}$
τ	0.073 ± 0.018	$0.073^{+0.035}_{-0.035}$	0.073 ± 0.019	$0.073^{+0.037}_{-0.036}$
$\ln(10^{10}\,A_\mathrm{s})$	3.078 ± 0.035	$3.078^{+0.069}_{-0.069}$	3.077 ± 0.036	$3.077^{+0.072}_{-0.070}$
n_s	$0.9657^{+0.0042}_{-0.0051}$	$0.9657^{+0.0098}_{-0.0086}$	$0.9659^{+0.0044}_{-0.0050}$	$0.9659^{+0.0095}_{-0.0089}$
$^{(z1)}b_1^\mathrm{NGC}$	1.810 ± 0.043	$1.810^{+0.085}_{-0.083}$	1.810 ± 0.044	$1.810^{+0.087}_{-0.086}$
$^{(z1)}b_1^\mathrm{SGC}$	1.852 ± 0.050	$1.85^{+0.10}_{-0.10}$	1.852 ± 0.051	$1.852^{+0.099}_{-0.10}$
$^{(z3)}b_1$	1.991 ± 0.042	$1.991^{+0.082}_{-0.083}$	1.992 ± 0.044	$1.992^{+0.084}_{-0.086}$
$^{(z1)}b_2^\mathrm{NGC}$	$-0.09^{+0.40}_{-0.59}$	$-0.09^{+0.98}_{-0.89}$	$-0.10^{+0.40}_{-0.59}$	$-0.10^{+0.99}_{-0.89}$
$^{(z1)}b_2^\mathrm{SGC}$	0.53 ± 0.66	$0.5^{+1.3}_{-1.2}$	0.52 ± 0.66	$0.5^{+1.3}_{-1.2}$
$^{(z3)}b_2$	$1.48^{+1.1}_{-0.45}$	$1.5^{+1.4}_{-2.1}$	$1.44^{+1.1}_{-0.43}$	$1.4^{+1.4}_{-2.2}$
$^{(z1)}\gamma_3^{-,\mathrm{NGC}}$	0.52 ± 0.25	$0.52^{+0.49}_{-0.50}$	0.51 ± 0.25	$0.51^{+0.49}_{-0.50}$
$^{(z1)}\gamma_3^{-,\mathrm{SGC}}$	$1.05^{+0.37}_{-0.33}$	$1.05^{+0.66}_{-0.71}$	$1.05^{+0.38}_{-0.33}$	$1.05^{+0.65}_{-0.71}$
$^{(z3)}\gamma_3^-$	1.13 ± 0.28	$1.13^{+0.55}_{-0.57}$	1.12 ± 0.29	$1.12^{+0.56}_{-0.58}$
$^{(z1)}a_\mathrm{vir}^\mathrm{NGC}$	$4.06^{+1.2}_{-0.99}$	$4.1^{+2.2}_{-2.3}$	$4.0^{+1.2}_{-1.0}$	$4.0^{+2.2}_{-2.3}$
$^{(z1)}a_\mathrm{vir}^\mathrm{SGC}$	6.8 ± 1.3	$6.8^{+2.4}_{-2.5}$	6.7 ± 1.2	$6.7^{+2.4}_{-2.5}$
$^{(z3)}a_\mathrm{vir}$	$6.34^{+1.8}_{-0.81}$	$6.3^{+2.6}_{-3.5}$	$6.27^{+1.8}_{-0.77}$	$6.3^{+2.5}_{-3.6}$
$^{(z1)}N^\mathrm{NGC}$	-127^{+360}_{-730}	—	-118^{+370}_{-730}	—
$^{(z1)}N^\mathrm{SGC}$	124^{+600}_{-400}	—	134^{+700}_{-400}	—
$^{(z3)}N$	264^{+300}_{-400}	264^{+900}_{-800}	259^{+300}_{-400}	259^{+900}_{-800}

Table B.6 – The 68% and 95% limits for the parameters of the 'gRPT+RSD' fit to the *Planck* 2015 TT+lowP (Ade *et al.*, 2015) and three power spectrum wedges of the DR12 combined sample in the low and high redshift bin, as well as the fit adding JLA SN Ia data (Betoule *et al.*, 2014), assuming a wCDM cosmology in both cases. Only basic cosmological parameters are shown.

Data	Planck 2015 + $P_{3\mathrm{w},n}(k)$		+ JLA SN Ia	
Parameter	68% limits	95% limits	68% limits	95% limits
$\Omega_\mathrm{b}\,h^2$	0.02219 ± 0.00022	$0.02219^{+0.00043}_{-0.00041}$	0.02221 ± 0.00021	$0.02221^{+0.00042}_{-0.00042}$
$\Omega_\mathrm{c}\,h^2$	0.1194 ± 0.0018	$0.1194^{+0.0035}_{-0.0035}$	0.1192 ± 0.0017	$0.1192^{+0.0035}_{-0.0033}$
$100\,\theta_\mathrm{MC}$	1.04087 ± 0.00047	$1.04087^{+0.00092}_{-0.00092}$	1.04090 ± 0.00046	$1.04090^{+0.00091}_{-0.00087}$
τ	0.070 ± 0.019	$0.070^{+0.039}_{-0.037}$	0.071 ± 0.019	$0.071^{+0.037}_{-0.037}$
w	$-1.029^{+0.070}_{-0.054}$	$-1.03^{+0.11}_{-0.14}$	$-1.019^{+0.048}_{-0.039}$	$-1.019^{+0.079}_{-0.090}$
$\ln(10^{10}\,A_\mathrm{s})$	3.073 ± 0.037	$3.073^{+0.075}_{-0.073}$	3.075 ± 0.037	$3.075^{+0.072}_{-0.071}$
n_s	0.9650 ± 0.0056	$0.965^{+0.011}_{-0.011}$	0.9656 ± 0.0054	$0.966^{+0.011}_{-0.011}$

Table B.7 – The 68% and 95% limits for the parameters of the 'gRPT+RSD' fit to the *Planck* 2015 TT+lowP (Ade *et al.*, 2015) and three power spectrum wedges of the DR12 combined sample in the low and high redshift bin, as well as the fit adding JLA SN Ia data (Betoule *et al.*, 2014), assuming a w_0w_aCDM cosmology in both cases. Only basic cosmological parameters are shown.

Data	Planck 2015 + $P_{3\mathrm{w},n}(k)$		+ JLA SN Ia	
Parameter	68% limits	95% limits	68% limits	95% limits
$\Omega_\mathrm{b}\,h^2$	0.02218 ± 0.00022	$0.02218^{+0.00043}_{-0.00043}$	0.02220 ± 0.00022	$0.02220^{+0.00044}_{-0.00043}$
$\Omega_\mathrm{c}\,h^2$	0.1197 ± 0.0019	$0.1197^{+0.0037}_{-0.0036}$	0.1195 ± 0.0019	$0.1195^{+0.0036}_{-0.0037}$
$100\,\theta_\mathrm{MC}$	1.04085 ± 0.00047	$1.04085^{+0.00092}_{-0.00092}$	1.04087 ± 0.00046	$1.04087^{+0.00093}_{-0.00090}$
τ	0.068 ± 0.020	$0.068^{+0.039}_{-0.039}$	0.069 ± 0.019	$0.069^{+0.038}_{-0.038}$
w_0	-1.03 ± 0.24	$-1.03^{+0.48}_{-0.47}$	-0.98 ± 0.11	$-0.98^{+0.22}_{-0.21}$
w_a	$-0.06^{+0.77}_{-0.62}$	$-0.1^{+1.2}_{-1.4}$	$-0.16^{+0.46}_{-0.36}$	$-0.16^{+0.75}_{-0.87}$
$\ln(10^{10}\,A_\mathrm{s})$	3.070 ± 0.038	$3.070^{+0.074}_{-0.075}$	3.071 ± 0.037	$3.071^{+0.072}_{-0.073}$
n_s	0.9645 ± 0.0057	$0.965^{+0.011}_{-0.011}$	0.9650 ± 0.0056	$0.965^{+0.012}_{-0.011}$

Table B.8 – The 68% and 95% limits for the parameters of the 'gRPT+RSD' fit to the *Planck* 2015 TT+lowP (Ade *et al.*, 2015) and three power spectrum wedges of the DR12 combined sample in the low and high redshift bin, as well as the fit adding JLA SN Ia data (Betoule *et al.*, 2014), assuming a ΛCDM cosmology with a free γ in both cases. Only basic cosmological parameters are shown.

Data	Planck 2015 + $P_{3\mathrm{w},n}(k)$		+ JLA SN Ia	
Parameter	68% limits	95% limits	68% limits	95% limits
$\Omega_\mathrm{b}\,h^2$	0.02221 ± 0.00021	$0.02221^{+0.00041}_{-0.00039}$	0.02222 ± 0.00021	$0.02222^{+0.00041}_{-0.00040}$
$\Omega_\mathrm{c}\,h^2$	$0.1192^{+0.0016}_{-0.0011}$	$0.1192^{+0.0024}_{-0.0030}$	$0.1190^{+0.0016}_{-0.0012}$	$0.1190^{+0.0024}_{-0.0030}$
$100\,\theta_\mathrm{MC}$	1.04089 ± 0.00043	$1.04089^{+0.00086}_{-0.00083}$	1.04094 ± 0.00044	$1.04094^{+0.00085}_{-0.00086}$
τ	0.071 ± 0.019	$0.071^{+0.037}_{-0.036}$	0.072 ± 0.019	$0.072^{+0.037}_{-0.037}$
$\ln(10^{10}\,A_\mathrm{s})$	3.075 ± 0.037	$3.075^{+0.072}_{-0.072}$	3.076 ± 0.037	$3.076^{+0.072}_{-0.074}$
n_s	$0.9655^{+0.0044}_{-0.0050}$	$0.9655^{+0.0098}_{-0.0089}$	$0.9660^{+0.0045}_{-0.0051}$	$0.9660^{+0.0098}_{-0.0090}$
γ	0.526 ± 0.099	$0.53^{+0.20}_{-0.19}$	0.523 ± 0.097	$0.52^{+0.19}_{-0.19}$

Table B.9 – The 68% and 95% limits for the parameters of the 'gRPT+RSD' fit to the *Planck* 2015 TT+lowP (Ade *et al.*, 2015) and three power spectrum wedges of the DR12 combined sample in the low and high redshift bin, as well as the fit adding JLA SN Ia data (Betoule *et al.*, 2014), assuming a wCDM cosmology with a free γ in both cases. Only basic cosmological parameters are shown.

Data	Planck 2015 + $P_{3\mathrm{w},n}(k)$		+ JLA SN Ia	
Parameter	68% limits	95% limits	68% limits	95% limits
$\Omega_\mathrm{b}\,h^2$	0.02219 ± 0.00023	$0.02219^{+0.00045}_{-0.00044}$	0.02220 ± 0.00022	$0.02220^{+0.00043}_{-0.00042}$
$\Omega_\mathrm{c}\,h^2$	0.1196 ± 0.0019	$0.1196^{+0.0037}_{-0.0037}$	0.1193 ± 0.0018	$0.1193^{+0.0036}_{-0.0035}$
$100\,\theta_\mathrm{MC}$	1.04086 ± 0.00048	$1.04086^{+0.00093}_{-0.00093}$	1.04090 ± 0.00047	$1.04090^{+0.00091}_{-0.00092}$
τ	0.069 ± 0.020	$0.069^{+0.039}_{-0.040}$	0.071 ± 0.019	$0.071^{+0.038}_{-0.039}$
w	$-1.041^{+0.092}_{-0.069}$	$-1.04^{+0.15}_{-0.17}$	$-1.020^{+0.052}_{-0.045}$	$-1.020^{+0.091}_{-0.10}$
$\ln(10^{10}\,A_\mathrm{s})$	3.071 ± 0.038	$3.071^{+0.075}_{-0.078}$	3.074 ± 0.038	$3.074^{+0.075}_{-0.077}$
n_s	0.9647 ± 0.0057	$0.965^{+0.011}_{-0.011}$	0.9654 ± 0.0054	$0.965^{+0.010}_{-0.011}$
γ	$0.56^{+0.12}_{-0.14}$	$0.56^{+0.27}_{-0.23}$	0.54 ± 0.11	$0.54^{+0.23}_{-0.21}$

Table B.10 – The 68% and 95% limits for the parameters of the 'gRPT+RSD' fit to the *Planck* 2015 TT+lowP (Ade *et al.*, 2015) and three power spectrum wedges of the DR12 combined sample in the low and high redshift bin, as well as the fit adding JLA SN Ia data (Betoule *et al.*, 2014), assuming a K-ΛCDM cosmology in both cases. Only basic cosmological parameters are shown.

Data	Planck 2015 + $P_{3\mathrm{w},n}(k)$		+ JLA SN Ia	
Parameter	68% limits	95% limits	68% limits	95% limits
$\Omega_\mathrm{b}\,h^2$	0.02226 ± 0.00024	$0.02226^{+0.00049}_{-0.00046}$	0.02226 ± 0.00024	$0.02226^{+0.00047}_{-0.00044}$
$\Omega_\mathrm{c}\,h^2$	0.1186 ± 0.0021	$0.1186^{+0.0042}_{-0.0042}$	0.1186 ± 0.0021	$0.1186^{+0.0041}_{-0.0041}$
$100\,\theta_\mathrm{MC}$	1.04098 ± 0.00049	$1.04098^{+0.00098}_{-0.00096}$	1.04099 ± 0.00050	$1.04099^{+0.00097}_{-0.00097}$
τ	0.074 ± 0.019	$0.074^{+0.038}_{-0.036}$	0.074 ± 0.019	$0.074^{+0.036}_{-0.036}$
Ω_K	-0.0008 ± 0.0027	$-0.0008^{+0.0056}_{-0.0052}$	$-0.0006^{+0.0025}_{-0.0028}$	$-0.0006^{+0.0056}_{-0.0052}$
$\ln(10^{10}\,A_\mathrm{s})$	3.079 ± 0.036	$3.079^{+0.073}_{-0.069}$	3.079 ± 0.036	$3.079^{+0.070}_{-0.070}$
n_s	0.9671 ± 0.0062	$0.967^{+0.012}_{-0.012}$	0.9672 ± 0.0062	$0.967^{+0.012}_{-0.012}$

Table B.11 – The 68% and 95% limits for the parameters of the 'gRPT+RSD' fit to the *Planck* 2015 TT+lowP (Ade *et al.*, 2015) and three power spectrum wedges of the DR12 combined sample in the low and high redshift bin, as well as the fit adding JLA SN Ia data (Betoule *et al.*, 2014), assuming a K-wCDM cosmology in both cases. Only basic cosmological parameters are shown.

Data	Planck 2015 + $P_{3\mathrm{w},n}(k)$		+ JLA SN Ia	
Parameter	68% limits	95% limits	68% limits	95% limits
$\Omega_\mathrm{b}\,h^2$	0.02226 ± 0.00024	$0.02226^{+0.00048}_{-0.00046}$	0.02226 ± 0.00024	$0.02226^{+0.00046}_{-0.00047}$
$\Omega_\mathrm{c}\,h^2$	0.1187 ± 0.0022	$0.1187^{+0.0042}_{-0.0043}$	0.1187 ± 0.0021	$0.1187^{+0.0043}_{-0.0041}$
$100\,\theta_\mathrm{MC}$	1.04096 ± 0.00050	$1.04096^{+0.00099}_{-0.0010}$	1.04098 ± 0.00049	$1.04098^{+0.00095}_{-0.00096}$
τ	0.070 ± 0.020	$0.070^{+0.039}_{-0.038}$	0.071 ± 0.019	$0.071^{+0.037}_{-0.038}$
Ω_K	$-0.0017^{+0.0032}_{-0.0036}$	$-0.0017^{+0.0073}_{-0.0065}$	$-0.0014^{+0.0029}_{-0.0033}$	$-0.0014^{+0.0065}_{-0.0060}$
w	$-1.052^{+0.088}_{-0.071}$	$-1.05^{+0.15}_{-0.17}$	$-1.027^{+0.052}_{-0.045}$	$-1.027^{+0.092}_{-0.10}$
$\ln(10^{10}\,A_\mathrm{s})$	3.070 ± 0.038	$3.070^{+0.075}_{-0.075}$	3.074 ± 0.036	$3.074^{+0.071}_{-0.073}$
n_s	0.9669 ± 0.0063	$0.967^{+0.013}_{-0.012}$	0.9670 ± 0.0062	$0.967^{+0.012}_{-0.012}$

Table B.12 – The 68% and 95% limits for the parameters of the 'gRPT+RSD' fit to the *Planck* 2015 TT+lowP (Ade *et al.*, 2015) and three power spectrum wedges of the DR12 combined sample in the low and high redshift bin, as well as the fit adding JLA SN Ia data (Betoule *et al.*, 2014), assuming a ΛCDM cosmology with a free $\sum m_\nu$ in both cases. Only basic cosmological parameters are shown.

Data	Planck 2015 + $P_{3w,n}(k)$		+ JLA SN Ia	
Parameter	68% limits	95% limits	68% limits	95% limits
$\Omega_b h^2$	0.02223 ± 0.00021	$0.02223^{+0.00041}_{-0.00040}$	0.02224 ± 0.00021	$0.02224^{+0.00041}_{-0.00040}$
$\Omega_c h^2$	$0.1186^{+0.0017}_{-0.0015}$	$0.1186^{+0.0029}_{-0.0032}$	$0.1186^{+0.0017}_{-0.0015}$	$0.1186^{+0.0029}_{-0.0032}$
$100\,\theta_{MC}$	1.04095 ± 0.00043	$1.04095^{+0.00086}_{-0.00083}$	1.04097 ± 0.00044	$1.04097^{+0.00088}_{-0.00085}$
τ	0.078 ± 0.019	$0.078^{+0.037}_{-0.036}$	0.078 ± 0.019	$0.078^{+0.038}_{-0.036}$
$\sum m_\nu$	< 0.151	< 0.275	< 0.143	< 0.260
$\ln(10^{10} A_s)$	3.086 ± 0.036	$3.086^{+0.072}_{-0.070}$	3.086 ± 0.037	$3.086^{+0.072}_{-0.071}$
n_s	0.9669 ± 0.0049	$0.9669^{+0.0099}_{-0.0094}$	0.9672 ± 0.0051	$0.967^{+0.010}_{-0.0099}$

Table B.13 – The 68% and 95% limits for the parameters of the 'gRPT+RSD' fit to the *Planck* 2015 TT+lowP (Ade *et al.*, 2015) and three power spectrum wedges of the DR12 combined sample in the low and high redshift bin, as well as the fit adding JLA SN Ia data (Betoule *et al.*, 2014), assuming a ΛCDM cosmology with a free N_{eff} in both cases. Only basic cosmological parameters are shown.

Data	Planck 2015 + $P_{3w,n}(k)$		+ JLA SN Ia	
Parameter	68% limits	95% limits	68% limits	95% limits
$\Omega_b h^2$	0.02222 ± 0.00025	$0.02222^{+0.00051}_{-0.00048}$	$0.02225^{+0.00024}_{-0.00027}$	$0.02225^{+0.00052}_{-0.00048}$
$\Omega_c h^2$	0.1192 ± 0.0036	$0.1192^{+0.0073}_{-0.0069}$	0.1193 ± 0.0036	$0.1193^{+0.0073}_{-0.0071}$
$100\,\theta_{MC}$	1.04093 ± 0.00056	$1.0409^{+0.0011}_{-0.0011}$	1.04090 ± 0.00057	$1.0409^{+0.0011}_{-0.0011}$
τ	0.073 ± 0.018	$0.073^{+0.036}_{-0.035}$	0.074 ± 0.018	$0.074^{+0.037}_{-0.036}$
N_{eff}	$3.05^{+0.20}_{-0.24}$	$3.05^{+0.46}_{-0.41}$	$3.08^{+0.21}_{-0.24}$	$3.08^{+0.46}_{-0.42}$
$\ln(10^{10} A_s)$	3.077 ± 0.037	$3.077^{+0.076}_{-0.072}$	3.080 ± 0.038	$3.080^{+0.076}_{-0.074}$
n_s	$0.9662^{+0.0081}_{-0.010}$	$0.966^{+0.019}_{-0.017}$	$0.9672^{+0.0081}_{-0.010}$	$0.967^{+0.020}_{-0.017}$

Table B.14 – The 68% and 95% limits for the parameters of the 'gRPT+RSD' fit to the *Planck* 2015 TT+lowP (Ade *et al.*, 2015) and three power spectrum wedges of the DR12 combined sample in the low and high redshift bin, as well as the fit adding JLA SN Ia data (Betoule *et al.*, 2014), assuming a ΛCDM cosmology with a free $\sum m_\nu$ and N_{eff} in both cases. Only basic cosmological parameters are shown.

Data	Planck 2015 + $P_{3w,n}(k)$		+ JLA SN Ia	
Parameter	68% limits	95% limits	68% limits	95% limits
$\Omega_b h^2$	$0.02232^{+0.00026}_{-0.00030}$	$0.02232^{+0.00057}_{-0.00052}$	$0.02234^{+0.00026}_{-0.00029}$	$0.02234^{+0.00055}_{-0.00052}$
$\Omega_c h^2$	0.1203 ± 0.0038	$0.1203^{+0.0075}_{-0.0073}$	0.1205 ± 0.0038	$0.1205^{+0.0077}_{-0.0073}$
$100\,\theta_{MC}$	1.04079 ± 0.00057	$1.0408^{+0.0011}_{-0.0011}$	1.04077 ± 0.00057	$1.0408^{+0.0011}_{-0.0011}$
τ	$0.081^{+0.020}_{-0.022}$	$0.081^{+0.042}_{-0.040}$	0.082 ± 0.021	$0.082^{+0.041}_{-0.039}$
$\sum m_\nu$	< 0.198	< 0.380	< 0.192	< 0.357
N_{eff}	$3.18^{+0.25}_{-0.29}$	$3.18^{+0.52}_{-0.51}$	$3.19^{+0.24}_{-0.29}$	$3.19^{+0.55}_{-0.48}$
$\ln(10^{10} A_s)$	$3.097^{+0.042}_{-0.048}$	$3.097^{+0.089}_{-0.082}$	3.099 ± 0.043	$3.099^{+0.087}_{-0.082}$
n_s	$0.972^{+0.010}_{-0.012}$	$0.972^{+0.022}_{-0.021}$	$0.9727^{+0.0099}_{-0.012}$	$0.973^{+0.022}_{-0.020}$

Table B.15 – The 68% and 95% limits for the parameters of the 'gRPT+RSD' fit to the *Planck* 2015 TT+lowP (Ade *et al.*, 2015) and three power spectrum wedges of the DR12 combined sample in the low and high redshift bin, as well as the fit adding JLA SN Ia data (Betoule *et al.*, 2014), assuming a wCDM cosmology with a free $\sum m_\nu$ in both cases. Only basic cosmological parameters are shown.

Data	Planck 2015 + $P_{3\mathrm{w},n}(k)$		+ JLA SN Ia	
Parameter	68% limits	95% limits	68% limits	95% limits
$\Omega_\mathrm{b}\,h^2$	0.02213 ± 0.00022	$0.02213^{+0.00045}_{-0.00043}$	0.02217 ± 0.00021	$0.02217^{+0.00042}_{-0.00041}$
$\Omega_\mathrm{c}\,h^2$	0.1193 ± 0.0018	$0.1193^{+0.0035}_{-0.0034}$	0.1191 ± 0.0017	$0.1191^{+0.0035}_{-0.0034}$
$100\,\theta_\mathrm{MC}$	1.04080 ± 0.00047	$1.04080^{+0.00093}_{-0.00090}$	1.04086 ± 0.00045	$1.04086^{+0.00089}_{-0.00088}$
τ	0.073 ± 0.021	$0.073^{+0.041}_{-0.040}$	0.075 ± 0.019	$0.075^{+0.037}_{-0.038}$
$\sum m_\nu$	$0.28^{+0.14}_{-0.20}$	< 0.556	< 0.239	< 0.416
w	$-1.14^{+0.12}_{-0.096}$	$-1.14^{+0.20}_{-0.21}$	$-1.059^{+0.067}_{-0.051}$	$-1.06^{+0.11}_{-0.12}$
$\ln(10^{10}\,A_\mathrm{s})$	3.077 ± 0.039	$3.077^{+0.078}_{-0.077}$	3.081 ± 0.037	$3.081^{+0.071}_{-0.074}$
n_s	0.9637 ± 0.0057	$0.964^{+0.011}_{-0.011}$	0.9651 ± 0.0054	$0.965^{+0.011}_{-0.010}$

Bibliography

(Abazajian *et al.*, 2003) K. N. Abazajian *et al.* (SDSS Collaboration), *The First data release of the Sloan Digital Sky Survey*, Astron. J. **126**, 2081 (2003), arXiv:astro-ph/0305492 [astro-ph] p. 8.

(Abazajian *et al.*, 2004) K. N. Abazajian *et al.* (SDSS Collaboration), *The Second data release of the Sloan digital sky survey*, Astron. J. **128**, 502 (2004), arXiv:astro-ph/0403325 [astro-ph] p. 8.

(Abazajian *et al.*, 2009) K. N. Abazajian *et al.* (SDSS Collaboration), *The Seventh Data Release of the Sloan Digital Sky Survey*, Astrophys. J. Suppl. **182**, 543 (2009), arXiv:0812.0649 [astro-ph] p. 9.

(Abbott *et al.*, 2016) B. P. Abbott, R. Abbott, T. D. Abbott, *et al.* (LIGO Scientific Collaboration and Virgo Collaboration), *Observation of Gravitational Waves from a Binary Black Hole Merger*, Phys. Rev. Lett. **116**, 061102 (2016) p. 4.

(Abbott *et al.*, 2005) T. Abbott *et al.* (Dark Energy Survey Collaboration), *The dark energy survey*, ArXiv e-prints (2005), arXiv:astro-ph/0510346 [astro-ph] p. 11.

(Abe *et al.*, 2011) K. Abe *et al.* (Super-Kamiokande), *Solar neutrino results in Super-Kamiokande-III*, Phys. Rev. **D83**, 052010 (2011), arXiv:1010.0118 [hep-ex] p. 150.

(Adam *et al.*, 2015) R. Adam *et al.* (Planck Collaboration), *Planck 2015 results. I. Overview of products and scientific results*, ArXiv e-prints (2015), arXiv:1502.01582 [astro-ph.CO] p. 3, 19, 75, 142.

(Ade *et al.*, 2014a) P. A. R. Ade *et al.* (Planck Collaboration), *Planck 2013 results. I. Overview of products and scientific results*, Astron.Astrophys. **571**, A1 (2014a), arXiv:1303.5062 [astro-ph.CO] p. 16.

(Ade *et al.*, 2014b) P. A. R. Ade *et al.* (Planck Collaboration), *Planck 2013 results. XV. CMB power spectra and likelihood*, Astron.Astrophys. **571**, A15 (2014b), arXiv:1303.5075 [astro-ph.CO] p. 167.

(Ade *et al.*, 2014c) P. A. R. Ade *et al.* (Planck Collaboration), *Planck 2013 results. XVI. Cosmological parameters*, Astron.Astrophys. **571**, A16 (2014c), arXiv:1303.5076 [astro-ph.CO] p. 77, 151, 167.

(Ade *et al.*, 2014d) P. A. R. Ade *et al.* (Planck Collaboration), *Planck 2013 results. XVII. Gravitational lensing by large-scale structure*, Astron.Astrophys. **571**, A17 (2014d), arXiv:1303.5077 [astro-ph.CO] p. 167.

(Ade *et al.*, 2015) P. A. R. Ade *et al.* (Planck Collaboration), *Planck 2015 results. XIII. Cosmological parameters*, ArXiv e-prints (2015), arXiv:1502.01589 [astro-ph.CO] p. 3, 32, 77, 131, 132, 142, 145, 150, 159, 172, 173, 174, 175, 176.

(Ahn *et al.*, 2012) C. P. Ahn *et al.* (SDSS Collaboration), *The Ninth Data Release of the Sloan Digital Sky Survey: First Spectroscopic Data from the SDSS-III Baryon Oscillation Spectroscopic Survey*, Astrophys.J.Suppl. **203**, 21 (2012), arXiv:1207.7137 [astro-ph.IM] p. 14, 15, 64.

(Ahn *et al.*, 2014) C. P. Ahn *et al.* (SDSS Collaboration), *The Tenth Data Release of the Sloan Digital Sky Survey: First Spectroscopic Data from the SDSS-III Apache Point Observatory Galactic Evolution Experiment*, Astrophys. J. Suppl. **211**, 17 (2014), arXiv:1307.7735 [astro-ph.IM] p. 15.

(Aihara *et al.*, 2011) H. Aihara *et al.* (SDSS Collaboration), *The Eighth Data Release of the Sloan Digital Sky Survey: First Data from SDSS-III*, Astrophys.J.Suppl. **193**, 29 (2011), arXiv:1101.1559 [astro-ph.IM] p. 14, 80.

(Alam *et al.*, 2015a) S. Alam *et al.* (SDSS-III), *The Eleventh and Twelfth Data Releases of the Sloan Digital Sky Survey: Final Data from SDSS-III*, Astrophys. J. Suppl. **219**, 12 (2015a), arXiv:1501.00963 [astro-ph.IM] p. 18, 64.

(Alam *et al.*, 2015b) S. Alam, S. Ho, M. Vargas-Magaña, & D. P. Schneider, *Testing General Relativity with Growth rate measurement from Sloan Digital Sky Survey III Baryon Oscillations Spectroscopic Survey galaxies*, Mon. Not. Roy. Astron. Soc. **453**, 1754 (2015b), arXiv:1504.02100 [astro-ph.CO] p. 17, 18, 19, 20, 139.

(Albrecht *et al.*, 2006) A. Albrecht, G. Bernstein, R. Cahn, *et al.*, *Report of the Dark Energy Task Force*, ArXiv e-prints (2006), arXiv:astro-ph/0609591 [astro-ph] p. 11.

(Alcock & Paczynski, 1979) C. Alcock & B. Paczynski, *An evolution free test for non-zero cosmological constant*, Nature **281**, 358 (1979) p. 51.

(Amendola & Sellentin, 2016) L. Amendola & E. Sellentin, *Optimizing parameter constraints: a new tool for Fisher matrix forecasts*, ArXiv e-prints (2016), arXiv:1602.01746 [astro-ph.CO] p. 145.

(Anderson *et al.*, 2013) L. Anderson, É. Aubourg, S. Bailey, *et al.* (BOSS Collaboration), *The clustering of galaxies in the SDSS-III Baryon Oscillation Spectroscopic Survey: Baryon Acoustic Oscillations in the Data Release 9 Spectroscopic Galaxy Sample*, Mon.Not.Roy.Astron.Soc. **428**, 1036 (2013), arXiv:1203.6594 [astro-ph.CO] p. 15, 16, 17, 72.

(Anderson *et al.*, 2014a) L. Anderson, É. Aubourg, S. Bailey, *et al.* (BOSS Collaboration), *The clustering of galaxies in the SDSS-III Baryon Oscillation Spectroscopic Survey: measuring D_A and H at $z = 0.57$ from the baryon acoustic peak in the Data Release 9 spectroscopic Galaxy sample*, Mon.Not.Roy.Astron.Soc. **439**, 83 (2014a), arXiv:1303.4666 [astro-ph.CO] p. 15, 16, 17.

(Anderson *et al.*, 2014b) L. Anderson, É. Aubourg, S. Bailey, *et al.* (BOSS Collaboration), *The clustering of galaxies in the SDSS-III Baryon Oscillation Spectroscopic Survey: Baryon Acoustic Oscillations in the Data Release 10 and 11 galaxy samples*, Mon.Not.Roy.Astron.Soc. **441**, 24 (2014b), arXiv:1312.4877 [astro-ph.CO] p. 3, 16, 17, 65, 72, 142, 158, 159.

(Anderson *et al.*, 2016) L. Anderson, É. Aubourg, S. Bailey, *et al.* (BOSS Collaboration), *DR12 galaxy clustering consensus paper*, in prep. (2016) p. 19, 20, 64, 75, 77, 116, 120, 127, 133, 139, 140, 141.

(Angulo *et al.*, 2008) R. Angulo, C. M. Baugh, C. S. Frenk, & C. G. Lacey, *The detectability of baryonic acoustic oscillations in future galaxy surveys*, Mon. Not. Roy. Astron. Soc. **383**, 755 (2008), arXiv:astro-ph/0702543 [astro-ph] p. 41, 50, 71.

(AS2 Proposal Team, 2007) AS2 Proposal Team (directed by Eisenstein, D.), "AS2: Surveys with the APO 2.5m Telescope After SDSS-II," `http://cosmology.lbl.gov/BOSS/as2_proposal.pdf` (2007), [Online; accessed 01-November-2015] p. 14.

(Aubourg *et al.*, 2015) É. Aubourg *et al.* (BOSS Collaboration), *Cosmological implications of baryon acoustic oscillation measurements*, Phys. Rev. **D92**, 123516 (2015), arXiv:1411.1074 [astro-ph.CO] p. 20.

(Bailey, 1933) W. N. Bailey, *On the product of two Legendre polynomials*, Mathematical Proceedings of the Cambridge Philosophical Society **29**, 173 (1933) p. 89.

(Baldauf *et al.*, 2013) T. Baldauf, U. Seljak, R. E. Smith, N. Hamaus, & V. Desjacques, *Halo stochasticity from exclusion and nonlinear clustering*, Phys. Rev. **D88**, 083507 (2013), arXiv:1305.2917 [astro-ph.CO] p. 69.

(Bardeen, 1980) J. M. Bardeen, *Gauge Invariant Cosmological Perturbations*, Phys.Rev. **D22**, 1882 (1980) p. 33, 42.

(Bardeen *et al.*, 1986) J. M. Bardeen, J. R. Bond, N. Kaiser, & A. S. Szalay, *The Statistics of Peaks of Gaussian Random Fields*, Astrophys. J. **304**, 15 (1986) p. 33.

(Baugh *et al.*, 1995) C. M. Baugh, E. Gaztanaga, & G. Efstathiou, *A comparison of the evolution of the density field in perturbation theory and numerical simulations - II Counts in cells analysis*, Mon. Not. Roy. Astron. Soc. **274**, 1049 (1995), arXiv:astro-ph/9408057 [astro-ph] p. 93.

(Bennett *et al.*, 2013) C. Bennett *et al.* (WMAP Collaboration), *Nine-Year Wilkinson Microwave Anisotropy Probe (WMAP) Observations: Final Maps and Results*, Astrophys.J.Suppl. **208**, 20 (2013), arXiv:1212.5225 [astro-ph.CO] p. 3, 167.

(Berlind & Weinberg, 2002) A. A. Berlind & D. H. Weinberg, *The Halo occupation distribution: Towards an empirical determination of the relation between galaxies and mass*, Astrophys.J. **575**, 587 (2002), arXiv:astro-ph/0109001 [astro-ph] p. 92.

(Bernardeau *et al.*, 2002) F. Bernardeau, S. Colombi, E. Gaztanaga, & R. Scoccimarro, *Large scale structure of the universe and cosmological perturbation theory*, Phys. Rept. **367**, 1 (2002), arXiv:astro-ph/0112551 [astro-ph] p. 42, 43.

(Bernardeau *et al.*, 2008) F. Bernardeau, M. Crocce, & R. Scoccimarro, *Multi-Point Propagators in Cosmological Gravitational Instability*, Phys. Rev. **D78**, 103521 (2008), arXiv:0806.2334 [astro-ph] p. 46.

(Bernstein, 1994) G. M. Bernstein, *The Variance of correlation function estimates*, Astrophys. J. **424**, 569 (1994) p. 88.

(Bertschinger, 1998) E. Bertschinger, *Simulations of Structure Formation in the Universe*, Ann. Rev. Astron. Astrophys. **36**, 599 (1998) p. 39.

(Betoule *et al.*, 2014) M. Betoule *et al.* (SDSS Collaboration), *Improved cosmological constraints from a joint analysis of the SDSS-II and SNLS supernova samples*, Astron.Astrophys. **568**, A22 (2014), arXiv:1401.4064 [astro-ph.CO] p. 4, 142, 145, 167, 172, 173, 174, 175, 176.

(Beutler *et al.*, 2011) F. Beutler, C. Blake, M. Colless, D. H. Jones, L. Staveley-Smith, *et al.*, *The 6dF Galaxy Survey: Baryon Acoustic Oscillations and the Local Hubble Constant*, Mon.Not.Roy.Astron.Soc. **416**, 3017 (2011), arXiv:1106.3366 [astro-ph.CO] p. 3, 11.

(Beutler *et al.*, 2012) F. Beutler, C. Blake, M. Colless, *et al.*, *The 6dF Galaxy Survey: $z \approx 0$ measurement of the growth rate and σ_8*, Mon. Not. Roy. Astron. Soc. **423**, 3430 (2012), arXiv:1204.4725 [astro-ph.CO] p. 11, 18.

(Beutler *et al.*, 2014a) F. Beutler *et al.* (BOSS Collaboration), *The clustering of galaxies in the SDSS-III Baryon Oscillation Spectroscopic Survey: Testing gravity with redshift-space distortions using the power spectrum multipoles*, Mon.Not.Roy.Astron.Soc. **443**, 1065 (2014a), arXiv:1312.4611 [astro-ph.CO] p. 16, 18, 19, 51, 61, 62, 67, 68, 69, 70, 72.

(Beutler *et al.*, 2014b) F. Beutler *et al.* (BOSS Collaboration), *The clustering of galaxies in the SDSS-III Baryon Oscillation Spectroscopic Survey: Signs of neutrino mass in current cosmological datasets*, Mon.Not.Roy.Astron.Soc. **444**, 3501 (2014b), arXiv:1403.4599 [astro-ph.CO] p. 159.

(Beutler *et al.*, 2015) F. Beutler, C. Blake, J. Koda, F. Marin, H.-J. Seo, A. J. Cuesta, & D. P. Schneider, *The BOSS-WiggleZ overlap region I: Baryon Acoustic Oscillations*, ArXiv e-prints (2015), 10.1093/mnras/stv1943, arXiv:1506.03900 [astro-ph.CO] p. 17.

(Beutler *et al.*, 2016a) F. Beutler *et al.* (BOSS Collaboration), *DR12 galaxy clustering power spectrum multipole BAO measurements*, in prep. (2016a) p. 20, 141.

(Beutler *et al.*, 2016b) F. Beutler *et al.* (BOSS Collaboration), *DR12 galaxy clustering power spectrum multipole RSD measurements*, in prep. (2016b) p. 20, 127, 139, 140, 141.

(Bianchi *et al.*, 2015) D. Bianchi, H. Gil-Marín, R. Ruggeri, & W. J. Percival, *Measuring line-of-sight dependent Fourier-space clustering using FFTs*, Mon. Not. Roy. Astron. Soc. **453**, L11 (2015), arXiv:1505.05341 [astro-ph.CO] p. 63, 76, 77.

(Bianchi *et al.*, 2016) D. Bianchi, W. Percival, & J. Bel, *Improving the modelling of redshift-space distortions - II. A pairwise velocity model covering large and small scales*, ArXiv e-prints (2016), arXiv:1602.02780 [astro-ph.CO] p. 160.

(Blake & Glazebrook, 2003) C. Blake & K. Glazebrook, *Probing dark energy using baryonic oscillations in the galaxy power spectrum as a cosmological ruler*, Astrophys. J. **594**, 665 (2003), arXiv:astro-ph/0301632 [astro-ph] p. 13, 52.

(Blake *et al.*, 2011a) C. Blake, S. Brough, M. Colless, C. Contreras, W. Couch, *et al.*, *The WiggleZ Dark Energy Survey: the growth rate of cosmic structure since redshift z=0.9*, Mon.Not.Roy.Astron.Soc. **415**, 2876 (2011a), arXiv:1104.2948 [astro-ph.CO] p. 61.

(Blake *et al.*, 2011b) C. Blake, E. Kazin, F. Beutler, T. Davis, D. Parkinson, *et al.*, *The WiggleZ Dark Energy Survey: mapping the distance-redshift relation with baryon acoustic oscillations*, Mon.Not.Roy.Astron.Soc. **418**, 1707 (2011b), arXiv:1108.2635 [astro-ph.CO] p. 10.

(Blake *et al.*, 2012) C. Blake *et al.*, *The WiggleZ Dark Energy Survey: Joint measurements of the expansion and growth history at $z < 1$*, Mon. Not. Roy. Astron. Soc. **425**, 405 (2012), arXiv:1204.3674 [astro-ph.CO] p. 18.

(Blanton, 2008) M. Blanton, "SDSS Redshift Diagrams," `http://sdss.physics.nyu.edu/pie/` (2008), [Online; accessed 30-October-2015] p. 8.

(Blas *et al.*, 2016) D. Blas, M. Crocce, & R. Scoccimarro, *gRPT: Gallilean-invariant renormalized perturbation theory*, in prep. (2016) p. 46, 47, 112.

(Bolton *et al.*, 2012) A. S. Bolton *et al.*, *Spectral Classification and Redshift Measurement for the SDSS-III Baryon Oscillation Spectroscopic Survey*, Astron. J. **144**, 144 (2012), arXiv:1207.7326 [astro-ph.CO] p. 14.

(Bouchet *et al.*, 1995) F. R. Bouchet, S. Colombi, E. Hivon, & R. Juszkiewicz, *Perturbative Lagrangian approach to gravitational instability*, Astron. Astrophys. **296**, 575 (1995), arXiv:astro-ph/9406013 [astro-ph] p. 37.

(Burden *et al.*, 2015) A. Burden, W. J. Percival, & C. Howlett, *Reconstruction in Fourier space*, Mon. Not. Roy. Astron. Soc. **453**, 456 (2015), arXiv:1504.02591 [astro-ph.CO] p. 10.

(Carlson *et al.*, 2009) J. Carlson, M. White, & N. Padmanabhan, *A critical look at cosmological perturbation theory techniques*, Phys. Rev. **D80**, 043531 (2009), arXiv:0905.0479 [astro-ph.CO] p. 44.

(Carroll, 2004) S. Carroll, *Spacetime and Geometry: An Introduction to General Relativity* (Addison Wesley, 2004) p. 23, 25.

(Carron, 2013) J. Carron, *On the assumption of Gaussianity for cosmological two-point statistics and parameter dependent covariance matrices*, Astron. Astrophys. **551**, A88 (2013), arXiv:1204.4724 [astro-ph.CO] p. 85.

(Carron *et al.*, 2015) J. Carron, M. Wolk, & I. Szapudi, *On the information content of the matter power spectrum*, Mon.Not.Roy.Astron.Soc. **453**, 450 (2015), arXiv:1412.5511 [astro-ph.CO] p. 107.

(Casas-Miranda *et al.*, 2002) R. Casas-Miranda, H. J. Mo, R. K. Sheth, & G. Boerner, *On the distribution of haloes, galaxies and mass*, Mon. Not. Roy. Astron. Soc. **333**, 730 (2002), arXiv:astro-ph/0105008 [astro-ph] p. 69.

(Catelan *et al.*, 2000) P. Catelan, C. Porciani, & M. Kamionkowski, *Two ways of biasing galaxy formation*, Mon. Not. Roy. Astron. Soc. **318**, 39 (2000), arXiv:astro-ph/0005544 [astro-ph] p. 48.

(Chan *et al.*, 2012) K. C. Chan, R. Scoccimarro, & R. K. Sheth, *Gravity and Large-Scale Non-local Bias*, Phys. Rev. **D85**, 083509 (2012), arXiv:1201.3614 [astro-ph.CO] p. 48, 49.

(Chevallier & Polarski, 2001) M. Chevallier & D. Polarski, *Accelerating universes with scaling dark matter*, Int.J.Mod.Phys. **D10**, 213 (2001), arXiv:gr-qc/0009008 [gr-qc] p. 28, 146.

(Chuang & Wang, 2012) C.-H. Chuang & Y. Wang, *Measurements of $H(z)$ and $D_A(z)$ from the Two-Dimensional Two-Point Correlation Function of Sloan Digital Sky Survey Luminous Red Galaxies*, Mon. Not. Roy. Astron. Soc. **426**, 226 (2012), arXiv:1102.2251 [astro-ph.CO] p. 15.

(Chuang & Wang, 2013) C.-H. Chuang & Y. Wang, *Modeling the Anisotropic Two-Point Galaxy Correlation Function on Small Scales and Improved Measurements of $H(z)$, $D_A(z)$, and $\beta(z)$ from the Sloan Digital Sky Survey DR7 Luminous Red Galaxies*, Mon. Not. Roy. Astron. Soc. **435**, 255 (2013), arXiv:1209.0210 [astro-ph.CO] p. 18.

(Chuang *et al.*, 2013a) C.-H. Chuang, F. Prada, A. J. Cuesta, D. J. Eisenstein, E. Kazin, *et al.*, *The clustering of galaxies in the SDSS-III Baryon Oscillation Spectroscopic Survey: single-probe measurements and the strong power of normalized growth rate on constraining dark energy*, Mon.Not.Roy.Astron.Soc. **433**, 3559 (2013a), arXiv:1303.4486 [astro-ph.CO] p. 16, 18.

(Chuang *et al.*, 2013b) C.-H. Chuang *et al.*, *The clustering of galaxies in the SDSS-III Baryon Oscillation Spectroscopic Survey: single-probe measurements from CMASS and LOWZ anisotropic galaxy clustering*, ArXiv e-prints (2013b), arXiv:1312.4889 [astro-ph.CO] p. 17, 18, 19.

(Chuang *et al.*, 2015) C.-H. Chuang, C. Zhao, F. Prada, E. Munari, S. Avila, *et al.*, *nIFTy Cosmology: Galaxy/halo mock catalogue comparison project on clustering statistics*, Mon. Not. Roy. Astron. Soc. **452**, 686 (2015), arXiv:1412.7729 [astro-ph.CO] p. 75.

(Cohn, 2006) J. D. Cohn, *Power spectrum and correlation function errors: Poisson vs. Gaussian shot noise*, New Astron. **11**, 226 (2006), arXiv:astro-ph/0503285 [astro-ph] p. 91.

(Cole, 1998) K. Cole, *The Universe and the Teacup: The Mathematics of Truth and Beauty* (Houghton Mifflin Harcourt, 1998) p. 83.

(Cole *et al.*, 2005) S. Cole *et al.* (2dFGRS Collaboration), *The 2dF Galaxy Redshift Survey: Power-spectrum analysis of the final dataset and cosmological implications*, Mon.Not.Roy.Astron.Soc. **362**, 505 (2005), arXiv:astro-ph/0501174 [astro-ph] p. 9.

(Colless *et al.*, 2001) M. Colless *et al.* (2dFGRS Collaboration), *The 2dF Galaxy Redshift Survey: Spectra and redshifts*, Mon.Not.Roy.Astron.Soc. **328**, 1039 (2001), arXiv:astro-ph/0106498 [astro-ph] p. 8.

(Colless *et al.*, 2003) M. Colless *et al.* (2dFGRS Collaboration), *The 2dF Galaxy Redshift Survey: Final data release*, ArXiv e-prints (2003), arXiv:astro-ph/0306581 [astro-ph] p. 9.

(Conley *et al.*, 2011) A. Conley, J. Guy, M. Sullivan, N. Regnault, P. Astier, *et al.*, *Supernova Constraints and Systematic Uncertainties from the First 3 Years of the Supernova Legacy Survey*, Astrophys.J.Suppl. **192**, 1 (2011), arXiv:1104.1443 [astro-ph.CO] p. 4, 167.

(Contreras *et al.*, 2013) C. Contreras *et al.* (WiggleZ), *The WiggleZ Dark Energy Survey: measuring the cosmic growth rate with the two-point galaxy correlation function*, Mon. Not. Roy. Astron. Soc. (2013), 10.1093/mnras/sts608, arXiv:1302.5178 [astro-ph.CO] p. 14.

(Cooray & Sheth, 2002) A. Cooray & R. K. Sheth, *Halo models of large scale structure*, Phys. Rept. **372**, 1 (2002), arXiv:astro-ph/0206508 [astro-ph] p. 41.

(Crocce & Scoccimarro, 2006a) M. Crocce & R. Scoccimarro, *Renormalized cosmological perturbation theory*, Phys. Rev. **D73**, 063519 (2006a), arXiv:astro-ph/0509418 [astro-ph] p. 13, 44, 45.

(Crocce & Scoccimarro, 2006b) M. Crocce & R. Scoccimarro, *Memory of initial conditions in gravitational clustering*, Phys. Rev. **D73**, 063520 (2006b), arXiv:astro-ph/0509419 [astro-ph] p. 44.

(Crocce & Scoccimarro, 2008) M. Crocce & R. Scoccimarro, *Nonlinear Evolution of Baryon Acoustic Oscillations*, Phys. Rev. **D77**, 023533 (2008), arXiv:0704.2783 [astro-ph] p. 10, 13, 46.

(Crocce *et al.*, 2006) M. Crocce, S. Pueblas, & R. Scoccimarro, *Transients from Initial Conditions in Cosmological Simulations*, Mon. Not. Roy. Astron. Soc. **373**, 369 (2006), arXiv:astro-ph/0606505 [astro-ph] p. 93.

(Crocce *et al.*, 2011) M. Crocce, A. Cabre, & E. Gaztanaga, *Modeling the angular correlation function and its full covariance in Photometric Galaxy Surveys*, Mon.Not.Roy.Astron.Soc. **414**, 329 (2011), arXiv:1004.4640 [astro-ph.CO] p. 87.

(Crocce *et al.*, 2012) M. Crocce, R. Scoccimarro, & F. Bernardeau, *MPTbreeze: A fast renormalized perturbative scheme*, Mon.Not.Roy.Astron.Soc. **427**, 2537 (2012), arXiv:1207.1465 [astro-ph.CO] p. 46, 47.

(Cuesta *et al.*, 2015) A. J. Cuesta *et al.*, *The clustering of galaxies in the SDSS-III Baryon Oscillation Spectroscopic Survey: Baryon Acoustic Oscillations in the correlation function of LOWZ and CMASS galaxies in Data Release 12*, ArXiv e-prints (2015), arXiv:1509.06371 [astro-ph.CO] p. 17, 19, 80.

(Curtis, 1921) H. D. Curtis, *The Scale of the Universe, part I*, Bull. Nat. Res. Coun. **2**, 171 (1921) p. 1.

(Das *et al.*, 2014) S. Das, T. Louis, M. R. Nolta, G. E. Addison, E. S. Battistelli, *et al.*, *The Atacama Cosmology Telescope: temperature and gravitational lensing power spectrum measurements from three seasons of data*, J. Cosmolo. Astropart. Phys. **1404**, 014 (2014), arXiv:1301.1037 [astro-ph.CO] p. 167.

(Davis & Peebles, 1983) M. Davis & P. J. E. Peebles, *A survey of galaxy redshifts. V - The two-point position and velocity correlations*, Astrophys.J. **267**, 465 (1983) p. 6.

(Davis *et al.*, 1977) M. Davis, E. J. Groth, & P. J. E. Peebles, *Study of galaxy correlations - Evidence for the gravitational instability picture in a dense universe*, Astrophys. J. Lett. **212**, L107 (1977) p. 5.

(Dawson *et al.*, 2013) K. S. Dawson *et al.* (BOSS Collaboration), *The Baryon Oscillation Spectroscopic Survey of SDSS-III*, Astron. J. **145**, 10 (2013), arXiv:1208.0022 [astro-ph.CO] p. 1, 14, 15.

(Dawson *et al.*, 2016) K. S. Dawson *et al.*, *The SDSS-IV extended Baryon Oscillation Spectroscopic Survey: Overview and Early Data*, Astron. J. **151**, 44 (2016), arXiv:1508.04473 [astro-ph.CO] p. 20.

(de Jong *et al.*, 2014) R. S. de Jong, S. Barden, O. Bellido-Tirado, *et al.*, *4MOST: 4-metre Multi-Object Spectroscopic Telescope*, in *Ground-based and Airborne Instrumentation for Astronomy V*, Proc. SPIE Conf. Ser., Vol. 9147, edited by S. K. Ramsay, I. S. McLean, & H. Takami (SPIE, Bellingham, 2014) p. 91470M p. 12, 151, 159.

(Delubac *et al.*, 2015) T. Delubac *et al.* (BOSS Collaboration), *Baryon acoustic oscillations in the Lyα forest of BOSS DR11 quasars*, Astron. Astrophys. **574**, A59 (2015), arXiv:1404.1801 [astro-ph.CO] p. 20.

(Deng *et al.*, 2007) X.-F. Deng, J.-Z. He, C.-G. He, C.-H. Luo, P. Wu, & X.-X. Tang, *The Sloan Great Wall from the SDSS Data Release 4*, Acta Physica Polonica B **38**, 219 (2007) p. 6.

(DESI Collaboration, 2015) DESI Collaboration, "DESI Two-Page Brochure," https://desi.lbl.gov/trac/attachment/wiki/PublicPages/DESI-brochure.pdf (2015), [Online; accessed 15-February-2016] p. 11.

(Dodelson, 2003) S. Dodelson, *Modern Cosmology* (Academic Press, 2003) p. 2, 23, 33, 35.

(Dodelson & Schneider, 2013) S. Dodelson & M. D. Schneider, *The Effect of Covariance Estimator Error on Cosmological Parameter Constraints*, Phys.Rev. **D88**, 063537 (2013), arXiv:1304.2593 [astro-ph.CO] p. 83, 86.

(Dodelson *et al.*, 2001) S. Dodelson *et al.* (SDSS Collaboration), *The three-dimensional power spectrum from angular clustering of galaxies in early SDSS data*, Astrophys. J. **572**, 140 (2001), arXiv:astro-ph/0107421 [astro-ph] p. 8.

(Doi *et al.*, 2010) M. Doi *et al.*, *Photometric Response Functions of the SDSS Imager*, Astron. J. **139**, 1628 (2010), arXiv:1002.3701 [astro-ph.IM] p. 14.

(Drinkwater *et al.*, 2010) M. J. Drinkwater *et al.*, *The WiggleZ Dark Energy Survey: Survey Design and First Data Release*, Mon. Not. Roy. Astron. Soc. **401**, 1429 (2010), arXiv:0911.4246 [astro-ph.CO] p. 10.

(Dunkley *et al.*, 2005) J. Dunkley, M. Bucher, P. G. Ferreira, K. Moodley, & C. Skordis, *Fast and reliable MCMC for cosmological parameter estimation*, Mon. Not. Roy. Astron. Soc. **356**, 925 (2005), astro-ph/0405462 p. 161.

(Efstathiou & Bond, 1999) G. Efstathiou & J. R. Bond, *Cosmic confusion: Degeneracies among cosmological parameters derived from measurements of microwave background anisotropies*, Mon. Not. Roy. Astron. Soc. **304**, 75 (1999), arXiv:astro-ph/9807103 [astro-ph] p. 149.

(Efstathiou *et al.*, 1990) G. Efstathiou, N. Kaiser, W. Saunders, A. Lawrence, M. Rowan-Robinson, R. S. Ellis, & C. S. Frenk, *Largescale Clustering of IRAS Galaxies*, Mon.Not.Roy.Astron.Soc. **247**, 10P (1990) p. 7.

(Efstathiou *et al.*, 2002) G. Efstathiou *et al.* (2dFGRS Collaboration), *Evidence for a non-zero lambda and a low matter density from a combined analysis of the 2dF Galaxy Redshift Survey and cosmic microwave background anisotropies*, Mon. Not. Roy. Astron. Soc. **330**, L29 (2002), arXiv:astro-ph/0109152 [astro-ph] p. 8.

(Einstein, 1915) A. Einstein, *Die Feldgleichungen der Gravitation. (German) [The Field Equations of Gravitation]*, Sitzungsberichte der Königlich-Preußischen Akademie der Wissenschaften , 844 (1915) p. 4, 24.

(Einstein, 1916) A. Einstein, *Die Grundlagen der Allgemeinen Relativitätstheorie. (German) [The Foundations of the Theory of General Relativity]*, Annalen der Physik (1900) (series 4) **354**, 769 (1916) p. 4, 24.

(Einstein, 1917) A. Einstein, *Kosmologische Betrachtungen zur allgemeinen Relativitätstheorie. (German) [Cosmological Considerations in the General Theory of Relativity]*, Sitzungsberichte der Königlich-Preußischen Akademie der Wissenschaften , 142 (1917) p. 4.

(Einstein & de Sitter, 1932) A. Einstein & W. de Sitter, *On the Relation between the Expansion and the Mean Density of the Universe*, Proceedings of the National Academy of Sciences of the United States of America **18**, 213 (1932) p. 5.

(Eisenstein & Hu, 1998) D. J. Eisenstein & W. Hu, *Baryonic features in the matter transfer function*, Astrophys. J. **496**, 605 (1998), arXiv:astro-ph/9709112 [astro-ph] p. 34.

(Eisenstein & White, 2004) D. J. Eisenstein & M. J. White, *Theoretical uncertainty in baryon oscillations*, Phys. Rev. **D70**, 103523 (2004), arXiv:astro-ph/0407539 [astro-ph] p. 13, 53.

(Eisenstein *et al.*, 1998) D. J. Eisenstein, W. Hu, & M. Tegmark, *Cosmic complementarity: H(0) and Omega(m) from combining CMB experiments and redshift surveys*, Astrophys. J. **504**, L57 (1998), arXiv:astro-ph/9805239 [astro-ph] p. 13.

(Eisenstein *et al.*, 2001) D. J. Eisenstein *et al.* (SDSS Collaboration), *Spectroscopic target selection for the Sloan Digital Sky Survey: The Luminous red galaxy sample*, Astron. J. **122**, 2267 (2001), arXiv:astro-ph/0108153 [astro-ph] p. 8.

(Eisenstein *et al.*, 2005) D. J. Eisenstein *et al.* (SDSS Collaboration), *Detection of the baryon acoustic peak in the large-scale correlation function of SDSS luminous red galaxies*, Astrophys.J. **633**, 560 (2005), arXiv:astro-ph/0501171 [astro-ph] p. 8, 9.

(Eisenstein *et al.*, 2007a) D. J. Eisenstein, H.-J. Seo, & M. J. White, *On the Robustness of the Acoustic Scale in the Low-Redshift Clustering of Matter*, Astrophys. J. **664**, 660 (2007a), arXiv:astro-ph/0604361 [astro-ph] p. 9.

(Eisenstein *et al.*, 2007b) D. J. Eisenstein, H.-J. Seo, E. Sirko, & D. Spergel, *Improving Cosmological Distance Measurements by Reconstruction of the Baryon Acoustic Peak*, Astrophys. J. **664**, 675 (2007b), arXiv:astro-ph/0604362 [astro-ph] p. 10.

(Eisenstein *et al.*, 2011) D. J. Eisenstein *et al.* (SDSS Collaboration), *SDSS-III: Massive Spectroscopic Surveys of the Distant Universe, the Milky Way Galaxy, and Extra-Solar Planetary Systems*, Astron. J. **142**, 72 (2011), arXiv:1101.1529 [astro-ph.IM] p. 1, 14, 18.

(Ellis *et al.*, 2014) R. Ellis *et al.* (PFS Team), *Extragalactic science, cosmology, and Galactic archaeology with the Subaru Prime Focus Spectrograph*, Publ.Astron.Soc.Jap. **66**, R1 (2014), arXiv:1206.0737 [astro-ph.CO] p. 12, 151, 159.

(Feldman *et al.*, 1994) H. A. Feldman, N. Kaiser, & J. A. Peacock, *Power spectrum analysis of three-dimensional redshift surveys*, Astrophys.J. **426**, 23 (1994), arXiv:astro-ph/9304022 [astro-ph] p. 58, 59, 69, 87, 88.

(Font-Ribera *et al.*, 2014) A. Font-Ribera *et al.* (BOSS Collaboration), *Quasar-Lyman α Forest Cross-Correlation from BOSS DR11 : Baryon Acoustic Oscillations*, J. Cosmolo. Astropart. Phys. **1405**, 027 (2014), arXiv:1311.1767 [astro-ph.CO] p. 20.

(Friedmann, 1922) A. Friedmann, *Über die Krümmung des Raumes (German) [On the Curvature of Space]*, Zeitschrift für Physik **10**, 377 (1922) p. 4.

(Friedmann, 1924) A. Friedmann, *Über die Möglichkeit einer Welt mit konstanter negativer Krümmung des Raumes (German) [On the Possibility of a World with constant negative Curvature of Space]*, Zeitschrift für Physik **21**, 326 (1924) p. 4.

(Fukugita *et al.*, 1996) M. Fukugita, T. Ichikawa, J. E. Gunn, M. Doi, K. Shimasaku, & D. P. Schneider, *The Sloan digital sky survey photometric system*, Astron. J. **111**, 1748 (1996) p. 14.

(Gaztanaga *et al.*, 2009) E. Gaztanaga, A. Cabre, & L. Hui, *Clustering of Luminous Red Galaxies IV: Baryon Acoustic Peak in the Line-of-Sight Direction and a Direct Measurement of $H(z)$*, Mon. Not. Roy. Astron. Soc. **399**, 1663 (2009), arXiv:0807.3551 [astro-ph] p. 15.

(Geller & Huchra, 1989) M. J. Geller & J. P. Huchra, *Mapping the universe*, Science **246**, 897 (1989) p. 6.

(Gelman & Rubin, 1992) A. Gelman & D. B. Rubin, *Inference from Iterative Simulation Using Multiple Sequences*, Statist. Sci. **7**, 457 (1992) p. 115, 166.

(Gelman *et al.*, 2013) A. Gelman, J. Carlin, H. Stern, D. Dunson, A. Vehtari, & D. Rubin, *Bayesian Data Analysis, Third Edition*, Chapman & Hall/CRC Texts in Statistical Science (Taylor & Francis, 2013) p. 161.

(George *et al.*, 2015) E. M. George *et al.*, *A measurement of secondary cosmic microwave background anisotropies from the 2500-square-degree SPT-SZ survey*, Astrophys. J. **799**, 177 (2015), arXiv:1408.3161 [astro-ph.CO] p. 3.

(Gil-Marin *et al.*, 2012) H. Gil-Marin, C. Wagner, L. Verde, C. Porciani, & R. Jimenez, *Perturbation theory approach for the power spectrum: from dark matter in real space to haloes in redshift space*, JCAP **1211**, 029 (2012), arXiv:1209.3771 [astro-ph.CO] p. 51.

(Gil-Marín *et al.*, 2015a) H. Gil-Marín, J. Noreña, L. Verde, W. J. Percival, C. Wagner, M. Manera, & D. P. Schneider, *The power spectrum and bispectrum of SDSS DR11 BOSS galaxies I: bias and gravity*, Mon. Not. Roy. Astron. Soc. **451**, 5058 (2015a), arXiv:1407.5668 [astro-ph.CO] p. 17, 19, 51, 68.

(Gil-Marín *et al.*, 2015b) H. Gil-Marín, L. Verde, J. Noreña, *et al.*, *The power spectrum and bispectrum of SDSS DR11 BOSS galaxies – II. Cosmological interpretation*, Mon. Not. Roy. Astron. Soc. **452**, 1914 (2015b), arXiv:1408.0027 [astro-ph.CO] p. 18.

(Gil-Marín *et al.*, 2015c) H. Gil-Marín *et al.*, *The clustering of galaxies in the SDSS-III Baryon Oscillation Spectroscopic Survey: BAO measurement from the LOS-dependent power spectrum of DR12 BOSS galaxies*, ArXiv e-prints (2015c), arXiv:1509.06373 [astro-ph.CO] p. 17, 80.

(Gil-Marín *et al.*, 2015d) H. Gil-Marín *et al.*, *The clustering of galaxies in the SDSS-III Baryon Oscillation Spectroscopic Survey: RSD measurement from the LOS-dependent power spectrum of DR12 BOSS galaxies*, ArXiv e-prints (2015d), arXiv:1509.06386 [astro-ph.CO] p. 18, 19, 51, 61, 72, 80, 139.

(Gong, 2008) Y. Gong, *The growth factor parameterization and modified gravity*, Phys. Rev. **D78**, 123010 (2008), arXiv:0808.1316 [astro-ph] p. 39, 148.

(Gott *et al.*, 2005) J. R. Gott, III, M. Juric, D. Schlegel, F. Hoyle, M. Vogeley, M. Tegmark, N. A. Bahcall, & J. Brinkmann, *A map of the universe*, Astrophys. J. **624**, 463 (2005), arXiv:astro-ph/0310571 [astro-ph] p. 6.

(Grieb *et al.*, 2016a) J. N. Grieb, A. G. Sánchez, S. Salazar-Albornoz, & C. Dalla Vecchia, *Gaussian covariance matrices for anisotropic galaxy clustering measurements*, Mon. Not. Roy. Astron. Soc. **457**, 1577 (2016a), arXiv:1509.04293 [astro-ph.CO] p. 63, 87, 96, 106.

(Grieb *et al.*, 2016b) J. N. Grieb, A. G. Sánchez, S. Salazar-Albornoz, R. Scoccimarro, M. Crocce, C. Dalla Vecchia, F. Montesano, *et al.* (BOSS Collaboration), *The clustering of galaxies in the SDSS-III Baryon Oscillation Spectroscopic Survey: Cosmological implication of the Fourier space clustering wedges using the final data release*, in prep. (2016b) p. 20, 112, 127.

(Gunn *et al.*, 1998) J. E. Gunn *et al.* (SDSS Collaboration), *The Sloan digital sky survey photometric camera*, Astron. J. **116**, 3040 (1998), arXiv:astro-ph/9809085 [astro-ph] p. 14.

(Gunn *et al.*, 2006) J. E. Gunn *et al.* (SDSS Collaboration), *The 2.5 m Telescope of the Sloan Digital Sky Survey*, Astron. J. **131**, 2332 (2006), arXiv:astro-ph/0602326 [astro-ph] p. 14.

(Guo *et al.*, 2012) H. Guo, I. Zehavi, & Z. Zheng, *A New Method to Correct for Fiber Collisions in Galaxy Two-Point Statistics*, Astrophys. J. **756**, 127 (2012), arXiv:1111.6598 [astro-ph.CO] p. 160.

(Guzzo *et al.*, 2008) L. Guzzo *et al.*, *A test of the nature of cosmic acceleration using galaxy redshift distortions*, Nature **451**, 541 (2008), arXiv:0802.1944 [astro-ph] p. 12.

(Hamaus *et al.*, 2010) N. Hamaus, U. Seljak, V. Desjacques, R. E. Smith, & T. Baldauf, *Minimizing the Stochasticity of Halos in Large-Scale Structure Surveys*, Phys. Rev. **D82**, 043515 (2010), arXiv:1004.5377 [astro-ph.CO] p. 69.

(Hamilton, 1997) A. Hamilton, *Towards optimal measurement of power spectra. 2. A basis of positive, compact, statistically orthogonal kernels*, Mon.Not.Roy.Astron.Soc. **289**, 295 (1997), arXiv:astro-ph/9701009 [astro-ph] p. 57.

(Hamilton *et al.*, 2000) A. J. S. Hamilton, M. Tegmark, & N. Padmanabhan, *Linear redshift distortions and power in the pscz survey*, Mon. Not. Roy. Astron. Soc. **317**, L23 (2000), arXiv:astro-ph/0004334 [astro-ph] p. 12.

(Hamilton *et al.*, 2006) A. J. Hamilton, C. D. Rimes, & R. Scoccimarro, *On measuring the covariance matrix of the nonlinear power spectrum from simulations*, Mon.Not.Roy.Astron.Soc. **371**, 1188 (2006), arXiv:astro-ph/0511416 [astro-ph] p. 84.

(Hartlap *et al.*, 2007) J. Hartlap, P. Simon, & P. Schneider, *Why your model parameter confidences might be too optimistic: Unbiased estimation of the inverse covariance matrix*, Astron.Astrophys. **464**, 399 (2007), arXiv:astro-ph/0608064 [astro-ph] p. 86, 104, 109.

(Hastings, 1970) W. Hastings, *Monte Carlo samping methods using Markov chains and their applications*, Biometrika **57**, 97 (1970) p. 163.

(Hawkins *et al.*, 2003) E. Hawkins *et al.*, *The 2dF Galaxy Redshift Survey: Correlation functions, peculiar velocities and the matter density of the universe*, Mon. Not. Roy. Astron. Soc. **346**, 78 (2003), arXiv:astro-ph/0212375 [astro-ph] p. 12.

(Hill *et al.*, 2008) G. J. Hill, K. Gebhardt, E. Komatsu, *et al.*, *The Hobby-Eberly Telescope Dark Energy Experiment (HETDEX): Description and Early Pilot Survey Results*, in *Panoramic Views of Galaxy Formation and Evolution*, ASP Conf.Ser., Vol. 399, edited by T. Kodama, T. Yamada, & K. Aoki (Astron. Soc. Pac., San Francisco, 2008) pp. 115–118, arXiv:0806.0183 [astro-ph] p. 11.

(Hinshaw *et al.*, 2013) G. Hinshaw *et al.* (WMAP Collaboration), *Nine-Year Wilkinson Microwave Anisotropy Probe (WMAP) Observations: Cosmological Parameter Results*, Astrophys.J.Suppl. **208**, 19 (2013), arXiv:1212.5226 [astro-ph.CO] p. 16.

(Hockney & Eastwood, 1988) R. W. Hockney & J. W. Eastwood, *Computer simulation using particles* (Adam Hilger, Bristol and New York, 1988) p. 39.

(Hu & Haiman, 2003) W. Hu & Z. Haiman, *Redshifting rings of power*, Phys.Rev. **D68**, 063004 (2003), arXiv:astro-ph/0306053 [astro-ph] p. 52.

(Hubble, 1925) E. P. Hubble, *Cepheids in spiral nebulae*, The Observatory **48**, 139 (1925) p. 4.

(Hubble, 1929) E. Hubble, *A Relation between Distance and Radial Velocity among Extra-Galactic Nebulae*, Proceedings of the National Academy of Science **15**, 168 (1929) p. 5.

(Huchra *et al.*, 1983) J. Huchra, M. Davis, D. Latham, & J. Tonry, *A survey of galaxy redshifts. IV - The data*, Astrophys. J. Suppl. **52**, 89 (1983) p. 6, 7.

(Jackson, 1972) J. C. Jackson, *Fingers of God: A critique of Rees' theory of primoridal gravitational radiation*, Mon. Not. Roy. Astron. Soc. **156**, 1P (1972), arXiv:0810.3908 [astro-ph] p. 38.

(Jelley *et al.*, 2009) N. Jelley, A. B. McDonald, & R. H. Robertson, *The Sudbury Neutrino Observatory*, Annual Review of Nuclear and Particle Science **59**, 431 (2009), http://dx.doi.org/10.1146/annurev.nucl.55.090704.151550 p. 150.

(Jenkins *et al.*, 2001) A. Jenkins, C. S. Frenk, S. D. M. White, J. M. Colberg, S. Cole, A. E. Evrard, H. M. P. Couchman, & N. Yoshida, *The Mass function of dark matter halos*, Mon. Not. Roy. Astron. Soc. **321**, 372 (2001), arXiv:astro-ph/0005260 [astro-ph] p. 41.

(Jeong & Komatsu, 2006) D. Jeong & E. Komatsu, *Perturbation theory reloaded: analytical calculation of non-linearity in baryonic oscillations in the real space matter power spectrum*, Astrophys. J. **651**, 619 (2006), arXiv:astro-ph/0604075 [astro-ph] p. 44.

(Jeong & Komatsu, 2009) D. Jeong & E. Komatsu, *Perturbation Theory Reloaded II: Non-linear Bias, Baryon Acoustic Oscillations and Millennium Simulation In Real Space*, Astrophys. J. **691**, 569 (2009), arXiv:0805.2632 [astro-ph] p. 44, 71.

(Jing, 2005) Y. P. Jing, *Correcting for the alias effect when measuring the power spectrum using FFT*, Astrophys. J. **620**, 559 (2005), arXiv:astro-ph/0409240 [astro-ph] p. 71.

(Jones *et al.*, 2004) D. H. Jones *et al.*, *The 6dF Galaxy Survey: Samples, observational techniques and the first data release*, Mon. Not. Roy. Astron. Soc. **355**, 747 (2004), arXiv:astro-ph/0403501 [astro-ph] p. 11.

(Jouvel *et al.*, 2015) S. Jouvel *et al.* (DES, BOSS), *Photometric redshifts and clustering of emission line galaxies selected jointly by DES and eBOSS*, Submitted to: Mon. Not. Roy. Astron. Soc. (2015), arXiv:1509.07121 [astro-ph.CO] p. 20.

(Kaiser, 1987) N. Kaiser, *Clustering in real space and in redshift space*, Mon.Not.Roy.Astron.Soc. **227**, 1 (1987) p. 12, 38, 39, 95.

(Kalus *et al.*, 2016) B. Kalus, W. J. Percival, & L. Samushia, *Cosmological parameter inference from galaxy clustering: The effect of the posterior distribution of the power spectrum*, Mon. Not. Roy. Astron. Soc. **455**, 2573 (2016), arXiv:1504.03979 [astro-ph.CO] p. 85.

(Kaufman, 1967) G. Kaufman, *Report No. 6710, Some Bayesian Moment Formulae*, Cent. Oper. Res. Econometrics, Catholic Univ. of Louvain, Heverlee, Belgium (1967) p. 86.

(Kazin *et al.*, 2012) E. A. Kazin, A. G. Sánchez, & M. R. Blanton, *Improving measurements of H(z) and Da(z) by analyzing clustering anisotropies*, Mon.Not.Roy.Astron.Soc. **419**, 3223 (2012), arXiv:1105.2037 [astro-ph.CO] p. 15, 57, 63, 71.

(Kazin *et al.*, 2013) E. A. Kazin, A. G. Sánchez, A. J. Cuesta, F. Beutler, C.-H. Chuang, *et al.*, *The Clustering of Galaxies in the SDSS-III Baryon Oscillation Spectroscopic Survey: Measuring $H(z)$ and $D_A(z)$ at $z = 0.57$ with Clustering Wedges*, Mon.Not.Roy.Astron.Soc. **435**, 64 (2013), arXiv:1303.4391 [astro-ph.CO] p. 15, 17, 71.

(Kazin *et al.*, 2014) E. A. Kazin *et al.*, *The WiggleZ Dark Energy Survey: improved distance measurements to z = 1 with reconstruction of the baryonic acoustic feature*, Mon. Not. Roy. Astron. Soc. **441**, 3524 (2014), arXiv:1401.0358 [astro-ph.CO] p. 3, 10, 17.

(Kitaura & Hess, 2013) F.-S. Kitaura & S. Hess, *Cosmological Structure Formation with Augmented Lagrangian Perturbation Theory*, Mon.Not.Roy.Astron.Soc. **435**, 78 (2013), arXiv:1212.3514 [astro-ph.CO] p. 75.

(Kitaura *et al.*, 2014) F.-S. Kitaura, G. Yepes, & F. Prada, *Modeling Baryon Acoustic Oscillations with Perturbation Theory and Stochastic Halo Biasing*, Mon.Not.Roy.Astron.Soc. **439**, 21 (2014), arXiv:1307.3285 [astro-ph.CO] p. 75.

(Kitaura *et al.*, 2015) F.-S. Kitaura, H. Gil-Marín, C. Scoccola, C.-H. Chuang, V. Müller, G. Yepes, & F. Prada, *Constraining the halo bispectrum in real and redshift space from perturbation theory and non-linear stochastic bias*, Mon. Not. Roy. Astron. Soc. **450**, 1836 (2015), arXiv:1407.1236 [astro-ph.CO] p. 75.

(Kitaura *et al.*, 2016) F.-S. Kitaura *et al.*, *The clustering of galaxies in the SDSS-III Baryon Oscillation Spectroscopic Survey: mock galaxy catalogues for the BOSS Final Data Release*, Mon. Not. Roy. Astron. Soc. **456**, 4156 (2016), arXiv:1509.06400 [astro-ph.CO] p. 75.

(Kitching *et al.*, 2016) T. D. Kitching, L. Verde, A. F. Heavens, & R. Jimenez, *Discrepancies between CFHTLenS cosmic shear & Planck: new physics or systematic effects?*, ArXiv e-prints (2016), arXiv:1602.02960 [astro-ph.CO] p. 159.

(Klypin *et al.*, 2014) A. Klypin, G. Yepes, S. Gottlober, F. Prada, & S. Hess, *MultiDark simulations: the story of dark matter halo concentrations and density profiles*, ArXiv e-prints (2014), arXiv:1411.4001 [astro-ph.CO] p. 76.

(Labatie *et al.*, 2012) A. Labatie, J. L. Starck, & M. Lachieze-Rey, *Effect of model-dependent covariance matrix for studying Baryon Acoustic Oscillations*, Astrophys. J. **760**, 97 (2012), arXiv:1210.0878 [astro-ph.CO] p. 84.

(Landy & Szalay, 1993) S. D. Landy & A. S. Szalay, *Bias and variance of angular correlation functions*, Astrophys. J. **412**, 64 (1993) p. 58, 96.

(Laureijs *et al.*, 2011) R. Laureijs *et al.* (EUCLID Collaboration), *Euclid Definition Study Report*, ArXiv e-prints (2011), arXiv:1110.3193 [astro-ph.CO] p. 12, 151.

(Lemaître, 1927) G. Lemaître, *Un Univers homogene de masse constante et de rayon croissant rendant compte de la vitesse radiale des nebuleuses extra-galactiques*, Annales de la Societe Scientifique de Bruxelles **A47**, 49 (1927), english translation in Lemaître (1931) p. 5, 191.

(Lemaître, 1931) G. Lemaître, *Expansion of the universe, A homogeneous universe of constant mass and increasing radius accounting for the radial velocity of extra-galactic nebulae*, Mon.Not.Roy.Astron.Soc. **91**, 483 (1931), english translation of Lemaître (1927) p. 5, 191.

(Lesgourgues, 2011) J. Lesgourgues, *The Cosmic Linear Anisotropy Solving System (CLASS) I: Overview*, ArXiv e-prints (2011), arXiv:1104.2932 [astro-ph.IM] p. 34.

(Lesgourgues & Pastor, 2012) J. Lesgourgues & S. Pastor, *Neutrino mass from Cosmology*, Adv. High Energy Phys. **2012**, 608515 (2012), arXiv:1212.6154 [hep-ph] p. 150.

(Levi *et al.*, 2013) M. Levi *et al.* (DESI), *The DESI Experiment, a whitepaper for Snowmass 2013*, ArXiv e-prints (2013), arXiv:1308.0847 [astro-ph.CO] p. 12, 151, 159.

(Lewis, 2013) A. Lewis, *Efficient sampling of fast and slow cosmological parameters*, Phys. Rev. **D87**, 103529 (2013), arXiv:1304.4473 [astro-ph.CO] p. 167.

(Lewis & Bridle, 2002) A. Lewis & S. Bridle, *Cosmological parameters from CMB and other data: a Monte- Carlo approach*, Phys. Rev. **D66**, 103511 (2002), astro-ph/0205436 p. 115, 132, 167.

(Lewis *et al.*, 2000) A. Lewis, A. Challinor, & A. Lasenby, *Efficient Computation of CMB anisotropies in closed FRW models*, Astrophys. J. **538**, 473 (2000), astro-ph/9911177 p. 34, 47, 93, 167.

(L'Huillier *et al.*, 2014) B. L'Huillier, C. Park, & J. Kim, *Effects of the initial conditions on cosmological N-body simulations*, New Astron. **30**, 79 (2014), arXiv:1401.6180 [astro-ph.CO] p. 93.

(Li *et al.*, 2014) Y. Li, W. Hu, & M. Takada, *Super-Sample Covariance in Simulations*, Phys.Rev. **D89**, 083519 (2014), arXiv:1401.0385 [astro-ph.CO] p. 106, 107.

(Liddle, 2003) A. Liddle, *An introduction to modern cosmology* (Wiley, 2003) p. 2.

(Liddle & Lyth, 2000) A. Liddle & D. Lyth, *Cosmological Inflation and Large-Scale Structure* (Cambridge University Press, 2000) p. 2, 32.

(Linder, 2003) E. V. Linder, *Exploring the expansion history of the universe*, Phys.Rev.Lett. **90**, 091301 (2003), arXiv:astro-ph/0208512 [astro-ph] p. 28, 146.

(Linder & Cahn, 2007) E. V. Linder & R. N. Cahn, *Parameterized Beyond-Einstein Growth*, Astropart. Phys. **28**, 481 (2007), arXiv:astro-ph/0701317 [astro-ph] p. 39, 148.

(L'vov & Procaccia, 1995) V. L'vov & I. Procaccia, *Exact Resummations in the Theory of Hydrodynamic Turbulence: 0. Line-Resummed Diagrammatic Perturbation Approach*, in *eprint arXiv:chao-dyn/9502010* (1995) p. 45.

(Lynds, 1971) R. Lynds, *The Absorption-Line Spectrum of 4c 05.34*, Astrophys. J., Letters **164**, L73 (1971) p. 20.

(Maddox *et al.*, 1990) S. J. Maddox, G. Efstathiou, W. J. Sutherland, & J. Loveday, *Galaxy correlations on large scales*, Mon.Not.Roy.Astron.Soc. **242**, 43P (1990) p. 5, 6, 7.

(Makarem *et al.*, 2014) L. Makarem, J.-P. Kneib, D. Gillet, H. Bleuler, M. Bouri, L. Jenni, F. Prada, & J. Sanchez, *Collision avoidance in next-generation fiber positioner robotic systems for large survey spectrographs*, Astron. Astrophys. **566**, A84 (2014), arXiv:1312.1644 [astro-ph.IM] p. 160.

(Manera & Gaztanaga, 2011) M. Manera & E. Gaztanaga, *The local bias model in the large scale halo distribution*, Mon. Not. Roy. Astron. Soc. **415**, 383 (2011), arXiv:0912.0446 [astro-ph.CO] p. 69.

(Manera *et al.*, 2012) M. Manera *et al.*, *The clustering of galaxies in the SDSS-III Baryon Oscillation Spectroscopic Survey: a large sample of mock galaxy catalogues*, Mon. Not. Roy. Astron. Soc. **428**, 1036 (2012), arXiv:1203.6609 [astro-ph.CO] p. 68, 75, 85, 87.

(Manera *et al.*, 2015) M. Manera, L. Samushia, R. Tojeiro, *et al.*, *The clustering of galaxies in the SDSS-III Baryon Oscillation Spectroscopic Survey: mock galaxy catalogues for the low-redshift sample*, Mon. Not. Roy. Astron. Soc. **447**, 437 (2015), arXiv:1401.4171 [astro-ph.CO] p. 75.

(Maraston *et al.*, 2013) C. Maraston, J. Pforr, B. M. Henriques, D. Thomas, D. Wake, *et al.*, *Stellar masses of SDSS-III BOSS galaxies at z 0.5 and constraints to galaxy formation models*, Mon.Not.Roy.Astron.Soc. **435**, 2764 (2013), arXiv:1207.6114 [astro-ph.CO] p. 14.

(Martinez & Saar, 2001) V. Martinez & E. Saar, *Statistics of the Galaxy Distribution* (CRC Press, 2001) p. 2.

(Matsubara, 2008a) T. Matsubara, *Resumming Cosmological Perturbations via the Lagrangian Picture: One-loop Results in Real Space and in Redshift Space*, Phys. Rev. **D77**, 063530 (2008a), arXiv:0711.2521 [astro-ph] p. 44.

(Matsubara, 2008b) T. Matsubara, *Nonlinear perturbation theory with halo bias and redshift-space distortions via the Lagrangian picture*, Phys. Rev. **D78**, 083519 (2008b), [Erratum: Phys. Rev.D78,109901(2008)], arXiv:0807.1733 [astro-ph] p. 44.

(Matsubara, 2011) T. Matsubara, *Nonlinear Perturbation Theory Integrated with Nonlocal Bias, Redshift-space Distortions, and Primordial Non-Gaussianity*, Phys. Rev. **D83**, 083518 (2011), arXiv:1102.4619 [astro-ph.CO] p. 115.

(McDonald, 2003) P. McDonald, *Toward a measurement of the cosmological geometry at Z 2: predicting lyman-alpha forest correlation in three dimensions, and the potential of future data sets*, Astrophys. J. **585**, 34 (2003), arXiv:astro-ph/0108064 [astro-ph] p. 20.

(McDonald, 2006) P. McDonald, *Clustering of dark matter tracers: Renormalizing the bias parameters*, Phys. Rev. **D74**, 103512 (2006), [Erratum: Phys. Rev.D74,129901(2006)], arXiv:astro-ph/0609413 [astro-ph] p. 48.

(McDonald & Roy, 2009) P. McDonald & A. Roy, *Clustering of dark matter tracers: generalizing bias for the coming era of precision LSS*, JCAP **0908**, 020 (2009), arXiv:0902.0991 [astro-ph.CO] p. 48, 51.

(McDonald *et al.*, 2000) P. McDonald, J. Miralda-Escude, M. Rauch, W. L. W. Sargent, T. A. Barlow, R. Cen, & J. P. Ostriker, *The Observed probability distribution function, power spectrum, and correlation function of the transmitted flux in the Lyman-alpha forest*, Astrophys. J. **543**, 1 (2000), arXiv:astro-ph/9911196 [astro-ph] p. 20.

(Mehta *et al.*, 2011) K. T. Mehta, H.-J. Seo, J. Eckel, D. J. Eisenstein, M. Metchnik, P. Pinto, & X. Xu, *Galaxy Bias and its Effects on the Baryon Acoustic Oscillations Measurements*, Astrophys. J. **734**, 94 (2011), arXiv:1104.1178 [astro-ph.CO] p. 10.

(Meiksin *et al.*, 1999) A. Meiksin, M. J. White, & J. A. Peacock, *Baryonic signatures in large scale structure*, Mon. Not. Roy. Astron. Soc. **304**, 851 (1999), arXiv:astro-ph/9812214 [astro-ph] p. 9.

(Metropolis *et al.*, 1953) N. Metropolis, A. W. Rosenbluth, M. N. Rosenbluth, A. H. Teller, & E. Teller, *Equation of State Calculations by Fast Computing Machines*, Journal of Chemical Physics **21**, 1087 (1953) p. 163.

(Mo *et al.*, 1997) H. J. Mo, Y. P. Jing, & S. D. M. White, *High-order correlations of peaks and halos: A Step toward understanding galaxy biasing*, Mon. Not. Roy. Astron. Soc. **284**, 189 (1997), arXiv:astro-ph/9603039 [astro-ph] p. 48.

(Montesano *et al.*, 2010) F. Montesano, A. G. Sanchez, & S. Phleps, *A new model for the full shape of the large-scale power spectrum*, Mon. Not. Roy. Astron. Soc. **408**, 2397 (2010), arXiv:1007.0755 [astro-ph.CO] p. 46, 47, 71.

(Montesano *et al.*, 2012) F. Montesano, A. G. Sanchez, & S. Phleps, *Cosmological implications from the full shape of the large-scale power spectrum of the SDSS DR7 luminous red galaxies*, Mon. Not. Roy. Astron. Soc. **421**, 2656 (2012), arXiv:1107.4097 [astro-ph.CO] p. 13, 46, 47, 71, 72.

(Mukhanov, 2005) V. Mukhanov, *Physical Foundations of Cosmology* (Cambridge University Press, 2005) p. 2.

(Myers *et al.*, 2015) A. D. Myers *et al.* (BOSS Collaboration), *The SDSS-IV extended Baryon Oscillation Spectroscopic Survey: Quasar Target Selection*, Astrophys. J. Suppl. **221**, 27 (2015), arXiv:1508.04472 [astro-ph.CO] p. 20.

(Naess *et al.*, 2014) S. Naess *et al.* (ACTPol), *The Atacama Cosmology Telescope: CMB Polarization at* $200 < \ell < 9000$, J. Cosmolo. Astropart. Phys. **1410**, 007 (2014), arXiv:1405.5524 [astro-ph.CO] p. 3.

(National Institute of Standards and Technology, 1998) National Institute of Standards and Technology, "The NIST reference on constants, units, and uncertainty," `http://physics.nist.gov/cuu/index.html` (1998), [Online; accessed 05-January-2016] p. xvi.

(Navarro *et al.*, 1996) J. F. Navarro, C. S. Frenk, & S. D. M. White, *The Structure of cold dark matter halos*, Astrophys. J. **462**, 563 (1996), arXiv:astro-ph/9508025 [astro-ph] p. 42.

(Neal, 2005) R. M. Neal, *Taking Bigger Metropolis Steps by Dragging Fast Variables*, ArXiv e-prints (2005), math.ST/0502099 p. 167.

(Nishimichi & Taruya, 2011) T. Nishimichi & A. Taruya, *Baryon Acoustic Oscillations in 2D II: Redshift-space halo clustering in N-body simulations*, Phys. Rev. **D84**, 043526 (2011), arXiv:1106.4562 [astro-ph.CO] p. 51.

(Noh *et al.*, 2009) Y. Noh, M. White, & N. Padmanabhan, *Reconstructing baryon oscillations*, Phys. Rev. **D80**, 123501 (2009), arXiv:0909.1802 [astro-ph.CO] p. 10.

(Nuza *et al.*, 2013) S. E. Nuza *et al.*, *The clustering of galaxies at z 0.5 in the SDSS-III Data Release 9 BOSS-CMASS sample: a test for the LCDM cosmology, Mon. Not. Roy. Astron. Soc., 432, 743-760, 2013*, Mon. Not. Roy. Astron. Soc. **432**, 743 (2013), arXiv:1202.6057 [astro-ph.CO] p. 15.

(O'Connell *et al.*, 2015) R. O'Connell, D. Eisenstein, M. Vargas, S. Ho, & N. Padmanabhan, *Large Covariance Matrices: Smooth Models from the 2-Point Correlation Function*, ArXiv e-prints (2015), arXiv:1510.01740 [astro-ph.CO] p. 107.

(Oka *et al.*, 2014) A. Oka, S. Saito, T. Nishimichi, A. Taruya, & K. Yamamoto, *Simultaneous constraints on the growth of structure and cosmic expansion from the multipole power spectra of the SDSS DR7 LRG sample*, Mon. Not. Roy. Astron. Soc. **439**, 2515 (2014), arXiv:1310.2820 [astro-ph.CO] p. 3, 18, 51, 139.

(Padmanabhan & White, 2008) N. Padmanabhan & M. J. White, *Constraining Anisotropic Baryon Oscillations*, Phys.Rev. **D77**, 123540 (2008), arXiv:0804.0799 [astro-ph] p. 56.

(Padmanabhan *et al.*, 2009) N. Padmanabhan, M. White, & J. D. Cohn, *Reconstructing Baryon Oscillations: A Lagrangian Theory Perspective*, Phys. Rev. **D79**, 063523 (2009), arXiv:0812.2905 [astro-ph] p. 10.

(Padmanabhan *et al.*, 2012) N. Padmanabhan, X. Xu, D. J. Eisenstein, R. Scalzo, A. J. Cuesta, *et al.*, *A 2Oscillations - I : Methods and Application to the Sloan Digital Sky Survey*, Mon. Not. Roy. Astron. Soc. **427**, 2132 (2012), arXiv:1202.0090 [astro-ph.CO] p. 10, 17.

(Parejko *et al.*, 2013) J. K. Parejko *et al.* (BOSS Collaboration), *The clustering of galaxies in the SDSS-III Baryon Oscillation Spectroscopic Survey: the low redshift sample*, Mon. Not. Roy. Astron. Soc. **429**, 98 (2013), arXiv:1211.3976 [astro-ph.CO] p. 14.

(Parkinson *et al.*, 2012) D. Parkinson, S. Riemer-Sorensen, C. Blake, G. B. Poole, T. M. Davis, *et al.*, *The WiggleZ Dark Energy Survey: Final data release and cosmological results*, Phys.Rev. **D86**, 103518 (2012), arXiv:1210.2130 [astro-ph.CO] p. 10, 14.

(Paz & Sanchez, 2015) D. J. Paz & A. G. Sanchez, *Improving the precision matrix for precision cosmology*, Mon. Not. Roy. Astron. Soc. **454**, 4326 (2015), arXiv:1508.03162 [astro-ph.CO] p. 84.

(Peacock, 1998) J. Peacock, *Cosmological Physics* (Cambridge University Press, 1998) p. 2, 30.

(Peacock & Dodds, 1996) J. A. Peacock & S. J. Dodds, *Nonlinear evolution of cosmological power spectra*, Mon. Not. Roy. Astron. Soc. **280**, L19 (1996), arXiv:astro-ph/9603031 [astro-ph] p. 41.

(Peacock & Nicholson, 1991) J. A. Peacock & D. Nicholson, *The large-scale clustering of radio galaxies*, Mon. Not. Roy. Astron. Soc. **253**, 307 (1991) p. 60.

(Peacock & Smith, 2000) J. A. Peacock & R. E. Smith, *Halo occupation numbers and galaxy bias*, Mon. Not. Roy. Astron. Soc. **318**, 1144 (2000), arXiv:astro-ph/0005010 [astro-ph] p. 41, 48, 92.

(Pearson & Samushia, 2015) D. W. Pearson & L. Samushia, *Estimating the power spectrum covariance matrix with fewer mock samples*, ArXiv e-prints (2015), arXiv:1509.00064 [astro-ph.CO] p. 84.

(Peebles, 1973) P. J. E. Peebles, *Statistical Analysis of Catalogs of Extragalactic Objects. I. Theory*, Astrophys.J. **185**, 413 (1973) p. 6.

(Peebles, 1980) P. Peebles, *The Large-scale Structure of the Universe*, Princeton series in physics (Princeton University Press, 1980) p. 59.

(Peebles, 1993) P. Peebles, *Principles of Physical Cosmology*, Princeton series in physics (Princeton University Press, 1993) p. 2.

(Percival & White, 2009) W. J. Percival & M. White, *Testing cosmological structure formation using redshift-space distortions*, Mon. Not. Roy. Astron. Soc. **393**, 297 (2009), arXiv:0808.0003 [astro-ph] p. 49.

(Percival *et al.*, 2001) W. J. Percival *et al.* (2dFGRS Collaboration), *The 2dF Galaxy Redshift Survey: The Power spectrum and the matter content of the Universe*, Mon. Not. Roy. Astron. Soc. **327**, 1297 (2001), arXiv:astro-ph/0105252 [astro-ph] p. 8, 13.

(Percival *et al.*, 2002) W. J. Percival *et al.* (2dFGRS Collaboration), *Parameter constraints for flat cosmologies from CMB and 2dFGRS power spectra*, Mon. Not. Roy. Astron. Soc. **337**, 1068 (2002), arXiv:astro-ph/0206256 [astro-ph] p. 145.

(Percival *et al.*, 2007a) W. J. Percival, R. C. Nichol, D. J. Eisenstein, *et al.*, *The shape of the SDSS DR5 galaxy power spectrum*, Astrophys.J. **657**, 645 (2007a), arXiv:astro-ph/0608636 [astro-ph] p. 72.

(Percival *et al.*, 2007b) W. J. Percival, S. Cole, D. J. Eisenstein, R. C. Nichol, J. A. Peacock, A. C. Pope, & A. S. Szalay, *Measuring the Baryon Acoustic Oscillation scale using the SDSS and 2dFGRS*, Mon. Not. Roy. Astron. Soc. **381**, 1053 (2007b), arXiv:0705.3323 [astro-ph] p. 9, 13.

(Percival *et al.*, 2010) W. J. Percival *et al.* (SDSS Collaboration), *Baryon Acoustic Oscillations in the Sloan Digital Sky Survey Data Release 7 Galaxy Sample*, Mon. Not. Roy. Astron. Soc. **401**, 2148 (2010), arXiv:0907.1660 [astro-ph.CO] p. 9.

(Percival *et al.*, 2014) W. J. Percival, A. J. Ross, A. G. Sánchez, *et al.*, *The Clustering of Galaxies in the SDSS-III Baryon Oscillation Spectroscopic Survey: Including covariance matrix errors*, Mon.Not.Roy.Astron.Soc. **439**, 2531 (2014), arXiv:1312.4841 [astro-ph.CO] p. 83, 86, 109.

(Perlmutter *et al.*, 1999) S. Perlmutter *et al.* (Supernova Cosmology Project), *Measurements of Omega and Lambda from 42 high redshift supernovae*, Astrophys. J. **517**, 565 (1999), arXiv:astro-ph/9812133 [astro-ph] p. 4, 8.

(Pope & Szapudi, 2008) A. C. Pope & I. Szapudi, *Shrinkage Estimation of the Power Spectrum Covariance Matrix*, Mon. Not. Roy. Astron. Soc. **389**, 766 (2008), arXiv:0711.2509 [astro-ph] p. 84.

(Press & Schechter, 1974) W. H. Press & P. Schechter, *Formation of Galaxies and Clusters of Galaxies by Self-Similar Gravitational Condensation*, Astrophys.J. **187**, 425 (1974) p. 41.

(de Putter *et al.*, 2012) R. de Putter, C. Wagner, O. Mena, L. Verde, & W. Percival, *Thinking Outside the Box: Effects of Modes Larger than the Survey on Matter Power Spectrum Covariance*, J. Cosmolo. Astropart. Phys. **1204**, 019 (2012), arXiv:1111.6596 [astro-ph.CO] p. 88, 106, 107.

(Ratra & Peebles, 1988) B. Ratra & P. J. E. Peebles, *Cosmological consequences of a rolling homogeneous scalar field*, Phys. Rev. D **37**, 3406 (1988) p. 29.

(Reichardt *et al.*, 2012) C. Reichardt, L. Shaw, O. Zahn, K. Aird, B. Benson, *et al.*, *A measurement of secondary cosmic microwave background anisotropies with two years of South Pole Telescope observations*, Astrophys.J. **755**, 70 (2012), arXiv:1111.0932 [astro-ph.CO] p. 167.

(Reid & White, 2011) B. A. Reid & M. White, *Towards an accurate model of the redshift space clustering of halos in the quasilinear regime*, Mon. Not. Roy. Astron. Soc. **417**, 1913 (2011), arXiv:1105.4165 [astro-ph.CO] p. 160.

(Reid *et al.*, 2010) B. A. Reid, W. J. Percival, D. J. Eisenstein, L. Verde, D. N. Spergel, *et al.*, *Cosmological Constraints from the Clustering of the Sloan Digital Sky Survey DR7 Luminous Red Galaxies*, Mon.Not.Roy.Astron.Soc. **404**, 60 (2010), arXiv:0907.1659 [astro-ph.CO] p. 9, 72.

(Reid *et al.*, 2012) B. A. Reid *et al.*, *The clustering of galaxies in the SDSS-III Baryon Oscillation Spectroscopic Survey: measurements of the growth of structure and expansion rate at z=0.57 from anisotropic clustering*, Mon. Not. Roy. Astron. Soc. **426**, 2719 (2012), arXiv:1203.6641 [astro-ph.CO] p. 15, 18.

(Reid *et al.*, 2014) B. A. Reid, H.-J. Seo, A. Leauthaud, J. L. Tinker, & M. White, *A 2.5 per cent measurement of the growth rate from small-scale redshift space clustering of SDSS-III CMASS galaxies*, Mon. Not. Roy. Astron. Soc. **444**, 476 (2014), arXiv:1404.3742 [astro-ph.CO] p. 17, 18, 19.

(Reid *et al.*, 2016) B. A. Reid, S. Ho, N. Padmanabhan, *et al.* (BOSS Collaboration), *SDSS-III Baryon Oscillation Spectroscopic Survey Data Release 12: galaxy target selection and large scale structure catalogues*, Mon. Not. Roy. Astron. Soc. **455**, 1553 (2016), arXiv:1509.06529 [astro-ph.CO] p. 18, 64, 65, 66, 67, 75, 80, 108.

(Riess *et al.*, 1998) A. G. Riess *et al.* (Supernova Search Team), *Observational evidence from supernovae for an accelerating universe and a cosmological constant*, Astron. J. **116**, 1009 (1998), arXiv:astro-ph/9805201 [astro-ph] p. 4, 8.

(Riess *et al.*, 2011) A. G. Riess, L. Macri, S. Casertano, *et al.*, *A 3the Hubble Space Telescope and Wide Field Camera 3*, Astrophys.J. **730**, 119 (2011), arXiv:1103.2976 [astro-ph.CO] p. 145.

(Robertson, 1935a) H. P. Robertson, *Kinematics and World-Structure*, Astrophys. J. **82**, 284 (1935a) p. 5.

(Robertson, 1935b) H. P. Robertson, *Kinematics and World-Structure. 2*, Astrophys. J. **83**, 187 (1935b) p. 5.

(Robertson, 1936) H. P. Robertson, *Kinematics and World-Structure. 3*, Astrophys. J. **83**, 257 (1936) p. 5.

(Rodríguez-Torres *et al.*, 2015) S. A. Rodríguez-Torres *et al.*, *The clustering of galaxies in the SDSS-III Baryon Oscillation Spectroscopic Survey: Modeling the clustering and halo occupation distribution of BOSS-CMASS galaxies in the Final Data Release*, ArXiv e-prints (2015), arXiv:1509.06404 [astro-ph.CO] p. 76.

(Ross *et al.*, 2007) N. P. Ross *et al.*, *The 2dF-SDSS LRG and QSO Survey: The 2-Point Correlation Function and Redshift-Space Distortions*, Mon. Not. Roy. Astron. Soc. **381**, 573 (2007), arXiv:astro-ph/0612400 [astro-ph] p. 12.

(Ross *et al.*, 2012) A. J. Ross *et al.* (BOSS Collaboration), *The clustering of galaxies in the SDSS-III Baryon Oscillation Spectroscopic Survey: Analysis of potential systematics*, Mon.Not.Roy.Astron.Soc. **424**, 564 (2012), arXiv:1203.6499 [astro-ph.CO] p. 65, 82.

(Ross *et al.*, 2013) A. J. Ross, W. J. Percival, A. Carnero, *et al.*, *The Clustering of Galaxies in SDSS-III DR9 Baryon Oscillation Spectroscopic Survey: Constraints on Primordial Non-Gaussianity*, Mon.Not.Roy.Astron.Soc. **428**, 1116 (2013), arXiv:1208.1491 [astro-ph.CO] p. 85.

(Ross *et al.*, 2015) A. J. Ross, L. Samushia, C. Howlett, W. J. Percival, A. Burden, & M. Manera, *The clustering of the SDSS DR7 main Galaxy sample – I. A 4 per cent distance measure at* $z = 0.15$, Mon. Not. Roy. Astron. Soc. **449**, 835 (2015), arXiv:1409.3242 [astro-ph.CO] p. 3, 10, 17.

(Ross *et al.*, 2016) A. J. Ross *et al.* (BOSS Collaboration), *DR12 galaxy clustering correlation function multipole BAO measurements*, in prep. (2016) p. 20, 80, 81, 82, 141.

(Rotenberg *et al.*, 1959) M. Rotenberg, R. Bivins, N. Metropolis, & J. Wooten, *The 3-j and 6-j Symbols* (MIT Press Cambridge, MA, 1959) p. 89.

(Salazar-Albornoz *et al.*, 2016) S. Salazar-Albornoz *et al.* (BOSS Collaboration), *DR12 galaxy clustering tomography*, in prep. (2016) p. 20, 112.

(Samushia *et al.*, 2013) L. Samushia *et al.*, *The Clustering of Galaxies in the SDSS-III DR9 Baryon Oscillation Spectroscopic Survey: Testing Deviations from Λ and General Relativity using anisotropic clustering of galaxies*, Mon. Not. Roy. Astron. Soc. **429**, 1514 (2013), arXiv:1206.5309 [astro-ph.CO] p. 15.

(Samushia *et al.*, 2014) L. Samushia, B. A. Reid, M. White, *et al.*, *The clustering of galaxies in the SDSS-III Baryon Oscillation Spectroscopic Survey: measuring growth rate and geometry with anisotropic clustering*, Mon. Not. Roy. Astron. Soc. **439**, 3504 (2014), arXiv:1312.4899 [astro-ph.CO] p. 17, 18, 19.

(Samushia *et al.*, 2015) L. Samushia, E. Branchini, & W. Percival, *Geometric Biases in Power-Spectrum Measurements*, Mon. Not. Roy. Astron. Soc. **452**, 3704 (2015), arXiv:1504.02135 [astro-ph.CO] p. 61, 62, 160.

(Sanchez *et al.*, 2006) A. G. Sanchez, C. M. Baugh, W. J. Percival, J. A. Peacock, N. D. Padilla, S. Cole, C. S. Frenk, & P. Norberg, *Cosmological parameters from CMB measurements and the final 2dFGRS power spectrum*, Mon. Not. Roy. Astron. Soc. **366**, 189 (2006), arXiv:astro-ph/0507583 [astro-ph] p. 3, 9, 13.

(Sánchez *et al.*, 2008) A. G. Sánchez, C. M. Baugh, & R. Angulo, *What is the best way to measure baryonic acoustic oscillations?*, Mon.Not.Roy.Astron.Soc. **390**, 1470 (2008), arXiv:0804.0233 [astro-ph] p. 41, 53, 87, 91, 101, 104.

(Sanchez *et al.*, 2009) A. G. Sanchez, M. Crocce, A. Cabre, C. M. Baugh, & E. Gaztanaga, *Cosmological parameter constraints from SDSS luminous red galaxies: a new treatment of large-scale clustering*, Mon. Not. Roy. Astron. Soc. **400**, 1643 (2009), arXiv:0901.2570 [astro-ph.CO] p. 3, 13, 46.

(Sanchez *et al.*, 2012) A. G. Sanchez *et al.*, *The clustering of galaxies in the SDSS-III Baryon Oscillation Spectroscopic Survey: cosmological implications of the large-scale two-point correlation function*, Mon. Not. Roy. Astron. Soc. **425**, 415 (2012), arXiv:1203.6616 [astro-ph.CO] p. 15, 17.

(Sánchez *et al.*, 2013) A. G. Sánchez, E. A. Kazin, F. Beutler, *et al.*, *The clustering of galaxies in the SDSS-III Baryon Oscillation Spectroscopic Survey: cosmological constraints from the full shape of the clustering wedges*, Mon.Not.Roy.Astron.Soc. **433**, 1202 (2013), arXiv:1303.4396 [astro-ph.CO] p. 16, 18, 46, 71, 93, 96.

(Sánchez *et al.*, 2014) A. G. Sánchez, F. Montesano, E. A. Kazin, *et al.*, *The clustering of galaxies in the SDSS-III Baryon Oscillation Spectroscopic Survey: cosmological implications of the full shape of the clustering wedges in the data release 10 and 11 galaxy samples*, Mon. Not. Roy. Astron. Soc. **440**, 2692 (2014), arXiv:1312.4854 [astro-ph.CO] p. 14, 17, 18, 19, 46, 71, 94, 96, 139, 158.

(Sánchez *et al.*, 2016) A. G. Sánchez *et al.* (BOSS Collaboration), *DR12 galaxy clustering configuration space RSD measurements*, in prep. (2016) p. 20, 47, 50, 112, 121, 122, 127, 132, 139, 140, 143.

(Satpathy *et al.*, 2016) S. Satpathy, S. Alam, S. Ho, *et al.* (BOSS Collaboration), *DR12 galaxy clustering configuration space RSD measurements*, in prep. (2016) p. 20, 127, 139, 140, 141.

(Saunders *et al.*, 1991) W. Saunders, C. Frenk, M. Rowan-Robinson, A. Lawrence, & G. Efstathiou, *The density field of the local universe*, Nature **349**, 32 (1991) p. 7.

(Saunders *et al.*, 2000) W. Saunders *et al.*, *The PSCz catalogue*, Mon. Not. Roy. Astron. Soc. **317**, 55 (2000), arXiv:astro-ph/0001117 [astro-ph] p. 7.

(Schlafly & Finkbeiner, 2011) E. F. Schlafly & D. P. Finkbeiner, *Measuring Reddening with SDSS Stellar Spectra and Recalibrating SFD*, Astrophys. J. **737**, 103 (2011), arXiv:1012.4804 [astro-ph.GA] p. 80.

(Schlegel *et al.*, 2009) D. Schlegel, M. White, & D. Eisenstein (with input from the SDSS-III Collaboration), *The Baryon Oscillation Spectroscopic Survey: Precision measurements of the absolute cosmic distance scale*, ArXiv e-prints (2009), arXiv:0902.4680 [astro-ph.CO] p. 14.

(Schmidt *et al.*, 2013) F. Schmidt, D. Jeong, & V. Desjacques, *Peak-Background Split, Renormalization, and Galaxy Clustering*, Phys. Rev. **D88**, 023515 (2013), arXiv:1212.0868 [astro-ph.CO] p. 48.

(Schmittfull *et al.*, 2015) M. Schmittfull, Y. Feng, F. Beutler, B. Sherwin, & M. Y. Chu, *Eulerian BAO Reconstructions and N-Point Statistics*, Phys. Rev. **D92**, 123522 (2015), arXiv:1508.06972 [astro-ph.CO] p. 10.

(Schneider *et al.*, 2011) M. D. Schneider, S. Cole, C. S. Frenk, & I. Szapudi, *Fast generation of ensembles of cosmological N-body simulations via mode-resampling*, Astrophys.J. **737**, 11 (2011), arXiv:1103.2767 [astro-ph.CO] p. 84.

(Scoccimarro, 1998) R. Scoccimarro, *Transients from initial conditions: a perturbative analysis*, Mon. Not. Roy. Astron. Soc. **299**, 1097 (1998), arXiv:astro-ph/9711187 [astro-ph] p. 93.

(Scoccimarro, 2004) R. Scoccimarro, *Redshift-space distortions, pairwise velocities and nonlinearities*, Phys. Rev. **D70**, 083007 (2004), arXiv:astro-ph/0407214 [astro-ph] p. 39, 44, 49, 50, 112.

(Scoccimarro, 2015) R. Scoccimarro, *Fast Estimators for Redshift-Space Clustering*, Phys. Rev. **D92**, 083532 (2015), arXiv:1506.02729 [astro-ph.CO] p. 63, 76, 77.

(Scoccimarro *et al.*, 1999) R. Scoccimarro, M. Zaldarriaga, & L. Hui, *Power spectrum correlations induced by nonlinear clustering*, Astrophys.J. **527**, 1 (1999), arXiv:astro-ph/9901099 [astro-ph] p. 88, 106.

(Scoccimarro *et al.*, 2001) R. Scoccimarro, R. K. Sheth, L. Hui, & B. Jain, *How many galaxies fit in a halo? Constraints on galaxy formation efficiency from spatial clustering*, Astrophys.J. **546**, 20 (2001), arXiv:astro-ph/0006319 [astro-ph] p. 92.

(Sefusatti *et al.*, 2015) E. Sefusatti, M. Crocce, R. Scoccimarro, & H. Couchman, *Accurate Estimators of Correlation Functions in Fourier Space*, ArXiv e-prints (2015), arXiv:1512.07295 [astro-ph.CO] p. 71.

(Seljak, 2000) U. Seljak, *Analytic model for galaxy and dark matter clustering*, Mon. Not. Roy. Astron. Soc. **318**, 203 (2000), arXiv:astro-ph/0001493 [astro-ph] p. 41.

(Seljak *et al.*, 2009) U. Seljak, N. Hamaus, & V. Desjacques, *How to suppress the shot noise in galaxy surveys*, Phys. Rev. Lett. **103**, 091303 (2009), arXiv:0904.2963 [astro-ph.CO] p. 69.

(Seo & Eisenstein, 2003) H.-J. Seo & D. J. Eisenstein, *Probing dark energy with baryonic acoustic oscillations from future large galaxy redshift surveys*, Astrophys. J. **598**, 720 (2003), arXiv:astro-ph/0307460 [astro-ph] p. 13.

(Seo & Eisenstein, 2005) H.-J. Seo & D. J. Eisenstein, *Baryonic acoustic oscillations in simulated galaxy redshift surveys*, Astrophys. J. **633**, 575 (2005), arXiv:astro-ph/0507338 [astro-ph] p. 13, 53.

(Seo *et al.*, 2010) H.-J. Seo, J. Eckel, D. J. Eisenstein, *et al.*, *High-precision predictions for the acoustic scale in the non-linear regime*, Astrophys. J. **720**, 1650 (2010), arXiv:0910.5005 [astro-ph.CO] p. 10.

(Shane & Wirtanen, 1967) C. Shane & C. Wirtanen, *The Distribution of Galaxies*, Publications of the Lick Observatory of the University of California (University of California, 1967) p. 6.

(Shectman *et al.*, 1996) S. A. Shectman, S. D. Landy, A. Oemler, D. L. Tucker, H. Lin, R. P. Kirshner, & P. L. Schechter, *The Las Campanas Redshift Survey*, Astrophys. J. **470**, 172 (1996), arXiv:astro-ph/9604167 [astro-ph] p. 8.

(Sheth & Tormen, 1999) R. K. Sheth & G. Tormen, *Large scale bias and the peak background split*, Mon. Not. Roy. Astron. Soc. **308**, 119 (1999), arXiv:astro-ph/9901122 [astro-ph] p. 41, 48.

(Sirko, 2005) E. Sirko, *Initial conditions to cosmological N-body simulations, or how to run an ensemble of simulations*, Astrophys. J. **634**, 728 (2005), arXiv:astro-ph/0503106 [astro-ph] p. 87.

(Slosar *et al.*, 2013) A. Slosar *et al.*, *Measurement of Baryon Acoustic Oscillations in the Lyman-alpha Forest Fluctuations in BOSS Data Release 9*, J. Cosmolo. Astropart. Phys. **1304**, 026 (2013), arXiv:1301.3459 [astro-ph.CO] p. 20.

(Smee *et al.*, 2013) S. Smee, J. E. Gunn, A. Uomoto, N. Roe, D. Schlegel, *et al.*, *The Multi-Object, Fiber-Fed Spectrographs for SDSS and the Baryon Oscillation Spectroscopic Survey*, Astron. J. **146**, 32 (2013), arXiv:1208.2233 [astro-ph.IM] p. 14.

(Smith *et al.*, 2002) J. A. Smith *et al.* (SDSS Collaboration), *The u'g'r'i'z' Standard star system*, Astron. J. **123**, 2121 (2002), arXiv:astro-ph/0201143 [astro-ph] p. 14.

(Smith *et al.*, 2003) R. E. Smith *et al.* (The Virgo Consortium), *Stable clustering, the halo model and nonlinear cosmological power spectra*, Mon. Not. Roy. Astron. Soc. **341**, 1311 (2003), astro-ph/0207664 p. 42, 47.

(Smith *et al.*, 2008) R. E. Smith, R. Scoccimarro, & R. K. Sheth, *Eppur Si Muove: On The Motion of the Acoustic Peak in the Correlation Function*, Phys. Rev. **D77**, 043525 (2008), arXiv:astro-ph/0703620 [ASTRO-PH] p. 41, 87.

(Spergel *et al.*, 2003) D. N. Spergel *et al.* (WMAP Collaboration), *First year Wilkinson Microwave Anisotropy Probe (WMAP) observations: Determination of cosmological parameters*, Astrophys. J. Suppl. **148**, 175 (2003), arXiv:astro-ph/0302209 [astro-ph] p. 8.

(Spergel *et al.*, 2007) D. N. Spergel *et al.* (WMAP Collaboration), *Wilkinson Microwave Anisotropy Probe (WMAP) three year results: implications for cosmology*, Astrophys. J. Suppl. **170**, 377 (2007), arXiv:astro-ph/0603449 [astro-ph] p. 9.

(Springel, 2005) V. Springel, *The Cosmological simulation code GADGET-2*, Mon.Not.Roy.Astron.Soc. **364**, 1105 (2005), arXiv:astro-ph/0505010 [astro-ph] p. 40, 93.

(Springel *et al.*, 2001) V. Springel, S. D. White, G. Tormen, & G. Kauffmann, *Populating a cluster of galaxies. 1. Results at z = 0*, Mon.Not.Roy.Astron.Soc. **328**, 726 (2001), arXiv:astro-ph/0012055 [astro-ph] p. 40, 93.

(Sun *et al.*, 2013) L. Sun, Q. Wang, & H. Zhan, *Likelihood of the Power Spectrum in Cosmological Parameter Estimation*, Astrophys.J. **777**, 75 (2013), arXiv:1306.5064 [astro-ph.CO] p. 85.

(Suzuki *et al.*, 2012) N. Suzuki, D. Rubin, C. Lidman, G. Aldering, R. Amanullah, *et al.*, *The Hubble Space Telescope Cluster Supernova Survey: V. Improving the Dark Energy Constraints Above z>1 and Building an Early-Type-Hosted Supernova Sample*, Astrophys.J. **746**, 85 (2012), arXiv:1105.3470 [astro-ph.CO] p. 4, 167.

(Szalay *et al.*, 2003) A. S. Szalay *et al.* (SDSS Collaboration), *KL estimation of the power spectrum parameters from the angular distribution of galaxies in early SDSS data*, Astrophys. J. **591**, 1 (2003), arXiv:astro-ph/0107419 [astro-ph] p. 8.

(Tadros *et al.*, 1999) H. Tadros *et al.*, *Spherical harmonic analysis of the pscz galaxy catalogue: redshift distortions and the real-space power spectrum*, Mon. Not. Roy. Astron. Soc. **305**, 527 (1999), arXiv:astro-ph/9901351 [astro-ph] p. 7, 12.

(Takada & Hu, 2013) M. Takada & W. Hu, *Power Spectrum Super-Sample Covariance*, Phys.Rev. **D87**, 123504 (2013), arXiv:1302.6994 [astro-ph.CO] p. 106, 107.

(Takahashi *et al.*, 2012) R. Takahashi, M. Sato, T. Nishimichi, A. Taruya, & M. Oguri, *Revising the Halofit Model for the Nonlinear Matter Power Spectrum*, Astrophys. J. **761**, 152 (2012), arXiv:1208.2701 [astro-ph.CO] p. 42, 47.

(Taruya *et al.*, 2010) A. Taruya, T. Nishimichi, & S. Saito, *Baryon Acoustic Oscillations in 2D: Modeling Redshift-space Power Spectrum from Perturbation Theory*, Phys. Rev. **D82**, 063522 (2010), arXiv:1006.0699 [astro-ph.CO] p. 50, 51, 90.

(Taruya *et al.*, 2011) A. Taruya, S. Saito, & T. Nishimichi, *Forecasting the Cosmological Constraints with Anisotropic Baryon Acoustic Oscillations from Multipole Expansion*, Phys. Rev. **D83**, 103527 (2011), arXiv:1101.4723 [astro-ph.CO] p. 63.

(Taruya *et al.*, 2012) A. Taruya, F. Bernardeau, T. Nishimichi, & S. Codis, *RegPT: Direct and fast calculation of regularized cosmological power spectrum at two-loop order*, Phys. Rev. **D86**, 103528 (2012), arXiv:1208.1191 [astro-ph.CO] p. 51.

(Taylor & Hamilton, 1996) A. N. Taylor & A. J. S. Hamilton, *Nonlinear cosmological power spectra in real and redshift space*, Mon. Not. Roy. Astron. Soc. **282**, 767 (1996), arXiv:astro-ph/9604020 [astro-ph] p. 37.

(Taylor & Joachimi, 2014) A. Taylor & B. Joachimi, *Estimating Cosmological Parameter Covariance*, Mon. Not. Roy. Astron. Soc. **442**, 2728 (2014), arXiv:1402.6983 [astro-ph.CO] p. 83, 86.

(Taylor *et al.*, 2013) A. Taylor, B. Joachimi, & T. Kitching, *Putting the Precision in Precision Cosmology: How accurate should your data covariance matrix be?*, Mon.Not.Roy.Astron.Soc. **432**, 1928 (2013), arXiv:1212.4359 [astro-ph.CO] p. 83, 86, 97.

(Tegmark *et al.*, 2002) M. Tegmark *et al.* (SDSS Collaboration), *The Angular power spectrum of galaxies from Early SDSS Data*, Astrophys. J. **571**, 191 (2002), arXiv:astro-ph/0107418 [astro-ph] p. 8.

(Tegmark *et al.*, 2004a) M. Tegmark *et al.* (SDSS Collaboration), *Cosmological parameters from SDSS and WMAP*, Phys. Rev. **D69**, 103501 (2004a), arXiv:astro-ph/0310723 [astro-ph] p. 8.

(Tegmark *et al.*, 2004b) M. Tegmark *et al.* (SDSS Collaboration), *The 3-D power spectrum of galaxies from the SDSS*, Astrophys. J. **606**, 702 (2004b), arXiv:astro-ph/0310725 [astro-ph] p. 8, 13.

(Tinker *et al.*, 2008) J. L. Tinker, A. V. Kravtsov, A. Klypin, K. Abazajian, M. S. Warren, G. Yepes, S. Gottlöber, & D. E. Holz, *Toward a halo mass function for precision cosmology: The Limits of universality*, Astrophys.J. **688**, 709 (2008), arXiv:0803.2706 [astro-ph] p. 41, 94.

(Tinker *et al.*, 2016) J. L. Tinker *et al.* (BOSS Collaboration), *DR12 galaxy clustering RSD challenge*, in prep. (2016) p. 20, 120.

(Tojeiro *et al.*, 2012) R. Tojeiro *et al.*, *The clustering of galaxies in the SDSS-III Baryon Oscillation Spectroscopic Survey: measuring structure growth using passive galaxies*, Mon. Not. Roy. Astron. Soc. **424**, 2339 (2012), arXiv:1203.6565 [astro-ph.CO] p. 15.

(Tojeiro *et al.*, 2014) R. Tojeiro *et al.*, *The clustering of galaxies in the SDSS-III Baryon Oscillation Spectroscopic Survey: galaxy clustering measurements in the low redshift sample of Data Release 11*, Mon. Not. Roy. Astron. Soc. **440**, 2222 (2014), arXiv:1401.1768 [astro-ph.CO] p. 16, 17.

(Tonry & Davis, 1979) J. Tonry & M. Davis, *A survey of galaxy redshifts. I - Data reduction techniques*, Astron.J. **84**, 1511 (1979) p. 6.

(de la Torre *et al.*, 2013) S. de la Torre *et al.*, *The VIMOS Public Extragalactic Redshift Survey (VIPERS). Galaxy clustering and redshift-space distortions at z=0.8 in the first data release*, Astron. Astrophys. **557**, A54 (2013), arXiv:1303.2622 [astro-ph.CO] p. 14.

(Uhlemann *et al.*, 2015) C. Uhlemann, M. Kopp, & T. Haugg, *Edgeworth streaming model for redshift space distortions*, Phys. Rev. **D92**, 063004 (2015), arXiv:1503.08837 [astro-ph.CO] p. 160.

(Vargas-Magaña *et al.*, 2016) M. Vargas-Magaña *et al.* (BOSS Collaboration), *DR12 galaxy clustering BAO systematics*, in prep. (2016) p. 20.

(Verde, 2007) L. Verde, *A practical guide to Basic Statistical Techniques for Data Analysis in Cosmology*, ArXiv e-prints (2007), arXiv:0712.3028 [astro-ph] p. 161.

(Verde *et al.*, 2002) L. Verde *et al.*, *The 2dF Galaxy Redshift Survey: The Bias of galaxies and the density of the Universe*, Mon. Not. Roy. Astron. Soc. **335**, 432 (2002), arXiv:astro-ph/0112161 [astro-ph] p. 12.

(Vikman, 2005) A. Vikman, *Can dark energy evolve to the phantom?*, Phys. Rev. **D71**, 023515 (2005), arXiv:astro-ph/0407107 [astro-ph] p. 29.

(Vogeley *et al.*, 1992) M. S. Vogeley, M. J. Geller, & J. P. Huchra, *Large scale clustering of galaxies in the CfA redshift survey*, Astrophys. J. **391**, L5 (1992) p. 7.

(Wagner *et al.*, 2015) C. Wagner, F. Schmidt, C.-T. Chiang, & E. Komatsu, *Separate Universe Simulations*, Mon. Not. Roy. Astron. Soc. **448**, L11 (2015), arXiv:1409.6294 [astro-ph.CO] p. 87.

(Walker, 1937) A. G. Walker, *On Milne's Theory of World-Structure*, Proceedings of the London Mathematical Society **s2-42**, 90 (1937), http://plms.oxfordjournals.org/content/s2-42/1/90.full.pdf+html p. 5.

(Weinberg, 1972) S. Weinberg, *Gravitation and cosmology: principles and applications of the General Theory of Relativity* (Wiley, New York, NY, USA, 1972) pp. xxviii + 657 p. 2, 25.

(Weinberg, 2008) S. Weinberg, *Cosmology* (Oxford University Press, Walton Street, Oxford OX2 6DP, UK, 2008) pp. xvii + 593 p. 2, 33.

(White, 1994) S. D. M. White, *Formation and evolution of galaxies: Lectures given at Les Houches, August 1993*, in *Summer School on Cosmology and Large Scale Structure (Session 60) Les Houches, France, August 1-28, 1993* (1994) arXiv:astro-ph/9410043 [astro-ph] p. 93.

(White, 2005) M. J. White, *Baryon oscillations*, Astropart. Phys. **24**, 334 (2005), arXiv:astro-ph/0507307 [astro-ph] p. 9.

(White *et al.*, 2011) M. White *et al.*, *The clustering of massive galaxies at z 0.5 from the first semester of BOSS data*, Astrophys. J. **728**, 126 (2011), arXiv:1010.4915 [astro-ph.CO] p. 15.

(White *et al.*, 2014) M. White, J. L. Tinker, & C. K. McBride, *Mock galaxy catalogs using the quick particle mesh method*, Mon.Not.Roy.Astron.Soc. **437**, 2594 (2014), arXiv:1309.5532 [astro-ph.CO] p. 76.

(White *et al.*, 2015) M. White, B. Reid, C.-H. Chuang, J. L. Tinker, C. K. McBride, F. Prada, & L. Samushia, *Tests of redshift-space distortions models in configuration space for the analysis of the BOSS final data release*, Mon.Not.Roy.Astron.Soc. **447**, 234 (2015), arXiv:1408.5435 [astro-ph.CO] p. 91.

(Wilson *et al.*, 2015) M. J. Wilson, J. A. Peacock, A. N. Taylor, & S. de la Torre, *Rapid modelling of the redshift-space power spectrum multipoles for a masked density field*, ArXiv e-prints (2015), arXiv:1511.07799 [astro-ph.CO] p. 74, 89.

(Xu *et al.*, 2013) X. Xu, A. J. Cuesta, N. Padmanabhan, D. J. Eisenstein, & C. K. McBride, *Measuring D_A and H at $z = 0.35$ from the SDSS DR7 LRGs using baryon acoustic oscillations*, Mon. Not. Roy. Astron. Soc. **431**, 2834 (2013), arXiv:1206.6732 [astro-ph.CO] p. 15, 17.

(Yamamoto *et al.*, 2006) K. Yamamoto, M. Nakamichi, A. Kamino, B. A. Bassett, & H. Nishioka, *A Measurement of the quadrupole power spectrum in the clustering of the 2dF QSO Survey*, Publ.Astron.Soc.Jap. **58**, 93 (2006), arXiv:astro-ph/0505115 [astro-ph] p. 60.

(Yoo & Seljak, 2015) J. Yoo & U. Seljak, *Wide Angle Effects in Future Galaxy Surveys*, Mon. Not. Roy. Astron. Soc. **447**, 1789 (2015), arXiv:1308.1093 [astro-ph.CO] p. 57, 60, 63, 90, 160.

(York *et al.*, 2000) D. G. York *et al.* (SDSS Collaboration), *The Sloan Digital Sky Survey: Technical Summary*, Astron. J. **120**, 1579 (2000), arXiv:astro-ph/0006396 [astro-ph] p. 6, 8.

(Zel'dovich, 1970) Y. B. Zel'dovich, *Gravitational instability: An approximate theory for large density perturbations.*, Astron. Astrophys. **5**, 84 (1970) p. 12, 37, 38.

(Zhao *et al.*, 2015) C. Zhao, F.-S. Kitaura, C.-H. Chuang, F. Prada, G. Yepes, & C. Tao, *Halo mass distribution reconstruction across the cosmic web*, Mon. Not. Roy. Astron. Soc. **451**, 4266 (2015), arXiv:1501.05520 [astro-ph.CO] p. 76.

(Zhao *et al.*, 2016) G.-B. Zhao, Y. Wang, A. J. Ross, *et al.*, *The extended Baryon Oscillation Spectroscopic Survey (eBOSS): a cosmological forecast*, Mon. Not. Roy. Astron. Soc. **457**, 2377 (2016), arXiv:1510.08216 [astro-ph.CO] p. 20, 151, 159.

(Zheng *et al.*, 2007) Z. Zheng, A. L. Coil, & I. Zehavi, *Galaxy Evolution from Halo Occupation Distribution Modeling of DEEP2 and SDSS Galaxy Clustering*, Astrophys.J. **667**, 760 (2007), arXiv:astro-ph/0703457 [ASTRO-PH] p. 93.

(Zwicky, 1933) F. Zwicky, *Die Rotverschiebung von extragalaktischen Nebeln*, Helvetica Physica Acta **6**, 110 (1933) p. 5.

(Zwicky, 1937) F. Zwicky, *On the Masses of Nebulae and of Clusters of Nebulae*, Astrophys.J. **86**, 217 (1937) p. 5.

(Zwicky & Kowal, 1968) F. Zwicky & C. T. Kowal, *"Catalogue of Galaxies and of Clusters of Galaxies", 1968, Volume VI Pasadena: California Institute of Technology, CGCG6"* (1968) p. 6.

(Zwicky *et al.*, 1961) F. Zwicky, E. Herzog, P. Wild, M. Karpowicz, & C. T. Kowal, *Pasadena: California Institute of Technology (CIT), |c1961* (1961) p. 6.

Acknowledgements

First, I want to express my gratitude to my thesis supervisor Prof. Dr. Ralf Bender for giving me the great opportunity to conduct research in cosmology at such renominated institutions that the University Observatory of the LMU Munich and the Max Planck Institute for Extraterrestrial Physics are. Very special thanks go to my research advisor Dr. Ariel Sánchez who helped a lot in shaping my project, gave invaluable advice with his excellent expertise in large-scale structure research, was a very patient counsel in times of writing this thesis, and who is just an extremely nice guy to work with. Without his great guidance I would have soon been lost in the jungle that working with the BOSS collaboration is. I would like to thank Prof. Dr. Eiichiro Komatsu at the neighbouring Max Planck Institute for Astrophysics for being in my thesis advisory board and writing the second referee report for my thesis, and for initiating and supporting the great scientific exchange between his LSS research group and ours. I thank Stefanie Phleps and Daniel Farrow for also sitting in and contributing to my thesis advisory board meetings.

Foremost of all my fellow PhD candiates I am grateful to Salvador Salazar-Albornoz for being a great colleague and having provided so many cosmological advice, tools and samples such as the HOD modelling of the Minerva galaxies. Running the Minerva simulations would not have been possible without the support of Claudio Dalla Vecchia (now at IAC, Tenerife). Francesco Montesano is to be thanked for laying down the groundwork for the power spectrum analysis in our group. Special thanks go to Martha Lippich for proofreading my thesis and to the full LSS team at MPE for counselling on its content and layout. Further, I thank our group members Jiamin Hou and Riccardo Bolze for helpful discussions during our meetings.

Besides all the intense and constructive exchange in the BOSS galaxy clustering working group, I acknowledge fruitful discussions with Román Scoccimarro, Martín Crocce, Héctor Gil-Marín, Francisco-Shu Kitaura, Ashley J. Ross, Jeremy L. Tinker, Rita Tojeiro, Chia-Hsun Chuang, Sergio Rodríguez-Torres, Antonio J. Cuesta, and Florian Beutler.

Among my colleagues and fellow PhD candidates at MPE, MPA, and USM, I would like to point out Chi-Ting Chiang and Christian Wagner for inspiring exchange, Daniel Grün for

constructive cooperation preparing and conducting tutorials, and Philipp Wullstein, Michael Opitsch, Philipp Lang, and Steffen Hagstotz for nice general support in the hard times of conducting research for a PhD. Everybody in the OPINAS group at MPE had his or her part in providing pleasant distraction in all the lunch and coffee breaks. Rob Yates, Henrike Ohlendorf, Dominika Wylezalek, Johannes Buchner, Marie-Luise Menzel, Laura Morselli, Julián Alvarado-Gómez, Philip Wiseman, and Vlas Sokolov have been great fellow PhD representatives at our IMPRS of Astrophysics. Further, among other PhD representatives at the various Max Plank Institutes in Munich, Xixi Feng, Mary Gazea, and Hendrik Vogel have given good advice for collaboration across institutes and fields. Within the Max Planck PhDnet, to which I served in 2013 as financial officer, I would like to thank 2014 Spokesperson Prateek Mahalwar for having taken such a thankworthy responsibility and just being great.

I acknowledge support from the Transregional Collaborative Research Centre TR33 'The Dark Universe' of the German Research Foundation (DFG). The computationally very expensive parts of the analysis have been performed on MPE's computing cluster for the *Euclid* project and the *Hydra* cluster at the Rechenzentrum Garching (RZG) which is now named the Max Planck Computing and Data Facility (MPCDF).

Funding for SDSS-III has been provided by the Alfred P. Sloan Foundation, the Participating Institutions, the National Science Foundation, and the U.S. Department of Energy Office of Science. The SDSS-III web site is http://www.sdss3.org/.

SDSS-III is managed by the Astrophysical Research Consortium for the Participating Institutions of the SDSS-III Collaboration including the University of Arizona, the Brazilian Participation Group, Brookhaven National Laboratory, Carnegie Mellon University, University of Florida, the French Participation Group, the German Participation Group, Harvard University, the Instituto de Astrofisica de Canarias, the Michigan State/Notre Dame/JINA Participation Group, Johns Hopkins University, Lawrence Berkeley National Laboratory, Max Planck Institute for Astrophysics, Max Planck Institute for Extraterrestrial Physics, New Mexico State University, New York University, Ohio State University, Pennsylvania State University, University of Portsmouth, Princeton University, the Spanish Participation Group, University of Tokyo, University of Utah, Vanderbilt University, University of Virginia, University of Washington, and Yale University.

Based on observations obtained with *Planck* (http://www.esa.int/Planck), an ESA science mission with instruments and contributions directly funded by ESA Member States, NASA, and Canada.

Nun noch einige Dankesworte in meiner Muttersprache, denn ich möchte mich ganz besonders bei meinen Eltern Gerhard und Beate, meinen Großeltern Heinrich, Elisabeth, Günther und Anna-Maria sowie meinen beiden jüngeren Schwestern Lisa und Nele für unendliche Unterstützung, familiäre Nähe und ein schönes Leben abseits des wissenschaftlichen Umfeldes bedanken. Ihnen habe ich auch meine Arbeit gewidmet. Ferner danke ich Jonas Schmöle, André Kochanke, Steffen Klemer, Jörn Hartung und Rabea Sandmann dafür, mich an der Uni Göttingen während der Bachelor- und Masterarbeit weiter auf vertiefende Forschung in der Physik und Kosmologie eingestimmt zu haben.